Cenozoic exhumation patterns across the Venezuelan Andes: insights from fission-track thermochronology

Mauricio Alberto Bermudez Cella

▶ **To cite this version:**

Mauricio Alberto Bermudez Cella. Cenozoic exhumation patterns across the Venezuelan Andes: insights from fission-track thermochronology. Applied geology. Université Joseph-Fourier - Grenoble I, 2009. English. NNT : . tel-00450838

HAL Id: tel-00450838
https://theses.hal.science/tel-00450838

Submitted on 27 Jan 2010

HAL is a multi-disciplinary open access archive for the deposit and dissemination of scientific research documents, whether they are published or not. The documents may come from teaching and research institutions in France or abroad, or from public or private research centers.

L'archive ouverte pluridisciplinaire **HAL**, est destinée au dépôt et à la diffusion de documents scientifiques de niveau recherche, publiés ou non, émanant des établissements d'enseignement et de recherche français ou étrangers, des laboratoires publics ou privés.

Université Joseph Fourier-Grenoble I

Thèse

Présentée par
Mauricio A BERMÚDEZ CELLA
pour l'obtention du grade de

Docteur en Sciences
de l'Université Joseph Fourier-Grenoble I

Cenozoic exhumation patterns across the Venezuelan Andes: insights from fission-track thermochronology

Exhumation Cénozoïque dans les Andes Vénézuéliennes: apport de la thermochronologie par traces de fission

Soutenue publiquement le 23, Novembre 2009 devant le jury composé de:

Bernard Colletta	Rapporteur
Edward Sobel	Rapporteur
Franck Audemard	Examinateur
John Garver	Examinateur
Etienne Jaillard	Examinateur
Peter van der Beek	Directeur de thèse
Matthias Bernet	Directeur de thèse

À mon épouse, *Isabel Cristina*, qui remplit ma vie de joie et qui donne sens à mon existence.
À la suite de ce grand amour entre nous deux: *Joachim David*.
À mes parents, *Ildemaro* et *María Rosa*.

REMERCIEMENTS

À Dieu pour son aide infinie et pour avoir mis sur mon chemin toutes les personnes suivantes:

Peter van der Beek: un grand merci, pour m'avoir accepté comme ton thésard, pour m'avoir donnée l'occasion de travailler avec toi, pour tes conseils, pour toute l'aide que tu m'as donnée, et pour ton intérêt à faire de moi un réel géologue.

Matthias Bernet: merci chef (jefe), pour tous tes conseils, pour m'avoir donné l'occasion de travailler avec toi, pour tes enseignements, pour m'avoir donné ton inestimable amitié, pour m'avoir écouté dans les moments de stress, et pour être un grand être humain.

À l'Université Central du Venezuela (UCV), et au CDCH-UCV pour m'avoir donné l'aide financière sans laquelle il n'aurait pas été possible d'atteindre cet objectif.

Barry Kohn: merci pour ton inestimable aide, pour tes conseils, pour ta confiance et pour ton intérêt à travailler dans les Andes Vénézuéliennes.

Carina Hoorn pour son aide et ses conseils.

Je suis reconnaisant à Etienne Jaillard, John Garver, Bernard Colleta, Ed Sobel et Franck Audemard qui ont accepté de faire partie de mon jury.

Christoph Glozbach: danke meines freund, pour m'avoir écouté ami, pour ta patience, et pour ta disposition à toujours de m'aider.

À toute ma famille Papá et Mamá, mes frères: Miguel, Jhorman, Ildemaro; mes sœurs: Jhorylma et Aicilef. À Yajaira, et à ma nièce Yaima, pour être l'espoir de ma maison. Grace à vous je suis qui je suis

À ma belle mère Gladys pour ton son aide, leurs conseils, la patience, et pour faciliter la mission de terrain. Merci à toute mon famille des Andes de Mérida pour le soutien pendant ces années. À toute ma famille de Maturin, mon beau père, belle sœurs, et Francisco.

À Pedro Alson pour son amitié et des conseils fournis au bon moment.

À Ricardo, Gatsbyd, Liz et Ricardo Alejandro.

À la grande famille du Laboratoire de Géodynamique des Chaînes Alpines (LGCA): François Senebier, Claudie Senebier, Claudine Meugniot, Rodolphe Pinon, Matthieu Corazzi, Pascale Talour, Jean Braun, Pascal Huyghes, Julien Carcaillet (un grand merci mon ami), Brice Randrinasolo, Vincent Bouvier, Andrea Amortegui, Abir Chihaoui, Pierre Valla, Xavier Robert, les deux Thibaud, Fabien, les deux Romain, François Chirouze, Antoine, Charlotte, Violaine, Jérémie, Jérome, et toutes les personnes que j'ai eu l'occasion de rencontrer au LGCA.

À Jorge Mora, Griselda Zorrilla, María Esculpi, Rebeca Sánchez, Carolina Torres, Morella Mikatti, Luis Chacón, Olga Rey, Sebastián Grande, Ricardo Alezones, Juan Flores, Antonio León, Freddy Sojo, Eduardo Carrillo et Crelia Padrón.

À tous les personnes qui m'ont aidé et de qui je ne me rappelle pas les noms…

ABSTRACT

This dissertation presents the results and observations of an investigation on the long-term (Miocene to present) exhumation history of the Venezuelan Andes, and the relationships between inherited structures and development of topography in response to tectonic and surface processes. The Venezuelan Andes are ideal for understanding the relationships between these processes, because they have involved through inversion and reactivation of pre-existing structures, they are associated with a major climatic gradient due to the orograpic effect of the belt and extensive data is available concerning their recent tectonic evolution. This mountain belt is the result of transpression caused by oblique convergence of the continental Maracaibo block and the South America Plate, controlled, on a larger scale, by the triple junction between the South American, Caribbean and Nazca plates. The complex kinematics of triple plate interaction and the continuous evolution of related structures coupled with surface processes have profoundly affected the evolution of the Venezuelan Andes.

An extensive low-temperature thermochronometer database composed of 47 new apatite fission-track (AFT) ages: 24 bedrock samples, 15 samples from synorogenic detrital sediments and 8 samples from modern rivers sediments is presented in this dissertation. The dataset is supplemented with 27 previously unpublished AFT bedrock ages and 10 revised AFT ages provided by B.P. Kohn. The AFT ages are converted into long-term exhumation rates using thermal modeling. Analyses of in-situ AFT data from seven tectonically delineated areas reveal variable exhumation patterns across the Venezuelan Andes. The Caparo and Valera blocks, which were separated by dextral movement along the Boconó strike-slip fault system, respectively have AFT ages ranging from 7 to 27 Ma, and 11 to 145 Ma, representing areas of relatively slow exhumation. In the central part of the Venezuelan Andes, AFT ages in the Sierra La Culata (5-8 Ma), El Carmen (2-3 Ma) and Sierra Nevada (5-8 Ma) blocks, record major recent exhumation in response to transpression and erosion along the Boconó fault system. To both sides of the chain, AFT ages in the Escalante block (5-6 Ma) on the far northern flank, and the Cerro Azul thrust block (5-8 Ma AFT age) on the southern flank provide evidence of significant compression, which produced the doubly vergent structure of the Venezuelan Andes during Late Miocene times. Fission-track analysis of detrital apatite from modern river samples permit a) verification and extrapolation of the bedrock cooling age patterns across the Venezuelan Andes, b) determination of sediment provenance, and c) analysis of relationships between exhumation rates and potential controlling factors. The results imply a strong correlation between relief and long-term exhumation rate but a lack of correlation between long-term exhumation rate and present-day precipitation or seismic energy release (measured during the last 20 years), indicating that the control of tectonic and/or climatic processes on exhumation cannot be discerned in a straightforward manner.

Fission-track data from synorogenic sediments in the Maracaibo and Barinas foreland basins permit tracing the present-day exhumation patterns back to the Late Miocene. Rock-Eval analyses of sediments sampled show that Mio-Pliocene sediments in these basins have not been buried deeper than the AFT partial annealing zone in the studied sections. Young AFT ages in samples from the Parángula Formation on the south flank imply that this formation is probably of Tortonian age, significantly younger than previously suggested. The AFT data, together with pollen analyses, imply that the Pliocene Betijoque Formation to the north corresponds in age to the upper part of the Río Yuca Formation to the south of the Venezuelan Andes.

Keywords: Venezuelan Andes, bedrock and detrital apatite fission-track, thermochronology, exhumation, thermal models, foreland basin, erosion, relief, climate, Boconó fault, strike-slip faults, transpression, tectonics, geodynamic.

RÉSUMÉ

Cette thèse présente les résultats d'une étude de l'histoire à long terme (Miocène – actuel) de l'exhumation des Andes vénézuéliennes, ses rapports avec des structures héritées et le développement de la topographie en réponse à la tectonique et les processus de surface. Les Andes vénézuéliennes constituent un exemple idéal pour étudier les rapports entre ces processus. Elles montrent des inversions et réactivations de structures pré-existantes et sont associées à un gradient climatique majeur dû à l'effet orographique de la chaîne. Par ailleurs, de nombreuses données sont disponibles concernant leur récente évolution tectonique. Cette chaîne de montagne résulte de la transpression causée par la convergence oblique du bloc continental de Maracaibo et de la plaque Amérique du Sud contrôlée, à plus grande échelle, par la jonction triple entre les plaques Amérique du Sud, Caraïbe et Nazca. La cinématique complexe de cette interaction triple et l'évolution continue des structures qui y sont liées, couplée avec les processus de surface, ont profondément affecté l'évolution des Andes vénézuéliennes.

Une base de données thermochronologiques de basse température est présentée dans cette thèse, composée de 47 nouveaux âges par traces de fission sur apatite (AFT): 24 échantillons in-situ provenant du substratum rocheux, 15 échantillons de sédiments synorogéniques et 8 échantillons de sédiments de rivières actuelles. La base de données a été augmentée de 27 âges AFT du substratum rocheux et 10 âges AFT existants ont été révisés, ces derniers 37 âges ayant été fournis par B.P Kohn (Université de Melbourne, Australie). Les âges AFT ont été convertis en taux d'exhumation à long terme en utilisant des modélisations numériques de l'évolution thermique. Les analyses des données AFT in-situ ont permis de délimiter sept blocs tectoniques avec des histoires d'exhumation variables à travers les Andes Vénézuéliennes. Les blocs de Caparo et de Valera sur les deux extrémités de la chaîne, qui ont été séparés par le mouvement dextre de la faille du Boconó, montrent des âges entre 7 et 27 Ma et entre 11 et 145 Ma respectivement. Ces blocs représentent des zones d'exhumation relativement lente. Dans la partie centrale des Andes Vénézuéliennes, les âges AFT des blocs de la Sierra La Culata (5-8 Ma), d'El Carmen (2-3 Ma) et de la Sierra Nevada (5-8 Ma) enregistrent une exhumation majeure récente qui répond à la transpression et l'érosion au long du système de failles du Boconó. Sur les deux flancs de la chaîne, les âges AFT dans le bloc d'El Escalante (5-6 Ma) au nord, et le bloc chevauché du Cerro Azul (5-8 Ma âge AFT) au sud indiquent une phase de compression importante, à l'origine de la structure à double vergence des Andes vénézuéliennes, pendant le Miocène Supérieur. Les analyses AFT sur apatite détritique dérivé de l'échantillonnage des rivières actuelles ont permis a) d'extrapoler les âges in-situ à travers les Andes vénézuéliennes, b) de déterminer la provenance des sédiments, et c) d'analyser les rapports entre taux d'exhumation et les facteurs de contrôle potentiels. Les résultats indiquent une forte corrélation entre le relief et le taux d'exhumation à long terme mais une absence de corrélation entre les taux d'exhumation à long terme et les précipitations actuelles ou la libération d'énergie sismique (mesurées au cours des 20 dernières années), indiquant que le contrôle de la tectonique et / ou des processus climatiques sur l'exhumation ne peut être distingué d'une manière simple.

L'analyse AFT sur des sédiments syn-orogéniques des bassins d'avant-pays de Maracaibo et de Barinas ont permis d'établir un schéma de l'exhumation depuis le Miocène tardif jusqu'à l'actuel. Des analyses Rock-Eval sur sédiments Mio-Pliocènes montrent que ces séries n'ont pas été enfouies plus profondément que la zone de recuit partiel des AFT (PAZ), au moins sur les sections étudiées. Des âges AFT jeunes dans des échantillons provenant de la Formation Parángula sur le flanc sud indiquent que cette formation a probablement un âge Miocène moyen, nettement plus jeune que précédemment admis. Les données AFT combinées avec des analyses palynologiques révèlent que la Formation Pliocène de Betijoque sur le flanc nord correspond à la partie supérieure de la Formation Río Yuca au sud des Andes vénézuéliennes.

Mots-clés: Andes Vénézuéliennes, thermochronologie par traces de fission sur apatites in-situ et détritiques, exhumation, modèles thermiques, bassin d'avant-pays, l'érosion, le relief, le climat, la faille de Boconó, failles décrochantes, transpression, la tectonique, geodynamique.

RESUMEN

Este trabajo investiga la historia de exhumación a gran escala (>1 Ma) y las relaciones entre estructuras heredadas y desarrollo de la topografía en respuesta los procesos tectónicos y superficiales que ocurren en un orógeno activo. Los Andes de Venezuela constituyen un área ideal para entender tales procesos, debido a que esta cadena es el resultado de la transpresión causada por la convergencia oblicua de dos bloques continentales: Maracaibo y Suramérica. A una escala mayor, la interacción entre esos bloques es controlada por la triple convergencia de la Placa del Caribe, la Placa Suraméricana y la Placa de Nazca. Si se considera la complejidad de este margen activo en conjunto con la acción de los procesos superficiales, todo esto altera de forma significativa la evolución del paisaje de Los Andes Venezolanos.

Esta tesis presenta 47 nuevos datos termocronológicos mediante trazas de fisión en apatitos: (24 in-situ, 15 de sedimentos synorogénicos y 8 de sedimentos actuales de ríos) con el propósito de interpretar las edades de trazas de fisión en apatitos en el contexto de exhumación a gran escala y utilizar modelado numérico de la historia termal. Esta base de datos fue completada con 27 edades de trazas de fisión en apatitos y 10 edades revisadas no publicadas, las cuales fueron suministradas por B.P Kohn de la Universidad de Melbourne, en Australia. Los análisis basados sobre las edades de apatitos “in-situ” revelan al menos siete areas con diferentes patrones de exhumación a lo largo de Los Andes. Los bloques de Caparo y Valera con edades de 7 a 27 Ma, y 11 a 145 Ma, respectivamente, representan las zonas más antiguas, que fueron separadas por el movimiento rumbo-deslizante destral del sistema de fallas de Boconó. En la parte central de la cadena y cercanos al sistema de fallas de Boconó, tres bloques: la Sierra La Culata (5-8 Ma), El Carmen (2-3 Ma) y la Sierra Nevada (5-8 Ma) reflejan una importante componente vertical, en respuesta a la transpresión y la erosión a lo largo de ese sistema de fallas. A ambos lados de la cadena, los bloques Escalante (5-6 Ma) en la parte norte y Cerro Azul (5-8 Ma) en la parte sur, proporcionan fuertes indicios de que la convergencia produce una estructura con doble vergencia durante el Mioceno tardío.

Las edades determinadas sobre las muestras de ríos modernos, permiten: a) verificar y extrapolar los patrones de exhumación a lo largo de la cadena, b) determinar la proveniencia sedimentaria y c) analizar las relaciones entre los patrones de exhumación y los factores potenciales que pudieran controlar dichos patrones. Los resultados sugieren una fuerte correlación (0.95) entre el relieve y los patrones de exhumación a largo plazo; y una pérdida de correlación entre la exhumación a largo plazo y los valores de precipitación promedio y/o energía sísmica liberada (durante los últimos 20 años) indican que los posibles controles ejercidos por procesos tectónicos y/o climáticos actuales sobre los patrones de exhumación no pueden ser determinados de una manera lineal.

Las edades obtenidas mediante termocronología por trazas de fisión en apatitos sobre los sedimentos sinorogénicos, pertenecientes a las formaciones: Betijoque en la cuenca de Maracaibo; Río Yuca y Parángula pertenecientes a la cuenca Barinas-Apure permiten analizar la proveniencia, transporte, depositación y subsidencia de las rocas sedimentarias en esas cuencas. Los análisis de materia orgánica (Rock-Eval) indican que las formaciones Betijoque y Río Yuca no fueron lo suficientemente soterradas para generar hidrocarburos, de lo cual se deduce que no ocurran fenómenos de borrados de trazas de fisión. Así, la primera componente de edades por trazas de fisión discriminada en esos sedimentos pueden ser utilizados como una aproximación a la edad de depositación. Edades recientes (9-11 Ma) encontradas en la Formación Parángula implican que esta última fue depositada durante la etapa Tortoniana, lo cual es significativamente más joven que la edad actualmente asumida. Los resultados termocronológicos en conjunto con los análisis palinógicos, sugieren que la Formación Betijoque (en el flanco norte) de edad Pliocena es correlacionable con el tope de la Formación Río Yuca en el flanco surandino.

Palabras claves: Andes de Venezuela, termocronología por trazas de fisión sobre apatitos in-situ y detríticos, exhumación, modelo termal, cuencas antepaís, erosión, relieve, clima, Falla de Boconó, fallas rumbo-deslizantes, transpresión, tectónica, geodinámica.

CONTENTS

Chapter 1

I. GENERAL INTRODUCTION

1.0 Introduction

The topography of a mountain belt is the result of competition between tectonically driven surface uplift, which increases topography, and erosion, which reduces topography and forms relief. In this manner, tectonic and surface processes can be positively or negatively coupled. Discriminating and categorizing these processes in their order of importance is not a simple task because the processes do not necessarily operate on the same time scales and at the same rates, resulting in a generally long and complex history that is recorded by the geology and geomorphology of a mountain belt.

In actively uplifting mountain belts surface processes are erosional, eliminating the record of past rock uplift (Fig. 1.1). Sedimentary basins adjacent to such mountain belts are usually filled with sediments that contain the record of past exhumation. The study of the thermal history of upper crustal rocks by *low-temperature thermochronology* provides information on rock uplift and exhumation on geological timescales. The vertical motion of rocks over time, according to England and Molnar (1990) and Ring et al. (1999) are summarized in two important concepts. First *denudation* is the difference between rock uplift and surface uplift. It describes the removal of material from the rock column by surface and/or tectonic processes. Second, *exhumation* describes the process by which rock material is brought closer to the Earth surface because of denudation. Thus, the amount of exhumation is equal to the amount of denudation.

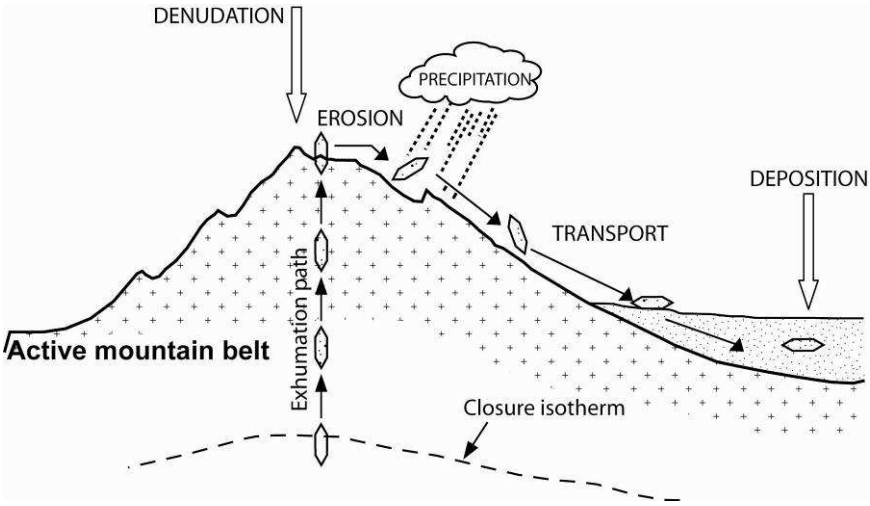

Fig. 1.1. Interactions among exhumation, denudation, erosion, transport, and deposition process across an active orogen (Modified from Crowley et al. 1989).

The basics of fission-track thermochronology are reviewed in chapter 3. Thermal histories can be extracted from fission track ages and track-length data in apatites using empirical equations that relate time, temperature, fission-track length, and fission-track density (e.g., Ketcham et al. 1999).

The orogenic life-cycle in general includes three phases of topographic growth, equilibrium, and decay (Jamieson and Beaumont, 1989). During these phases erosion rates vary in response to temporal and spatial changes in climate, topographic relief and slope, and deformation. The application of fission-track thermochronology on minerals that have been eroded, transported and deposited in adjacent basins is call *detrital fission-track thermochronology* (Wagner and Van den Haute, 1992; Naeser et al. 1989). Detrital apatite fission-track (AFT) thermochronology on samples collected from synorogenic basin deposits or modern rivers is a well established tool for quantifying erosion histories during orogenic evolution, as well as for establishing sediment provenance and landscape evolution (e.g. Garver et al. 1999).

Detrital or bedrock fission-track analysis has been widely used during the last three decades to constrain the low-temperature thermal histories of numerous igneous, metamorphic and sedimentary rocks in diverse geological settings. These include orogenic belts, rifted margins, faults, sedimentary basins and cratons, among others. The types of geologic problems that can be addressed include the timing and rates of tectonic events, sedimentary basin evolution, the timing of hydrocarbon generation, the absolute age of volcanic deposits, the effects of major climatic changes on the near-surface geothermal gradient, and long-term landscape evolution

(Gallagher et al. 1998; Gleadow and Brown, 2000; Blythe et al. 2000, 2002; Spotila et al. 2002).

For two reasons the Venezuelan Andes constitute an interesting target for using AFT thermochronology to study the relationships between climate, exhumation, and tectonic process. First, the Venezuelan Andes are located along the active margin of South America, whose geodynamical setting is complicated and varied rapidly over geologic time (Fig. 1.2). Second, the Venezuelan Andes separate two of the major petroleum bearing basins of Venezuela, the Maracaibo basin and the Barinas-Apure basin (Fig. 1.2). The Maracaibo basin is one of the most prolific hydrocarbon basins in the world, where over 40 billion barrels of hydrocarbons have been produced (James, 2000a, b; Escalona, 2003). The Barinas-Apure basin is the third largest oil-producing basin of Venezuela. It has an extension of about 95,000 km² and a maximum sediment depth of about 5 km in its centre (James, 2000a, b; Jácome and Chacín, 2008).

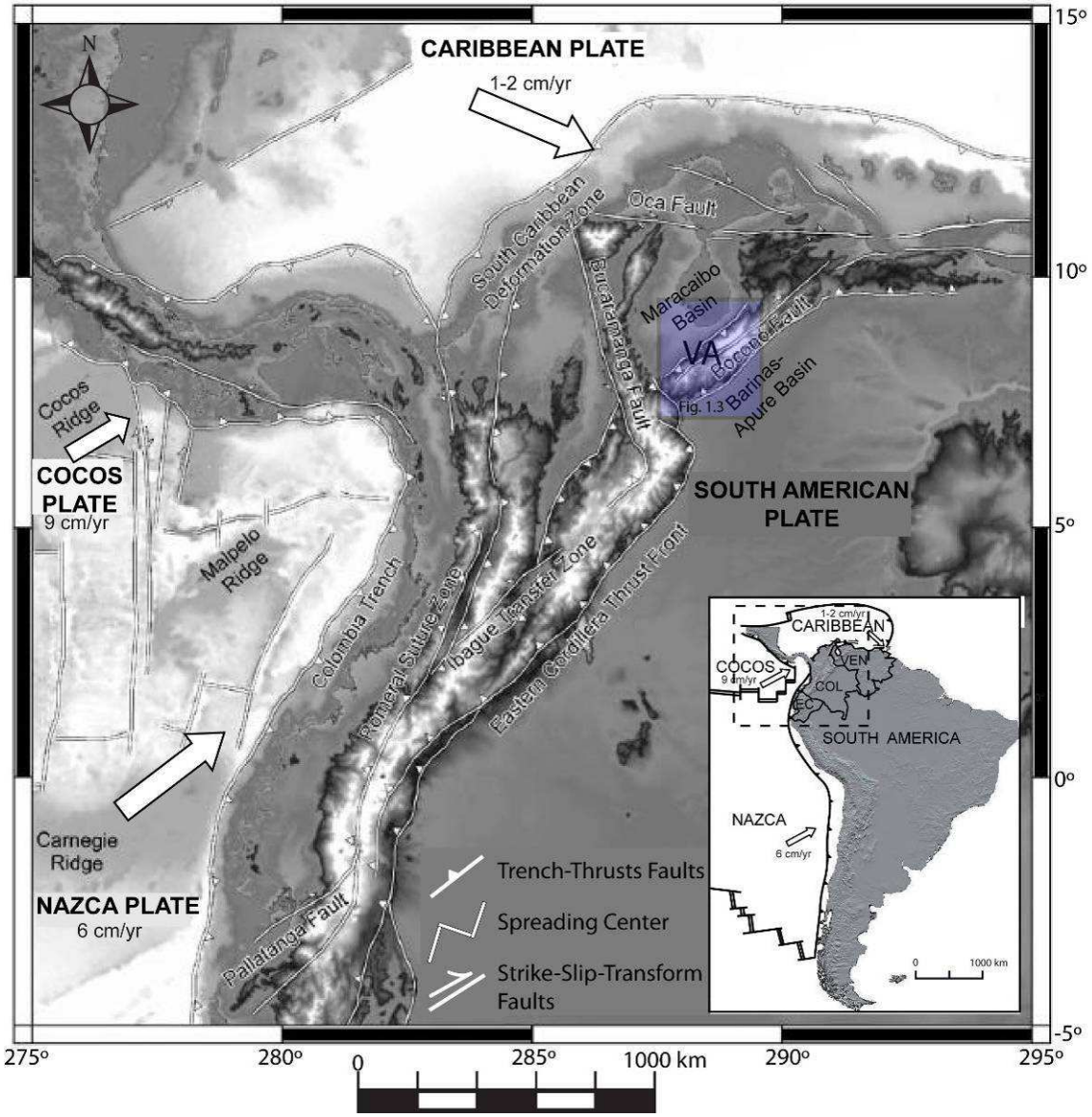

Fig. 1.2. Regional tectonic map of northwestern South America showing the present-fay configuration of the Nazca, Cocos, South American and Caribbean plates, and the main tectonic features in the Northern Andes (Modified from Corredor, 2003).

The origin of the present-day Venezuelan Andes and its hydrocarbon basins is related to complex interactions between the Caribbean, South American and Nazca plates (Fig. 1.2), which generate on a regional scale the oblique convergence and transpression between the Maracaibo continental blocks and the South America plate (Colletta et al. 1997). This collision has led to fault reactivation in strike-slip and thrusting modes, and rotation of individual blocks.

The goal of this dissertation is to apply AFT thermochronology on bedrock and detrital samples to quantify the exhumation history of the Venezuelan Andes in the geodynamic context of the Northern Andes, besides studying in general the exhumation patterns associated

with continental strike-slip faulting in transpressive settings (Spotila et al. 2007a, b; Cruz et al. 2007). In this dissertation, the first detailed thermochronologic study in the Venezuelan Andes since the work of Kohn et al. (1984) and Shagam et al. (1984) is presented. I constrain exhumation in the Venezuelan Andes using mainly AFT thermochronology (on 24 bedrock samples, 15 synorogenic and 8 modern rivers samples, Fig. 1.3), but also quantitative methods for data interpretation, such as thermal history and Pecube modeling (Braun, 2003; Ketcham, 2005; Braun et al. 2006). These results are complemented with data on precipitation and seismicity, palynology, and organic matter analysis of synorogenic sediments. The purpose of this work was testing the following hypotheses: (1) Exhumation patterns vary spatially in the Venezuelan Andes, (2) inherited structures control these variable exhumation patterns, (3) tectonics and erosion are not independently operating processes but are strongly coupled, which would imply a correlation between short- and long-term processes, (4) exhumation patterns are faithfully reflected in detrital thermochronology data.

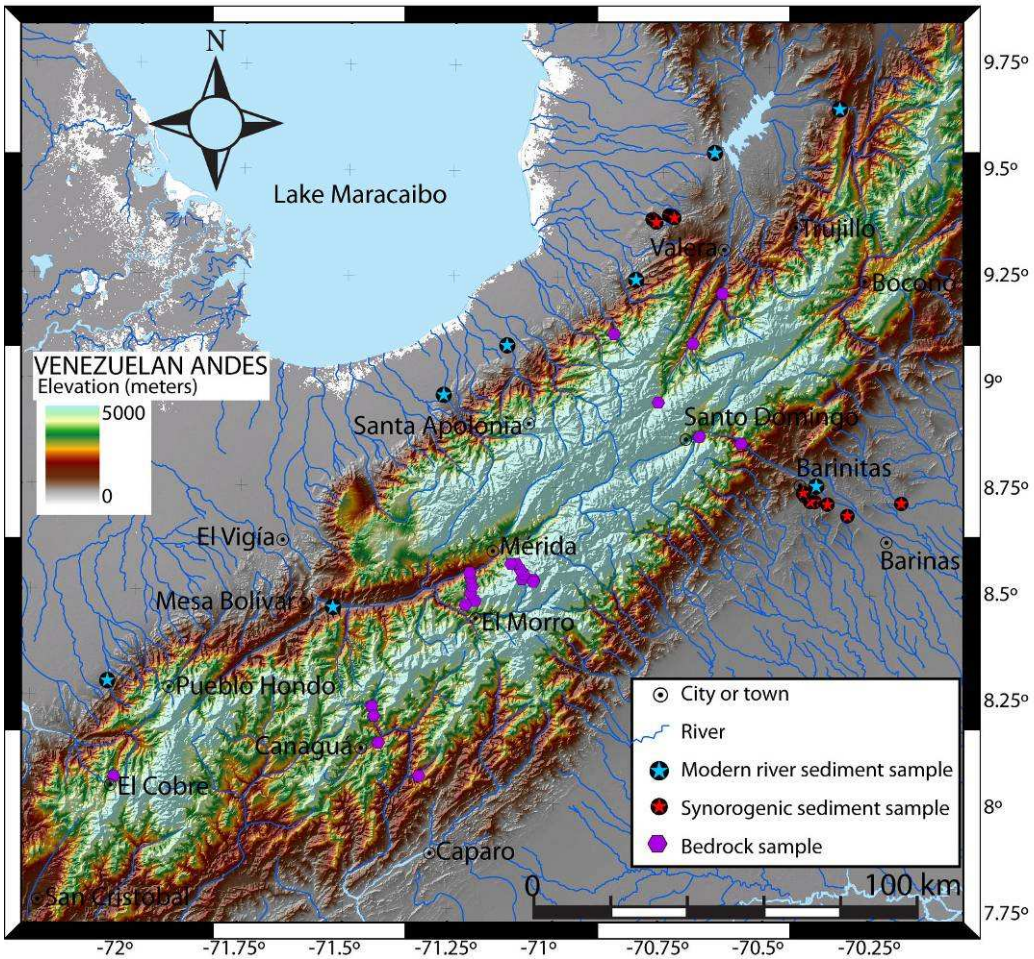

Fig. 1.3. Digital elevation model of the Venezuelan Andes with the samples location for AFT thermochronology collected in this work.

1.1 Overview of chapters and results

This dissertation comprises three introductory chapters, four manuscripts (ready for submission to international journals) containing the main results, conclusions, synthesis and an appendix section. The second chapter (after this introduction) presents the main theories and models developed to explain the origin of the Venezuelan Andes in a plate tectonic context. In this chapter the different current tectonic models and present-day geodynamic setting are also presented. The third chapter, AFT thermochronology and quantitative methods for interpreting the data are presented. The four chapter (manuscript one) include a large number of samples comprising the entire in-situ AFT dataset. Topographical analyses are included in this manuscript to show geomorphic differences between blocks that are exhumed at different rates in distinct episodes. Barry Kohn (University of Melbourne, Australia) has provided me with twenty four new ages and ten revised ages, which contributed significantly to the AFT database and facilitated its interpretation. In the second manuscript (chapter 5), 3-D forward modeling using the Pecube code (Braun, 2003; Braun et al. 2006) and HeFTy code (Ketcham, 2005) is used to interpret two age-elevation profiles in the central Venezuelan Andes, the first collected by Kohn et al. (1984) and the second during this work. Manuscript three (chapter 6) extends the temporal scale by including eight modern river samples. Correlations between long-term exhumation rates and short-term potential controlling factors are developed. Manuscript 4 (chapter 7) extends the database to synorogenic sediments exposed at both flanks of the Venezuelan Andes. These sediments are the product of erosion of the Venezuelan Andes; thus, it is possible to analyze the relations among exhumation, transport, sedimentation, burial and recycling across the foothills by combining multidisciplinary methods (detrital apatite fission-track thermochronology, palynology, petrology and organic matter characterization).

Findings from these four manuscripts address the presented hypotheses. It is in fact possible to distinguish different exhumation patterns, which are controlled by inherited tectonic structures that are the product of rifting during separation of Africa, South and North America. The major dextral Boconó strike-slip fault system was possibly present before Eocene times (Schubert, 1982) and produced the separation between the Caparo and Valera Blocks. Two blocks in the central part of the Venezuelan Andes, the Sierra Nevada and Sierra la Culata, present contrasting cooling histories and are the direct result of surface uplift by transpression and erosion, produced by the collision between the Maracaibo block and South American

continent. The two blocks record significant vertical movements on the dextral Boconó strike-slip fault system. At 8 Ma, maximum surface uplift is achieved in the Sierra Nevada, which coincides with major drainage reorganization, involving the Orinoco and Magdalena rivers, as suggested by Hoorn et al. (1995) or Díaz de Gamero (1996).

Detrital AFT thermochronology results are consistent with the AFT bedrock results, and point to at least five stages of continuous exhumation around 2-3 Ma, 3-5 Ma, 5-8 Ma, 8-15 Ma and 15-30 Ma. These phases are associated with regional tectonic events that occurred across the Northern Andes (Cooper et al. 1995; Murdock et al. 1997; Parra et al. 2009). The intervals between 2-3 and 3-5 can be related to final closure of the Panama Isthmus (Murdock et al. 1997; Grafë et al. 2002). From 5 to 8 Ma occurred the accommodation of the Maracaibo Block, caused by the compression of the Panamá arc in the western part of South America and movement of the Caribbean plate to the north (Cruz et al. 2007). This compression produced reactivation of different branches of the Boconó fault system. During 8-15 Ma compression and inversion associated with the formation of the frontal fold and thrust belt of the Eastern Cordillera have led to rapid exhumation/surface uplift rates in the Northern Andes (Parra et al. 2009). According to Montes et al. (2005), during this interval the Maracaibo Block arrived in its current position. During the phase between 15 and 30 Ma, accretion of the Eastern Cordillera in Colombia against the southwestern part of the Venezuelan Andes occurred (Caparo and Trujillo or Valera Blocks). AFT ages older than 30 Ma in the Venezuelan Andes can be associated with old paleotopography created during an early compressional deformation event that affected the Magdalena Valley and the western margin of the Eastern Cordillera due to an increase in convergence rates between the Nazca and South American plates (Pardo-Casas and Molnar, 1987; Daly, 1989). An age of 145 Ma found to the north of the Valera Granite can be related to the Triassic-Early Cretaceous Rift basins developed as a result of the separation of North and South America, when the Caribbean opened (~235–130 Ma); this is the synrift megasequence (Cooper et al. 1995).

1.2 Publications and abstracts from this dissertation

1.2.1 Publications

Bermúdez, M.A., Kohn, B.P., van der Beek, P., Bernet, M., O'Sullivan P.B., Shagam, R., Spatial and temporal patterns of exhumation across the Venezuelan Andes: Implications for Cenozoic Caribbean geodynamics, to be submitted to *Tectonics* (Chapter 4).

Bermúdez, M.A., van der Beek, P., Bernet, M., Thermochronologic evidence for km-scale vertical offset across the Boconó strike-slip fault, central Venezuelan Andes, to be submitted to *Geology* (Chapter 5)

Bermúdez, M.A., Bernet, M., van der Beek, P., Tectonic versus climatic control on exhumation in the Venezuelan Andes, to be submitted to *Earth and Planetary Science Letters* (Chapter 6).

Bermúdez, M.A., Bernet, M., Hoorn, C., van der Beek, P., Mora, J., Carrillo, E., Neogene relations among sedimentation, exhumation, and recycling in the Mérida Andes foothills: an integrated vision of detrital apatite fission-track thermochronology, palinology and organic matter characterization, to be submitted to *Basin Research* (Chapter 7).

Bermúdez, M.A, Glotzbach, C., Alson, P., New Poissonian Method for determining fission-track ages, to be submitted to *Mathematical Geology* (Appendix 1).

Bermúdez-Cella, M., 2008, Detección de mezclas Poisson por p-Partición. *Divulgaciones Matemáticas*, 16, 1, 73-86. (Appendix 2).

Bermúdez-Cella, M., López, A., Bálcazar-García, M., Zarazúa-Ortega, G., Bona, R., 2009, Caracterización de Cristales de Apatito y Circón del Estándar Internacional Fish Canyon Tuff para su uso en un Laboratorio de Termocronología, *Interciencia*, vol. 34, No. 4, p. 240-246. (Appendix 3).

1.2.2 Abstracts

Bermúdez, M.A., van der Beek, P., Bernet, M., 2008, *Spatial and temporal patterns of exhumation across the Venezuelan Andes from in-situ and detrital apatite fission-track analysis: Implications for Cenozoic Caribbean geodynamics*. 11th International Conference on Thermochronometry, 16-20 September 2008, Anchorage-Alaska.

Bermúdez, M.A., van der Beek, P., Bernet, M., 2008, *Spatial and temporal patterns of exhumation across the Venezuelan Andes from apatite fission-track analysis:*

Implications for Cenozoic Caribbean geodynamics. 7th International Symposium on Andean Geodynamics (ISAG) 2-4 September 2008, Nice-France.

Bermúdez, M.A., van der Beek, P., Bernet, M., 2008, *Fission-track thermochronological evidence for km-scale vertical offsets across the Boconó strike-slip fault, central Venezuelan Andes*. European Geosciences Union (EGU) General Assembly, 13-18 April 2008, Vienna-Austria.

Bermúdez, M.A., Alson, P., 2008, *p-partition and Methodology Alternating Proposal (MAP): new statistic-mathematical methodology that involves uranium densities to estimate ages of rocks by means of fission track dating.* European Conference on Thermochronology, 30 July to 4 August 2008, Bremen-Germany.

Chapitre 1

I. INTRODUCTION GÉNÉRALE

1.0 Introduction

La topographie des chaînes de montagnes résulte de la concurrence entre la tectonique, qui fait croître le relief, et les processus de surface, qui le réduisent. Ainsi, les processus tectoniques et de surface peuvent être couplés avec des rétro-actions positives ou négatives. Discriminer et catégoriser ces processus selon leur importance relative n'est pas une tâche simple car que les processus n'opèrent pas nécessairement sur les mêmes échelles de temps, ni avec les mêmes taux, et résultent généralement en une histoire longue et complexe enregistrée par la géologie et géomorphologie d'une chaîne de montagnes.

Dans les chaînes de montagnes sujettes au soulèvement tectonique, les processus de surface sont généralement érosives, éliminant ainsi l'histoire passée du soulèvement (Fig. 1.1). Les bassins sédimentaires adjacents aux chaînes sont remplis de sédiments qui archivent l'histoire d'exhumation passée. L'étude de l'histoire thermique de la croute supérieure en utilisant la *thermochronologie de basse température* donne des informations sur le soulèvement et l'exhumation des roches sur les échelles de temps géologiques. England et Molnar (1990) et Ring et al. (1999) ont résumé deux concepts importants concernant le mouvement vertical des roches avec le temps. Premièrement, la *dénudation* est la différence entre le soulèvement des roches et le soulèvement de la surface. Ce terme décrit l'enlèvement de matière de la colonne de roche à cause des processus tectoniques et/ou de surface. Deuxièmement, l'*exhumation* décrit le processus de rapprochement des roches de la surface de la terre à cause de la dénudation. Ainsi, la quantité d'exhumation est égale à la quantité de dénudation.

Les bases de la thermochronologie par traces de fission sont passées en revue dans le Chapitre 3. Une histoire thermique peut être extraite des âges et des données de longueurs des traces de fission dans les apatites avec l'aide d'équations empiriques qui associent le temps, la température, les longueurs et la densité des traces de fission (par exemple, Ketcham et al. 1999).

En général, le cycle de vie d'un orogène comprend trois phases: une phase de croissance topographique, d'équilibre et de décroissance (Jamieson et Beaumont, 1989). Les taux d'érosion peuvent varier au cours de ces phases en réponse aux changements temporels et

spatiaux du climat, du relief et de la déformation. L'application de la thermochronologie par traces de fission sur les minéraux érodés, transportés et déposés dans les bassins adjacents est appellée *thermochronologie détritique* (Wagner et Van den Haute, 1992; Naeser et al. 1989). La thermochronologie détritique par traces de fission sur apatites (AFT) prélevés de dépôts sédimentaires synorogéniques ou de rivières actuelles est devenu un outil bien établi pour quantifier l'histoire d'érosion au cours de l'évolution orogénique, ainsi que pour établir la provenance des sédiments et l'évolution du relief (e.g., Garver et al. 1999).

Des analyses AFT détritiques ou *in-situ* (sur des échantillons prélevés du substratum rocheux) ont été largement utilisé au cours des trois dernières décennies pour contraindre l'histoire thermique à basse température de nombreuses roches ignées, métamorphiques et sédimentaires dans divers contextes géologiques. De nombreux travaux ont notamment ciblé les ceintures orogéniques, les marges divergentes, les failles, les bassins sédimentaires et les cratons, entre autres. Les types de problèmes géologiques abordés comprennent le calendrier et les taux d'événements tectoniques, l'évolution des bassins sédimentaires, le timing de la production d'hydrocarbures, l'âge absolu de dépôts volcaniques, les effets des changements climatiques sur le gradient géothermique, et l'évolution à long terme du relief (Gallagher et al. 1998; Gleadow et Brown, 2000; Blythe et al. 2000, 2002; Spotila et al. 2002).

Les Andes vénézuéliennes constituent une cible intéressante pour l'utilisation de la thermochronologie AFT, dans le but d'étudier les relations entre le climat, l'exhumation et le processus tectoniques, pour deux raisons: premièrement, les Andes du Venezuela sont situés au long de la marge active d'Amérique du Sud, ou le contexte géodynamique est compliqué et a varié rapidement au cours des temps géologiques (Fig. 1.2). Deuxièmement, les Andes vénézuéliennes séparent deux des plus importants réservoirs pétroliers du Venezuela, le bassin de Maracaibo et le bassin de Barinas-Apure (Fig. 1.2). Le bassin de Maracaibo est un des réservoirs pétroliers les plus prolifiques au monde, où plus de 40 milliards de barils d'hydrocarbures ont été produits (James, 2000a, b; Escalona, 2003). Le bassin de Barinas-Apure est le troisième plus grand gisement de production pétrolière du Venezuela. Ce bassin a une extension d'environ 95.000 km² et une profondeur maximale de sédiments d'environ 5 km dans son centre (James, 2000a, b; Jácome et Chacín, 2008).

L'origine de l'actuelle chaîne des Andes vénézuéliennes et ses bassins pétroliers est liée à des interactions complexes entre les plaques Caraïbe, Amérique du Sud et Nazca (Fig. 1.2) qui

produisent, à l’échelle régionale, la convergence oblique et la transpression entre le bloc continental de Maracaibo et la plaque Amérique du Sud (Colletta et al. 1997). Cette collision a produit la réactivation de différentes structures avec des mouvements décrochants, inverses ou normaux, ainsi que la rotation de blocs.

Le but de cette thèse est d'appliquer la thermochronologie AFT sur des échantillons provenant du substrat rocheux et des échantillons détritiques, afin de quantifier l'histoire d'exhumation des Andes vénézuéliennes dans le contexte géodynamique des Andes du Nord. Plus en général, la thèse traite des modèles d'exhumation liée au mouvement de failles décrochantes dans les milieux transpressifs (Spotila et al. 2007; Cruz et al. 2007). Cette thèse représente la première étude thermochronologique détaillée dans les Andes vénézuéliennes depuis les travaux de Kohn et al. (1984) et de Shagam et al. (1984). Je quantifie l'exhumation dans les Andes vénézuéliennes en utilisant principalement la méthode des traces de fission sur apatites (sur 24 échantillons de socle, 15 échantillons de sédiments synorogéniques et 8 échantillons de sédiments de rivières actuels, Fig. 1.3), mais j’ai également utilisé des méthodes quantitatives pour l'interprétation de ces données, telles que des modélisations de l'histoire thermique des échantillons (Ketcham, 2005) et de l’évolution thermique de la croute, ce dernier en utilisant le code Pecube (Braun, 2003; Braun et al. 2006). Ces résultats sont complétés par des données de précipitation et de sismicité, ainsi que des données palynologiques et des analyses de la matière organique des sédiments synorogéniques. Le but de ce travail a été de tester les hypothèses suivantes: (1) l’histoire d'exhumation varie spatialement au long des Andes vénézuéliennes, (2) les structures héritées contrôlent cette variabilité de l'exhumation, (3) la tectonique et l'érosion ne sont pas des processus qui fonctionnent indépendamment mais sont fortement couplés, ce qui impliquerait une corrélation entre les processus sur le court- et sur le long-terme, (4) la variabilité spatiale de l'exhumation est fidèlement enregistrée par la thermochronologie détritique.

1.1 Résumé des chapitres et principaux résultats

Cette thèse est comprise par trois chapitres d'introduction, quatre manuscrits (prêts à soumettre à des revues internationales) qui contiennent les principaux résultats, une conclusion et synthèse, et des annexes. Le premier chapitre après cette introduction présente les principaux différents théories et modèles qui ont été développés pour expliquer l'origine

des Andes vénézuéliennes dans le contexte de la tectonique des plaques. Dans ce chapitre sont également présentés les différents modèles tectoniques proposés aujourd'hui et le contexte géodynamique actuel de la chaîne. Le troisième chapitre présente les aspects théoriques de la thermochronologie par traces de fission sur apatite ainsi que les méthodes quantitatives pour interpréter ces données. Dans le premier manuscrit (Chapitre 4), notre base de données thermochronologiques *in-situ* entière est considérée. Ce manuscrit inclut également des analyses topographiques, afin de mettre en évidence des différences géomorphologiques entre les blocs qui sont exhumés à différentes vitesses et pendant des épisodes distincts. Barry Kohn (Université de Melbourne, Australie) m'a fourni vingt-quatre nouveaux âges et dix âges révisés qui ont contribué considérablement à compléter la base de données et ont facilité son interprétation. Dans le deuxième manuscrit (Chapitre 5), des modèles numériques en utilisant les codes Pecube (Braun, 2003; Braun et al. 2006) et HeFTy (Ketcham et al. 2005) sont utilisés pour interpréter deux profils âge - altitude récoltés dans les Andes vénézuéliennes centrales, le premier par Kohn et al. (1984) et le second pendant ce travail. Le troisième manuscrit (Chapitre 6) étend l'échelle temporelle en incluant huit échantillons de rivières actuelles. Dans ce manuscrit des corrélations entre les taux d'exhumation à long terme et de facteurs tectoniques ou climatiques (sismicité, précipitation) qui pourraient contrôler l'exhumation, mais qui sont enregistrés à court terme, ont été établies. Le quatrième manuscrit (Chapitre 7) étend la base de données aux sédiments syn-orogéniques affleurants sur les deux flancs des Andes vénézuéliennes. Ces sédiments sont le produit de l'érosion de la chaîne : ainsi, il est possible d'analyser les relations entre exhumation, transport, sédimentation, enfouissement et recyclage dans les piedmonts en combinant des méthodes pluridisciplinaires (thermochronologie par AFT détritique, palynologie, pétrologie et caractérisation de la matière organique).

Les résultats de ces quatre manuscrits adressent les hypothèses présentées. Il est possible de distinguer différents modèles d'exhumation, qui sont contrôlés par des structures tectoniques héritées, produits du rifting lors de la séparation entre l'Afrique, l'Amérique du Sud et l'Amérique du Nord. Le système de failles décrochant dextre du Boconó était peut-être déjà présent dès l'Eocène (Schubert, 1982) et a produit la séparation entre les blocs de Caparo et de Valera. Deux blocs dans la partie centrale des Andes vénézuéliennes, la Sierra Nevada et la Sierra La Culata, présentent des histoires de refroidissement contrastantes ; les phases de refroidissement enregistrées sont le résultat direct du soulèvement de surface et de l'érosion produits par transpression liée à la collision entre le bloc de Maracaibo et le continent sud-

américain. Les différentes histoires de refroidissement entre les deux blocs enregistrent d'importants mouvements verticaux sur la Faille du Boconó. A 8 Ma le soulèvement de surface dans la Sierra Nevada atteint son maximum ; ce timing coïncide avec la réorganisation de différents paléo-drainages de l'Orénoque Rivier et de la Rivière Magdalena, comme suggéré précédemment par Hoorn et al. (1995) ou Díaz de Gamero (1996).

Les résultats thermochronologiques sur apatites détritiques sont cohérents avec les résultats obtenus dans le socle, et permettent de discriminer au moins cinq différents stades d'exhumation en continu autour de 2-3 Ma, 3-5 Ma, 5-8 Ma, 8-15 Ma et 15-30 Ma. Ces phases sont associées à des événements tectoniques régionaux qui ont eu lieu à travers des Andes du Nord (Cooper et al. 1995; Murdock et al. 1996; Parra et al. 2009). Les intervalles entre 2-3 et 3-5 Ma peuvent être liés à la fermeture définitive de l'isthme de Panama (Murdock et al. 1996; Grafé et al. 2002). De 5 au 8 Ma a eu lieu l'accommodation du bloc de Maracaibo, causé par la compression de l'arc de Panama dans la partie occidentale de l'Amérique du Sud et le mouvement de la plaque Caraïbe au nord (Cruz et al. 2007). Cette compression est responsable de la réactivation des différentes branches du système de failles de Boconó. Pendant l'intervalle 8-15 Ma se produit la compression et l'inversion associées à la déformation de la Cordillère Orientale colombienne ; cette phase a généré une exhumation rapide associée à un soulèvement de surface de surface dans les Andes du Nord (Parra et al. 2009). Selon Montes et al. (2005), le bloc de Maracaibo est parvenu dans sa position actuelle au cours de cet intervalle. Au cours de la phase entre 15 et 30 Ma, l'accrétion de la Cordillère Orientale colombienne contre la partie sud-ouest des Andes vénézuéliennes produit l'exhumation de deux blocs de Caparo et de Valera qui à cette époque n'étaient pas encore séparés par le mouvement sur la faille de Boconó. Des âges AFT de plus de 30 Ma dans les Andes du Venezuela peuvent être associés à une paléo-topographie créée pendant des phases de déformation par compression qui ont affecté la vallée de la Magdalena et la marge occidentale de la Cordillère Orientale, en raison d'une augmentation des taux de convergence entre la plaque Nazca et la plaque sud-américaine (Pardo-Casas et Molnar, 1987; Daly, 1989). Un âge de 145 Ma trouvé au nord du Granite de Valera peut être lié à la formation de bassins entre le Trias inférieur et le Crétacé, en conséquence du rifting menant à la séparation entre l'Amérique du Nord et l'Amérique du Sud, lorsque les bassins des Caraïbes s'ouvrent (~ 235-130 Ma).

Capítulo 1

I. INTRODUCCIÓN GENERAL

1.0 Introducción

La topografía actual que las montañas exhiben es el resultado de dos procesos que actúan en competición el *levantamiento superficial o "surface-uplift"*, el cual incrementa la topografía, y la *erosión* la cual la reduce y forma el relieve. De esta manera, los procesos tectónicos y superficiales pudieran ser positivamente o negativamente correlacionados. Discriminar y categorizar estos procesos en orden de importancia no es una tarea sencilla, debido a que tales procesos no necesariamente operan a la misma escala de tiempo geológico ni con la misma velocidad, resultando generalmente en una historia larga y compleja que es registrada por la geología y geomorfología del orógeno.

En orógenos activos, los procesos superficiales son erosionales, los cuales eliminan el registro antiguo (paleoregistro) sobre el levantamiento superficial (Fig. 1.1). Las cuencas sedimentarias adyacentes a los orógenos están rellenas de sedimentos que guardan las señales antiguas de levantamiento superficial. El estudio de la historia termal de rocas de la corteza superior mediante *termocronología de baja temperatura* proporciona información sobre el levantamiento superficial y la exhumación a lo largo del tiempo geológico. El estudio de los movimientos verticales de grandes masas de rocas en el transcurso del tiempo es resumido de acuerdo con England y Molnar (1990), y Ring et al. (1999) en dos conceptos importantes. Primero, la *denudación* (o "denudation"), la cual es definida como la diferencia entre el levantamiento de rocas y el levantamiento superficial. Es decir, el desprendimiento de la parte más externa de la corteza terrestre provocada por la acción procesos superficiales y/o tectónicos. *Exhumación*, describe los mecanismos que producen el transporte del material rocoso a la superficie terrestre debido a la denudación. Así, la cantidad de exhumación puede ser la misma que la denudación (Fig. 1.1).

Los aspectos teóricos de la termocronología por trazas de fisión son proporcionados en el capítulo 3. La historia termal puede ser extraída de las edades y las longitudes de las trazas de fisión en apatitos usando ecuanciones empíricas que relacionan, tiempo, temperatura, longitudes y densidad de trazas (por ejemplo, Ketcham et al. 1999).

El ciclo de vida orogénico generalmente comprende tres fases: crecimiento topográfico, equilibrio y decaimiento (Jamieson and Beaumont, 1989). Durante esas fases las tasas de erosión varían en respuesta a cambios temporales y espaciales en el clima, el relieve, la pendiente y la deformación. La aplicación de termocronología por trazas de fisión en minerales que han sido arrancados por la erosión de su roca recipiente, transportados y depositados en las cuencas adyacentes recibe el nombre de termocronología detrítica por trazas de fisión (Wagner and Van den Haute, 1992; Naeser et al. 1989). La termocronología por trazas de fisión en apatitos detríticos aplicada a muestras recolectadas de sedimentos sinorogénicos de cuencas o de sedimentos actuales de ríos es un método que ha sido bien establecido con el fin de cuantificar las historias de erosión durante la evolución del orógeno, como también para establecer proveniencia sedimentaria y evolución del paisaje (por ejemplo, Garver et al. 1999).

Los análisis por trazas de fisión sobre rocas sedimentarias e in-situ, han sido ampliamente usados durante las últimas tres décadas para establecer la historia termal a baja temperatura de numerosas rocas ígneas, metamórficas y sedimentarias, en diversos marcos geológicos. Estos incluyen: cinturones orogénicos, zonas de rifting, fallas, cuencas sedimentarias, entre otros. Los tipos de problemas geológicos que pueden ser resueltos comprenden: determinación de intervalos de tiempo y velocidades cinemáticas de eventos tectónicos; evolución termal de cuencas sedimentarias, la edad de generación de hidrocarburos; la edad absoluta de depósitos volcánicos; los principales efectos del cambio climático con respecto a la superficie que afecten el gradiente geotérmico y la evolución del paisaje a largo plazo (Gallagher et al. 1998; Gleadow and Brown, 2000; Blythe et al. 2000, 2002; Spotila et al. 2002).

Con el fin de estudiar las relaciones entre clima, exhumación y los procesos tectónicos, Los Andes de Venezuela constituyen una región interesante para aplicar la termocronología por trazas de fisión en apatitos, por dos razones: primero, debido a su situación geográfica, en la parte nor-oeste del margen activo de Suramérica, siendo dominada por la triple convergencia de las placas Caribe, Surámerica y Nazca; esto hace que su contexto geodinámico sea complicado y varíe rápidamente en el transcurso del tiempo geológico (Fig. 1.2). Segundo, Los Andes de Venezuela separan dos de las principales cuencas petrolíferas de Venezuela: la cuenca del Lago de Maracaibo y la cuenca Barinas-Apure (Fig. 1.2). La cuenca del Lago de Maracaibo es una de las más prolíficas del mundo, en la cual más de 40 billones de barriles de petróleo han sido producidos (James, 2000a, b; Escalona, 2003). La cuenca Barinas-Apure es

el tercer yacimiento petrolífero de Venezuela. Esta cuenca tiene un área de 95.000 km² y un espesor máximo de sedimentos cercanos a los 5 km en el centro de la cuenca (James, 2000a, b; Jácome and Chacín, 2008).

El origen de Los Andes Venezolanos actuales y sus cuencas petrolíferas se relacionan con la compleja interacción de las placas tectónicas antes mencionadas (Fig. 1.2), la cual genera a una escala regional la convergencia oblicua y transpresión entre el bloque continental de Maracaibo y la placa Suramericana (Colletta et al. 1997). Esta colisión ha producido la reactivación de antiguas zonas de fallas y estructuras que han evolucionado actualmente en fallas rumbo-deslizantes hacia la derecha o hacia la izquierda, corrimientos y rotación individual de bloques.

El objetivo de la presente investigación es aplicar termocronología por trazas de fisión en apatitos detríticos e in-situ para cuantificar la historia de exhumación de Los Andes Venezolanos en el contexto geodinámico de Los Andes del Norte de Suramérica, además de estudiar los patrones de exhumación asociados con fallamiento continental rumbo-lateral ("continental strike-slip faulting") en márgenes transpresivos (Spotila et al. 2007a, b; Cruz et al. 2007). Esta investigación constituye el primer trabajo científico detallado de Los Andes de Venezuela en esa dirección después de los trabajos de Kohn et al. (1984) y Shagam et al. (1984). En el presente trabajo, se determinaron los patrones de exhumación a lo largo de Los Andes Venezolanos usando principalmente 47 nuevos datos termocronológicos por trazas de fisión en apatitos, (24 in-situ, 15 pertenecientes a las formaciones Miocenas-Pliocena de las cuencas antepaís de Maracaibo y Barinas-Apure, y 8 pertenecientes a los sedimentos transportados por los ríos modernos, Fig. 1.3), también se emplearon métodos cuantitativos para la interpretación de los datos, tales como historia termal y modelos numéricos mediante Pecube (Braun, 2003; Ketcham, 2005; Braun et al. 2006). Estos resultados fueron complementados con el análisis de otros datos como: precipitación, sismicidad, palinología, y análisis de materia orgánica de los sedimentos sinorogénicos. En esta investigación, las siguientes hipótesis fueron examinadas: (1) los patrones de exhumación varían espacialmente a lo largo de Los Andes Venezolanos, (2) estructuras preexistentes heredadas controlan dichos patrones de exhumación, (3) la tectónica y la erosión no necesariamente actúan de forma independiente, pero podrían estar fuertemente acopladas, lo cual debería implicar una correlación entre los procesos a largo y a corto plazo, (4) los patrones de exhumación podrían estar reproducidos fielmente en los datos termocronológicos detríticos.

1.1 Distribución de los capítulos y resultados

La presente tesis doctoral se organiza en tres capítulos introductorios (incluyendo el presente), cuatro manuscritos (listos para ser enviados a las respectivas revistas especializadas) los cuales contienen los resultados principales de este trabajo, conclusiones, síntesis y anexos. El segundo capítulo (después de la presente introducción), presenta las principales teorías y modelos desarrollados para explicar el origen de Los Andes de Venezuela en el contexto de la tectónica de placas. También, en este capítulo se muestran los diferentes modelos tectónicos y el contexto geodinámico actual. El tercer capítulo presenta los fundamentos teóricos de la termocronología por trazas de fisión en apatitos in-situ y detríticos; se describen los métodos cuantitativos (Pecube, Braun, 2003) empleados en esta investigación para interpretar los datos termocronológicos. Seguidamente, el primer manuscrito (capítulo 4), comprende toda la base de datos termocronológica in-situ existente con el propósito de estudiar los patrones de exhumación a lo largo de Los Andes Venezolanos. En este manuscrito se incluyeron análisis topográficos con la finalidad de establecer diferencias en cuanto a los patrones de exhumación y las características geomorfológicas de dichos bloques. Barry Kohn (Universidad de Melbourne, Australia) proporcionó para este manuscrito 24 nuevas edades por trazas de fisión en apatitos, así como 10 edades revisadas, con la finalidad de contribuir con la base de datos termocronológicos y facilitar su interpretación. El segundo manuscrito (capítulo 5), contempla el modelado directo ("forward") en tres dimensiones mediante el código Pecube (Braun, 2003; Braun et al. 2006) y el código HeFTy (Ketcham, 2005) los cuales se emplearon para interpretar dos perfiles verticales o de edad-elevación, en la parte central de Los Andes de Venezuela. El primero compilado por Kohn et al. (1984) en el Bloque El Carmen en la Sierra de La Culata y el segundo realizado durante el transcurso de la presente investigación en la Sierra Nevada de Mérida.

El tercer manuscrito (capítulo 6) extiende la escala temporal mediante la inclusión de 8 datos provenientes de sedimentos transportados por los ríos actuales en Los Andes Venezolanos. En este manuscrito se realizó un análisis de correlación entre las tasas de exhumación a largo plazo y factores potenciales a corto plazo, con la finalidad de discriminar cual de estos últimos pudieran controlar los patrones de exhumación encontrados a lo largo de la cadena andina. El cuarto manuscrito (capítulo 7) abarca los sedimentos sinorogénicos depositados a ambos lados de los flancos andinos. Esos sedimentos, productos de la erosión de Los Andes

Venezolanos permiten analizar las relaciones entre exhumación, transporte, sedimentación, subsidencia y reciclaje en las cuencas antepaís, mediante la combinación con otros métodos multidisciplinarios (termocronología por huellas de fisión en apatitos detríticos, palinología, petrología sedimentaria y análisis de la materia orgánica).

Estos cuatro manuscritos (capítulos 4 al 7) permiten validar las hipótesis presentadas anteriormente. En efecto, es posible distinguir diferentes patrones de exhumación, los cuales son controlados por estructuras heredadas tectónicamente (generadas durante el proceso de separación de Norteamérica, Suramérica y Africa), que han sido reactivadas como consecuencia de la compleja interacción geodinámica entre las placas Caribe, Nazca y Suramérica. Posiblemente, el sistemas de fallas de Boconó ya estaba presente desde el Eoceno (Schubert, 1982) y produjo la separación de los bloques de Caparo y Valera. Dos bloques en la parte central de la cadena: Sierra Nevada de Mérida y Sierra La Culata presentan historias contrastantes de enfriamiento y son el resultado directo del levantamiento superficial, la transpresión y la erosión, producidas por la colisión oblicua entre el bloque continental de Maracaibo y Suramérica. Estos dos bloques reflejan movimientos verticales significativos del sistema de fallas de Boconó. A 8 Ma, ocurre un máximo levantamiento de superficie en la Sierra Nevada de Mérida, lo cual coincide con un importante período de reorganización de drenajes de los paleo-ríos Orinoco y Magdalena (Hoorn et al. 1995; Díaz de Gamero, 1996).

Los resultados de la termocronología detrítica son consistentes con los resultados in-situ, e indican al menos 5 etapas de exhumación continua alrededor de 2-3 Ma, 3-5 Ma, 5-8 Ma, 8-15 Ma y 15-30 Ma. Esas fases son asociadas con eventos tectónicos regionales que ocurren a través de Los Andes del Norte (Cooper et al. 1995; Murdock et al. 1997; Parra et al. 2009). Los intervalos entre 2-3 y 3-5 pueden ser relacionados con el cierre final del Istmo de Panamá (Murdock et al. 1997; Grafë et al. 2002). De 5 a 8 Ma ocurre la reacomodación del Bloque de Maracaibo, causado por la compresión del Arco de Panamá en la parte occidental de Suramérica y el movimiento de la Placa del Caribe al norte (Cruz et al. 2007). Esta compresión produce la reactivación de diferentes ramales del sistema de fallas de Boconó. Durante 8 a 15 Ma la compresión e inversión asociada con la formación de los corrimientos de la Cordillera Oriental de Colombia produce altas tasas de exhumación/levantamiento en Los Andes del Norte (Parra et al. 2009). De acuerdo con Montes et al. (2005) durante este intervalo el bloque de Maracaibo llega a su posición actual. Durante la fase entre 15 y 30 Ma, se produce la acreción de la Cordillera Oriental de Colombia contra la parte sur-oeste de Los

Andes Venezolanos (en una zona conformada por la unión del bloque Caparo y parte del bloque de Valera). Edades por trazas de fisión en apatitos mayores a 30 Ma en Los Andes Venezolanos pudieran ser asociadas con paleotopografías creadas durante una etapa temprana de deformación compresional que afecto el Valle del Magdalena y la parte occidental de la Cordillera Oriental de Colombia debido al incremento en las tasas de convergencia entre las placas de Nazca y Suramérica (Pardo-Casas and Molnar, 1987; Daly, 1989). Una edad de 145 Ma encontrada al norte del granito de Valera con las cuencas de extensión generadas durante el proceso de rifting ocurrido durante el Triásico a Cretácico Temprano como un resultado de la separación de Norteamérica y Suramérica, cuando ocurre la apertura del Caribe (~235–130 Ma); conocida como la megasecuencia synrift (Cooper et al. 1995).

Chapter 2

II. PLATE TECTONIC EVOLUTION OF THE NORTHERN ANDEAN REGION

2.0 Introduction

This chapter provides a plate-tectonic reconstruction of the interactions between tectonic plates (Caribbean, Nazca, Cocos, North and South American, and the Panamá arc) and blocks involved in the development of the Northern Andes, with particular interest in the origin of the Venezuelan Andes.

2.1 Tectonic assembly of the Northern Andes

The present-day Northern Andes occupy the north-western corner of South America. This mountain range is dominated by four principal lithospheric plates: the Cocos, Nazca and Caribbean plates of oceanic affinity, and the continental South American plate (Fig. 2.1). The South America plate is dominated in this region by the Precambrian Guyana Shield.

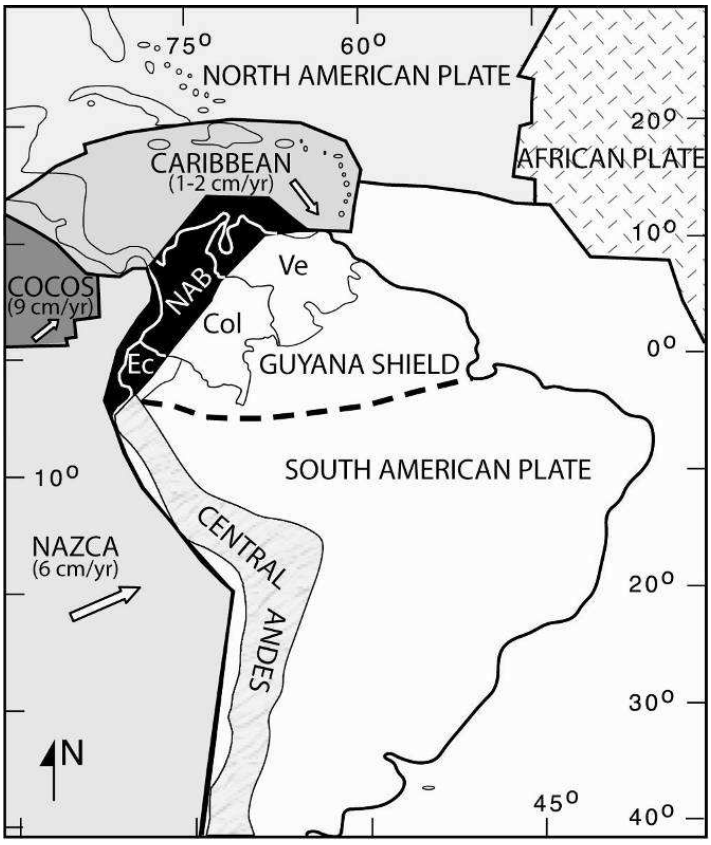

Fig. 2.1. Tectonic framework of north-western South America. NAB = Northern Andean Block; Ec, Col, Ve = geographic limits of Ecuador, Colombia and Venezuela, respectively (modified from Cediel et al. 2003).

The Northern Andes differ significantly from the Central Andes (Fig. 2.1) in many aspects, including the nature and age of the underlying basement and continental margin, the nature and evolution of stress regimes during uplift, the nature and age of subducting oceanic crust, and the timing and style of deformation and magmatism.

The Northern Andes are an assemblage of different continental blocks, oceanic plateaux, ridges and intra-oceanic arc complexes, which collided with the northern South American plate since the Jurassic along a variety of newly developed or reactivated fault zones (Fig. 2.2). Because of the complexity of the tectonic relationships between the different blocks, plateaux and ridges, the exact mechanisms and timing of collision remain a matter of debate (Cediel et al. 2003). This is based mainly on different authors (Case et al. 1990; Aleman and Ramos, 2000; Cediel et al. 2003, Montes et al. 2005).

The Northern Andes can be subdivided into the Venezuelan Andes (Mérida Andes), the Colombian Andes and the Ecuadorian Andes (Fig. 2.1). The Colombian and Ecuadorian Andes are typical products of subduction and correlative processes (magmatism, shortening, collisions of allochtonous terranes, etc). In contrast, the Venezuelan Andes is an intra-continental mountain belt resulting from the interaction between the Caribbean, Nazca and South America Plates resulting in Neogene tectonic inversion. The difference in orientation of the Colombian and Ecuadorian ranges with respect to Venezuelan Andes result from variations during the Mesozoic extension (Aleman and Ramos, 2000) and the fact that Western Colombia was located in the area affected by the passage of the Caribbean plate. The Colombian Andes consist of three distinct and separate chains: the Western, Central and Eastern Cordillera (Fig. 2.2) and are bounded to the east by the Romeral fault system. This fault separates the Western and Central Cordilleras and has been interpreted as a suture or subduction zone (Toussaint and Restrepo, 1982). The Western Cordillera is constituted by Cretaceous tholeiitic basalt and deep-water sediments that rest on the oceanic crust. In the Baudó range, located in the Western Cordillera, ophiolites have been reported (Toussaint, 1978).

The Central and Eastern Cordillera are separated by the Magdalena Depression and are underlain by continental crust. The separation of these chains mentioned previously dates back to the Mesozoic extensional phase. A first collision of the Dagua-Piñón Terrane (DAP;

Fig. 2.2) during the Late Cretaceous produced the exhumation of the Central Cordillera (Aleman and Ramos, 2000) and the deformation of the Eastern Cordillera. This collision and the Late Cretaceous docking of the DAP also affected the Ecuadorian Andes, causing shortening and thrusting of Mesozoic oceanic crust and the accretion of the Western Cordillera into a single geomorphical unit. The extrusion of the Caribbean plate was associated with middle Eocene and late Miocene accretion in the Western Cordillera. The complex plate interaction prior to the formation of the Caribbean plate produced different domains that were later accreted to the northern part of the Western Colombia. This periodic terrain docking enhanced by oblique convergence has led to strain partitioning and continuously reactivated old suture zones within the Northern Andes.

To south, Ecuador can be divided into three geographic zones from east to west (Fig. 2.2): the eastern basin or "East", the Ecuadorian Andes or "Sierra", and the coastal zone or "Costa" (Amortegui, 2007). The eastern basin is filled with continental red Jurassic sandstones, marls and calcareous marine Cretaceous, Palaeogene deposits topped with patchy continental to brackish, coarse Miocene to Recent deposits. Dextral-slip faults form in depth positive flower structures explored by the oil industry. The Sierra is formed by the Cordillera Real and the Western Cordillera. The Cordillera Real to the east consists of Paleozoic and Mesozoic rocks metamorphosed, partly covered or intersected by intrusive rocks and Tertiary volcanic (Litherland et al. 1994). La Costa is the current zone of fore arc. This consists of a substrate of basic lavas, dolerites and pyroclastic rocks with oceanic affinity plateaus, crowned by island arc type rocks of Upper Cretaceous age (Vanmelle et al. 2008).

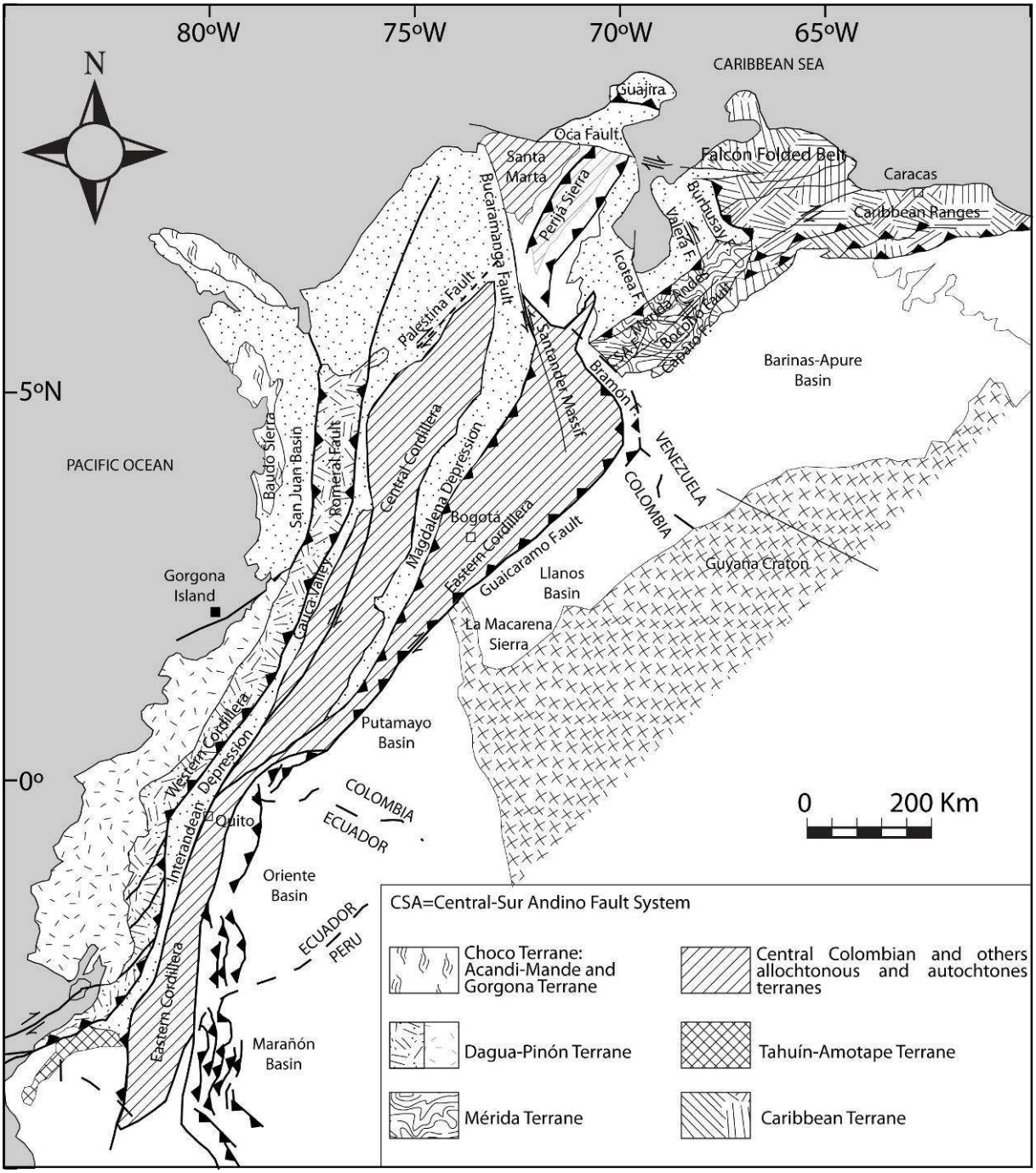

Fig. 2.2. Main structural provinces and terranes of the Northern Andes (Modified from Alemán and Ramos, 2000)

The Mérida or Venezuelan Andes are characterized by late Tertiary uplift and exhumation and high current seismicity. This belt is crossed by different strike-slip faults: the northeast-southwest trending dextral Boconó, Central-Sur Andino and Caparo faults and the north-south sinistral Icotea, Valera and Burbusay faults. The chain is flanked by two currently active foreland fold-and-thrust belts to the northwest and southeast, which incorporate Plio-Pleistocene sediments (Fig. 2.2). The basement includes Precambrian and Paleozoic metamorphic and igneous rocks, which are overlain by Paleozoic sedimentary rocks,

Mesozoic bed reds, marine clastic and carbonate strata, and Tertiary marine and continental deposits with variable thickness. Most of the northeast-trending faults appear relatively steep at shallow crustal depths (Case et al. 1990). The Venezuelan Andes is separated from the Eastern Cordillera of Colombia by the Táchira Depression, along which the latter may overthrust the former to the Northeast (Macellari, 1984). In its central part, the Venezuelan Andes are split symmetrically by the Boconó Fault System. To the east, the Trujillo Block (Backé et al. 2006) displays a more complex tectonic regime imposed by the convergence among the Boconó, Valera and Burbusay faults. Focal mechanism solutions of earthquakes in the northern part of the Trujillo block display compressional to transpressional shearing (Backé et al. 2006). Thus, the Venezuelan Andes present at least three contrasting histories for the Táchira Depression, the Central Venezuelan Andes and the Trujillo Block.

Despite the inherent complexity a simplified reconstruction of this part of South America is given here, in order to discuss the origin of the Northern Andes, and particularly of the Venezuelan Andes.

2.2 Pangaea break-up and origin of the Caribbean plate

The evolution of the Caribbean region started with the separation of North America, South America and Africa during Pangaea breakup in the early Jurassic (Wadge and Burke, 1983; Pindell and Kennan, 2001). This evolution has been marked by phases of extension, convergence, translation, subduction and exhumation, resulting in the current plate-tectonic configuration of the Caribbean region (Fig. 2.2; Chicangana, 2005).

2.2.1 Continental rifting and formation of structural discontinuities

Continental rifting creates and can exploit pre-existing weaknesses in the continental crust which can be reactivated during convergence and collision (Vauchez et al. 1997). For example, the break-up of Gondwana has left a system of fractures on the North American and South American continents. These fracture zones were formed during Permo-Triassic super plume activity (Maruyama, 1994) and Jurassic rifting. The Permo-Triassic super plume caused heating of the north-western South American lithosphere, and produce volcanic rocks which was contemporaneous with NE-SW extension along the axis of the Cordillera Central, on the La Guajira Peninsula (Maya, 2001), and in the Sierra Nevada de Santa Marta (Tschanz

et al. 1974; Chicangana, 2005; Montes et al. 2005) in Colombia (Fig. 2.2). The super plume activity resulted in rifting and formation of a triple junction which eventually caused the separation of Laurentia from Gondwana (Fig. 2.3). Widespread rifting in north-western South American started during the Early Jurassic. The Uribante or Trujillo Rift and Espino Graben (Fig. 2.3A) in Venezuela are evidences for this process, which is responsible for the development of N30°W striking weaknesses in the crust and possibly lithosphere of north-western South America. For example, the Romeral Fault System in Colombia (Fig. 2.2) represents today the former margin of South America (Von Estorff, 1946; James, 2000a). Therefore, paleo-structures are important for explaining the current tectonic structures in the Northern Andes (Fig. 2.2, 2.3B).

The modern strike-slip faults systems in northern South America (Fig. 2.2) are also related to the reactivation of these paleodiscontinuities (Figs. 2.3 A and B). The strike-slip systems control the recent exhumation patterns across the Northern Andes as will be discussed in the following chapters. During the Middle to Late Jurassic, a magmatic arc developed along the margin of South America. This magmatic arc crops out today from the Sierra Nevada de Santa Marta to the north of the Cordillera Real in south-eastern Ecuador (Figs. 2.2 and 2.3B). The origin of this magmatic arc is related to subduction of the Pacific plate beneath the South American plate that initiated in the Middle Jurassic (Chicangana, 2005). The regional tectonic development during the Middle to Late Jurassic shows the formation of large shear zones as a result of a transtensive regime, which originated from rifting in a back-arc rift setting, related to subduction of the Pacific plate (Jaillard et al. 1990). Two sets of major pre-Mesozoic crustal discontinuities (Von Estorff, 1946; Mora et al. 1993; James, 2000a, Jacques, 2004) can be recognized in the cratonic areas of northern South America and constitute a rectangular network (Fig. 2.3B). A N 50ºE trend is parallel to Espino and Apure grabens. The other set is oriented N40ºW, parallel to the northeastern continental margin of South America, the El Baúl and Mérida arches, the southeastern projection of the Santa Marta fault and the Sierra La Macarena (Fig. 2.2 and 2.3).

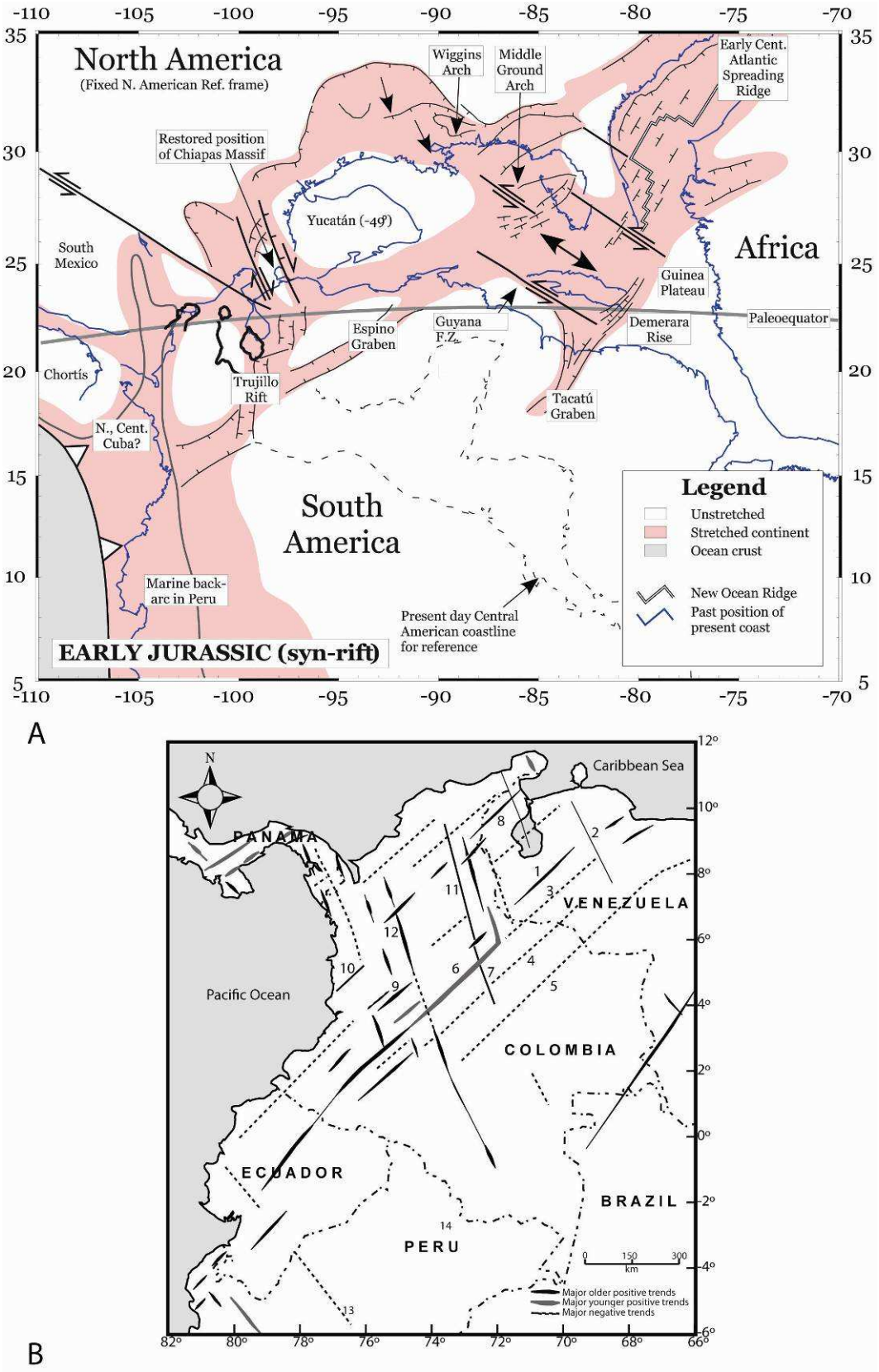

Fig. 2.3. A) Early Jurassic plate tectonic reconstruction (modified from Pindell and Kennan, 2001). B) Fault pattern in north-western South America. These (or similar) structures originated from the Pangaea breakup: 1. Paleo-Boconó fault limited the Uribante or Trujillo Rift. 2. El Baúl Arc, 3. Apure-Mantecal Graben, 4. Llanos Graben, 5. Guyana Shield, 6. Western Cordillera, 7. Cordillera de la Macarena, 8. Sierra de Perijá, 9. Cordillera Central, 10. Eastern Cordillera, 11. Santa Marta-Bucaramanga Fault, 11. Romeral Fault, 12. Cordillera Real and 14. Ibague Fault (modified after Von Estorff, 1946).

According to Mora et al. (1993), the tectonic reconstructions suggest that, depending on the angular relation between the displacement field of the surrounding plates and the orientation of the discontinuities, some of them were activated as extensional systems while others suffered transpressional deformation. Due to changes of the relative displacement fields through time, a given discontinuity may show inversion with respect to its previous behaviour. The network of discontinuities bounds blocks which suffered translation and rotation with respect to their neighbours and, in some cases, minor internal deformation. Thus, these rectangular network controlled the location of the following Mesozoic tectonic features: (a) Jurassic grabens (Espino, Uribante, and Machiques); (b) active mountains belts surrounding the Maracaibo block (Santander massif, Venezuelan Andes and the Perijá range); (c) major offsets of the Caribbean-related frontal deformation (Goajira); and the pull-apart basin development.

2.2.2 Origin of the Caribbean plate, the western and central Cordillera (Ecuador and Colombia)

The Caribbean plate formed from the end of the Late Jurassic to the Early Cenomanian, during the Late Cretaceous (Fig. 2.4). A widely accepted model is that the Caribbean plate moved into its inter-American position from the Pacific (Wilson, 1965; Malfait and Dinkleman, 1972; Pindell and Dewey, 1982; Pindell et al. 1988, and many others). This model forms the foundation for complex tectonic models for the development of the Venezuelan margin. In contrast, other authors (e.g. Ball et al. 1969, 1971; James, 1990; Meschede, 1998; Meschede and Frisch, 1998) proposed that the Caribbean plate most probably formed as part of the North American plate when that plate began separating from Gondwana during the Jurassic. The Caribbean plate subsequently interacted in convergent and strike-slip tectonics with the surrounding North and South American plates. Both models for the origin of the Caribbean plate deserve equal consideration.

The oceanic crust of the Caribbean plate is relatively thick (12 km) near the Beata Ridge, (Diebold, 1995). In contrast, it is only 3 km thick in the south-eastern part of the Venezuela basin. According to Donnelly (1973), Donnelly et al. (1990), and Driscoll and Diebold (1998), the Caribbean plate comprises a dominantly Late Cretaceous oceanic basalt province. It formed during spreading, as North America drifted away from South America, and during a widespread flood basalt event in the Early to middle Cretaceous (Fig. 2.4). A coeval, primitive

to calc-alkaline island-arc formed in the periphery of the flood basalt province. More recently, mid-Tertiary to Holocene alkalic basaltic suites formed in Central America and in the Lesser Antilles in response to subduction of the Cocos and North American plates respectively. Because of the over-thickening of Late Cretaceous Caribbean oceanic crust, magnetic data in the Caribbean area do not show a well-defined ocean-floor signature. Ghosh et a1., (1984) reported NE trending magnetic anomalies of possible Jurassic age in the Venezuela basin.

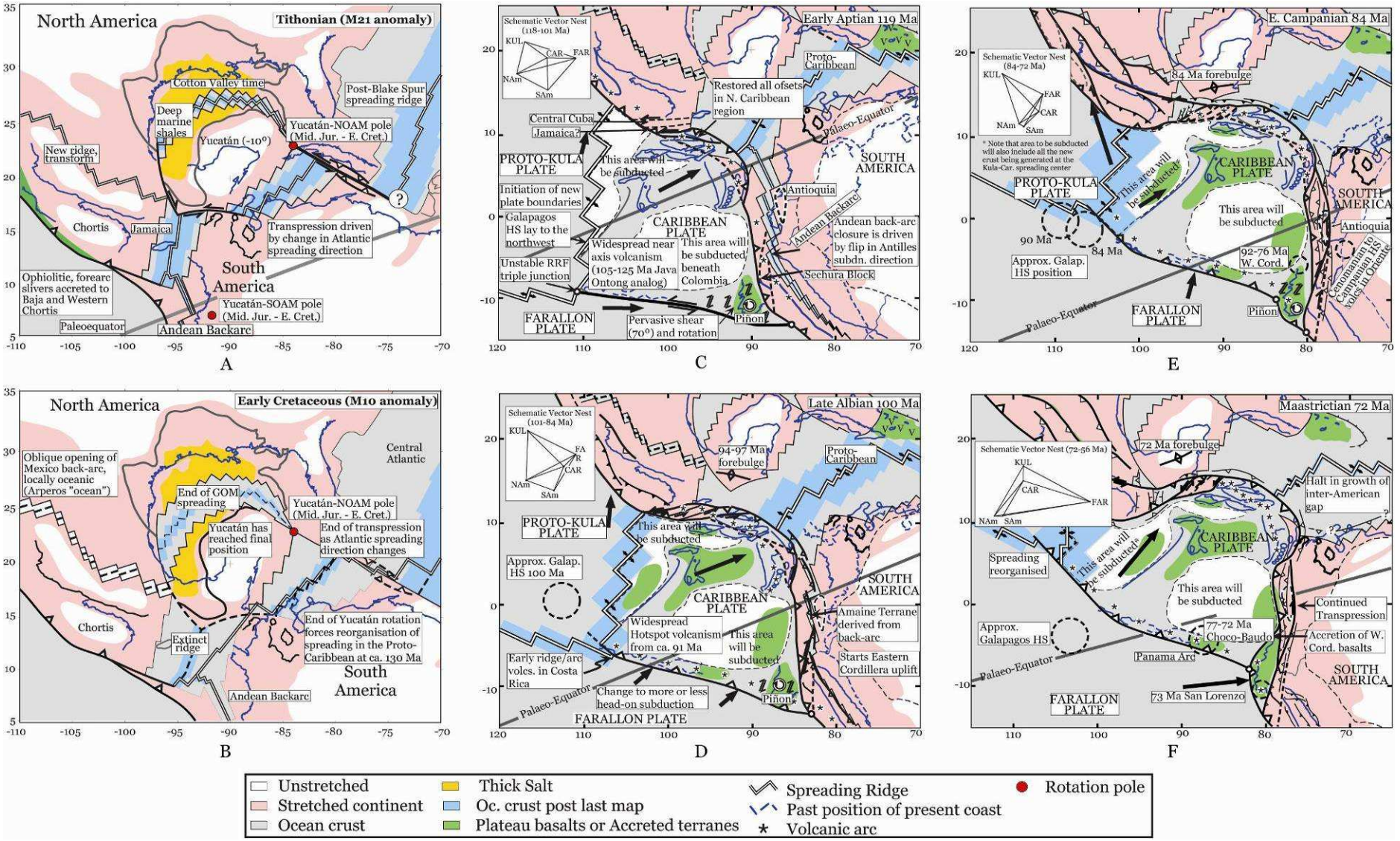

Fig. 2.4. Origin of the Caribbean plate and evolution of Caribbean tectonics after the reconstruction of Pindell and Kennan (2001).

To the west of the Romeral Fault System (RFS, Fig. 2.2), thick oceanic crust was formed during Aptian-Albian plume activity (Fig. 2.4C) of the Pacific super plume in the Pacific Ocean (Aspden et al. 1987 b, 1992 b; Larson, 1991). This oceanic crust was part of the paleo-Pacific plate or paleo-Caribbean plate (Mauffret and Leroy, 1997), which began to be accreted to the western margin of South America in Ecuador during the Campanian (Fig. 2.4 D; Aspden and McCourt, 2002; Kerr et al. 2002). During this epoch uplift of the Eastern and Western Cordillera in Colombia started (Fig. 2.4 E and F).

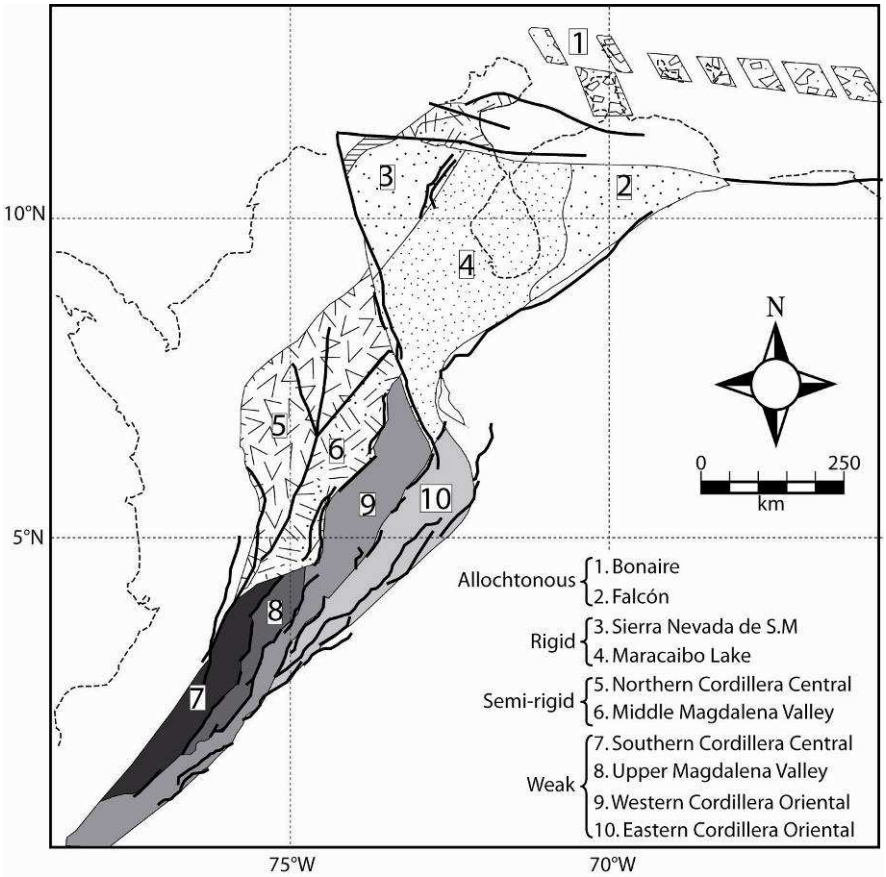

Fig. 2.5. Present today crustal blocks of the northern Andean region. Cordillera Oriental–Upper Magdalena in shades of grey, Cordillera Central–Middle Magdalena in line patterns, and Maracaibo block in dotted patterns. Note that each block is subdivided along major fault systems. (Modified from Montes et al. 2005).

Figure 2.5 shows the position of crustal blocks in the northern Andean region, which Montes et al. (2005) used for their tectonic reconstruction (Fig. 2.6). These blocks are the allochthonous Bonaire and Falcón terrains (denoted by 1, Fig. 2.5), and eight individual crustal blocks, the Sierra Nevada de Santa Marta block, the Maracaibo block, the Northern Cordillera Central block, the Middle Magdalena Valley block, Southern Cordillera Central, Upper Magdalena Valley, Western Cordillera Oriental, and Eastern Cordillera Oriental (Fig. 2.5 and 2.6) are necessary for this reconstruction.

According to Montes et al. (2005), the collision of the Caribbean plate with the South America plate between the Late Cretaceous and the Late Paleocene caused northward translation and 20° of internal deformation (rotation) of the rigid Cordillera Central Block (Fig. 2.6 A, B). At the same time oblique accretion of oceanic sequences west of the Northern Cordillera Central occurred, and dextral transpression of the Middle Magdalena Valley to the Eastern Cordillera Oriental started.

In Colombia, accretion moved gradually toward the north until the Middle Eocene, when the Provincia Litosferica Oceánica de la Cordillera Occidental (PLOCO) and the San Jacinto accretionary wedge were accreted (Duque, 1984, 1980; Nivia, 1996). Contemporaneously, clockwise rotation of the Sierra Nevada de Santa Marta and Maracaibo blocks started, sinistral slip on Santa Marta Bucaramanga fault was initiated, the Northern Cordillera Central fragmented block and 20° clockwise rotation of Middle Magdalena Valley block occurred (Fig. 2.6C). Oblique collision and dextral displacement of the Caribbean plate toward the NE along the South American margin during the Paleogene resulted in surface uplift and a regional unconformity during gradual exhumation of Romeral Fault System (Fig. 2.2) rocks. In several sectors mylonite belts were developed, mainly in faults of the former subduction zone and the Early - Late Cretaceous volcanic arc.

During the Late Eocene the blocks of the Southern Cordillera Central and the Eastern Cordillera Oriental experienced 30° internal deformation, and the Sierra Nevada de Santa Marta and Maracaibo blocks rotated clockwise by 20° (Fig. 2.6D). In addition, the Northern Cordillera Central and the Middle Magdalena Valley blocks were translated northward, and extrusion of the southern tip of the Falcon terrain started (Montes et al. 2005).

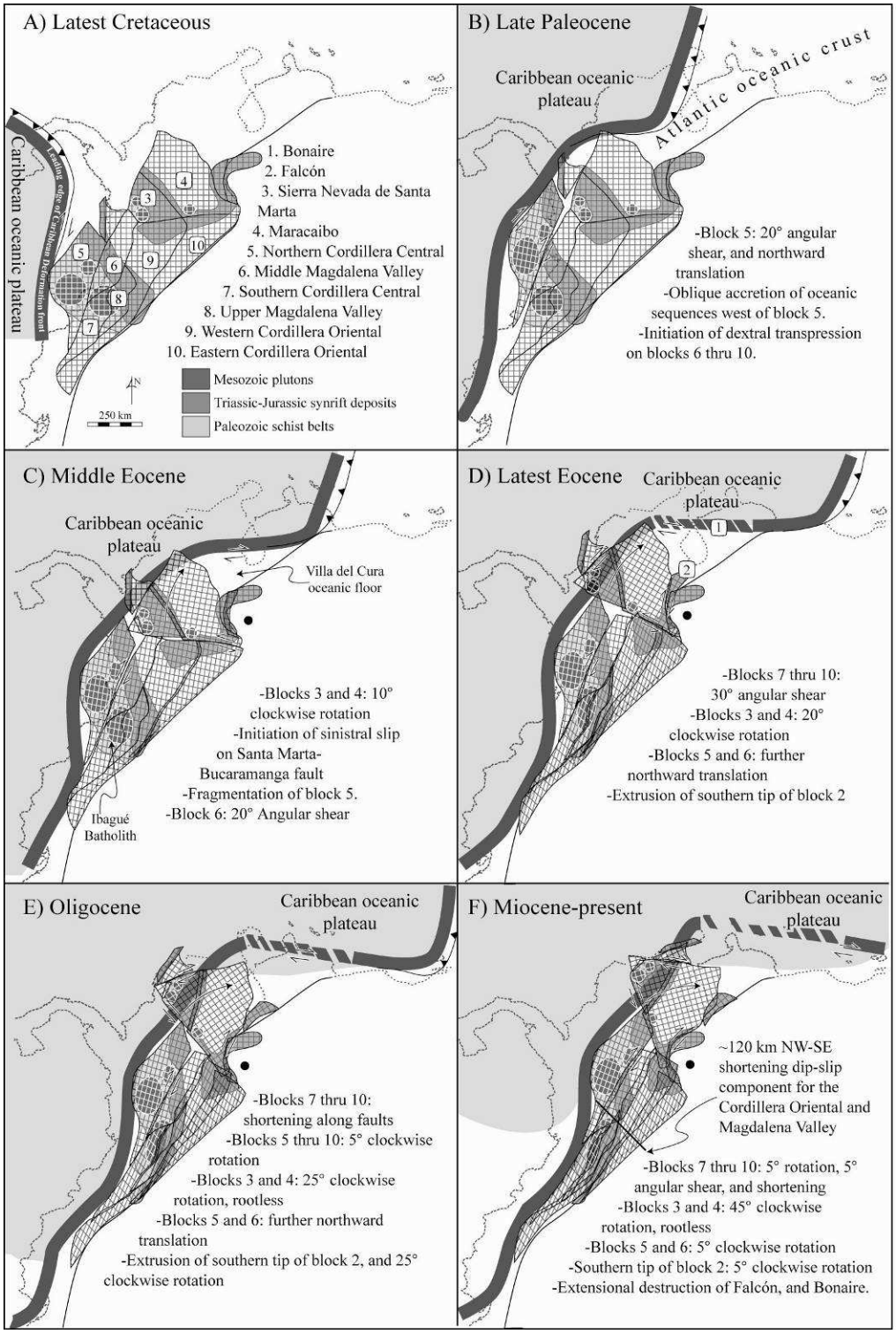

Fig. 2.6. Schematic sequential reconstruction of the movement of northern Andean blocks. (a) Predeformational state. (b) Northward translation of the rigid Cordillera Central block. (c) Fragmentation of the rigid Cordillera Central block as activity along the sinistral Santa Marta–Bucaramanga fault, and rotation of the Maracaibo block begin. (d) Initiation of significant dextral transpressional deformation in the Cordillera Oriental–Upper Magdalena block, further rotation of the Maracaibo block, causing the emplacement of the Villa del Cura rocks on the South American margin. (e) Rotation of the Maracaibo block is almost complete and extensional opening of the Falcon–Bonaire basin starts as the Caribbean deformation front continues to migrate east, result of a right-lateral, releasing bend (Muessig, 1984). (After Montes et al. 2005).

2.2.3 Maracaibo block rotation, reactivation of paleo-structures

The Maracaibo block rotated clockwise from the Middle Eocene to the Oligocene (Fig. 2.6), but it was not until the Miocene that rotation of the Maracaibo block triggered reactivation of faults associated with Jurassic graben structures, in what are today the Venezuelan Andes. This rotation is supported by the paleomagnetic studies of Hargraves and Shagam (1969) for the La Quinta Formation and for the Santa Marta-Bucaramanga and Maracaibo block, according to Bayona et al. (2008).

The Mesozoic graben structures (Fig. 2.3B) were inverted during the Neogene as a result of the collision of the Panamá arc with South America in the west, and by continuous oblique collision of the Caribbean plate with South America in eastern Venezuela (Ostos et al. 2005). During the late Oligocene-early Miocene (Fig. 2.6 E, F), the northern part of the Falcón basin, the Maracaibo basin, and the Andean foreland basins were formed (Montes et al. 2005). With increasing rotation of the Maracaibo block during the Miocene, according to James (2000a), the interaction between this block and South America controlled transpression in the Venezuelan Andes. The Maracaibo block continued its rotation during the Pliocene (Montes et al. 2005), causing tranpressional movement on the Boconó fault and associated strike slip faults systems (see Fig. 2.2; Valera, Burbusay, Burro Negro, and Icotea fault systems), and along the NW and SE thrusts. Inside the Maracaibo block small fragments suffered rotation during Jurassic to Eocene times (Lugo and Mann, 1995). Probably these rotations could be extrapolated to other small tectonic blocks across the Venezuelan Andes, which may complicate the exhumations patterns across the Venezuelan Andes.

2.3 Current tectonic models for the origin of the Venezuelan Andes

From the work of Gansser (1973) it is clear that the Venezuelan Andes are a distinct mountain chain, separated from the Eastern Cordillera of Colombia. The separation is based on changes in orientation of structural features and the presence of Precambrian crystalline rocks in the Venezuelan Andes. Since the 1950s, two different types of tectonic models were proposed to explain the origin of the Venezuelan Andes, symmetric and asymmetric models.

2.3.1 Symmetric models

In this type of model the Venezuelan Andes are regarded as a symmetric chain with a major strike-slip fault in the centre, and with bounding reverse faults on both sides of the mountain belt (Audemard and Audemard, 2002). Dewey (1972) and Schubert (1981) postulated that the Boconó fault represents the plate boundary between the South America and the Caribbean plate or Maracaibo block. The Venezuelan Andes would then be the result of compression between two plates and would comprise two separate chains, split by the Boconó fault (Soulas, 1985).

Bucher (1952), González de Juana (1952), Hargraves and Shagam (1969), and Shagam (1972) proposed for the origin of the Venezuelan Andes a mega-anticline, containing a horst and graben block complex in the centre and with both flanks bounded by high-angle reverse faults (Fig. 2.7). In contrast, Rod (1956), Deratmiroff (1971), Schubert (1985), White (1985), Stephan (1982), Boesi et al. (1988), and Monsalve (1988) proposed a mushroom-like transpressional uplift with shear deformation along the Boconó fault and imbricate thrusting toward both flanks.

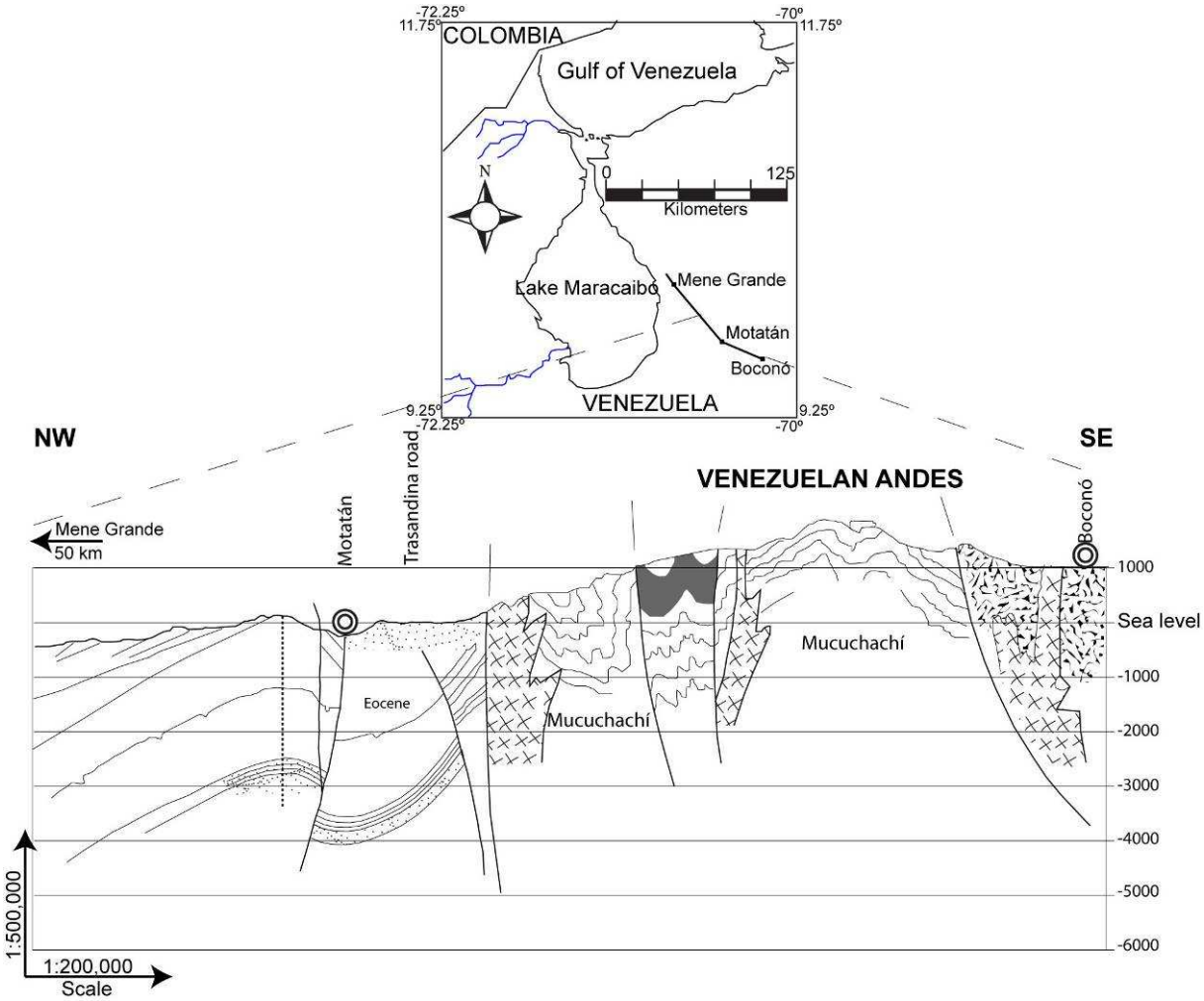

Fig. 2.7. Cross-section across the Venezuelan Andes, elaborated by González de Juana (1952), in this figure the Venezuelan Andes are considered as a mega-anticline, containing a horst and graben block complex in the centre and with both flanks bounded by high-angle reverse faults.

Based on field observations, Schubert (1969) suggested that uplift of the Venezuelan Andes began after the Eocene in the Barinitas-Santo Domingo region. This author proposed that uplift was characterized by a pronounced vertical movement of large blocks of basement rock through the reactivation of pre-existing faults. The sedimentary cover experienced monoclinal folding along the margins of the range. Reverse faulting affected the flanks of the chain and normal faulting the central part. Schubert (1969) also proposed that because of rapid uplift the poorly consolidated sediments of the Late Eocene Paguey Formation became unstable and slid off the uplifting mountain range to the southeast, in the form of blocks and cascading folds.

2.3.2 Asymmetric models

De Cizancourt (1933), Bucher (1952), and Gerth (1955) observed the asymmetric form of the chain (Fig. 2.8), but their models did not display either the crustal structure or the stratigraphy. The major conclusion reached by these authors was that the present Venezuelan Andes were uplifted vertically into large horsts, stepped faults, and grabens. Bucher (1952) attributed this tectonic development to tensional stresses produced by stretching of the crust, resulting from subcrustal bulging-up of material. The asymmetric models were developed based on the first gravity data collected in the region by Hospers and Van Wijnen (1959). These authors suggested that the observed asymmetry in the gravity pattern is produced by an overthrust of the southeastern part of the crust over the northwestern part (Fig. 2.8; Maracaibo Basin). Compressive stress is, therefore, invoked in this hypothesis. Rod (1960) criticized this hypothesis, pointing that field geology data does not support the overthrust hypothesis, and that a cross section of the mountain range reveals a fan-shaped structure with thrusting along both the southeastern and northwestern edges. In addition, according to Schubert (1969), the Hospers and van Wijnen (1959) hypothesis does not explain the presence of the Boconó fault zone.

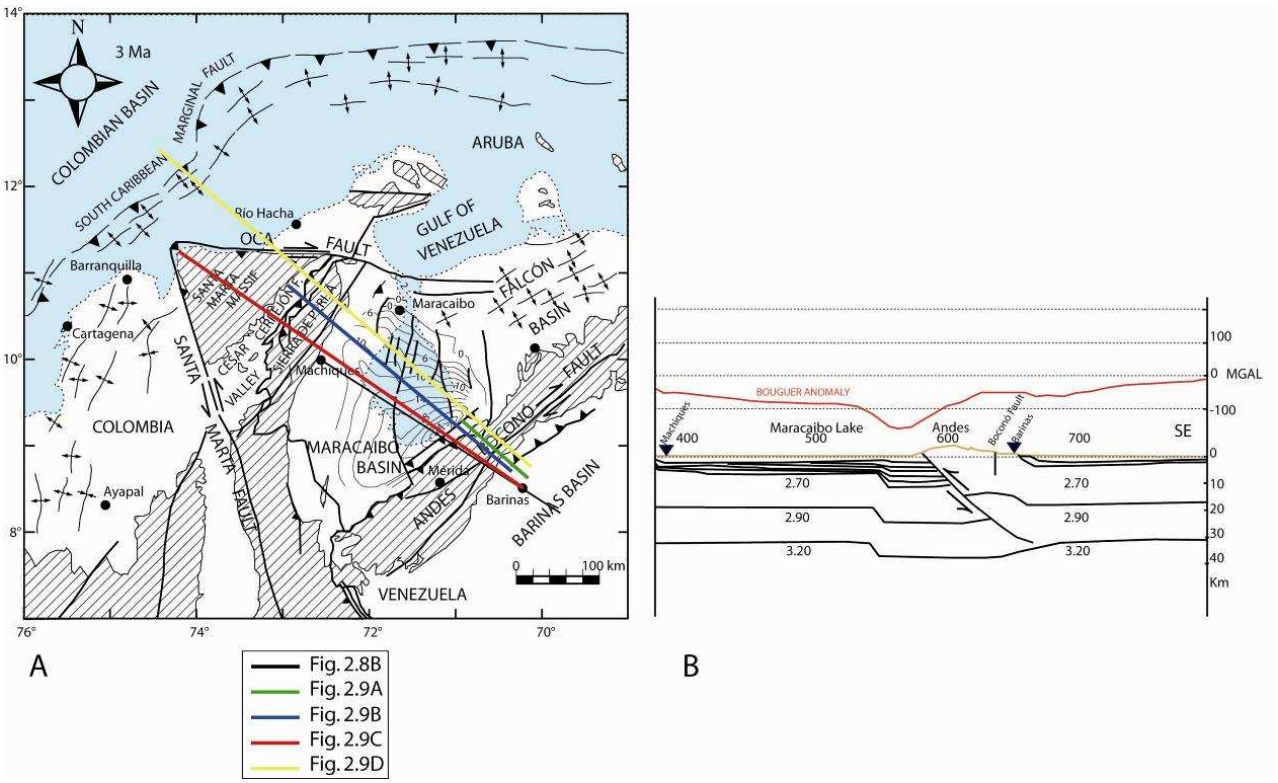

Fig. 2.8. Northwest-southeast gravity model for the Venezuelan Andes from Kellogg and Bonini (1982). This figure shows the asymmetry of the Venezuelan Andes. Cross section lines for gravity model (B) as well as tectonic models are shown at the Fig. 2.9.

Thus, taking into account these observations and the present-day tectonic concepts the current discussion focuses in two aspects: (1) the vergence/asymmetry of the chain and (2) the rooting depth of structures, with “orogenic float” versus “continental subduction” models having been proposed.

Among the authors that supported a “double-vergence” structure (in sense of Willet et al. 1993) are Kellogg and Bonini (1982), De Toni and Kellogg (1993) and Colletta et al. (1997). This structure is interpreted to be produced by the incipient continental subduction of the Maracaibo block toward the southeast (Fig. 1.8A). Others authors, as Yoris and Ostos (1997), Audemard and Audemard (2002), Cediel et al. (2003) or Monod et al. (2008) apply an “orogenic float” model (in the sense of Oldow et al. 1990) to the whole of the Caribbean-South American plate boundary zone. These authors envisage a major mid-crustal detachment underlying the Venezuelan Andes, Maracaibo Basin, Perijá and Santa Marta ranges (Figs. 2.9 B-D) with either northwest- or southeast-directed subduction of the underlying lower crust, and varying importance of strike-slip faults.

The Figures 2.9A to D show different recent geological models for the Venezuelan Andes. The great variety of models results from the fact that the deep structure and the exhumation patterns of the Venezuelan Andes are poorly understood. For example, Colletta et al. (1997) argued that the Cenozoic pro- and retro-side basins surrounding the Andean chain show different levels of subsidence (Fig. 2.9A). Towards the northwest, the Maracaibo basin is characterized by high subsidence rates during the Neogene, much larger than those associated with the Barinas-Apure basin. Colletta et al. (1997) explain the obvious difference in sediment thickness and gravimetric asymmetry between the Maracaibo and the Barinas-Apure basin by southeast directed A-type subduction of the Maracaibo block beneath the South American plate in the Venezuelan Andes, creating a 6 km deep foreland basin on the pro-side and an only 2 km deep retro-side basin (Fig. 2.9A). It is still a matter of debate of how deep the Boconó fault extends, as well as how much lateral and vertical displacement occurred along this fault system. It is not clear what role the Boconó Fault System plays in the “orogenic float” models (e.g., Yoris and Ostos, 1997; Audemard and Audemard, 2002; Cediel et al. 2003), and what is the relationship of this fault zone with the northwestern and southeastern thrusts and the Maracaibo and Barinas-Apure foreland basins.

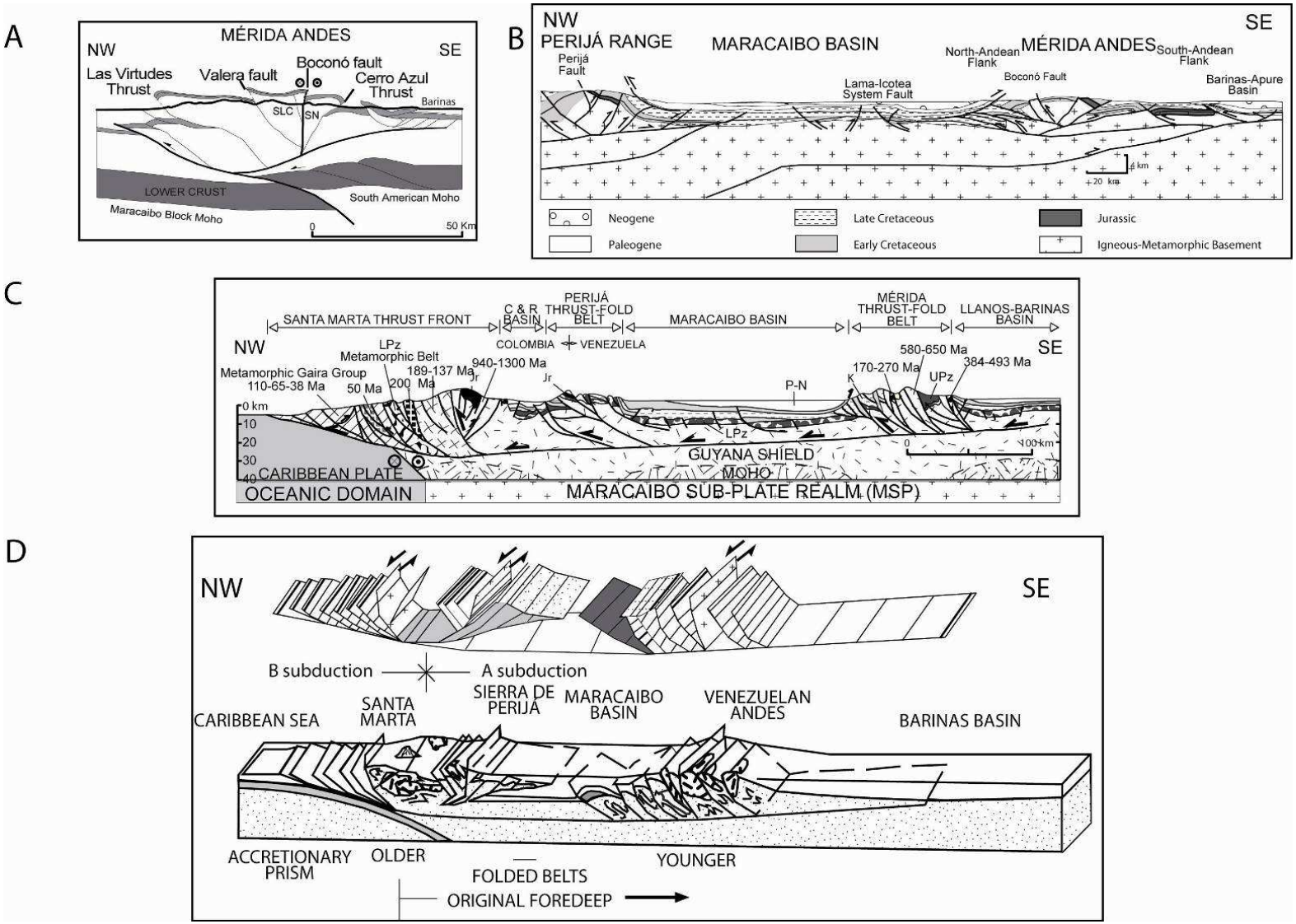

Fig. 2.9. Different geological models for the Venezuelan or Mérida Andes: A) Intracontinental collision of Colleta et al. 1997. Orogenic float model (of Oldow et al. 1990): B) Yoris and Ostos (1997). C) Cediel et al. (2003). D) Audemard and Audemard (2002). The locations of these cross sections are shown in the Fig. 2.8A.

.3.3 Present-day tectonic

The Cenozoic evolution of the Northern Andes, and in particular of the Venezuelan Andes has been dominated by the relative north-eastward, and subsequent eastward advance of the buoyant Caribbean plate with respect to stable South America (Fig. 2.10; Molnar and Sykes, 1969; Case et al. 1971; Bell 1972; Malfait and Dinkelman 1972; Jordan 1975; Pindell and Dewey 1982; Sykes et al. 1982; Wadge and Burke 1983; Burke et al. 1984; McCourt et al. 1984; Laubscher, 1987; Avé Lallemant, 1997; Villamil and Pindell, 1998; James, 2000a; Colmenares and Zoback, 2003; Audemard et al. 2006). This eastward motion of the Caribbean plate is supported by results of recent GPS surveys (Fig. 2.10A; Freymueller et al. 1993, Kaniuth et al. 1999, Weber et al. 2001, Pérez et al. 2001, Trenkamp et al. 2002, Colmenares and Zoback, 2003) and the seismicity record (Fig. 2.10B; Colmenares and Zoback, 2003; Cortés and Angelier, 2005). The eastward movement of the Caribbean plate is accommodated by well-developed transcurrent plate boundaries to the north (Rosencrantz et al. 1988) and south (Kafka and Weidner, 1981; Pennington, 1981). Unlike the sharp northern boundary, however, the southern Caribbean plate boundary is a collection of continental fragments that resisted the advance of the Caribbean plate (Montes et al. 2005). Continued movement of the Caribbean plate led to the progressive dextral transpressional distortion, dismembering, rigid-body translation, and clockwise rotation of the continental fragments that make up the northwestern Andes. This process is responsible for the difficulties in interpreting and locating the Caribbean-South America plate boundary (Soulas 1986, Beltrán 1994). In western Venezuela, the plate boundary covers a 600 km wide zone and comprises a set of discrete tectonic blocks or microplates (Fig. 2.2, Fig. 2.10A), which move independently among the surrounding larger plates (Caribbean, South America and Nazca).

One of these tectonic blocks is defined between the Boconó, Oca, and Bucaramanga-Santa Marta faults, which define a roughly triangular block (Fig. 2.10; Audemard 1993, 1998; Dhont et al. 2005; Backé et al. 2006; Audemard et al. 2006) with an intervening northeast-trending foldbelt (Perijá mountains, Kellogg, 1984), a northwest corner out of isostatic equilibrium (Sierra Nevada de Santa Marta, Tschanz et al. 1974), a northeast region limited to the east by allochthonous oceanic sequences (Villa del Cura, Bell, 1971), and a central depression where a great thickness of sediment has accumulated (Maracaibo basin, James, 2000a). The relatively undeformed stratal geometry reported in the central part of this block (Maracaibo basin, Fig. 2.10A) is evidence of its relative rigidity.

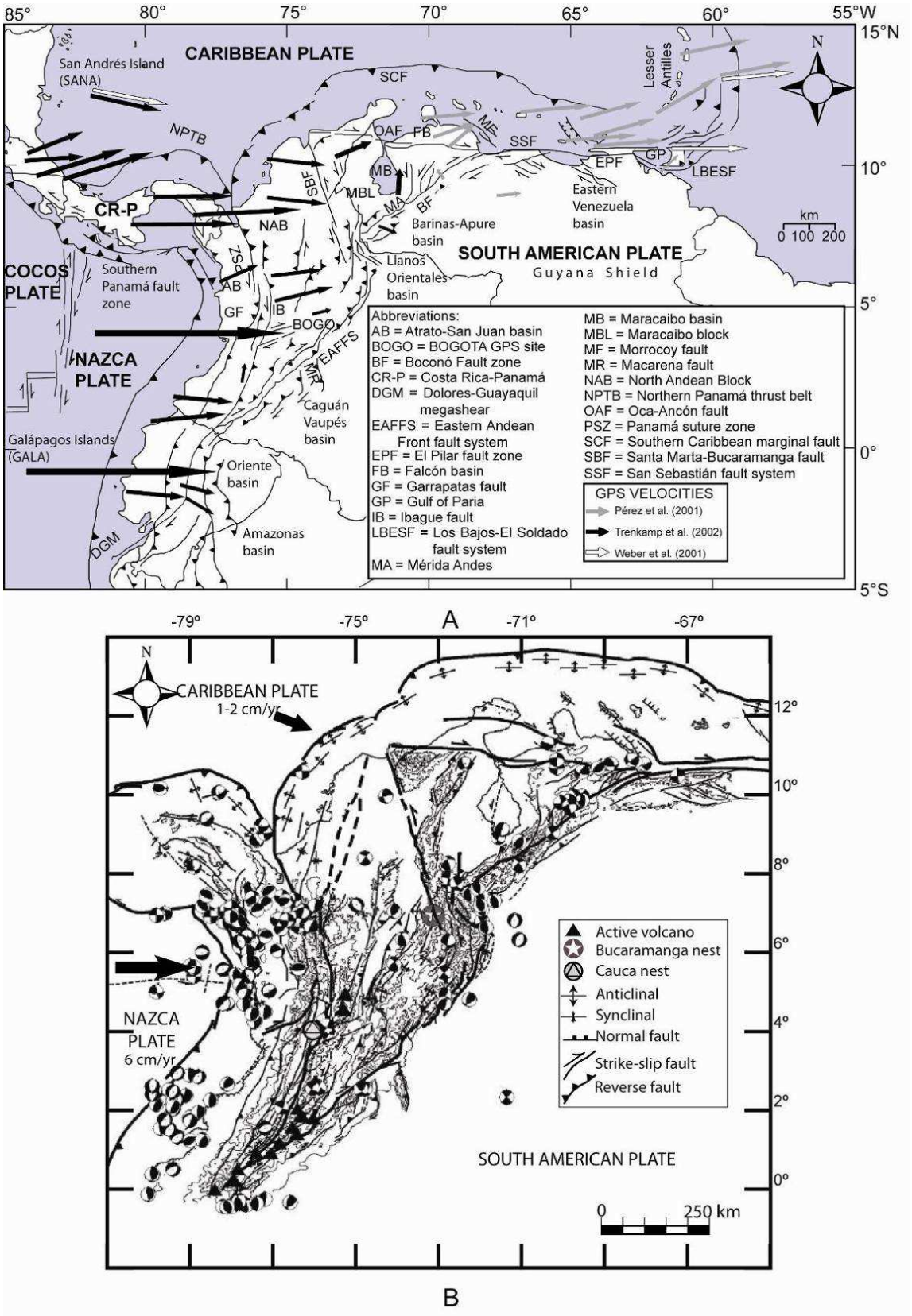

Fig. 2.10. A) Major tectonic features of northern South America and Global Positioning System (GPS) velocity vectors from different studies. All vectors denote velocities with respect to South America, and shading denotes different studies (After Colmenares and Zoback, 2003). B) Focal mechanisms of shallow earthquakes (<60 km) in the northern Andes. Usual representation as "beachballs" (Schmidth projection lower hemisphere); with P-extensional quadrangles white and T-compressive black (After Cortés and Angelier, 2005).

The kinematics of two of the bounding faults (dextral Oca, and sinistral Bucaramanga-Santa Marta faults) have been used to propose a general north-westward escape of this block with respect to stable South America (Kellogg and Bonini, 1982). This hypothesis is supported by a GPS study that indicates relative migration consistent with the proposed kinematics (Fig. 2.10A; Freymueller et al. 1993; Kellogg et al. 1995; Kaniuth et al. 1999; Trenkamp et al. 2002), and by a kinematic analysis within the Perijá Range (Kellogg and Bonini, 1982). According to Audemard et al. (2006), the north-westward escape of this block could generate the Southern Caribbean Deformation Belt (SCDB) north of the Netherlands Leeward Antilles (Fig. 2.10A). However, this hypothesis ignores the third bounding fault on this block (dextral Boconó Fault System, Schubert, 1981), as well as the paleomagnetic observations that indicate large clockwise rotations (Hargraves and Shagam, 1969; MacDonald and Opdyke, 1972; Skerlec and Hargraves, 1980; Castillo et al. 1991; Gose et al. 2003; Bayona et al. 2008). Some of these paleomagnetic studies have obtained ambiguous results, such as counterclockwise rotation for the Perijá Range (Maze and Hargraves, 1984), or partial rotation of the Sierra Nevada de Santa Marta (MacDonald and Opdyke, 1984), studies that have been rejected by Montes et al. (2005) on the basis of the large error-bars reported. An alternative hypothesis, presented by Montes et al. (2005), incorporates all kinematic and paleomagnetic data to model the Maracaibo block as a rigid block that underwent large clockwise rotations, expressed in the paleomagnetic data and the seemingly contradicting kinematics of the faults bounding this block.

The main lateral movement across the South America-Caribbean plate boundary zone is accommodated by the right-lateral strike-slip Boconó-San Sebastián-El Pilar-Los Bajos fault system (Molnar and Sykes 1969; Minster and Jordan 1978; Pérez and Aggarwal 1981; Schubert 1980a, 1980b; Schubert, 1982; Stephan 1982; Aggarwal 1983; Schubert 1984; Soulas 1986; Beltrán and Giraldo 1989; Singer and Audemard 1997; Audemard et al. 2000; Weber et al. 2001; Pérez et al. 2001; Audemard et al. 2006). The precise interaction between the Caribbean plate and South America remains a matter of debate and depends on the proposed geodynamic models of the previous section. Classically, most authors have accepted that the major right-lateral strike-slip fault system constitutes the boundary between the Caribbean and South America plates (Hess and Maxwell 1953, Schubert 1979, Aggarwal 1983, among many others), but more recently different plate boundary models have been proposed along this right-lateral strike-slip plate boundary zone: (a) orogenic float type for

the Andes (Fig. 2.9B-D; Audemard, 1991; Jácome, 1994; Yoris and Ostos, 1997; Audemard and Audemard 2002; Cediel et al. 2003; Monod et al. 2008) or eastern Venezuelan Coastal and Interior ranges (Ysaccis et al. 2000), thus being flanked by both A- and B-type subductions; and (b) SE-directed A-subduction or underthrusting of the Maracaibo block under the Mérida Andes (Fig. 2.9A; Kellogg and Bonini 1982, De Toni and Kellogg 1993, Colletta et al. 1996, 1997). Audemard et al. (2006) indicate that the incorporation of the Boconó fault into this major right-lateral strike-slip fault system is a rather recent event that could possibly explain the northward extrusion of the Maracaibo block, because the former transcurrent boundary comprised the east-west striking Oca-Ancón fault system (OAF) located farther north in northwestern Venezuela (Audemard 1993, 1998). Although the Caribbean plate is moving at rates between 1.2 cm/year in the west, and ~2.0 cm/year in the east with respect to South America (Weber et al. 2001), the present major strike-slip (Boconó-San Sebastián-El Pilar-Warm Spring faults, Fig. 2.10A) boundary slips at ~1 cm/year (Pérez and Aggarwal, 1981; Soulas, 1986; Freymueller et al. 1993; Audemard et al. 2000; Pérez et al. 2001, Weber et al. 2001, Trenkamp et al. 2002, Colmenares and Zoback, 2003, Cortés and Angelier, 2005). Other secondary faults have slip rates an order of magnitude less and in fact most of them exhibit slip rates under 0.5 mm/year, with the exception of the Oca-Ancón (2 mm/year, estimated from a paleoseismic study by Audemard, 1996), the Burbusay (<3 mm/year), Valera and La Victoria (<1 mm/year) faults.

However, all these observations do not take into account the vertical components and rotations of small blocks, which possibly accommodate the deformation caused by the triple convergence of plates. For this dissertation, I use apatite fission-track thermochronology in an attempt to bring new data that may be of relevance to the debate on the Caribbean geodynamic.

Chapter 3

III. APATITE FISSION-TRACK THERMOCHRONOLOGY

3.0 Introduction

Fission-track thermochronology is a powerful tool for deriving the low-temperature cooling history of upper crustal rocks, and for calculating the influence of surface processes. For this thesis I applied fission-track thermochronology on apatites separated from bedrock, modern river and ancient sandstone samples. In this chapter a brief introduction of the methodology and analytical procedure is given for the apatite fission-track dating method. For detailed methodological information the reader is referred to Wagner and Van den Haute (1992), Gallagher et al. (1998), Tagami and O'Sullivan (2005) or Donelick et al. (2005), among others.

3.1 Fission-track formation theory

The apatite fission track (AFT) method is based on the accumulation of fission tracks, caused by spontaneous fission decay of heavy elements (Price and Walker, 1962a, b). Spontaneous decay is restricted to elements with an atomic number ≥90 and a mass number ≥230, thus only the actinides are affected. Of these elements only ^{232}Th, ^{235}U and ^{238}U occur in measurable amounts in rocks. ^{238}U causes almost all tracks in natural samples; due to their low abundance and very long half life, the contribution by spontaneous fission of ^{235}U and ^{232}Th is negligible (Wagner and Van den haute, 1992; Tagami and O'Sullivan, 2005).

Fission of a ^{238}U nucleus releases two daughter particles, some neutrons and an energy of 210 MeV (with Cinetic Energy between 160 to 190 MeV). The emerging neutrons can induce new fission in adjacent ^{238}U nuclei. The mass ratios of the two newly formed daughter particles are in the range of 1.4 and in extreme conditions exceed 2 (Wagner and Van den Haute, 1992). After fission, the heavy charged particles move in opposite directions and interact with the crystal lattice, in the form of electronic and nuclear interactions, which leads to ionization and resulting vacancies in the lattice (Wagner and Van den haute, 1992; Tagami and O'Sullivan, 2005). This process is show in Fig. 3.1.

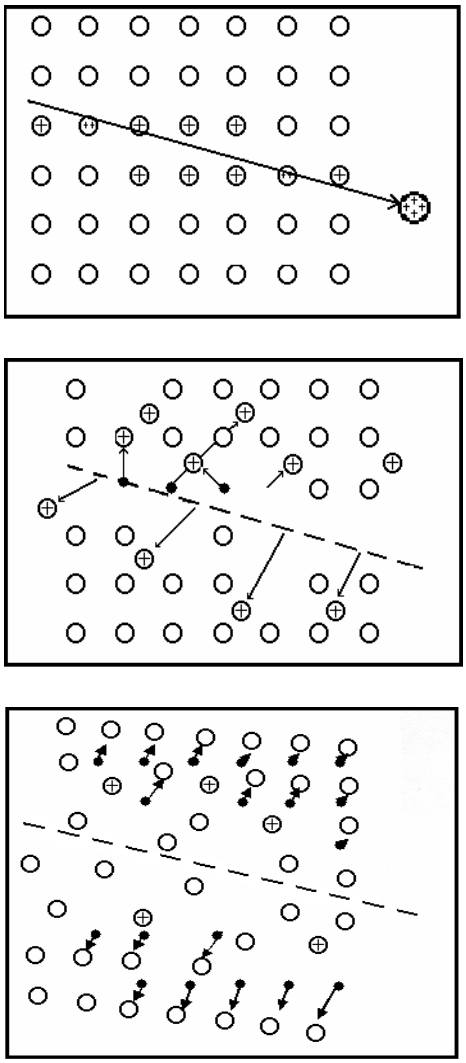

The three stages of formation and registration of charged particle tracks in a dielectric solid according to the "Ion Explosion Spike" model of Fleischer et al. (1975) are:

A

A.- Ionization of the atoms of the lattice, through the movement of the charged particles.

B

B.- The resulting clusters of positive ions are displaced from their original lattice sites as a result of Coulomb repulsion.

C

C.-The stressed region relaxes elastically, straining the surrounding undamaged lattice.

Fig. 3.1. Fission-track formation by the ion explosion spike model (modified from Fleischer et al. 1975).

Spontaneous fission tracks are only observable by optical microscopy after etching (Fig. 3.2). Because both particles have the same kinetic energy, the lighter particle causes ionization over a longer distance. The crystal lattice is completely destroyed in the track core and the ends of tracks show broad zones of damage (Fig. 3.1C).

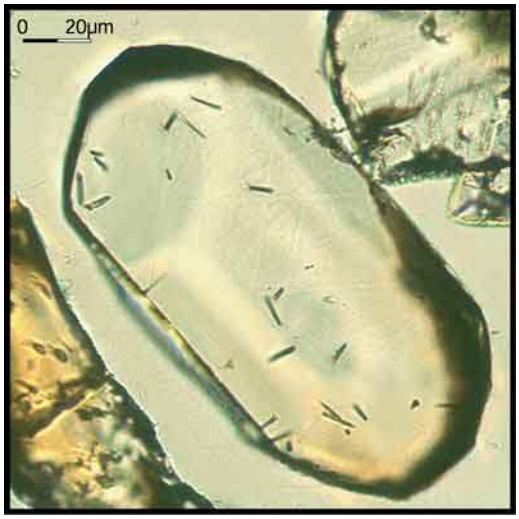

Fig. 3.2. Spontaneous fission track in apatite crystal. Magnification 1250X.

3.2 Fission-track age equation

The radioactive element ^{238}U can decay in two ways (Faure, 1986): by nuclear fission and by alpha (α) decay; thus, the total decay constant λ_d for this element can be described as:

$$\lambda_d = \lambda_\alpha + \lambda_f$$

where λ_α and λ_f are the alpha and fission decay constants respectively ($\lambda_\alpha = 1.55125 \times 10^{-10}$ yrs^{-1} and $\lambda_f = 8.46 \times 10^{-17}$ yrs^{-1}). Note that $\lambda_\alpha >> \lambda_f$; i.e α-decay is much more (about $2.10^6\times$) frequent than spontaneous fission.

The total number of decaying ^{238}U isotopes can be determined with the following expression (Faure, 1986):

$$D = D_\alpha + D_f = \frac{\lambda_\alpha}{\lambda_d} {}^{238}N\left[\exp(\lambda_d t) - 1\right] + \frac{\lambda_f}{\lambda_d} {}^{238}N\left[\exp(\lambda_d t) - 1\right] \qquad (3.1)$$

Where, ^{238}N is the total number of ^{238}U isotopes that are to decay. In this equation, the second term is important for fission-track thermochronology. Assuming that each fission event creates one fission-track ($D_f = N_s$) it is possible to calculate the number of spontaneous fission tracks:

$$N_s = \frac{\lambda_f}{\lambda_d} {}^{238}N\left[\exp(\lambda_d t) - 1\right] \qquad (3.2)$$

In virtue that the nuclear fission is much more rare (by seven orders of magnitude) than regular α-decay, it can be said that $\lambda_d \approx \lambda_\alpha$, and therefore:

$$\frac{\lambda_f}{\lambda_d} \approx \frac{\lambda_f}{\lambda_\alpha}.$$

By separating the variable *t* of equation (3.2) one obtains the fundamental age equation:

$$t = \frac{1}{\lambda_\alpha} \ln\left(\frac{\lambda_\alpha}{\lambda_f}\frac{N_s}{^{238}N} + 1\right) \tag{3.3}$$

The variable *t* depends on the number of spontaneous fission tracks (N_s) and the total number (^{238}N) of ^{238}U atoms. Using equation (3.3), a simple mathematical problem arises, because both *t* and ^{238}N are unknown variables.

The currently standard method for obtaining ^{238}N, or in other words the U concentration, is by means of irradiation of apatites or zircons with thermal neutrons (580.2×10^{-24} cm^2) in a research reactor (Wagner and Van Den Haute, 1992). This procedure produces induced fission tracks (Fig. 3.3), which are denoted by N_i. The number of induced tracks can be used to calculate ^{238}N in equation (3.3).

Induced fission tracks are generated by the collision of thermal neutrons with ^{235}U atoms in the apatite or zircon crystal. The thermal neutrons collide with ^{235}U instead of the ^{238}U because the activation cross-section (σ) of ^{238}U is negligible. Therefore, considering the neutron flux (ϕ), the activation cross-section (σ) and the ^{235}U concentration, the following equation can be used to calculate N_i:

$$N_i = {}^{235}N\sigma\phi \tag{3.4}$$

Because the ratio between the number of atoms of ^{235}U and ^{238}U is constant in nature (~7.2527×10^{-3}, Wagner and van den Haute, 1992), one can write:

$$\frac{^{235}N}{^{238}N} = k$$

Equation (3.4) can be rewritten as:

$$N_i = {}^{238}Nk\sigma\phi\ .$$

By combing the new equation 3.4 with equation (3.3), the following age equation is found:

$$t = \frac{1}{\lambda_\alpha} \ln\left(\frac{\lambda_\alpha}{\lambda_f} \frac{N_s}{N_i} k\sigma\phi + 1 \right) \tag{3.5}$$

3.2.1 External detector method and ζ calibration method or Z factor

In practical terms, during fission track counting we determine the density of etched tracks on internal crystal surface (ρ_s and ρ_i) and not the number of tracks per volume (N_s and N_i). Therefore $N_{s,i}$ is substituted by $\rho_{s,i}$ in the following equations, for details see Wagner and Van den Haute (1992).

A major problem is the accurate measurement of the decay constant for spontaneous fission, where individual determinations range from 7 to 8.5×10^{-17} y^{-1} (cf. compilation in Wagner and Van den Haute (1992). In addition, uncertainties are related to the determination of the thermal neutron flux ϕ (Hurford and Green, 1982), which is determined by using glass monitors with known uranium concentration. To overcome the uncertainty of the λ_f, value, Fleischer and Hart (1972) introduced the ζ-dating method, which affords to determine a personal calibration factor ζ for every individual dating method (e. g. apatite and zircon). To calculate this value, is usually applied the External Detector Method (Wagner and van den Haute, 1992; Gallagher et al. 1998). In this process, samples are irradiated and bombarded with neutrons which induce fission tracks that can be measured. In order to produce a surface to observe the induced fission tracks, each grain mount (Fig. 3.3) is covered by a thin, low-uranium muscovite mica sheet placed in intimate contact with the polished and etched apatite crystals. Following irradiation and subsequent cooling down, the mica sheets are etched to reveal the induced tracks resulting from the induced fission of the ^{235}U in the sample. For standardisation a similar mica sheet is also placed in contact with a small chip of ^{235}U doped glass. This is dealt with similarly and the results from the induced track densities for the apatite grains and the doped glass allow the 238U concentration in the apatite grain to be calculated (Donelick et al. 2005).

Single ζ-values are determined with the following equation (Hurford and Green, 1983):

$$\zeta = \frac{\exp(\lambda_\alpha t_{known}) - 1}{\lambda_\alpha \left(\frac{\rho_s}{\rho_i}\right)_{known} G\rho_d} \tag{3.6}$$

In equation 3.6 t_{known} is the known age of a standard (Fish Canyon Tuff and/or Durango for apatite); ρ_s, ρ_i and ρ_d are the spontaneous, induced, and dosimeter track density, respectively; G is the geometry factor, which is 0.5 for the external detector method (Fig. 3.4A). Once zeta is established, it is used to calculate the age of an unknown sample of interest (t_{uk}), which is given by the following equation:

$$t_{uk} = \frac{1}{\lambda_\alpha} \ln\left[\lambda_\alpha \left(\frac{\rho_s}{\rho_i}\right)_{uk} G\zeta\rho_d + 1\right] \tag{3.7}$$

The track density of the glass monitor ρ_d is proportional to the fluence (i.e, $\phi = B\rho_d$, where B is the factor expressing the proportionality of neutrons and tracks). Personal ζ-values are between 250 and 390 yr/cm² for the AFT system, depending on the U concentration of the glass monitor used. Widely used age standards are the Fish Canyon tuff for apatite and zircon with an independent age of 27.8 ± 0.2 Ma (biotite Ar/Ar age) and Durango apatite the t_{known}= 31.4 ± 0.6 Ma (K-Ar).

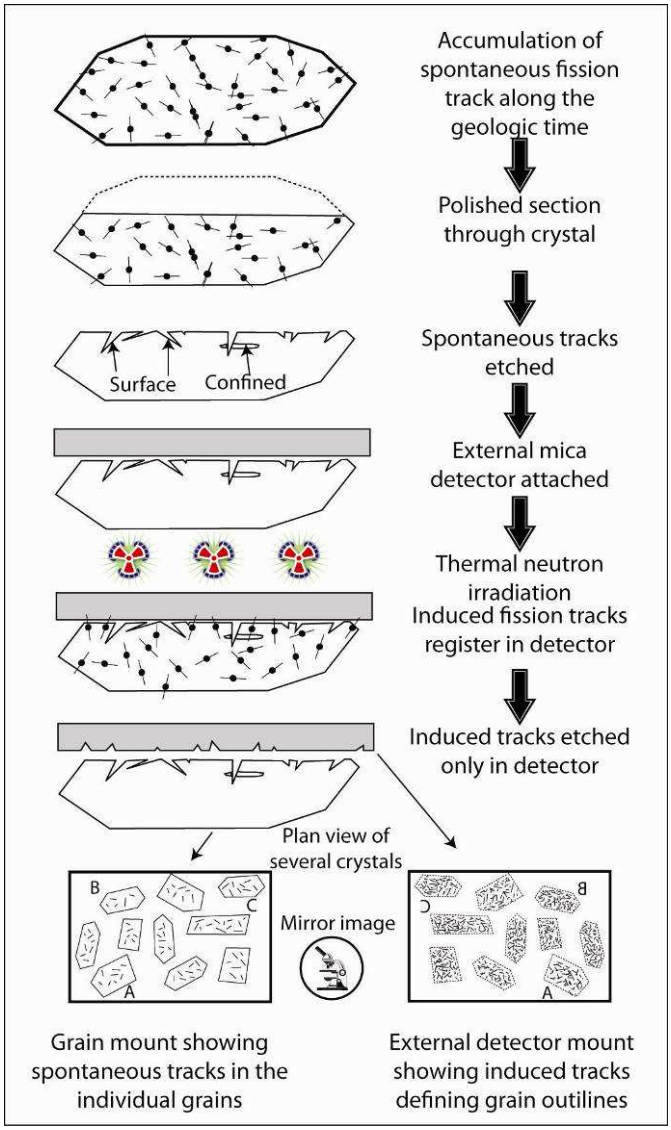

Fig. 3.3. The external detector method, after Hurford and Carter (1991). The surface of a given mineral is polished and etched under appropriate conditions to reveal spontaneous (surface) tracks intersecting what was an internal surface. Tracks (confined) below the surface can also be revealed if there is a pathway for the etchant (a surface track, cleavage, or fracture). Then an essentially uranium-free detector (typically a muscovite mica) is sealed against this surface, and this sandwich is sent to a nuclear reactor. The sample is irradiated with low-energy thermal neutrons, which induces fission in ^{235}U. During the fission process, some heavy particles cross the interface between the mineral and the mica, producing a mirror image of the original grain. When the sample is returned to the laboratory, only the mica is etched to reveal the induced tracks. By counting the number of induced tracks in the mica, thus, the uranium, or parent, concentration of the mineral grain is estimated, whereas by counting the number of spontaneous tracks in the mineral, is possibly estimate the concentration of the daughter product. A major advantage of this method is that fission track ages are determined on individual grains (From Gallagher et al. 1998).

The external detector method yields an individual age for each analysed grain. The counting of ρ_s, ρ_i for each grain are made on the same areas. With this technique the equation (3.8) is simplified to:

$$t = \frac{1}{\lambda_\alpha} \ln\left(\lambda_\alpha RG\zeta\rho_d + 1\right) \tag{3.8}$$

where,

$$R = \frac{N_{sj}}{N_{ij}} \tag{3.9}$$

for each grain *j*.

Resulting single grain ages in any given sample show a variation. The age dispersion depends mainly on the individual ages, U-content, sample quality, kinetic parameters and cooling history. Age calculations of the sample assume a Poissonian distribution of single grain ages, for this reason there are different ways for estimating *R*. For the purpose of checking if a sample has only one Poisson distribution, the modified χ^2-test or Galbraith test exists (Galbraith, 1981, 2005). The different statistics for $\hat{R}$ and the Galbraith test are shown in the next section

3.3 Conventional statistics for in-situ FT thermochronology

3.3.1 Estimators for *R*

3.3.1.1 Isochron fitting

Isochron fitting consists of fitting a linear regression with intercept equal to zero to the (N_i, N_s) pairs (Green, 1981; Burchart, 1981), assuming that if the ^{238}U concentration is zero, no fission tracks should exist. The slope of this straight line is considered as the estimator of *R* and the uncertainties for this method can be calculated in the usual way. The method can be applied with weighting or without. It requires more of five counts of pairs (N_s, N_i) to assure statistical significance. This method does not take into account the possible Poissonian distribution of N_s and/or N_i.

3.3.1.2. Mean ratio

According to Green (1981) it is possible to determinate the mean ratio with the following equation:

$$\overline{R} = \overline{\left(\frac{N_s}{N_i}\right)}_t = \frac{1}{n}\sum_{j=1}^{n}\frac{N_{sj}}{N_{ij}} \tag{3.10}$$

where j represents the grain number.

3.3.1.3 Pooled Mean

This estimator for *R* (Burchart, 1981; Green, 1981) is given for the following equation:

$$\overline{R} = \overline{\left(\frac{N_s}{N_i}\right)}_t = \frac{\sum_{j=1}^{n} N_{sj}}{\sum_{j=1}^{n} N_{ij}} \tag{3.11}$$

3.3.1.4. Central Age

The central age is calculated using a specific algorithm (Galbraith and Laslett, 1993; Galbraith, 2005), which takes into account the weight (w_j) on the observations N_s and N_i. The estimate of *R* is given for:

$$\overline{R} = \frac{\eta}{1-\eta} \tag{3.12}$$

where :

$$\eta = \frac{\sum_{j=1}^{n} w_j N_{sj}}{\sum_{j=1}^{n} w_j}$$

This is currently the most generally used age estimator because with many observations converge numerically to the maximum likelihood estimator for the ratio *R* (Galbraith, 2005), and will also be used in this work.

3.3.2 Standard error on fission-track age

The standard error (*se*) for the different estimations of the age (*t*), are give by the equation:

$$se(t) = t \times \sqrt{\left[\frac{1}{\sum_{j=1}^{n} N_{sj}} + \frac{1}{\sum_{j=1}^{n} N_{ij}} + \frac{1}{N_d} + \left(\frac{se(\zeta)}{\zeta}\right)^2\right]} \tag{3.13}$$

3.3.3 Galbraith test

For the purpose of discriminating if the counted fission tracks of a sample belong to only one Poisson distribution, Galbraith (1981, 2005) proposed a test based on the Chi-square distribution (χ^2) and Pearson`s approach (Kendall and Stuart., 1958).This test is calculated with:

$$X = \sum_{j=1}^{n} \frac{\left(N_{sj} - \overline{N_{sj}}\right)^2}{\overline{N_{sj}}} + \sum_{j=1}^{n} \frac{\left(N_{ij} - \overline{N_{ij}}\right)^2}{\overline{N_{ij}}} \tag{3.14}$$

where:

$$\overline{N_{sj}} = \left[\frac{N_s}{N_s + N_i}\right]\left(N_{sj} + N_{ij}\right)$$

$$\overline{N_{ij}} = \left[\frac{N_i}{N_s + N_i}\right]\left(N_{sj} + N_{ij}\right)$$

N_{sj} and N_{ij} are the spontaneous and induced fission track counts for each grain j=1,…n, and $N_s = \sum_{j=1}^{n} N_{sj}$ and $N_i = \sum_{j=1}^{n} N_{si}$. In case the data come from a single Poisson distribution, X has a distribution χ^2 with n *-1* degrees of freedom. Galbraith suggests a level of 95%, that is to say, α = 0.05. If the data fail Galbraith's test (usually α > 0.05), it means that the data do not satisfy the Poisson hypothesis of belonging to a single Poisson distribution.

According to Galbraith (2005), this test only gives an idea about the homogeneity of the estimation of the age. However, Galbraith does not make any strict recommendation to when the test rejects the hypothesis. Therefore, from a statistical point of view Galbraith (1981, 2005) does not provide an equation for obtaining the errors associated with this statistical test.

A χ^2 probability of >5% is representative of a single age population. The age of the sample can be calculated in the different ways mentioned above (e.g., isochron, mean, pooled, central). In this thesis, for convenience only central ages are reported with standard errors of 1σ. When the Poisson hypothesis is satisfied, there is no difference between the different equations for age estimation. The appendix I, I present a new method for determining age populations in a sample in the case that different Poisson populations are found.

3.4 Fission-track annealing and modeling

The fission event causes damage in the solid crystal structure of apatite or zircon crystals. The latent tracks in the crystal may be repaired, mainly depending on ambient temperature and residence time at a given temperature (Fleischer et al. 1975). This process, also known as *annealing*, leads to a reduction in track length and density, making it a unique tool for determining time-temperature (t-T) histories of rocks (Wagner and Van den Haute, 1992).

Annealing of fission tracks depends mainly on the temperature and the kinetic and chemical properties in case of apatite of single crystals. The properties must be approximated to derive reliable t-T history predictions. Apatite can have a wide variety of chemical composition with coupled substitution within the cation and anion positions, resulting in F, Cl or OH apatites. The relationship between composition, crystal structure and annealing kinetics leads to a complex behaviour of FT annealing in apatite (Carlson et al. 1999; Barbarand et al. 2003a, b).

Fission-track annealing experiments on apatites clearly show that the track lengths in compositionally different apatites are shortened by different amounts given the same temperature and residence time (Barbarand et al. 2003a, b). This behaviour represents the summed effect of the type and amount of elemental substitution, and site of substitution in the crystal structure. The substitution directly affects the apatite unit cell, resulting in different FT annealing rates. Barbarand et al. (2003a, b) found a strong correlation (greater than 0.8) between the level of annealing and the unit-cell parameters (positive for unit cell axes dimensions *a* and *c*, respectively). Thus, the unit cell parameter can be used as a key indicator of the response to annealing in apatite (Barbarand et al. 2003a, b). Unit cell parameter variations can be partly explained by levels of Chlorine, Fluor or Hydroxyl ion substitutions.

This indicates that no single substitution can explain the bulk change in lattice parameters although Green et al. (2005) proposed that even for fluorine apatite a good correlation between annealing and wt.% Cl exists. An alternative approach for describing the annealing properties of apatite is to use its solubility as a proxy for the bulk composition. For this reason D_{par} can be measured; the mean length of well-defined etch pits of fission tracks parallel to the crystallographic c-axis (Burtner et al. 1994). D_{par} values vary according to apatite composition (Barbarand et al. 2003a, b), and show a positive correlation with cell parameter *a* and MTL.

X-ray diffraction (XRD) measurement of unit cell is attractive, but impractical as a routine tool. Alternatively there are two approaches: (1) Electron probe micro-analyser (EPMA) measurements can rapidly determine the chemical composition of apatite. (2) Etch pit measurements provide a clear correlation with cell parameter *a* and MTL values. Barbarand et al. (2003 a, b) demonstrated that the etch-pit size is a valuable estimator of annealing properties of individual apatite grains, only limited by the precision of the measurement.

Annealing kinetics of single grains can thus be determined by microprobe analyses measuring apatite compositions or by D_{par} measurements. Annealing experiments and field observations show that chlorine-apatite is more resistant to annealing than pure fluorine-apatite. The same correlation can be observed for D_{par} values, which usually vary around 1.5 μm for apatites that are less resistant to annealing, and reach up to 5.0 μm for apatites that are more resistant to annealing (Carlson et al. 1999; Ketcham et al. 1999). AFT dating conducted on boreholes shows that end member F-apatites are fully annealed at a present-day down-hole temperature of 92°C, and apatites with 2.2 wt% Cl retain tracks up to temperatures of above 124°C (e.g., Green et al. 1989).

The concept of closure temperature (T_c) cannot be easily applied to fission-track dating and should be regarded as a simplified concept in the case of monotonic cooling because: (1) there is no geologically reasonable temperature at which annealing is negligible (Donelick et al. 1990, Spiegel et al. 2007); (2) fission-tracks anneal at relative low temperatures near the surface and thus many samples have experienced a complicated history. Therefore, Wagner et al. (1972) introduced the concept of the partial annealing zone (PAZ), which accounts for the fact that annealing occurs over a range of temperatures. The PAZ ranges from 60 to 120°C for apatite and about 200 to 280°C for α-damaged zircon, depending of duration of heating (Wagner and Van den Haute, 1992; Hurford, 1986; Brandon et al. 1998; Garver et al. 1999).

Track length data can be used to derive information about the t-T history of analysed samples. Implemented annealing models are used for forward and inverse modelling of possible t-T paths. Ketcham et al. (2007b) implemented a multikinetic inversion model, requiring kinetic parameters such as D_{par} values of each grain.

Fission-track annealing in apatite is anisotropic, and strongly controlled by the track orientation relative to the crystallographic c-axis (Barbarand et al. 2003a, b), which has an impact on track length distributions. C-axis projection of measured track lengths can be used to correct for this bias (Ketcham et al. 2007a).

3.5 Length measurements

Track lengths are routinely measured on confined tracks. There are two types of confined tracks: (1) tracks in track (TINTs) and (2) tracks in cleavage (TINCLEs) (Wagner and Van den Haute, 1992). There is a clear trend to longer tracks in TINCLEs (Barbarand et al. 2003 a, b), resulting from several sources of bias: (1) a TINCLE is more likely to intersect a fracture if its angle to the fracture is higher, resulting in a non-uniform distribution. (2) Fractures may be widened during polishing and etching. (3) Fractures exhibit higher etching rates, because the etchant can access the confined tracks more easily (Fig. 3.4). Therefore, for reducing the bias of track length data and thus for more reliable t-T reconstructions, only TINTs were measured.

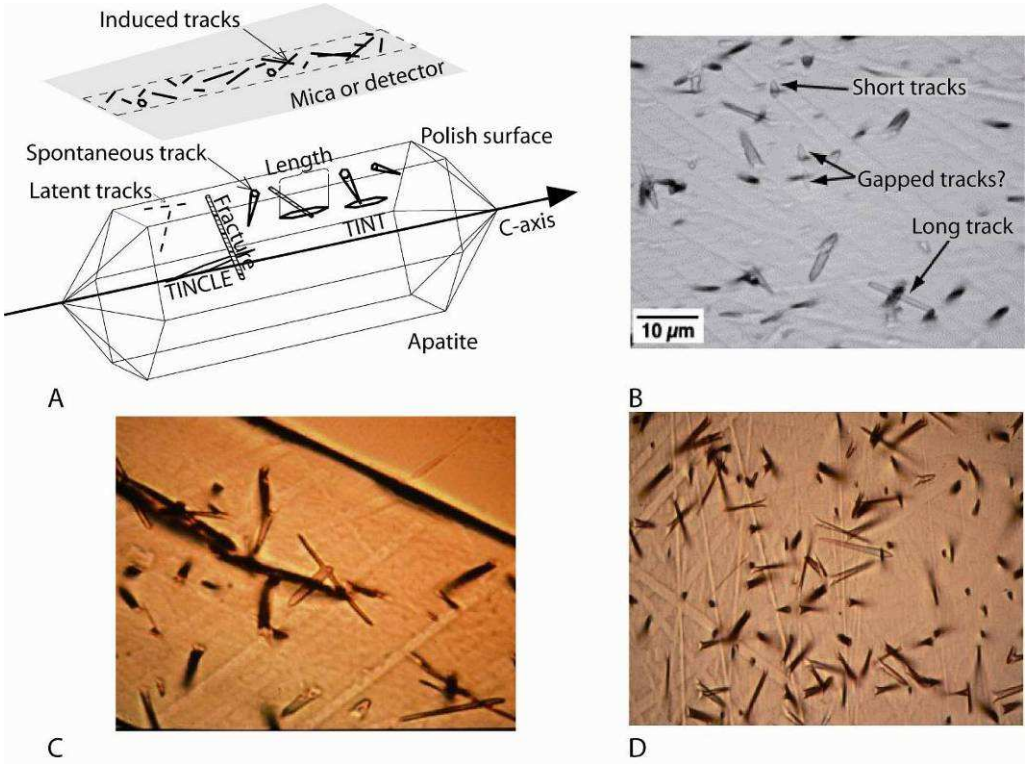

Fig. 3. 4. A) Features related to apatite fission-track thermochronology analysis and position of detector or mica. Confined fission-tracks under the microscope: B) tracks observed in a partially annealed Durango apatite sample comparing long, short and possibly gapped tracks. Sample etched with 5 M HNO_3, at 20±1°C, for 30 s. (From Barbarand et al. 2003a, b). C) TINCLE or Track IN CLEavage. D) TINT or Track IN Track. The images C to D were taken using transmitted illumination and a dry objective (pictures C and D were taked from Geotrack website: www.geotrack.com.au).

Another problem in length measurements is that the amount of shorter tracks will always be underestimated, because tracks between 5 and 2 μm are difficult to observe and for tracks <2 μm it is impossible to distinguish between a confined track and etch pits (Barbarand et al. 2003a, b). Chemical properties of the etchant (e.g. concentration) cause different track revelation, e.g. in apatite with concentrated or diluted HNO_3 as etchant (Wagner and Van den Haute, 1992). The etched tracks can be identified by some distinct characteristics: (1) line defects of limited length (<20 μm), (2) straight, (3) exhibiting no preferred orientation and (4) disappear after suitable heating. Irradiation with a collimated beam of heavy ions (e.g. ^{252}Cf) results in an increased proportion of TINTs, thus improving the analytical precision. For aliquots with MTL <14 μm there is a slight systematic shift to longer values for Cf-irradiated samples, which is within the standard error for replicate measurements (Barbarand et al. 2003a, b).

Interlaboratory comparisons show that length measurements of the same sample often yield differences of 20 % (Wagner and Van den Haute, 1992). It is of great importance to ensure that annealing models used by different analysts are comparable to each other. Recent investigations show that there are large variations in AFT length distributions both intra- and interlaboratory, which can be up to ~ 30 % in extreme cases for samples with short mean track length measured by different analysts (Barbarand et al. 2003 a, b; Ketcham et al. 2009). The reliability of the deduced t-T history from AFT data depends mainly on the size of the dataset, especially the amount of the measured track lengths. For complex thermal histories a minimum value of 100 length measurements is required, whereas simple t-T histories can be reliably deduced from ~50 length measurements (Barbarand et al. 2003a, b).

3.6 Analytical procedure

Samples were disaggregated and minerals separated using standard magnetic and gravimetric techniques: crushing, sieving and electromagnetic and heavy liquid separation (sodium polytungstate and Methylene Iodide or Diiodomethane). Apatites were mounted in epoxy, and polished to expose internal surfaces. The apatite mounts were etched with 5.5M HNO_3 for 20s at 20°C. All mounts were irradiated together with Fish Canyon Tuff and Durango apatite standards and IRMM-540 uranium dosimeter glasses at the Orphée reactor at Laboratoire Léon Brillouin, Centre d'Etudes Nucléaires de Saclay, Gif-sur-Yvette, France.

During the mounting process I assured that numerous grains (~800) were randomly distributed within the mounts. This helps avoiding a sampling bias when counting and provides a better variability with respect to cooling ages and uranium content of individual apatites. During the counting process the grains with well exposed and polished surfaces were marked for counting using transmitted light–at 125x magnification. Marked grains were counted at 1250x (dry) using an Olympus BH-60 microscope.

The samples were dated with the external detector method (Naeser, 1978; Gleadow, 1981) using the zeta calibration approach (Hurford and Green, 1982; Hurford and Green, 1983). AFT zeta values of 288.66 ± 5.23 yr/cm² and 129.82 ± 5.02 yr/cm² (M. Bermúdez) for IRMM-540 and Corning-1 (CN-1) dosimeter glass respectively, were determined from Durango and Fish Canyon Tuff apatite age standards (see appendix section). Age calculation, visualization and statistics were carried out with the Trackkey 4.2f program (Dunkl, 2002), BINOMFIT (Brandon, 1992, 1996) and p-partition algorithm (Bermúdez-Cella, 2008). More details about the used analytics are described in appendix.

Apatite samples with young cooling ages or low-U content were irradiated with a ^{252}Cf source in Melbourne (Australia), to enhance the number of etchable confined tracks. Predicted time-temperature (t-T) paths for individual samples were used for forward modeling of AFT and AHe data. Modeling was carried out with the program HeFTy v. 1.5.6 (Ketcham, 2005) based on the multikinetic annealing model of Ketcham et al. (2007b) and with *c*-axis projected track-length data (Ketcham et al. 2007a). t-T paths were statistically evaluated and categorized by a value of goodness of fit (GOF), in which a 'good' result corresponds to a value of 0.5, an 'acceptable' result corresponds to a value of 0.05, and a GOF of 1 is the optimum. The input parameters for each sample used in this study are its central FT age with 1σ error, the predicted t-T path, and, if available, the *c*-axis projected track-length distribution, and, as a kinetic parameter, the D_{par} value.

3.7 Detrital apatite fission-track thermochronology

Detrital thermochronology provides the opportunity to study different processes: long-term evolution of mountain belts, their cooling history, changes in topography, and changes in river drainage paths, as among others (Bernet and Spiegel, 2004). In this work I used detrital apatite fission-track thermochronology for three purposes: provenance analysis, landscape

evolution and exhumation studies. Figure 3.5 represents the history of one detrital apatite grain inside the exhumation-erosion-deposition cycle in the Venezuelan Andes system. In this figure:

t_c= time of closure, or time at which the apatite crosses the closure isotherm surface (~110°C) and the fission-track clock starts (applying the simplified closure temperature concept).
t_e= time when the apatite arrives at the surface because of exhumation and is eroded; at this point the sedimentary cycle starts.
t_d= time of deposition in the sedimentary basin.
Thus,

$t_u = t_c - t_e$ = time between closure at depth and exposure at the surface

$t_t = t_e - t_d$ = transport time in the fluvial system, between erosion at the surface an deposition in a sedimentary basin

$t_s = t_d - t_{today}$ = time between deposition in the basin and today, that is to say, the stratigraphic age of the sediment

$l_t = t_c - t_d$ = lag time, is the time required for the sample to cool, get exhumed to the surface, and then get deposited in a nearby basin (Bernet and Garver, 2005).

For determining rates of exhumation from detrital apatite fission-track ages it is necessary to known t_t and t_s. The stratigraphic age (t_s) can be obtained by techniques such as magnetostratigraphy, palinology or biostratigraphy. The fission-track dating method can provide a stratigraphic age for volcanic ash layers (Crowley et al. 1989; Bernet and Garver, 2005). In the case of the pro- and retro-side foreland basins of the Venezuelan Andes, it is difficult to determine precise stratigraphic ages because the sedimentary rocks are poor in fossils and because their make trend poor quality for magnetostratigraphic analyses.

The stratigraphic ages are therefore poorly strained and the best indication for the age of deposition is the youngest AFT age component in the detrital samples and the estimated average lag time. The youngest age component of a modern river samples provides the present day lag time, which can be used as a first order estimated lag-time in the past. The youngest age component is determined by decomposition of age components through

statistical analyses and the results are presented in probability density or radial plots (Galbraith and Green, 1990; Brandon, 1996).

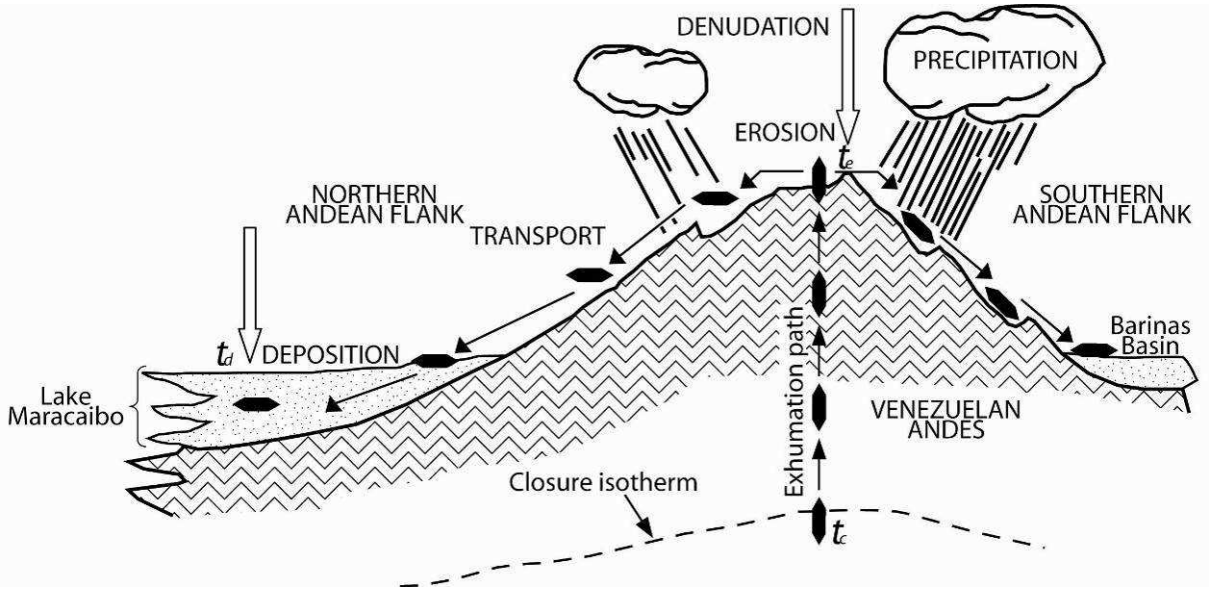

Fig. 3.5. Schematic representation of the lag-time concept for detrital apatite or zircon (solid symbol) in the Venezuelan Andes (Modified from Crowley et al. 1989).

For discussing lag time and its relation to exhumation it is necessary to define the terms *exhumation* and *denudation* (Fig. 3.5). Exhumation has been defined as the difference between rock uplift and surface uplift (England and Molnar, 1990), or the unroofing history of a rock caused by tectonic and/or surface processes such as erosion (Ring et al. 1999). Denudation refers to the removal of rock by tectonic and/or surface processes at the Earth's surface or in the upper crust (Ring et al. 1999). Exhumation describes the fact that rock is brought closer to the Earth surface because of denudation. Thus, the amount of exhumation equals denudation, but they are defined with a different perspective.

The histories of the Lake Maracaibo basin and the Barinas basins (Fig. 3.5), are somewhat different in that the Lake Maracaibo basin is three times as deep as the Barinas basin. Here arises another application of apatite fission-track thermochronology: the thermal reconstruction of these sedimentary basins.

To generate liquid hydrocarbon under natural conditions, sediments should be buried until they reach the "oil-window", between 60 and 130°C. This zone is shown in Figure 3.6, together with the paleo-temperature and the AFT PAZ, which overlaps to a large part with the

oil-window. AFT age and track-length analysis allows reconstructing the thermal history of sedimentary basins (Armstrong, 2005).

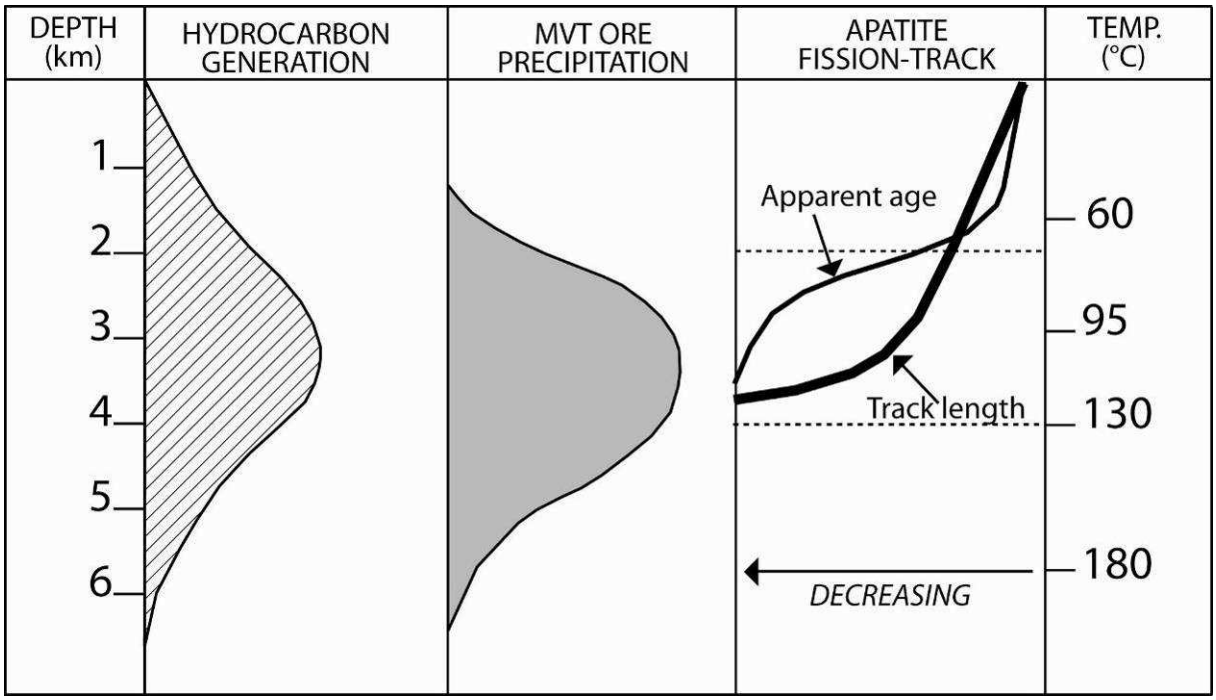

Fig. 3.6. Comparison among temperature and depth for hydrocarbon generation, MVT ore precipitation and annealing of fission-track in apatites (After Wagner and van den Haute, 1992).

3.8 Conventional statistics for detrital FT thermochronology

Application of detrital apatite fission-track thermochronology requires gathering sufficient data for obtaining the best information possible. The quantities of grains necessary for application of detrital thermochronology has been the subject of discussion for a long time (Carter, 2007). Dobson et al. (1988) established that 60 grains are enough to achieve 95% detection probability. Vermeesch (2004) considers that at least 117 grains are needed for achieving the same probability, however this was postulated for U/Pb analyses of detrital zircon smaller error.

In this work, I tried to date more than 100 grains per detrital sample, but this number was difficult to obtain for certain samples because of poor apatite quality. The mixed distribution of grain ages in a detrital sample requires deconvolution into component ages. The presentation of detrital grain-age distribution in histograms has its limitations because the uncertainties of single-grain ages cannot be shown. In addition to histograms, many researchers use probability density plots for representing grain-age distributions and age

components of detrital samples. However, there are several problems with these types of plots. For example, the overlap effect associated with broad, imprecise peaks, or poorly estimated age components. Detailed discussion of the limitations of probability density plots are given by Galbraith (1988, 1990, 2005), who proposed the use of radial plots for visualizing the distribution of populations of FT grain ages. Other graphical displays (cluster clouds, dendograms, best probability contour plots, barplots, hierarchical plots, etc; Wilk and Gnanadesikan, 1968; Chambers et al. 1983) of single-grain ages provide a simple way for discriminating age components; these graphical or mathematical tools require other complex statistical-mathematical treatment for extracting component ages and standard errors (Carter, 2007).

The different methods for deconvolving mixed-age datasets include the decomposition into Gaussian distribution components (Brandon, 1992) or Poisson distribution models (Galbraith, 2005). The most common method at present is the binomial peak fitting algorithm of Galbraith and Green (1990), which has been incorporated into the BINOMFIT software developed by Brandon (Brandon, 1996; Steward and Brandon, 2004).

Figure 3.7 illustrates the plots commonly used for presenting detrital fission-track ages, here given with the example of the Chama River in the Venezuelan Andes. In Figure 3.7A an example of a histogram with a superimposed probability density function (PDF) is shown. The plot indicates that different age populations or components are present in this sample. This PDF is decomposed in three components using BINOMFIT. The unimodal curves in this plot represent the binomial best-fit peaks. The radial plot of Galbraith (1988) is shown in the Figure 3.7B. In a simple case each population should be represented by points plotting along discrete radii. The *x*-axis in this plot indicates the relative error (%). The *y*-axis (left) is referred to as an estimation of the standard error, which is calculated by the equation:

$$y_i = \frac{(z_i - z_0)}{\sigma} \tag{3.15}$$

where z_0 is the central age (*y*-axis, to right) and z_i is the individual age of crystal *i*.

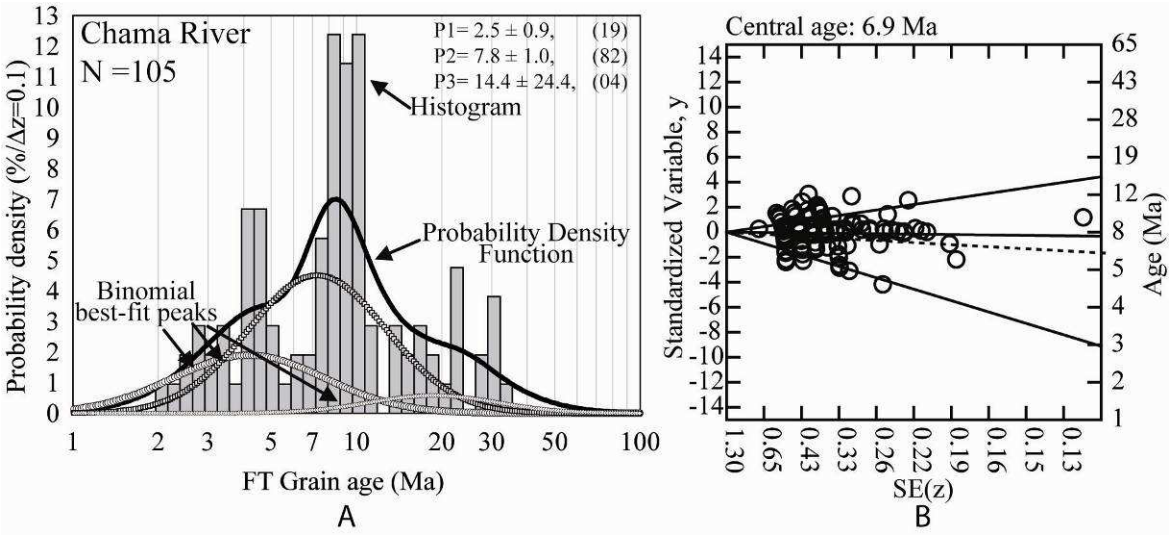

Fig. 3.7. The usual representation for detrital fission-track data. A) Histogram, Probability Density Function and binomial best-fit peaks. B) Radial plot of Galbraith (Galbraith, 1988).

3.9 Data interpretation and quantitative thermochronology methods

The most common way of interpreting bedrock thermochronologic data is by means of age-elevation profiles. From this approach an Age-Elevation Relationship (AER) can be inferred. It is commonly assumed that this relationship provides an estimate of exhumation/erosion rates, but this is a simplification. According to Moore and England (2001), the inference of denudation rates from temperature-time histories of rocks is not straightforward. Many factors may perturb simple AER (Braun, 2002), and the interpretation of thermochronometric ages (Ehlers, 2005). For example, geothermal gradients may change over time. These changes can be caused by advection of isotherms towards the surface because of normal faulting or erosion, changes in relief or the background thermal state of the crust because of magmatism, or fluid flow, and even sedimentation. All these can cause perturbations in the geothermal gradient, and modify the curvature in the temperature-time path.

Figure 3.8 illustrates schematically the thermo-tectonic processes that influence the interpretation of data thermochronometric.

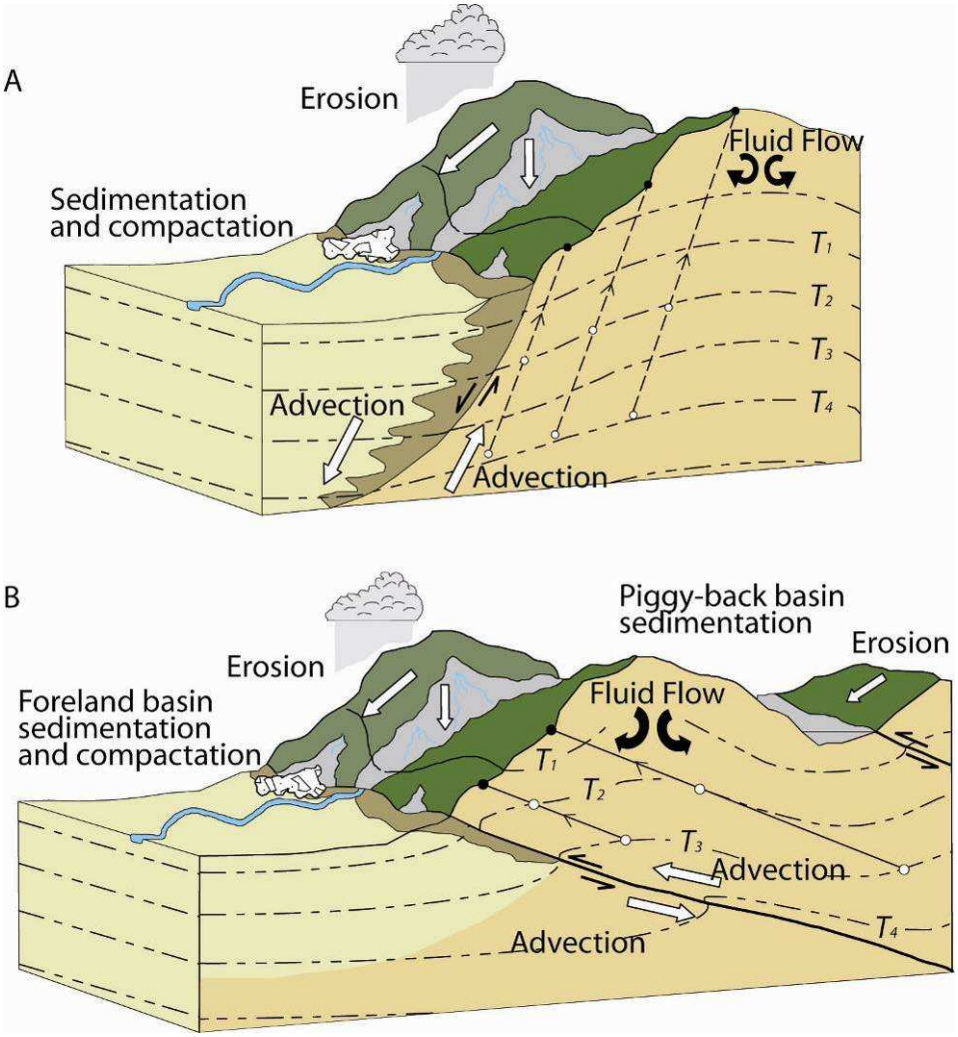

Fig. 3.8. Thermo-tectonic processes that influencing thermochronometry interpretation (Modified from Ehlers, 2005).

In chapter 2, I showed that there is no clear consensus on the structure and origin of the Venezuelan Andes. Thus, for the purpose of interpreting fission-track results of this work in a geodynamical context, I used the PECUBE code developed by Braun (2003) to test different tectonic configurations and thermo-kinematic parameters. In the following section I provide a summary of the principles of quantitative thermochronology.

3.9.1 Quantitative thermochronology

The PECUBE code was developed by Braun (2003) and constitutes a fundamental part of quantitative thermochronology (Braun et al. 2006). This code solves the three dimensional heat equation using the finite element method (FEM); PECUBE permits solving the following boundary value problem (BVP):

$$\rho c\left(\frac{\partial T}{\partial t} + u\frac{\partial T}{\partial x} + v\frac{\partial T}{\partial y} + w\frac{\partial T}{\partial z}\right) = k\Delta T + \rho A$$

$$\begin{cases} T_0 = T_0(x, y, z, t = 0) \\ T(x, y, z = S(x, y, t), t) = T_{MSL} + \beta S \\ T(x, y, z = -L, t) = T_1 \\ \dfrac{\partial T}{\partial n} = 0 \text{ at the boundary} \end{cases} \tag{3.16}$$

where: *T(x,y,z,t)* is the temperature; ρ is the rock density; *c* is the heat capacity; *k* is the thermal conductivity; *A* is the heat production; *u*, *v*, *w* are the advection velocity of rocks; T_0 is the initial temperature; *S(x,y,t)* is the altitude of the surface, with respect to the sea-level; T_1 is the temperature at the base of the model, assuming that this is located at $z = -L$; T_{MSL} temperature at sea-level; β atmospheric temperature gradient (lapse rate). In this model, the basal temperature is defined rather than a heat flux, which simplifies the thermal calculations.

The BVP (3.16) predicts the age of closure using different thermochronometric systems. In this case the heat equation in a crustal block can be affected by the thermo-tectonic processes as shown in Figure 3.8 (vertical and horizontal movements and / or erosion).

In these models, I neglect heat transfer by fluids, because its relative importance to the significant vertical advection of the flux through the exhumation of the rocks is unknown (Ehlers, 2005) although it could be significant (Whipp and Ehlers, 2007). I assume that heat transfer by advection and conduction of rocks are the dominant mechanisms of heat transfer.

PECUBE uses a mixed Lagrangian and Eulerian specification approach for the displacement field. This is a way of looking at motion that focuses on specific locations in space through which the material moves. These specifications can be applied to any observer's frame of reference, and in any coordinate system used within the chosen frame of reference. This permits PECUBE to produce frequent re-interpolation of the temperature field in the vertical direction. Thus t-T paths are calculated, and used to predict thermochronologic ages for apatite system. The AFT ages are calculated by direct modeling of the accumulation of daughter products, in this case fission-tracks, and not simply by taking the cooling age (Wolf et al. 1998). For AFT the model of Laslett et al. (1987) and Lutz and Omar (1991) are used, and are described in van der Beek (1995), and Stephenson et al. (2006).

For tectonic-kinematic modeling I will use the AFT data from age-elevation profiles (Kohn et al. 1984, and the new data of this work), and PECUBE with the objective of forward modeling, without taking the tectonic configuration into account, I will test the timing of different exhumation scenarios and topography settings, generate t-T paths for the samples, and compare the results with thermal modeling (HeFTy) and transdimensional modeling (Gallagher et al. 2009). Thus, I should recognize if the AERs are affected by the problems described above.

The best forward model means PECUBE is chosen according to the lowest misfit value, which is calculated in the following way:

$$misfit = \frac{1}{n}\sqrt{\frac{\sum_{i=1}^{n}\left(t_{obs}^{i} - t_{cal}^{i}\right)^2}{error_{obs}^{i}}} \tag{3.17}$$

where n is the number of observations, t_{obs} and t_{cal} correspond to observed and calculated fission-track age for each sample i.

Chapter 4

IV. SPATIAL AND TEMPORAL PATTERNS OF EXHUMATION ACROSS THE VENEZUELAN ANDES: IMPLICATIONS FOR CENOZOIC CARIBBEAN GEODYNAMICS

Mauricio Bermúdez[a,b*], Barry P. Kohn[c], Peter van der Beek[a], Matthias Bernet[a], Paul B. O'Sullivan[d] and Reginald Shagam[e,†]

[a] Laboratoire de Géodynamique des Chaînes Alpines, Université Joseph Fourier, BP53, 38041 Grenoble, France
[b] Laboratorios de Termocronología y Geomatemáticas, Escuela de Geología, Minas y Geofísica. Facultad de Ingeniería, Universidad Central de Venezuela, Caracas, Venezuela.
[c] School of Earth Sciences, University of Melbourne, VIC 3010, Australia.
[d] Apatite to Zircon, Inc. 1075 Matson Road Viola, Idaho 83872-9709, U.S.A.
[e] Geological and Environmental Sciences, Ben-Gurion University of the Negev, Beer Sheva, 84105, Israel.

4.0 Abstract

The Venezuelan Andes formed by complex geodynamic interaction between the Caribbean Plate, the Panamá Arc, the South American Plate and the continental Maracaibo block. We study the spatial and temporal patterns of exhumation across the Venezuelan Andes using apatite fission-track (AFT) thermochronology (48 new ages) and topographic analysis. This approach permits the identification of at least seven tectonic blocks with contrasting exhumation and cooling histories. Blocks located in the central part of the Venezuelan Andes and separated by the Boconó fault system, cooled rapidly but diachronously during the late Miocene–Pliocene. These blocks coincide with the highest topography and steepest relief of the belt. The Caparo and Valera blocks at the southwestern and northeastern terminations of the Venezuelan Andes respectively, experienced a phase of slow cooling from the late Oligocene to late Miocene. Unravelling the cooling history of the individual blocks and the faults that delimit them are key to better understanding the control of Caribbean geodynamics on the evolution of the Venezuelan Andes. Our data indicate: (1) a strong control of the exhumation patterns by major fault zones, consistent with the notion that these are inherited structures that may be rooted in the lower-crust and (2) temporal correlation between phases of rapid exhumation in different blocks with major tectonic events (e.g. collision of the Panamà arc; rotation of the Maracaibo block).

Keywords: Venezuelan Andes, apatite fission-track, exhumation, Boconó fault, thermal history modeling, transpression, tectonics.

4.1 Introduction

The Venezuelan Andes form a complex orogen characterized by high seismicity and localized rapid Neogene exhumation (Kohn et al. 1984; Case et al. 1990). This northeast trending orogen constitutes the northwestern termination of the stable South American plate (Colletta et al. 1997), extending 400 km from the Colombia-Venezuela border to south of Barquisimeto (Figs. 4.1 and 4.2). The Venezuelan or Mérida Andes were formed as a result of oblique convergence between the Caribbean and South American plates, accretion of the Panamá arc, and rotation and translation of the continental Maracaibo block (Aleman and Ramos, 2000; Pindell and Kennan, 2001). The reactivation of pre-existing tectonic discontinuities of different ages and origins, mostly developed along the former passive margin of the South American plate, has played an important role in the evolution of the orogen (Mora et al. 1993; Jacques, 2004; Mora et al. 2009). Oblique plate convergence resulted in local thrusting, rotation, translation, transtension, and extension of many of these structures, which led to exhumation of individual blocks at different times and rates from the Late Eocene to the Pliocene (Hargraves and Shagam, 1969; Schubert, 1980a, 1981; Shagam et al. 1984; Kohn et al. 1984; Lugo and Mann, 1995).

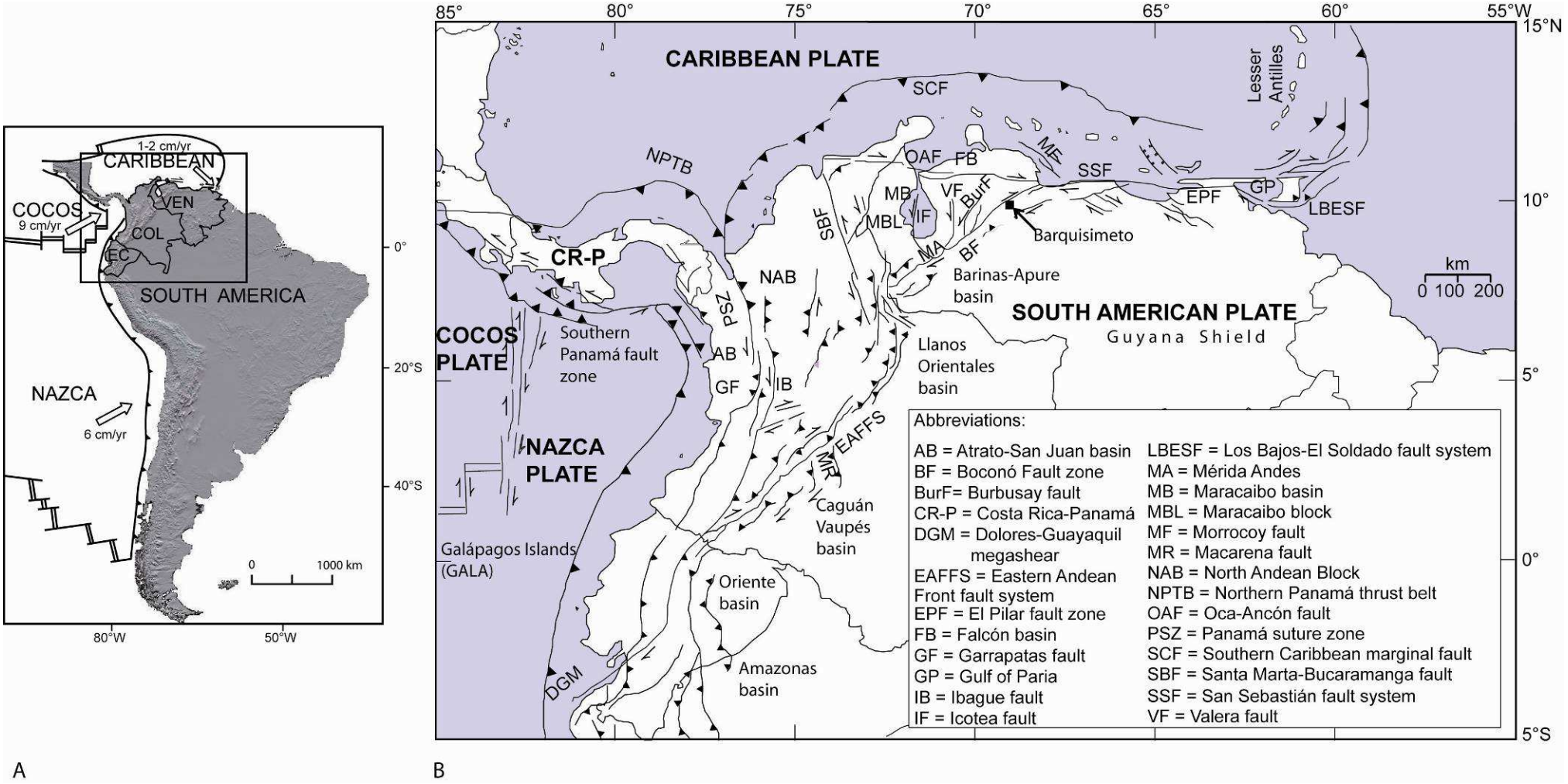

Fig. 4.1. A) Shaded relief map of South America showing present-day plate configuration. The Northern Andes comprise mountains ranges in Ecuador (EC), Colombia (COL), and Venezuela (VEN). B) Major tectonic features of northern South America (modified from Colmenares and Zoback, 2003).

The structure of the Venezuelan Andes is controlled by a complex system of strike-slip faults and thrusts. Several tectonic models for the evolution of the Venezuelan Andes have been proposed based on geochronology, field observations, and seismic data (e.g. Kellogg and Bonini, 1982; Colletta et al. 1997; Audemard and Audemard, 2002), but due to the complex interaction of oblique plate motion involving several microplates with pre-existing structures, as well as the absence of deep crustal seismic data, their structure and kinematics remain controversial.

The purpose of this paper is to provide new constraints on the timing and rate of exhumation, and the topographic evolution of individual tectonic blocks within the Venezuelan Andes, by using apatite fission-track (AFT) thermochronology and Digital Elevation Model (DEM) analysis. AFT thermochronology expands on the existing data of Kohn et al. (1984) and Bermúdez et al. (submitted, chapter 5 in this work), by presenting 44 new AFT ages, as well as track-length and kinetic data. In this paper we attempt to explain the evolution of the Venezuelan Andes within the Caribbean tectonic framework from the Miocene to the present, taking into account current tectonic models. Because the deep structure of the Venezuelan Andes and the arrangement and distribution of faults in the subsurface is poorly understood, very different tectonic models have been proposed (Fig. 4.2). Here we provide low-temperature information that could help constrain the geodynamic evolution of the orogen.

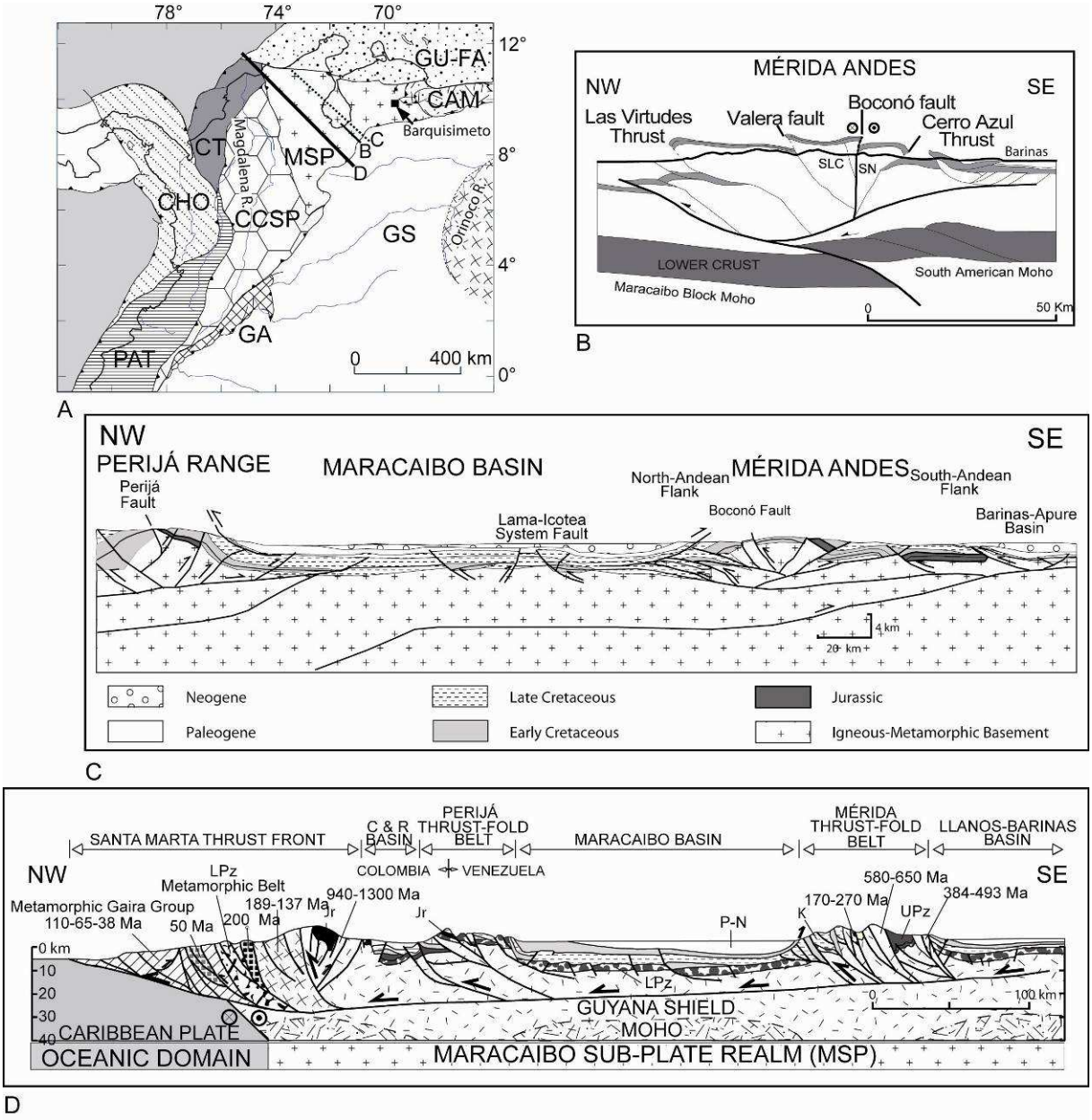

Fig. 4.2. A) Subdivision of northern Andes into tectonics domains: CAM: Caribbean Mountain terrane; CCSP: Central Continental Sub-Plate (Eastern Cordillera, Cordillera Real, San Lucas block, Ibague block); CHO: Chocó Arc; CT: Caribbean Terranes; GA: Garzón Massif; GS: Guyana Shield; GU-FA: Guajira-Falcón Composite Terrane; MSP: Maracaibo Sub-Plate; PAT: Pacific assemblages (after Cediel et al. 2003). B-D: Different tectonic models presented as NW-SE structural cross sections: B) across the Mérida Andes (Colleta et al. 1997; SLC: Sierra la Culata block; SN: Sierra Nevada block); C) Through the Maracaibo Basin from the Mérida Andes to the Perijá Range (Yoris and Ostos, 1997); D) Along the Maracaibo subplate (after Cediel et al. 2003). Abbreviations: C&R basin: César and Ranchería basin; LPz: lower Paleozoic; UPz: upper Paleozoic; Jr: Jurassic; K: Cretaceous; P: Paleogene; N: Neogene.

4.2 Geodynamic setting and structure of the Venezuelan Andes

Current tectonic models for the Venezuelan Andes remain controversial with regards to the crustal structure, asymmetry and kinematics of the belt. Several authors (Kellogg and Bonini, 1982; De Toni and Kellogg, 1993 Colletta et al. 1997) have proposed a “thick-skinned”

deformation model for the belt, envisaging it as a doubley-vergent orogenic wedge (Willett et al. 1993) resulting from incipient continental subduction of the Maracaibo block toward the southeast (Fig. 4.2B). Others have applied an “orogenic float” model (e.g., Oldow et al. 1990; Yoris and Ostos, 1997; Audemard and Audemard, 2002; Cediel et al. 2003) to the whole of the Caribbean-South American plate boundary zone, envisaging a major mid-crustal detachment underlying the Mérida Andes, Maracaibo Basin and Perijá and Santa Marta ranges (Figs. 4.2C, D) with either northwest- or southeast-directed subduction of the underlying lower crust. Although the seismic data are disputed (Audemard and Audemard, 2002), the most compelling evidence for southeast, instead of northwest-directed continental subduction is the formation of the deep (> 6 km depth) Maracaibo foreland basin to the northwest (i.e., on the proto-side of the orogenic wedge), compared to the shallow retro-side Barinas basin (2 km depth), as shown by gravity and subsidence analyses (Chacín et al. 2005).

The amount of shortening and the partitioning between shortening and strike-slip across the Mérida Andes are also disputed. Shortening estimates across the belt range from 10 to 60 km (Coletta et al. 1997; Audemard and Audemard, 2002; Duerto et al. 2006). The belt has absorbed significant lateral motion along major pre-existing crustal faults, the foremost of which is the Boconó fault, and features indicative of strike-slip deformation, such as pop-up structures or releasing bend-basins, are widespread (Schubert, 1980a, 1982; Colletta et al. 1997; Audemard and Audemard, 2002; Backé et al. 2006; Duerto et al. 2006). Estimates for the total right-lateral displacement on the Boconó fault system reach 80 km (Audemard and Audemard, 2002). The present-day kinematics of the region, as shown by GPS analyses, are dominated by northeastward block escape of the Maracaibo block, driven by the ongoing motion of the Caribbean plate and northern Andean tectonics in Colombia (Kellogg and Vega, 1995; Weber et al. 2001; Pérez et al. 2001).

The Venezuelan Andes are characterized by six major strike-slip fault systems (Figs. 4.1-4.4), which are the right-lateral Boconó fault, Caparo fault and Central-Sur Andino fault system, and the left-lateral Icotea, Valera, and Carache or Burbusay faults systems. The orogen is delineated by two currently active foreland fold-and-thrust belts to the northwest and southeast, which incorporate Plio-Pleistocene sediments (Figs. 4.1 and 4.3). The foremost of the strike-slip fault systems is the Boconó fault, which extends ~500 km in a NE-SW direction along the entire Venezuelan Andes. The Boconó fault system is expressed at the

surface by escarpments and aligned valleys and divides the Venezuelan Andes almost symmetrically in its central part (Mérida Andes). The Caparo fault is a dextral strike-slip system parallel to the Boconó fault in the southwestern part of Venezuelan Andes. The Central-Sur Andino fault is located between the Boconó and Caparo faults and does not show the same continuity as the other two fault systems (Fig. 4.3), being subdivided into a southern and a northern part, without an apparent connection (Soulas, 1983). The Burbusay and Valera faults are a system of continuous N-S trending faults that locally control the triangular Trujillo block in the northwest of the orogen (Fig. 4.3). Running parallel to these, the Icotea fault bisects the Maracaibo block (MBL in Fig. 4.1B) and possibly converges with the Boconó fault close to the town of El Vigía (Fig. 4.3). These fault systems separate distinct tectonic blocks (Colletta et al. 1997).

In this work we distinguish seven blocks (Fig. 4.4B), based on their topographic signature and exhumation history. In the southwest, the Caparo block is truncated by the Boconó fault to the north, and the Caparo fault and Cerro Azul thrust block to the south. The Escalante block, to the north of the Caparo block, is limited to the north by the NW foreland fold-and-thrust belt and to the south by the Boconó fault (Figs. 4.3 and 4.4B). The Cerro Azul thrust block along the southeastern flank of the Venezuelan Andes is enclosed by the Boconó fault and the Central-Sur Andino fault to the north, and the SE fold-and-thrust belt to the south. In the central part of the Venezuelan Andes the Sierra Nevada block is bounded by the Boconó fault to the north and the Caparo block and Cerro Azul thrust to the south. The Sierra La Culata block is bordered by the NW fold-and-thrust belt to the north, the Boconó fault to the south and the Valera Block to the east. Within the Sierra La Culata block, the El Carmen block can be defined. This block is restricted by two branches of the Boconó fault, the Mucujún and the Gavilán faults (Figs. 4.3 and 4.4B). The Valera block at the northeastern end of the orogen is a triangular block defined by the Valera fault, Boconó fault, and the Burbusay fault.

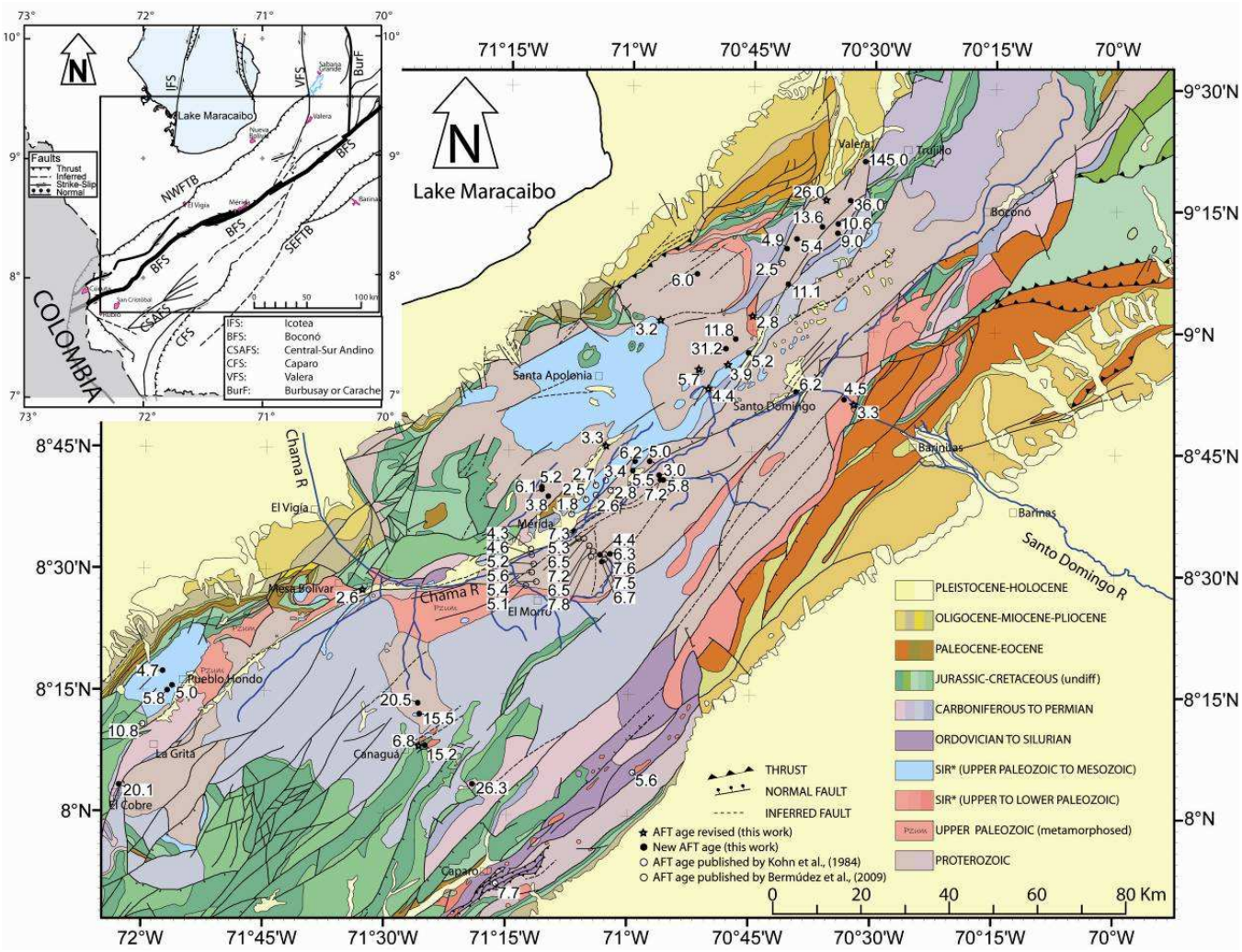

Fig. 4.3. Geologic and structural map of the Venezuelan Andes (modified from Hackley et al. 2005; Audemard et al. 2000) showing previously published and new samples used in this study. Numbers correspond to AFT ages. For detailed information on samples see Tables 4.1 and 4.2. Inset shows major fault systems of the Venezuelan Andes.

4.3 Methods and analytical procedures

4.3.1 Topographic characteristics

Geological and topographic features of the Venezuelan Andes were characterised using a 90-m Digital Elevation Model (DEM; Fig. 4.4A), compiled from the Shuttle Radar Topography Mission (SRTM) data set. Topographic characteristics, such as mean elevation, mean hillslope angle and hypsometric parameters were calculated for individual tectonic blocks from the DEM using ArcMap, Matlab and Splus software.

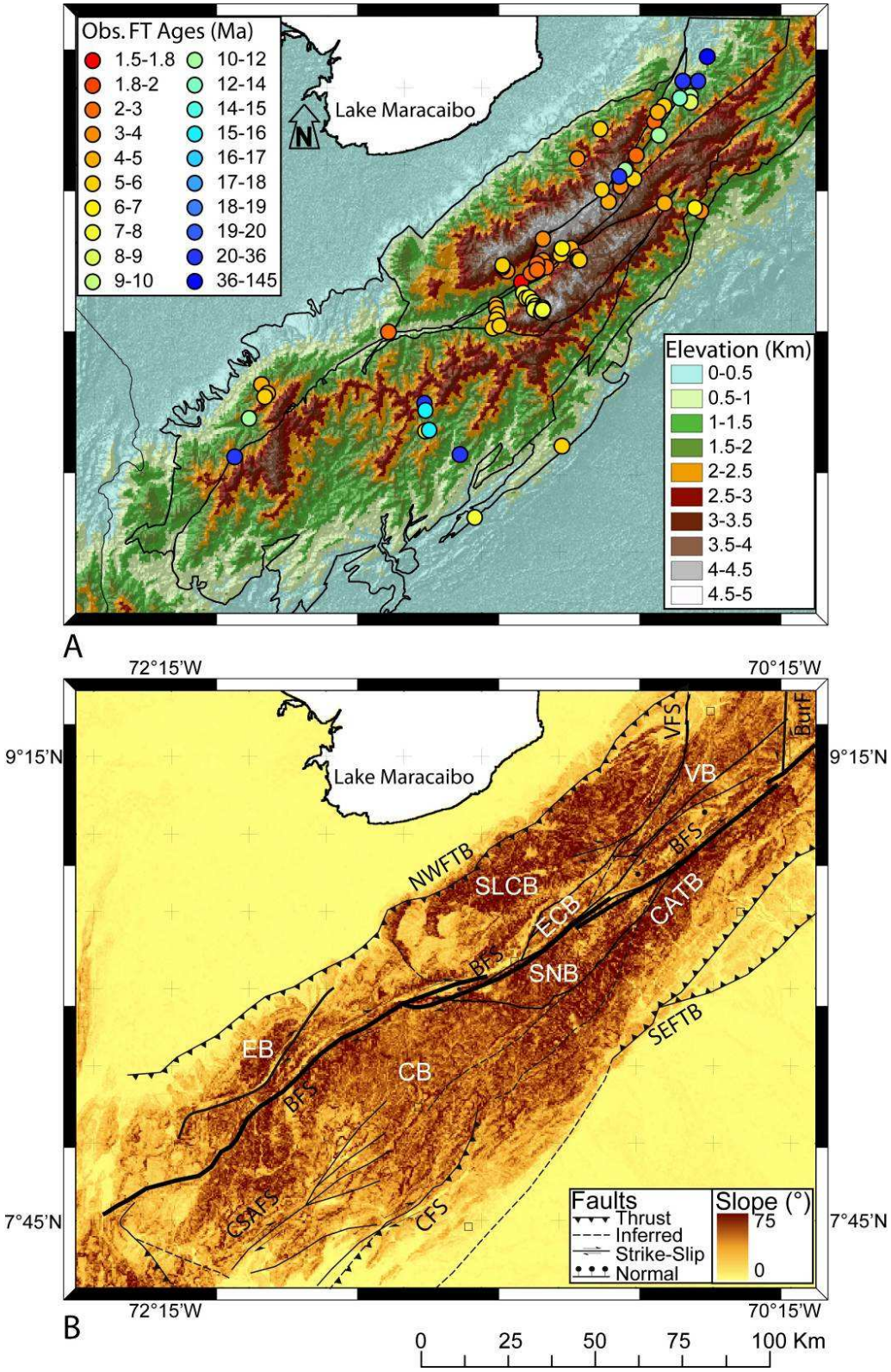

Fig. 4.4. A) Digital Elevation Model of the study area (data from NASA SRTM 90-m resolution topographic database), showing major fault systems and AFT ages. B) Slope map of the Venezuelan Andes with tectonic blocks defined in this work (CB = Caparo; VB = Valera; SNB = Sierra Nevada; EB = Escalante; ECB = El Carmen; SLCB = Sierra La Culata and CATB = Cerro Azul Thrust Blocks) and major fault systems (BFS = Boconó fault system; Burf: Burbusay fault; CFS: Caparo fault system; CSAFS: Central-Sur Andino fault system; NWFTB: northwestern fold-and-thrust belt; SEFTB: southeastern fold-and-thrust belt; VFS: Valera fault system).

4.3.2 Apatite fission-track thermochronology

Samples were collected along the Venezuelan Andes in two different campaigns: the first assembled by Shagam in the 1980's; the second, in 2007 by the Grenoble group in the Caparo, Valera, Cerro Azul, Sierra Nevada, Sierra La Culata and Escalante blocks. Twenty AFT ages for the Venezuelan Andes were published by Kohn et al. (1984). Ten of these samples were reanalyzed for this study using modern analytical techniques (external detector method, a zeta calibration and track length measurements) compared to the population method and absolute neutron dose calculation used in the earlier analyses. Where repeat determinations have been made AFT ages are compared with those previously reported (Table 4.2). Recently, thirteen AFT ages were published by Bermúdez et al. (submitted, chapter 5 in this work) for the Sierra Nevada block in the Mérida Andes. This pre-existing dataset is presented in Table 4.1. To extend on this existing AFT database, an additional 47 new AFT ages are presented in Table 4.2, which were dated at the fission-track laboratories at Grenoble (11 samples) and Melbourne (26 new samples and 10 repeat samples from Kohn et al. 1984). New sampling focused on regions that had not previously been targeted for AFT thermochronology. All sample locations used in this study are shown in Figs. 4.3 and 4.4A.

*Sample	§Block	Lithology or locality	Latitude (°N)	Longitude (°W)	Elevation (m)	Fission track age (Ma) (± 1s)	‡Mean track length ± std error (mm)	Std. dev. (mm)	Dpar ±SD (mm)
78-4	CATB	Tapo-Cambur granite	7.8600	-71.2700	380	7.7 ± 0.2	-	-	-
78-8	CATB	Rio Quiu Granite	8.0900	-70.9900	400	5.6 ± 1.5	-	-	-
S-87-W	EB	La Quinta rhyolite	8.1800	-72.0000	1200	10.8 ± 2.1	-	-	-
SA-79-26	SLCB	Valera Granite	9.1400	-70.6900	2000	2.5 ± 0.4	-	-	-
SA-79-1	ECB	El Carmen Granodiorite	8.6200	-71.1200	1520	1.8 ± 0.4	-	-	-
SA-79-2	ECB	El Carmen Granodiorite	8.6500	-71.0900	1840	2.5 ± 0.4	-	-	-
SA-79-4	ECB	El Carmen Granodiorite	8.6900	-71.0500	3100	3.4 ± 0.6	-	-	-
SA-79-5	ECB	El Carmen contact (meta sst)	8.6700	-71.0400	2500	2.8 ± 0.4	-	-	-
SA-79-6	ECB	El Carmen Granodiorite	8.6800	-71.0700	2600	2.7 ± 0.5	-	-	-
SA-79-7	ECB	El Carmen Granodiorite	8.6600	-71.0700	2375	2.6 ± 0.5	-	-	-
7007	SNB	Gneiss El Morro P6	8.5476	-71.2028	1250	4.3 ± 0.3	14.5 ± 0.1 (118)	1.1	1.6 ± 0.2
6907	SNB	Gneiss El Morro P5	8.5355	-71.2015	1765	4.6 ± 0.7	14.3 ± 0.1 (51)	1.0	1.5 ± 0.2
6807	SNB	Gneiss El Morro P4	8.5164	-71.1968	2060	5.2 ± 0.7	14.0 ± 0.2 (15)	0.8	1.3 ± 0.1
6707	SNB	Gneiss El Morro P3	8.4995	-71.2011	2250	5.6 ± 0.5	13.9 ± 0.1 (100)	1.1	1.5 ± 0.2
6607	SNB	Gneiss El Morro P2	8.4721	-71.2129	2490	5.1 ± 0.9	-	-	-
5407	SNB	Agua Montaña	8.5698	-71.1055	2760	5.3 ± 1.4	-	-	-
6507	SNB	Gneiss El Morro P1	8.4801	-71.1909	2770	5.4 ± 0.6	-	-	-
5307	SNB	Aguada-La Montaña	8.5700	-71.0940	3285	6.5 ± 0.8	-	-	-
5207	SNB	Loma Redonda-Aguada	8.5556	-71.0826	3633	7.2 ± 1.1	14.4 ± 0.3 (27)	1.3	1.3 ± 0.1
5107	SNB	Loma Redonda	8.5437	-71.0752	3999	6.5 ± 0.6	14.1 ± 0.3 (22)	1.4	1.4 ± 0.1
5007	SNB	Alto de la Cruz	8.5332	-71.0790	4236	7.8 ± 1.6	13.9 ± 0.3 (10)	1.0	1.3 ± 0.1
4907	SNB	Pico Espejo 2	8.5273	-71.0516	4622	7.5 ± 1.0	14.4 ± 0.1 (110)	1.4	1.5 ± 0.1
4807	SNB	Pico Espejo1	8.5317	-71.0527	4718	7.6 ± 0.9	14.1 ± 0.1 (108)	1.5	1.4 ± 0.2

Table 4.1. Summary of previously reported apatite fission-track data from Kohn et al. (1984) and Bermúdez et al. (submitted, chapter 5 in this work).
*Samples highlighted in gray were dated using the population method (Kohn et al. 1984). Samples shown in italics were presented by Bermudez et al. (submitted, chapter 5 in this work). §Blocks: CATB = Cerro Azul Thrust; CB = Caparo; EB = Escalante; SLCB = Sierra La Culata; ECB = El Carmen; SNB = Sierra Nevada, and VB = Valera blocks (see Figs. 4.3, 4.4 and 4.7) ‡Parenthesis show number of tracks lengths measured.

Samples analyzed in Grenoble were separated from crushed rocks using standard magnetic and heavy liquid separation techniques. Apatite aliquots were mounted in epoxy, polished and etched for 20 seconds in 5.5 M HNO_3 at 20°C. After fixing a low-U mica sheet used as external detector, these samples were irradiated in the well-thermalized ORPHEE facility of the *Centre d'Etudes Nucléaires* in Gif-sur-Yvette, France, with a nominal fluence of ~5×10^{15} neutrons/cm^2. Neutron fluences were monitored using IRMM540 dosimeter glasses. Mica detectors were etched in 48% HF at 20°C for 18 minutes. All grains were dated under dry conditions at 1250× magnification, using an Olympus BH2 microscope.

Those samples analyzed in Melbourne were mounted in epoxy resin on glass slides, ground and polished to an optical finish to expose internal grain surfaces. The mounts were etched in 5M HNO_3 for 20 seconds at room temperature to reveal fossil tracks. The external detector method was used for age determinations, with Brazil Ruby muscovite attached to the polished mounts to record induced tracks. Thermal neutron fluence was monitored by measuring the track density in muscovite plates attached to the Corning-5 (CN-5) standard glass. Neutron irradiations were carried out in the well-thermalised X-7 position of the Australian HIFAR Research Reactor at Lucas Heights, NSW, Australia. After irradiation, all muscovite detectors were etched for 27 minutes in 48% HF at room temperature to reveal induced tracks. Track counting and horizontal confined track length measurements were performed on a Zeiss Axiotron microscope under transmitted light, using a dry 100× objective at a total magnification of 1250×.

Where possible, fission tracks in 20 suitable apatite grains were counted and 100 horizontal confined track lengths measured per sample (see Table 4.2). Fission-track ages were calculated using the zeta calibration method and standard fission-track age equation (Hurford and Green, 1983). The observed age spread is determined statistically using the Chi-square test (Galbraith, 1981), which indicates the probability that all grains counted belong to a single population of ages. A probability of <5 % is evidence of an asymmetric spread of single grain ages and the "conventional analysis" (as defined by Green, 1981) based purely on Poissonian variation is not valid. All ages reported here are the 'central age' (Galbraith and Laslett, 1993), which is essentially a weighted-mean age. For samples that pass the Chi-square test, this age is concordant with the pooled age within error (expressed here at the $\pm1\sigma$ level) and calculated using the techniques of Green (1981).

Horizontally confined track lengths were measured in 43 of all available samples. Aliquots of all these samples were irradiated using a ^{252}Cf source under vacuum for 140 minutes at the Thermochronology Laboratory at the University of Melbourne. Subsequently, these irradiated samples were etched under the same conditions as described above. Only fully etched and horizontal confined track lengths (HCTL) (Laslett et al. 1982) were measured in grains with polished surfaces parallel to prismatic crystal faces. Suitable track lengths were measured using a projection tube and a digitizing tablet (attached to a microcomputer) calibrated using a stage micrometer. For this procedure, the same magnification was applied as for track counting.

The kinetics of AFT annealing is a function of the duration of heating, chemical composition (Green et al. 1985; Gleadow et al. 1986a, 1986b; O'Sullivan and Parrish, 1995; Barbarand et al. 2003a) and mineralogical properties (Carlson et al. 1999). Burtner et al. (1994) have shown that this may amount to a variation in total annealing temperature by as much as ± 20°C. We take the possible kinetic variability in our samples into account by using the diameter of etched tracks at the surface of the apatite parallel to the crystallographic *c*-axis (D_{par}) as a proxy for the annealing kinetics of the grains (Burtner et al. 1994). D_{par} of 100 tracks crossing the etched internal surface was measured using the same digitizing technique as used for measuring track lengths; for select samples measured at the University of Melbourne apatite chlorine content was also determined on grains measured for age determinations (Table 4.2).

4.3.3. Thermal history modeling

AFT ages, track lengths and D_{par} measurements of representative samples were used for determining time-temperature paths through inverse Monte Carlo modeling, using the HeFTy software of Ketcham (2005), version 1.6.7, based on the multikinetic annealing model of Ketcham et al. (2007b), and with *c*-axis projected track length data (Ketcham et al. 2007a). For modeling purposes each sample was constrained to a subsurface temperature of about 120 °C at a time somewhat older than the AFT age, and present-day surface temperature at the elevation where the sample was collected (typically ~10-25°C). The modeling strategy was to allow for a large time-temperature sampling space for model inversions beyond these first order assumptions. Therefore, a single large sampling space was used to allow models as much freedom as possible. Cooling paths are monotonic and composed of 16 random segments to allow for sufficient variability in the exhumation path. The D_{par} kinetic parameter

was used to calculate initial confined track lengths. The Kolmogorov-Smirnov statistical test was used to assess the goodness of fit between modeled and measured track length distributions, with merit values of 0.5 and 0.05 for good and acceptable fits, respectively.

4.4 Results

4.4.1 Topographic characteristics

In order to highlight the topographic differences between individual tectonic blocks, we determined their mean elevations and mean hillslope angles; these data are summarized in Figures 4.4 and 4.5 and Table 4.3. The mean elevation of the Venezuelan Andes is about 2024 m, with a standard deviation (σ) of 855 m and a maximum elevation of 4981 m at Pico Bolívar in the Sierra Nevada block. The mean slope angle for the entire orogen is 21° (σ = 9º). The Escalante, Cerro Azul, Valera and Caparo blocks exhibit lower values of mean elevation between 1160 and 1695 m (Fig. 4.5C). These four blocks show positively skewed elevation distributions (Fig. 4.5A, Table 4.3), implying relatively large areas at low elevations. The highest topography is encountered in the Sierra La Culata, El Carmen and Sierra Nevada blocks, the latter two having mean elevations of ~3000-3200 m, respectively. The form of the hypsometric curve for the Sierra La Culata block is very wide and almost symmetric (weakly negative skewness of -0.1). The hypsometric curves for the El Carmen and Sierra Nevada blocks are negatively skewed, implying preponderance of areas at relatively high elevation. The slope distributions as a function of elevation (Fig. 4.5D) of the Sierra La Culata and El Carmen blocks show a distinct minimum at high elevations, comparable to the slope distributions of the lower-elevation blocks and indicative of low-relief landforms at high elevations. This minimum is conspicuously absent in the Sierra Nevada. The high-elevation low-relief surfaces in the Sierra La Culata are associated with ubiquitous glacial erosion features (cirque lakes, glacially widened valley heads etc.), which we interpret as the result of Pleistocene glaciation of the Mérida Andes (Schubert, 1974; Schubert and Clapperton, 1990).

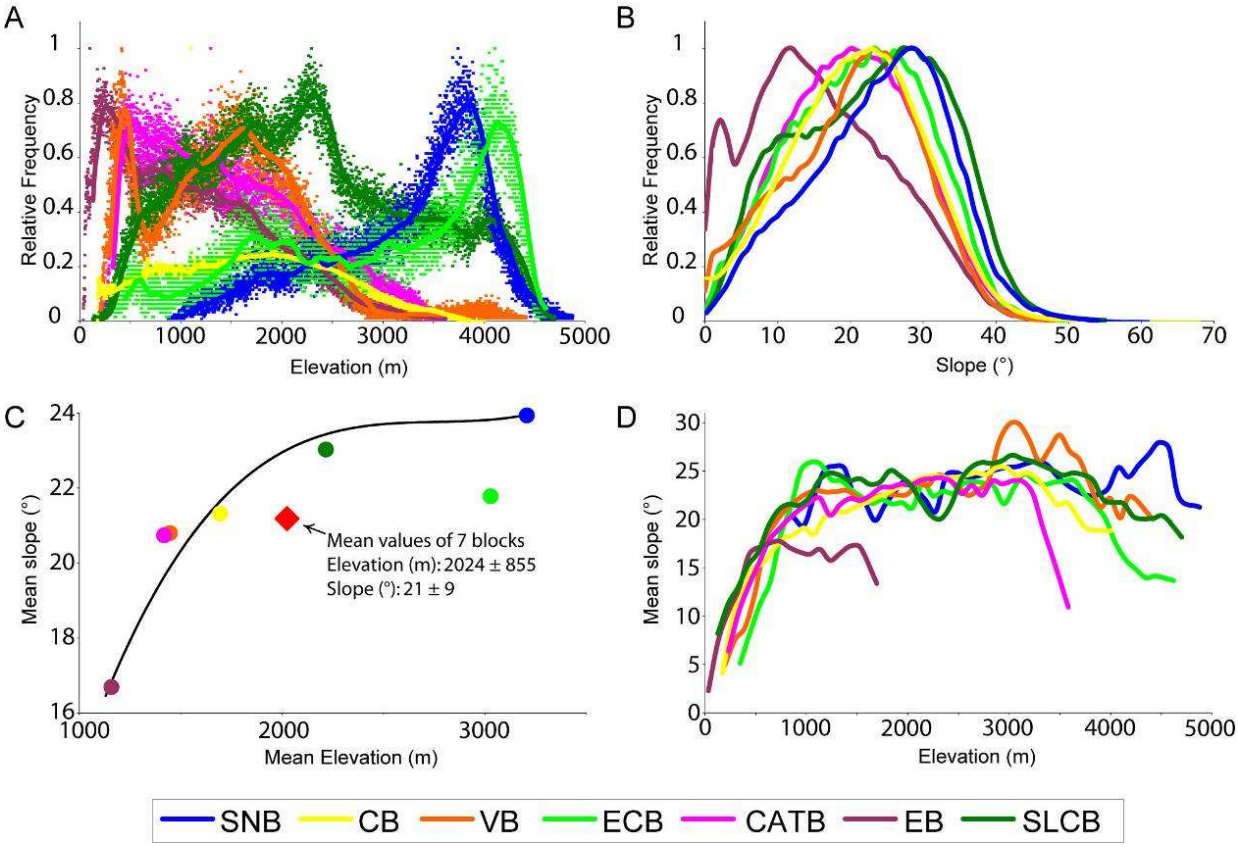

Fig. 4.5. Hypsometric and geomorphic characteristics for the different tectonic blocks (annotation as in Fig. 4.4): A) Elevation distribution (dots: individual values; continuous line: 100-m bins), B) Slope distribution, C) Mean elevation versus mean slope for each block, D) Altitudinal dependence of slopes for each block (100-m elevation bins). See text for discussion.

4.4.2. Apatite fission-track data

All new AFT ages reported in this study are summarized in Table 4.2 and shown together with previously published AFT ages in Table 4.1 and Figures 4.3 and 4.4A. Almost all samples passed the chi-square test at the 95% confidence interval. The available dataset of 72 AFT ages for the Venezuelan Andes shows that different tectonic blocks have highly variable exhumation histories (Figs. 4.4, 4.6, 4.7). Youngest AFT ages range between 1-3 Ma and are found close to the Boconó fault, specifically in samples from the El Carmen block and at the limit between the Sierra La Culata and Escalante blocks. AFT ages between 4-8 Ma are concentrated in the central part of the Venezuelan Andes, in the Sierra La Culata and Sierra Nevada blocks, and on both flanks of the chain in the Escalante block and the Cerro Azul thrust block. In the Caparo block, AFT ages range between 7-30 Ma and are all substantially younger than the depositional ages of the Triassic-Jurassic La Quinta Formation (Hargraves and Shagam, 1969) from which they were collected. The Valera block is characterized by a wide range of AFT ages, increasing from 8 Ma at its southeastern limit to 145 Ma in the north.

A strong correlation between AFT age and elevation is observed in the El Carmen and Sierra Nevada blocks, whereas this correlation is much weaker in the other blocks (Fig. 4.6A). However, part of this difference is due to the fact that the sampling strategy in these two blocks was specifically aimed at obtaining an age-elevation profile (Kohn et al. 1984; Bermúdez et al. submitted, chapter 5 in this work), whereas this was not the case in the other blocks.

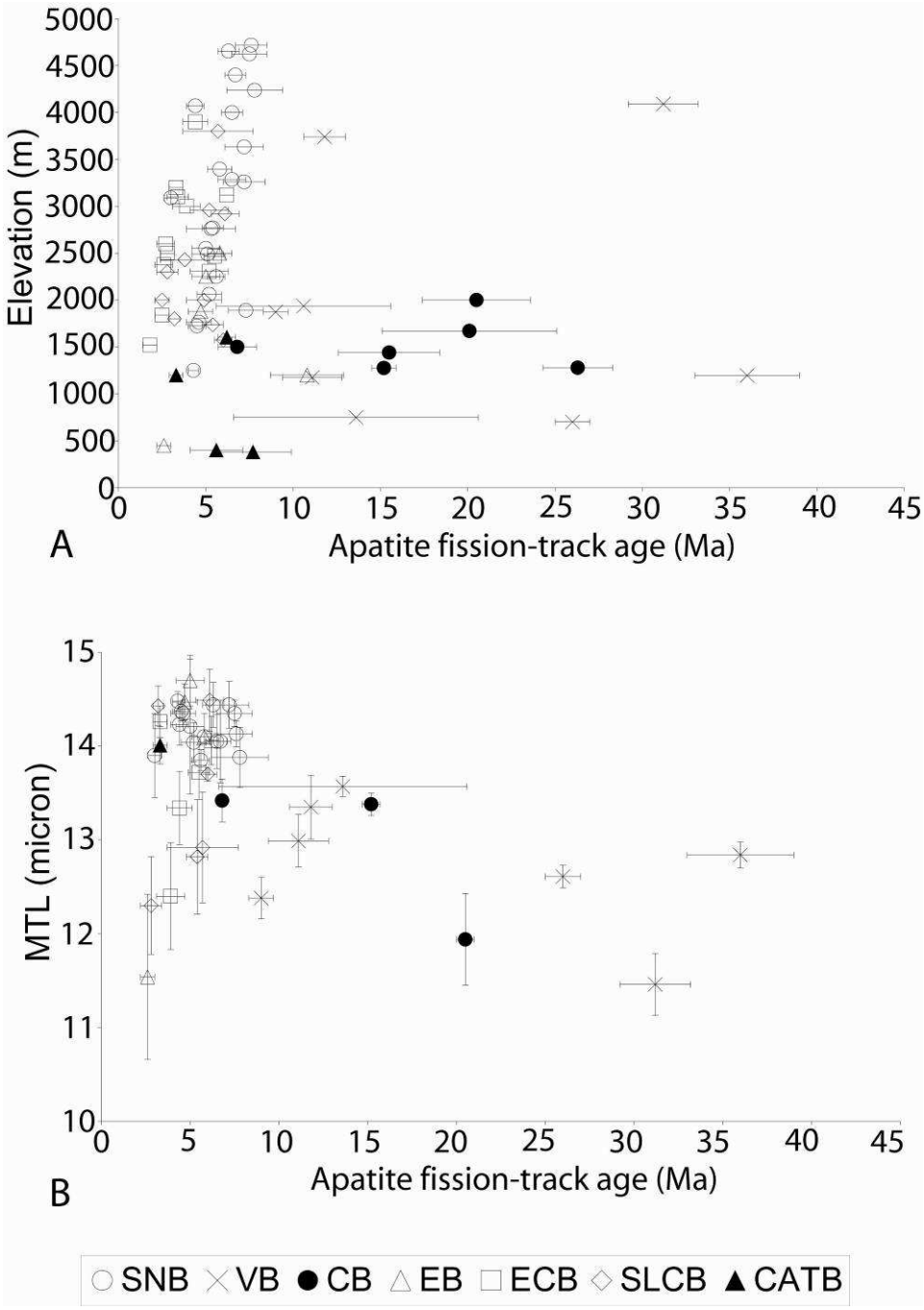

Fig. 4.6. AFT age versus A) Elevation and B) Mean Track Length (MTL) for individual samples from different tectonic blocks (annotation as for Fig. 4.4).

After ^{252}Cf irradiation, we were able to obtain track length measurements from 34 new samples (Table 4.2), although only 10 samples provided a sufficient number for meaningful thermal history modeling (>50 track length measurements; see below). Bermúdez et al. (submitted, chapter 5 in this work) report 9 more track-length measurements, of which 5 are suitable for modeling (Table 4.1). Overall, blocks with the youngest AFT ages (e.g., Sierra Nevada, Sierra La Culata, El Carmen) are characterized by relatively long mean track lengths (MTL) of ~13 to 14.5 µm and narrow track-length distributions (typically ~1 µm). A plot of MTL versus AFT age (Fig. 4.6B) shows a clear peak (MTL >14 µm) for ages of 5±1 Ma. Blocks characterized by older AFT ages (e.g., Valera and Caparo, Fig. 4.7) have shorter and wider track-length distributions: MTL ranges from 11.5 to 13.8 µm and standard deviations are generally >2 µm. A secondary peak of MTL ≈13.5 µm occurs for ages of ~13 Ma in these blocks (Figs. 4.6B and 4.7B). No track-length data could be measured in samples from the Cerro Azul block. D_{par} values were determined for 15 samples and range from 1.1 to 1.6 µm; Cl contents were measured for 7 samples and are generally <0.1 %. Both the Cl determinations and the D_{par} measurements indicate that apatite composition is relatively homogeneous and close to fluorapatite (Carlson et al. 1999).

Our sampling for AFT thermochronology in the Venezuelan Andes focused on specific areas, in order to obtain age-elevation profiles or because of proximity to major faults, but partly also because of limited access to the terrain. Nonetheless, the current AFT age database permits mapping out the spatial distribution of AFT ages and track lengths, as shown in Figures 4.7A and B respectively. These maps were created by interpolating all available AFT ages and MTL using the spline with barriers method (Terzopoulos, 1988) in ArcMap. For each of the seven tectonic blocks delineated, the spatial interpolation of AFT ages was limited to the block boundaries defined by the major fault systems (Boconó, Valera, Central-Sur Andino and Caparo). These maps should be regarded as a first-order attempt to visualize the distribution of AFT ages and MTL in the Venezuelan Andes, keeping in mind that data coverage remains poor in many areas. Despite these limitations, a clear spatial pattern emerges, with most of the youngest AFT ages and longest MTL in the Venezuelan Andes located in the central part of the range, close to the Boconó fault system (Fig. 4.7).

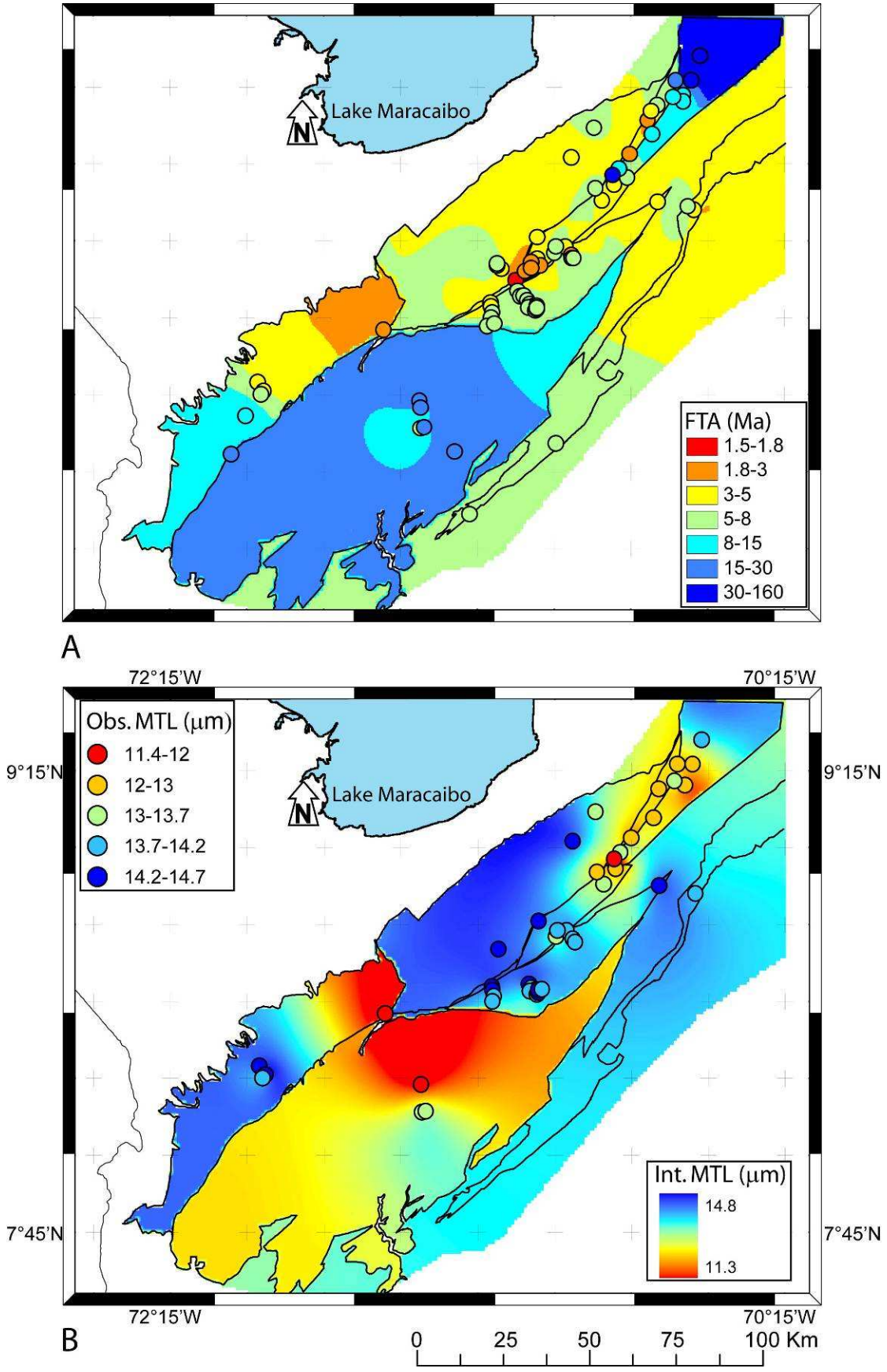

Fig. 4.7. Interpolated maps of A) AFT ages and B) Mean Track Lengths (MTL) for each block. The maps were generated using the 'spline with barrier' interpolation method (Terzopoulos, 1988), using the major block-bounding faults as barriers.

4.4.3 Thermal history modeling

Modeling of cooling histories using HeFTy was performed on samples from the Sierra Nevada, Sierra La Culata, Caparo, and Valera blocks for which at least 50 confined track-length measurements were available (Fig. 4.8). Thermal histories for the Sierra Nevada block were determined for sample 4907 from 4600 m elevation at Pico Bolívar (Fig. 4.8A) and sample 6407 from Santo Domingo, at 1700 m elevation ~45 km to the northeast (Fig. 4.8B). Both samples show a rapid, but diachronous phase of cooling (at rates of ~70°C/Myr), from ~7.5 to 5 Ma for sample 4907 and from ~5 to 3.5 Ma for sample 6407, slowing down since that time. Bermúdez et al. (submitted, chapter 5 in this work) used the 3D forward thermal-kinematic model *Pecube* (Braun, 2003; Braun et al. 2006) to model the AFT ages and MTL for the complete Sierra Nevada profile and showed that the observed diachronous cooling along the profile can be explained by a phase of rapid exhumation that commenced during middle – late Miocene time (~10-14 Ma) and slowed down in the Pliocene (~4 Ma), together with continuous relief increase (valley carving) since that time.

Sample 1407 (Fig. 4.8C) from the Sierra La Culata block shows an initial phase of rapid cooling between 6.5 and 5.5 Ma, at a rate of about 60°C/Myr, followed by a phase of slow cooling between ~5.5 and ~2.6 Ma. From ~2.6 Ma to the present, cooling again accelerated to a rate of about 15°C/Myr. Bermúdez et al. (submitted, chapter 5 in this work) predicted a similar increase in exhumation rate from *Pecube* modeling of AFT ages along an age-elevation profile in the Sierra La Culata collected by Kohn et al. (1984), but with an earlier increase in exhumation rate at 4 Ma. The time lag between increased exhumation and cooling rates is due to the transient response of the thermal structure to increased exhumation rates (e.g., Braun et al. 2006; Rahl et al. 2007).

For the Caparo block, thermal modeling of sample 5807 is presented in Figure 4.8D and shows nearly linear cooling for this block since the early Miocene (~22 Ma). The sampled cooled through the AFT partial annealing zone (PAZ) at a rate of ~7°C/Myr between 19 and 10 Ma; but cooling rates have possibly slowed down somewhat since that time. The Valera block sample 6207 (Fig. 4.8E) documents a clearer decrease in cooling rates, from ~12°C/Myr between 16 and 12 Ma (middle Miocene) to ~4°C/Myr from the middle – late Miocene (12 Ma) to the present.

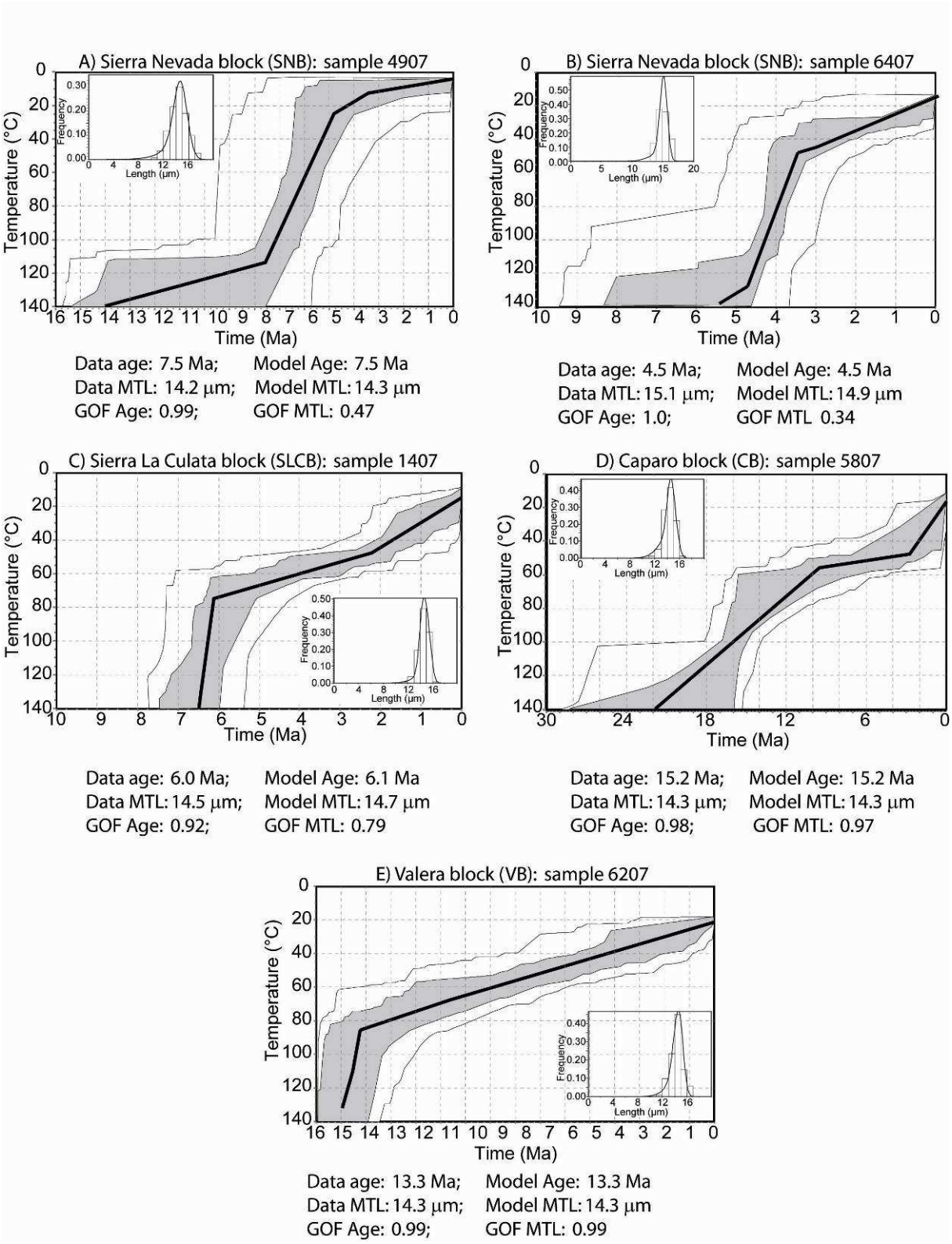

Fig. 4.8. Time-temperature paths obtained from thermal-history modeling using HeFTy software (Ketcham, 2005) for representative samples of Sierra La Culata, Sierra Nevada, Caparo and Valera blocks. Outer envelope contains acceptable fits; inner, shaded envelope contains good fits (as defined by Ketcham, 2005); thick black line indicates best-fit model: fit is indicated below the plot where measured and model results are compared (MTL is mean track length; SD is standard deviation; GOF is goodness of fit) and comparison of measured (histogram) and predicted (thin line) track-length distribution is shown in the inset. Note that modeled t-T paths are best constrained within the limits of the PAZ (~60-120 °C).

4.5 Discussion

4.5.1 Data Synthesis

AFT ages and track-length distributions in the Sierra Nevada, Sierra La Culata and El Carmen blocks (Fig. 4.8) are compatible with rapid cooling through the apatite PAZ, followed by residence at shallower depths. Blocks cooled through the PAZ at different times: middle – late Miocene for the Sierra Nevada block, Pliocene for the El Carmen and Sierra La Culata blocks. AFT ages and track-length distributions for the Escalante block, although insufficient for thermal history modeling, suggest a cooling history similar to the Sierra La Culata block. The Boconó fault, a right-lateral strike-slip fault that also displays vertical offset (Giegengack et al. 1976; Schubert, 1981, 1982; Giegengack, 1984), thus appears to have played a fundamental role in delimiting blocks with contrasting exhumation histories (see also Bermúdez et al. submitted, chapter 5 in this work). During the late Miocene to early Pliocene, oblique convergence between the Maracaibo block and the South American plate was enhanced by collision of the Panamá arc with South America (Pindell and Kennan, 2001; Montes et al. 2005). The oblique movement of small individual tectonic blocks in the Venezuelan Andes along the Boconó fault system, during phases of transpression, appears to have controlled the timing of rapid exhumation by creating topography. Exhumation itself was driven by erosion of the newly created topography through river incision, with trunk rivers following the trend of the Boconó fault (e.g. Chama River, Santo Domingo River, Fig. 4.3). As shown in Figure 4.5, the small Sierra La Culata block and the Sierra Nevada block currently host the highest topography, with mean elevations over 3000 and 3200 m respectively, and the largest number of peaks over 4000 m elevation in the Venezuelan Andes. The Sierra La Culata block as a whole has a mean elevation of about 2216 m, but also contains several peaks over 4000 m (Figs. 4.5C, D). The few available AFT cooling ages for this block are similar to those of the Sierra Nevada block, suggesting a similar exhumation history (Figs. 4.6, 4.7).

Contrasting with the relatively young AFT ages in the central part of the Venezuelan Andes, middle Miocene and older AFT cooling ages are found in other areas of this mountain belt (Fig. 4.7A). Samples in the Caparo block yield ages ranging from 12 to 26 Ma (samples LB-71-VE-5 and 6106 respectively), with MTL varying from 11.5 to 13 µm, indicating

comparatively slow cooling through the AFT PAZ (Fig. 5.7B; sample 5807 in Fig. 4.8). Therefore, this block experienced relatively slow cooling well before rapid exhumation started in the Sierra Nevada, Sierra La Culata, and El Carmen blocks. The topography of the Caparo block is more subdued (Fig. 4.5D), with many peaks around 2000 m elevation. Nonetheless, slopes remain fairly steep (20-25°C) for the highest elevations (Fig. 4.5B and D), as determined by DEM analysis.

AFT ages of >30 Ma are restricted to the Valera block (Fig. 4.7A); the oldest AFT age encountered in this study (sample SVA-80-44; 145±7 Ma) is from the Valera Granite, located in the north of this block and away from major strike-slip faults. The MTL of this sample is 13.8 ± 0.1 µm, which suggests relatively fast cooling through the apatite PAZ during the Late Jurassic – Early Cretaceous, with little subsequent exhumation. Mesozoic denudation of parts of the Andean basement is consistent with the widespread deposition of Jurassic-Cretaceous sandstones, which are mainly preserved in the southwest of the belt (Escalante and Caparo blocks). While the northern part of the Valera block appears to record an older, pre-orogenic cooling history, younger AFT ages are observed in the southwest of the block (Fig. 4.7). The average MTL for the southwestern Valera block samples is 13.2 ± 0.3 µm. The modeled cooling path of sample 6207 in the southwestern Valera block (Fig. 4.8E) suggests cooling through the PAZ at a rate of about 14°C/Myr during the middle Miocene, and slower cooling from the Late Miocene to the present. Clearly, the Valera block was not affected by the rapid exhumation observed in the central Mérida Andes.

4.5.2. Tectonic Implications

The structure and development of the Venezuelan Andes have been controlled by the reactivation of preexisting faults and structures (Fig. 4.9A), and the inversion of Jurassic rift grabens (Kellogg and Bonini, 1982; Mora et al. 1993; Colletta et al. 1997; Audemard and Audemard, 2002; Jacques, 2004), as is also the case for the Eastern Cordillera in Colombia (Corredor 2003; Cortés et al. 2006; Mora et al. 2009; Parra et al. 2009). These pre-existing faults delimit tectonic blocks that are characterized by strongly variable exhumation histories, as observed in other transpressional mountain belts (e.g. Spotila et al. 2007a, b).

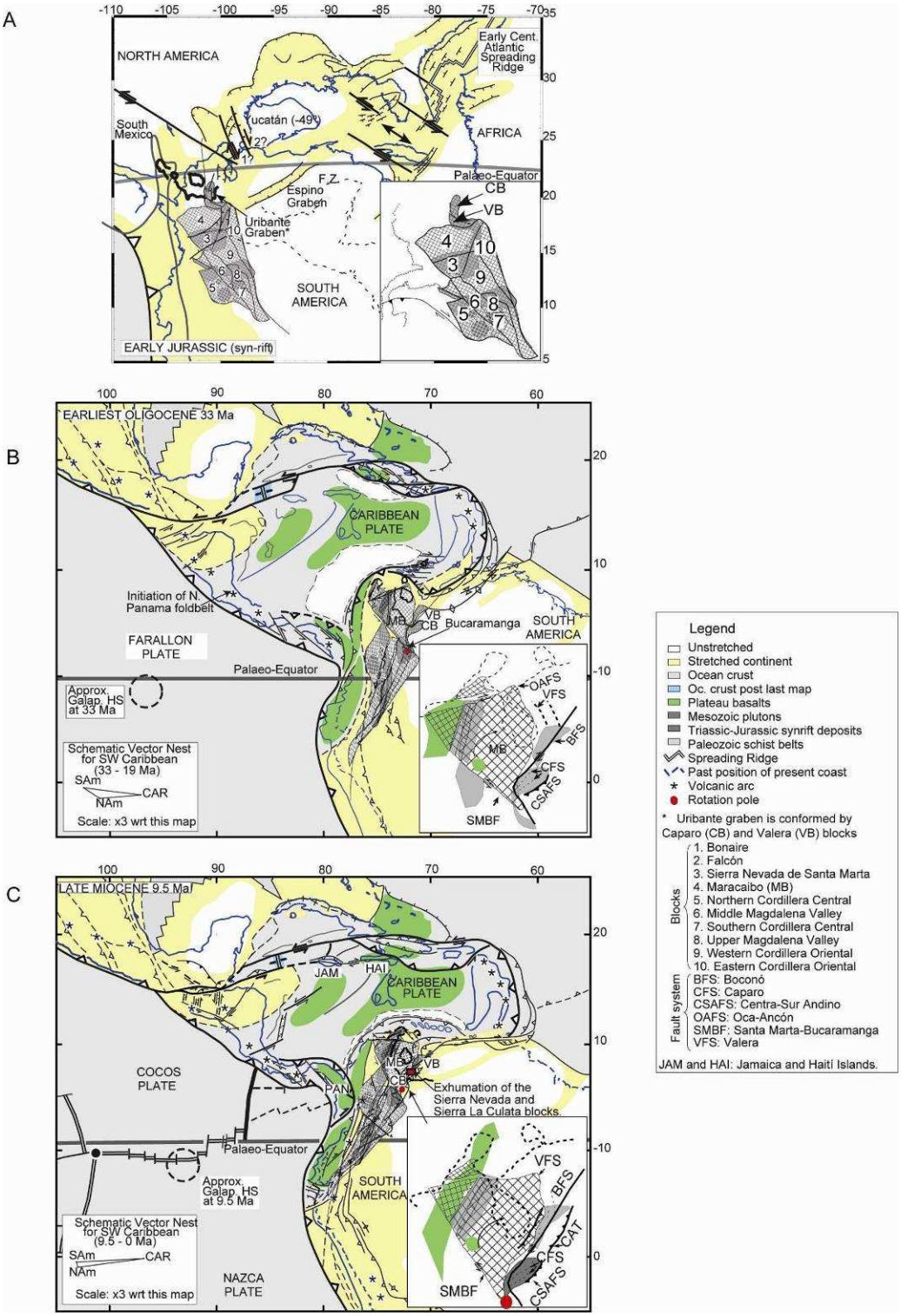

Fig. 4.9. Kinematic reconstruction for the South American – Caribbean plate boundary zone through time (insets show enlargement of northwestern Venezuela and surrounding regions): (A) Early Jurassic; showing graben system and connection to the central Atlantic. (B) Paleogene; initiation of clockwise rotation of the Maracaibo block with rotation pole located close to the present northeastern termination of the orogen (red dot). This first phase of convergence is driven by oblique convergence between the Caribbean, South America and Nazca Plates and produces inversion of the Mezozoic rifts (including the Uribante Graben in the present-day Caparo and Valera blocks). (C) Rotation of the Maracaibo block is almost completed during the late Miocene, left-lateral strike-slip displacement between the Maracaibo block and the South American plate is concentrated on the BFS, producing translation and minor rotation in the Valera block (VB) during its tectonic escape. Major exhumation of the SNB and SLCB occurs during this phase. See text for more detailed discussion (modified from Montes et al. 2005; Pindell and Kennan, 2001).

The signal of early (pre-Miocene) exhumation across the Venezuelan Andes is not very strong, because it is mostly overprinted by late Miocene to Pliocene exhumation. Only a few samples from the Valera and Caparo granite record Paleogene (AFT ages of 26-36 Ma) or, in one case, Jurassic-Cretaceous (AFT age 145 Ma) exhumation. By contrast, existing zircon FT data for the Venezuelan Andes (Kohn et al. 1984) are all late Mesozoic, ranging from ~70 to ~160 Ma, indicating that Miocene tectonics did not involve sufficient exhumation to expose rocks with reset zircon FT ages at the surface.

Distinct tectonic blocks in the Venezuelan Andes, limited by preexisting faults, responded in different ways to tectonic events that occurred in this zone, driven by the triple convergence of the South American, Caribbean and Farallon/Nazca plates (Fig. 4.9). The similar early to middle Miocene exhumation history of the present-day Caparo and Valera blocks suggests that they were juxtaposed at that time, before being separated by ~80 km of right-lateral translation along the Boconó fault system (Audemard and Audemard, 2002). In effect, both blocks contain remnants of the inverted Jurassic Uribante graben (Mora et al. 1993; Lugo and Mann, 1995; Jacques, 2004; Fig. 4.9A) that continued into the Eastern Cordillera in Colombia. As AFT ages from the Caparo and Valera blocks are compatible with AFT ages of 20-26 Ma observed in the Eastern Cordillera, it is suggested that they also record similar exhumation histories (Parra et al. 2009). The Oligocene - Miocene evolution of these blocks is possibly related to block rotation, associated with Andean deformation (Hargraves and Shagam, 1969), with a rotation pole close to Bucaramanga (Fig. 4.9B).

In the central part of the Venezuelan Andes and on both its flanks, the Escalante, El Carmen, Sierra La Culata, Sierra Nevada and Cerro Azul blocks record late Miocene – Pliocene exhumation resulting from transpression generated by clockwise rotation of the Maracaibo block (Fig. 4.2A, 4.9C) and oblique convergence of this continental block with the stable South American plate during Miocene to present time (Colletta et al. 1997; Montes et al. 2005). Block rotation, as supported by paleomagnetic analyses (Montes et al. 2005 and references therein; Bayona et al. 2008), was driven by eastward movement of the Caribbean plate to the north of the Maracaibo block and collision of the Panamá arc with the northern Andes in Colombia. The Panamá arc collision commenced in the middle Miocene (15-12 Ma) but reached its climax between 8 and 3 Ma, resulting in the closure of the Panamá seaway during the Pliocene (Duque-Caro, 1990; Coates et al. 2004; Montes et al. 2005; Lunt et al.

2008). The timing of these events is compatible with the late Miocene – Pliocene evolution of foreland basins on both the pro- and retro-side of the mountain belt (De Toni and Kellogg, 1993). According to De Toni and Kellogg (1993), two sedimentary sequences of fluvial molasse deposits in the foreland basin to the northwest of the Venezuelan Andes are separated by a late Miocene discontinuity, at least in the southwestern part of the basin. The unconformity is possibly related to surface uplift as a consequence of the Panamá arc collision (Duque-Caro, 1990). The onset of exhumation in the Sierra Nevada at ≥8 Ma is also consistent with surface uplift and creation of significant topography around this time, as recorded by the Late Miocene deflection of the tributaries of Orinoco and Magdalena rivers (Fig. 4.2A) inferred from the Neogene sedimentary record (Hoorn et al. 1995; Díaz de Gamero, 1996).

In the northeastern part of the Venezuelan Andes, the Trujillo Andes are controlled by the interaction of the Boconó, Valera and Burbusay faults, which delimit the Valera block. Analysis of the AFT ages, cooling history and topography of the Valera block shows it does not record rapid exhumation during the Late Miocene and Pliocene, hence the evolution of the Trujillo Andes is somewhat different from that of the Mérida Andes, The Trujillo Andes currently appears to be a site of active extension and tectonic escape (Backé et al. 2006), occurring as a result of the combination of oblique convergence between the South American plate and the Maracaibo block, with the presence to the north of the Caribbean plate considered as a free boundary. The oblique convergence and block rotation of the Maracaibo block thus leads to transpression and exhumation in the central part of the belt occurring simultaneously with extension and collapse to the northeast, consistent with the current stress field in the northern Andes as resolved from earthquake focal mechanisms (Colmenares and Zoback, 2003; Cortés and Angelier, 2005).

The flanks of the central and southwestern Venezuelan Andes are bounded by NW and SE vergent foreland fold-and-thrust belts. The few available AFT ages from these areas are between 7.7 and 5.0 Ma (Fig. 4.7). These thrusts are possibly the product of deformation related to inversion of the Jurassic rift basins (Colletta et al. 1997; Duerto et al. 2006) and reactivation of pre-existing faults. According to Duerto et al. (2006) the widespread Jurassic rifts suggest the possibility of thick-skinned reactivation of moderately to steeply dipping normal faults instead of low-angle thrusts as depicted in balanced cross sections (De Toni and Kellogg, 1993; Colletta et al. 1997). By contrast, Yoris and Ostos (1997), Audemard and

Audemard (2002) and Cediel et al. (2003) apply a relatively “thin-skinned” orogenic-float model to the Venezuelan Andes, suggesting that the entire orogen is underlain by a mid-crustal detachment. Our data cannot clearly discriminate between these models: on the one hand, the strong control of major fault zones on the pattern of exhumation suggests that these are long-lived structures that may be rooted in the lower-crust or lithosphere; on the other hand, the absence of deeply exhumed rocks (as indicated by the lack of reset ZFT ages; Kohn et al. 1984) appears more compatible with a shallow detachment underlying the mountain belt. Further analysis of the higher-temperature zircon (U-Th)/He system may contribute to resolving the issue of the total amount of Cenozoic exhumation in the Venezuelan Andes.

4.6 Conclusions

AFT thermochronology and topographic analysis document the history of individual tectonic blocks in the Venezuelan Andes. Phases of rapid cooling and erosional exhumation as a consequence of tectonic surface uplift and development of high relief during the Late Miocene and Late Pliocene in the central part of the orogen contrast with older exhumation histories of the northeastern and southwestern parts of the Venezuelan Andes. These exhumation patterns are consistent with the tectonic assembly of individual blocks of the Northern Andes. Exhumation in the central part of the Venezuelan Andes (Mérida Andes) and its flanks is the result of Late Miocene to Pliocene transpression. Major surface uplift and exhumation occurred in the Sierra Nevada block since ≥8 Ma, in concordance with fluvial reorganization recorded by the sedimentary record during this period. A second phase of uplift and exhumation affected the Sierra La Culata and Escalante blocks during the late Miocene-Pliocene, as also recorded by a major unconformity in the NW foreland basin succession. At the same time, the north-eastern part of the mountain belt records extension and tectonic escape. The spatial and temporal patterns of exhumation in the Venezuelan Andes appear to be strongly controlled by pre-existing faults delimiting major tectonic blocks, as is the case in many transpressional mountain belts elsewhere.

4.7 Acknowledgements

This study was supported by the Consejo de Desarrollo Científico y Humanístico (CDCH-UCV) de la Universidad Central de Venezuela (UCV), Project PI 08-00-6219-2006, and ECOS Nord project V08U01. We thank the Teléferico System, Mérida-Venezuela and the Instituto Nacional de Parques (INPARQUES) de la Región Andina for permission to sample in the Sierra Nevada National Park and logistical support during field work. The University of Melbourne thermochronology laboratory receives infrastructure support under the AuScope Program of NCRIS. Neutron irradiation costs for samples analysed there were covered by the Australian Institute of Nuclear Science and Engineering (AINSE). This work is dedicated to the memory and career of Reginald Shagam, also known as 'El Tigre De Los Andes', who died on April 19, 2008, in Beer Sheva, Israel. One of us (BPK) in particular remembers him warmly as a colleague and friend, and as an inspirational human being and geoscientist who made invaluable contributions to the understanding of Andean tectonics.

Sample	§Block	Lithology/Location	Latitude (°N)	Longitude (°W)	Elevation (m)	No. of grains	Standard track density ($x10^6$ cm^{-2})	Fossil track density ($x10^6$ cm^{-2})	Induced track density ($x10^6$ cm^{-2})	$P(c^2)$ %	Age dispersion %	U (ppm)	Fission track age (Ma) (± 1s)	Mean track length ± std error (mm)	Std. dev. (mm)	Dpar ± SD (µm)	†Range of Cl wt%	**Previously published apatite fission track age (Ma)
4006	CATB	*La Soledad Granite*	*8.8600*	*-70.5600*	*1604*	*29*	*0.616 (7837)*	*0.001(208)*	*0.021 (3094)*	*3.6*	*0.4*	*50*	*6.2 ±0.5*	-	-	-	-	
LB-71-VE-9	CATB	La Soledad Qtz Monzonite	8.8500	-70.5400	1200	20	1.318 (5142)	0.083 (77)	6.362 (5878)	33.1	16.1	60	3.3 ± 0.4	14.01 ± 0.24 (21)	1.1	-	0.00-0.03	3.0 ± 0.4
LB-71-VE-5	CB	Canaguá Granite	8.1400	-71.4300	1500	20	1.318 (5142)	0.067 (42)	1.415 (1116)	73.7	2.5	15	11.9 ± 1.7	13.42 ± 0.23 (23)	1.1	-	-	3.3 ± 0.6
5607	CB	*Mucutampó Sandstones*	*8.2286*	*-71.4333*	*2000*	*28*	*0.641 (5435)*	*0.001 (73)*	*0.003 (351)*	*59.2*	*0.3*	*6*	*20.5 ±3.1*	*11.94 ±0.4 9 (7)*	*1.31*	*1.48 ±0.2*	-	
5707	CB	*Mucutampó-Chacanta Gneiss*	*8.2062*	*-71.4297*	*1440*	*24*	*0.638 (5411)*	*0.000 (47)*	*0.002 (392)*	*3.6*	*0.4*	*5*	*15.5 ±2.9*	-	-	-	-	
5807	CB	*La Quinta Canagua-Mucuchachi Sandstones*	*8.1416*	*-71.4180*	*1276*	*73*	*0.635 (5388)*	*0.156 (913)*	*0.942 (5511)*	*20.1*	*0.1*	*22*	*15.2 ±0.7*	*13.38 ±0.12 (77)*	*1.07*	*1.37 ±0.1*	-	
6106	CB	*Caparo Granite*	*8.0639*	*-71.3200*	*1278*	*12*	*0.633 (8042)*	*0.003 (242)*	*0.01 (837)*	*99.4*	*0,0*	*23*	*26.3 ±2.0*	-	-	-	-	
3307	CB	*El Cobre Granite*	*8.0554*	*-72.0474*	*1670*	*5*	*0.649 (5506)*	*0.001 (20)*	*0.002 (93)*	*94.3*	*0,0*	*6*	*20.1 ±5.0*	-	-	-	-	
SVA-80-1	EB	Pueblo Hondo silicic rock	8.2900	-71.9600	1879	25	1.318 (5142)	0.032 (44)	1.683 (2316)	88.3	0.3	16	4.7 ± 0.7	14.47 ± 0.19 (12)	0.65	-	-	
SVA-80-5	EB	Pueblo Hondo silicic rock	8.2600	-71.9400	2251	20	1.318 (5142)	0.032 (45)	1.580 (2241)	91.1	0.1	15	5.0 ± 0.8	14.70 ± 0.27 (10)	0.86	-	-	
SVA-80-6	EB	Pueblo Hondo silicic rock	8.2500	-71.9500	2499	15	1.454 (5774)	0.065 (75)	3.078 (3555)	24.6	11.7	26	5.8 ± 0.7	14.10 ± 0.25 (12)	0.86	-	-	
LB-71-VE-27	EB	Estanques Granodiorite	8.4600	-71.5500	450	20	1.318 (5142)	0.084 (51)	7.906 (4824)	27.9	27.1	75	2.6 ± 0.4	11.54 ± 0.88 (5)	1.98	-	-	1.4 ± 0.2
SVA-80-56	SLCB	Valera Granite	9.1900	-70.6600	1735	20	1.703 (6407)	0.053 (72)	3.184 (4310)	97.7	0,0	23	5.4 ± 0.6	12.82 ± 0.61 (10)	1.94	-	-	
SVA-80-64	SLCB	Valera Granite	9.1700	-70.6800	1999	14	1.720 (6407)	0.020 (24)	1.834 (1604)	38.2	8.9	13	4.9 ± 1.0	-	-	-	-	
SV-81-13	SLCB	Sierra Nevada Gneiss - Rio Chama Milla	8.6565	-71.1679	2430	4	1.377 (5774)	0.030 (7)	2.076 (486)	78.9	0,0	19	3.8 ± 1.4	-	-	-	-	
SV-81-15	SLCB	Sierra Nevada Gneiss - Rio Chama Milla	8.6698	-71.1814	2920	20	1.428 (5774)	0.035 (55)	1.556 (2428)	68.8	4.8	14	6.1± 0.8	14.49 ± 0.33 (13)	1.2	-	0.00-0.01	
SV-81-14	SLCB	Sierra Nevada Gneiss - Rio Chama Milla	8.6752	-71.1813	2960	20	1.403 (5774)	0.018 (22)	0.929 (1126)	88.1	0.1	8	5.2 ± 1.1	-	-	-	-	
LB-71-VE-32	SLCB	El Carmen Satellite body	8.9200	-70.8600	3800	7	1.318 (5142)	0.037 (8)	1.607 (351)	75.9	0.1	15	5.7 ± 2.0	12.92 ± 0.59 (21)	2.68	-	-	4.9 ± 0.9
LB-71-VE-39	SLCB	La Culata adamellite	9.0200	-70.9400	1800	20	1.318 (5142)	0.090 (112)	6.964 (8629)	85.9	0.1	66	3.2 ± 0.3	14.43 ± 0.21 (31)	1.17	-	-	3.0 ± 0.5
LB-71-VE-29	SLCB	Timotes granodiorite	9.0300	-70.7500	2300	20	1.318 (5142)	0.025 (23)	2.179 (2020)	80,0	0.04	21	2.8 ± 0.6	12.30 ± 0.52 (22)	2.42	-	-	3.8 ± 0.7
SV-81-9	ECB	Granite. Schist - Mucurubá	8.7106	-70.9943	2466	20	1.325 (5774)	0.054 (78)	2.494 (3561)	80.4	0,0	24	5.5 ± 0.6	13.72 ± 0.29 (14)	1.07	-	-	
SV-81-12	ECB	Granite. Schist - Mucurubá	8.7300	-70.9600	2551	20	1.351 (5774)	0.155 (43)	7.862 (5774)	91.1	0.4	73	5.0 ± 0.8	14.21 ± 0.72 (4)	0.65	-	-	
LB-71-VE-2	ECB	El Carmen Granodiorite	8.8800	-70.8400	3900	28	1.318 (5142)	0.025 (41)	1.451 (2345)	83.9	3.1	14	4.4 ± 0.7*	13.34 ± 0.39 (36)	1.65	-	-	4.7 ± 0.6; 4.9 ± 0.7
SV-81-27	ECB	El Carmen Granite. Schist - Mucurubá	8.7300	-70.9900	3120	20	1.564 (6407)	0.225 (292)	10.69 (13885)	94.7	0,0	85	6.2 ± 0.4	14.06 ± 0.26 (28)	1.37	-	-	
LB-71-VE-35	ECB	El Valle Dyke	8.7600	-71.0500	3200	20	1.318 (5142)	0.049 (64)	3.649 (4778)	58.5	6,0	35	3.3 ± 0.4	14.26 ± 0.17 (74)	1.11	-	0.00-0.04	4.2 ± 0.7
1407	ECB	*Palmira Granite*	*9.1162*	*-70.8648*	*1574*	*30*	*0.657 (5578)*	*0.094 (169)*	*1.47 (2654)*	*100*	*0,0*	*34*	*6.0 ±0.5*	*13.70 ±0.07 (14 8)*	*0.91*	*1.45 ±0.2*	-	
SV-81-18	SNB	Sierra Nevada Gneiss - Q. Gavidia	8.7020	-70.9402	3090	13	1.506 (5774)	0.093 (69)	8.809 (6516)	99.5	0,0	73	3.0 ± 0.4	13.90 ± 0.45 (12)	1.57	-	-	
SV-81-17	SNB	Sierra Nevada Gneiss - Q. Gavidia	8.6924	-70.9378	3260	11	1.480 (5774)	0.072 (42)	2.794 (1624)	39.9	9,0	24	7.2 ± 1.2	-	-	-	-	
SV-81-16	SNB	Sierra Nevada Gneiss - Q. Gavidia	8.6920	-70.9318	3395	15	1.454 (5774)	0.069 (75)	3.078 (3555)	24.6	11.7	26	5.8 ± 0.7	14.10 ± 0.25 (12)	0.86	-	-	
SV-81-29	SNB	Sierra Nevada Gneiss -Desembarrancadero	8.5852	-71.1144	1890	6	1.581 (6407)	0.113 (53)	4.658 (2181)	78.5	0.4	37	7.3 ± 1.0	-	-	-	-	
SV-81-21	SNB	Sierra Nevada Gneiss - Pico Espejo	8.5373	-71.0613	4070	20	1.609 (5774)	0.045 (69)	3.095 (4734)	99.9	0,0	24	4.4 ± 0.5	14.23 ± 0.22 (15)	0.86	-	-	
1373	SNB	Sierra Nevada Gneiss - Pico Espejo	8.5227	-71.0570	4400	20	1.738 (6407)	0.092 (122)	4.494 (5975)	98.1	0,0	32	6.7 ± 0.6	14.05 ± 0.44 (11)	1.46	-	-	
SV-81-20	SNB	Sierra Nevada Gneiss - Pico Espejo	8.5377	-71.0515	4655	20	1.558 (5774)	0.114 (144)	5.337 (6755)	8.9	12.5	43	6.3 ± 0.6	14.44 ± 0.24 (28)	1.24	-	-	
6407	SNB	*Santo Domingo Gneiss*	*8.8755*	*-70.6594*	*1723*	*21*	*0.590 (5872)*	*0.001 (102)*	*0.011 (1922)*	*87.9*	*0,0*	*29*	*4.5 ±0.5*	*14.37±0. 10 (101)*	*0.98*	*1.45 ±0.1*	-	
LB-71-VE-7	VB	Valera Granite	9.2700	-70.6000	700	20	1.318 (5142)	0.715 (953)	6.853 (9139)	38.2	3.24	65	26.0 ± 1.0	12.61 ± 0.16 (100)	1.56	-	0.00-0.02	21.5 ± 2.1; 24.0 ± 2.1
SVA-80-44	VB	Valera Granite	9.3500	-70.5200	859	20	1.616 (6407)	1.038 (631)	2.165 (1316)	68.6	0.3	17	145.0 ± 7.0	13.81 ± 0.11 (101	1.11	-	0.08-0.22	
SVA-80-46	VB	Valera Granite	9.2700	-70.5500	1195	20	1.668 (6407)	0.460 (348)	3.986 (3014)	41.8	12.5	30	36.0 ± 3.0	12.84 ± 0.14 (100)	1.97	-	0.00-0.04	
SVA-80-55	VB	Valera Granite	9.2214	-70.575	1937	6	1.685 (6407)	0.060 (5)	1.809 (151)	76.6	0,0	13	10.6 ± 4.8	-	-	-	-	
SVA-80-45	VB	Valera Granite	9.2026	-70.5757	1873	20	1.633 (6407)	1.068 (165)	3.651 (5641)	79.8	1.2	28	9.0 ± 0.7	12.38 ± 0.22 (74)	2.75	-	0.00-0.02	
SV-81-23	VB	El Carmen Granite - Piñango Rd	8.9831	-70.7851	3740	20	1.529 (6407)	0.073 (95)	1.790 (2333)	57.4	2,0	15	11.8 ± 1.2	13.35 ± 0.34 (21)	1.58	-	-	
SV-81-23	VB	El Carmen Granite - Piñango Rd	8.9831	-70.7851	3740	14	1.529 (6407)	0.078 (69)	2.013 (1791)	68.8	0.1	17	11.3 ± 1.4*	-	-	-	-	
SV-81-24	VB	El Carmen Granite - Piñango Rd	8.9626	-70.805	4090	20	1.546 (6407)	0.301(449)	2.854 (4254)	53,0	0.4	23	31.2± 2.0	11.46 ± 0.33 (86)	2.79	-	0.00-0.12	
SV-81-24	VB	El Carmen Granite - Piñango Rd	8.9626	-70.805	4090	11	1.546 (6407)	0.221 (154)	2.175 (1517)	31.4	6.7	18	30.0 ± 3.0*	-	-	-	-	
6107	VB	*Chachopo Granite*	*8.9550*	*-70.7581*	*2306*	*10*	*0.629 (5340)*	*0.001 (26)*	*0.011 (452)*	*100*	*0,0*	*26*	*5.2 ±1.1*	-	-	-	-	
LB-71-VE-31	VB	Chachopo Granodiorite	8.9300	-70.8000	3000	20	1.318 (5142)	0.027 (26)	1.763 (1669)	96.2	0,0	17	3.9 ± 0.8	12.40 ± 0.57 (15)	2.21	-	-	2.8 ± 0.6
6207	VB	*La Quebrada Augengneiss*	*9.2155*	*-70.6079*	*749*	*30*	*0.627 (5316)*	*0.001 (276)*	*0.01 (1874)*	*87.2*	*0.1*	*23*	*13.6 ±1.0*	*13.57 ± 0.12 (102)*	*1.16*	*1.37 ±0.1*	-	
6307	VB	*Puente Vía Jajo Gneiss*	*9.0963*	*-70.6774*	*1174*	*26*	*0.624 (5293)*	*0.001 (52)*	*0.005 (420)*	*100*	*0,0*	*11*	*11.1 ±1.7*	*12.99 ± 0 .28 (18)*	*1.18*	*1.10 ±0.2*	-	

Table 4.2. New apatite fission-track data from the Venezuelan Andes. §CATB = Cerro Azul Thrust; CB = Caparo; EB = Escalante; SLCB = Sierra La Culata; ECB = El Carmen; SNB = Sierra Nevada, and VB = Valera blocks (Figs. 5.3, 5.4 and 5.7) Italics letters indicate central ages determined by MBC using zeta = 289.66 ± 5.23, for dosimeter glass IRMM-540R. Brackets show number of tracks counted or measured. Standard and induced track densities measured on external mica detectors (g= 0.5) and fossil track densities on internal mica surfaces.

Central ages determined by POS using zeta = 379.3 ± 3 for dosimeter glass Corning-5. *Central ages determined by BPK using zeta = 383.5±5, for dosimeter glass Corning-5. †Chlorine was determined on a Cameca SX50 electron microprobe running at an accelerating voltage of 15kV, beam spot size of 10 m and beam current of 35nA; samples were calibrated using Durango apatite. For values <0.02% Cl errors are about ±100%; for values of ~0.10%, Cl errors are about ±25%; and for values ~1%, Cl errors are about ±15%. Analyses were performed at the University of Melbourne. **Published by Kohn et al. (1984) using the population method on same apatite concentrate.

Block	Elevation (m)				Slope (°)			
	mean	st. dev.	mode	skewness	mean	st. dev.	mode	skewness
Caparo (CB)	1694	815	1098	0.7	21	9	23	-0.2
Cerro Azul Thrust (CATB)	1418	759	1291	0.2	21	9	20	0.1
Escalante (EB)	1159	750	96	1.4	17	10	12	0.5
Sierra La Culata (SLCB)	2216	1044	2289	-0.1	23	10	28	-0.5
Sierra Nevada (SNB)	3207	802	3740	-0.7	24	9	28	-0.4
El Carmen (ECB)	3028	1066	4105	-1.0	22	9	23	-0.1
Valera (VB)	1448	748	409	1.4	21	9	23	-0.2

Table 4.3. Topographic characteristics, mean elevation and mean slope angle for different tectonic blocks in the Venezuelan Andes.

Chapter 5

V. THERMOCHRONOLOGIC EVIDENCE FOR KM-SCALE VERTICAL OFFSET ACROSS THE BOCONÓ STRIKE-SLIP FAULT, CENTRAL VENEZUELAN ANDES

Mauricio A. Bermúdez[1,2], Peter van der Beek[1], and Matthias Bernet[1]

[1]Laboratoire de Géodynamique des Chaînes Alpines, Université Joseph Fourier, BP53, 38041 Grenoble, France (mauricio.Bermúdez-cella@e.ujf-grenoble.fr / Fax: +33 476 514058 / Phone: +33 476 635964)
[2]Laboratorios de Termocronología y Geomatemáticas, Escuela de Geología, Minas y Geofísica. Facultad de Ingeniería, Universidad Central de Venezuela, Caracas, Venezuela

5.0 Abstract

The controls on the spatial patterns of exhumation in oblique convergent orogens remain incompletely understood. We address this question in the central Venezuelan Andes, which are traversed by the 500-km long Boconó strike-slip fault. We present a new apatite fission-track (AFT) age-elevation profile from Pico Bolívar in the Sierra Nevada, to the south of the Boconó Fault, and compare the results with previously published AFT data for the Sierra La Culata to the north of the fault. The AFT data are combined with 3D thermal modeling to constrain the exhumation and relief history of both blocks, which show significant differences: the Sierra Nevada shows decreasing exhumation rates from ~1.0 km/Ma before 9 Ma to ~0.3 Ma at present. The Sierra La Culata, in contrast, experienced much more recent and rapid exhumation, with rates between 0.8 and 1.1 km/Ma since 4 Ma. The data suggest 2.6 km of relative rock uplift of the Sierra La Culata with respect to the Sierra Nevada since this time and support significant uplift of basement blocks along major pre-existing discontinuities during transpression in the Northern Andes. Rapid exhumation in the Sierra Nevada before 8 Ma may be related to surface uplift that caused Late Miocene deflection of the Orinoco River, as inferred from the Neogene sedimentary record.

Keywords: Venezuelan Andes, apatite fission-track, exhumation, Boconó Fault, thermal models.

5.1 Introduction

The spatial and temporal patterns of exhumation in oblique convergent systems are complex and controlled by several parameters. The obliquity of plate motion with respect to pre-existing major faults controls the degree of partitioning between shortening, leading to uplift and exhumation, and strike-slip (e.g., Braun and Beaumont, 1995; Burbidge and Braun, 1998). Local changes in orientation of major strike-slip faults, lithological variability, as well as climatic effects may lead to localized uplift and exhumation (Cruz et al. 2007; Spotila et al. 2007a, b). Finally, far-field stress transfer resulting from changes in plate motions or local variations in plate configuration due to migration of plate triple junctions may be recorded as temporal variations in uplift and exhumation rates (Fitzgerald et al. 1995; Lock et al. 2006).

The Venezuelan Andes (VA) provide an ideal case for studying the relation between exhumation and strike-slip faulting because the evolution of this mountain belt is coupled to movement on major strike-slip faults with variable vertical components (Fig. 5.1). However, the exhumation history of the VA has remained poorly understood, with only few detailed thermochronology studies providing constraints on the timing and spatial variability of exhumation (Kohn et al. 1984). Here we report new apatite fission-track (AFT) data collected along an age-elevation profile within the highest part of the VA. We compare these new data to previously published age-elevation trends, using thermal modeling to reconstruct the evolution of the central VA and to document significant spatial and temporal variations in exhumation rates in this area.

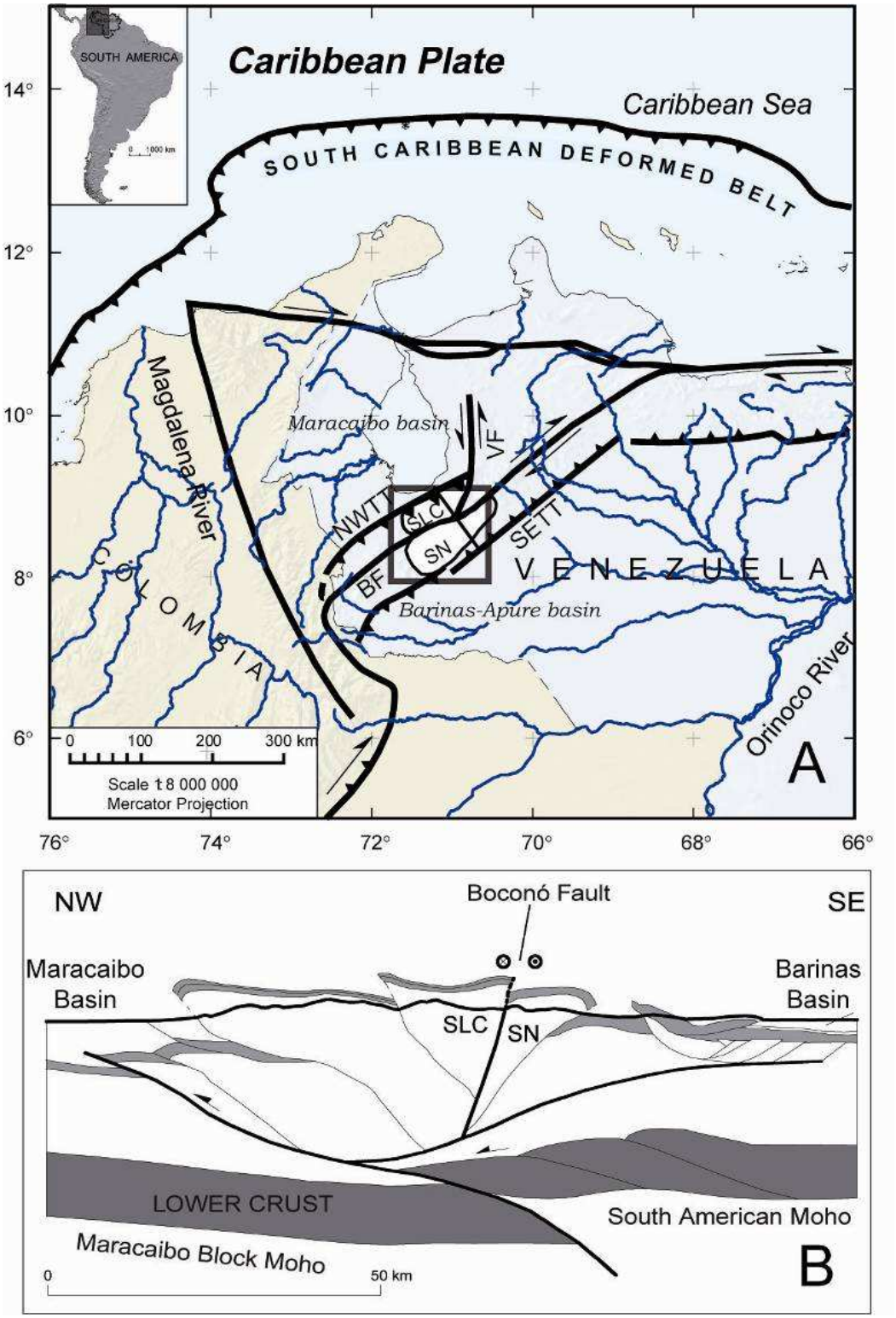

Fig. 5.1.A) Simplified structural map of the Venezuelan Andes and surrounding regions, showing the location of Sierra La Culata (SLC) and Sierra Nevada (SN) blocks, the Boconó (BF) and Valera (VF) strike-slip faults, and the north-west (NWTT) and south-east (SETT) thrust systems bounding the Venezuelan Andes. Inset shows location within South America; box shows location of Figure 5.2. B) Simplified structural cross-section of the central Venezuelan Andes, modified from Colletta et al. (1997). Light shaded marker horizon represents Cretaceous series.

5.2 Tectonic setting

The VA constitutes a 400 kilometer long NE-SW trending orogen in western Venezuela (Fig. 5.1A). The present-day VA results from complex geodynamic interaction between the Caribbean Plate, the Panama Arc and the South American Plate (Taboada et al. 2000). This three-plate interaction is regionally expressed by the oblique convergence of a small continental block, the Maracaibo Block, and the South American Plate (Colletta et al. 1997; Montes et al. 2005). Pre-existing tectonic discontinuities, related to Mesozoic rifting (Case et al. 1990), were reactivated during convergence between the Maracaibo block and the South American plate, which resulted in local thrusting, translation and rotation as well as exhumation of individual blocks at different times and rates from the late Eocene to the Pliocene.

The orogen has a crystalline core of Precambrian gneiss and schist and Paleozoic to Mesozoic plutonic rocks (Fig. 5.2), overlain by Jurassic and Cretaceous clastic sediments and flanked by Eocene to Pliocene molasse deposits to the north and south. The VA is characterized by numerous major strike-slip fault systems and flanked by foreland thrust belts to the NW and SE (Figs. 5.1, 5.2). The foremost of these faults is the Boconó Fault that extends 500 km in a NE-SW direction along the entire VA. Regional geological evidence compiled by Schubert (1982) suggests that strike-slip displacement along the great fault zones of northern Venezuela began during the Late Tertiary and that the Boconó Fault has experienced both right-lateral strike-slip and local vertical components of motion. The Boconó Fault is morphologically expressed by escarpments and aligned valleys dividing the VA almost symmetrically in its central part (the Mérida Andes), where the Sierra La Culata and Sierra Nevada are located to the north and south of the fault, respectively (Figs. 5.1, 5.2). These two ranges form the morphologically highest part of the VA, with mean elevations ~3000 m and numerous peaks over 4000 m elevation (including Pico Bolívar, Venezuela's highest point at 4981 m).

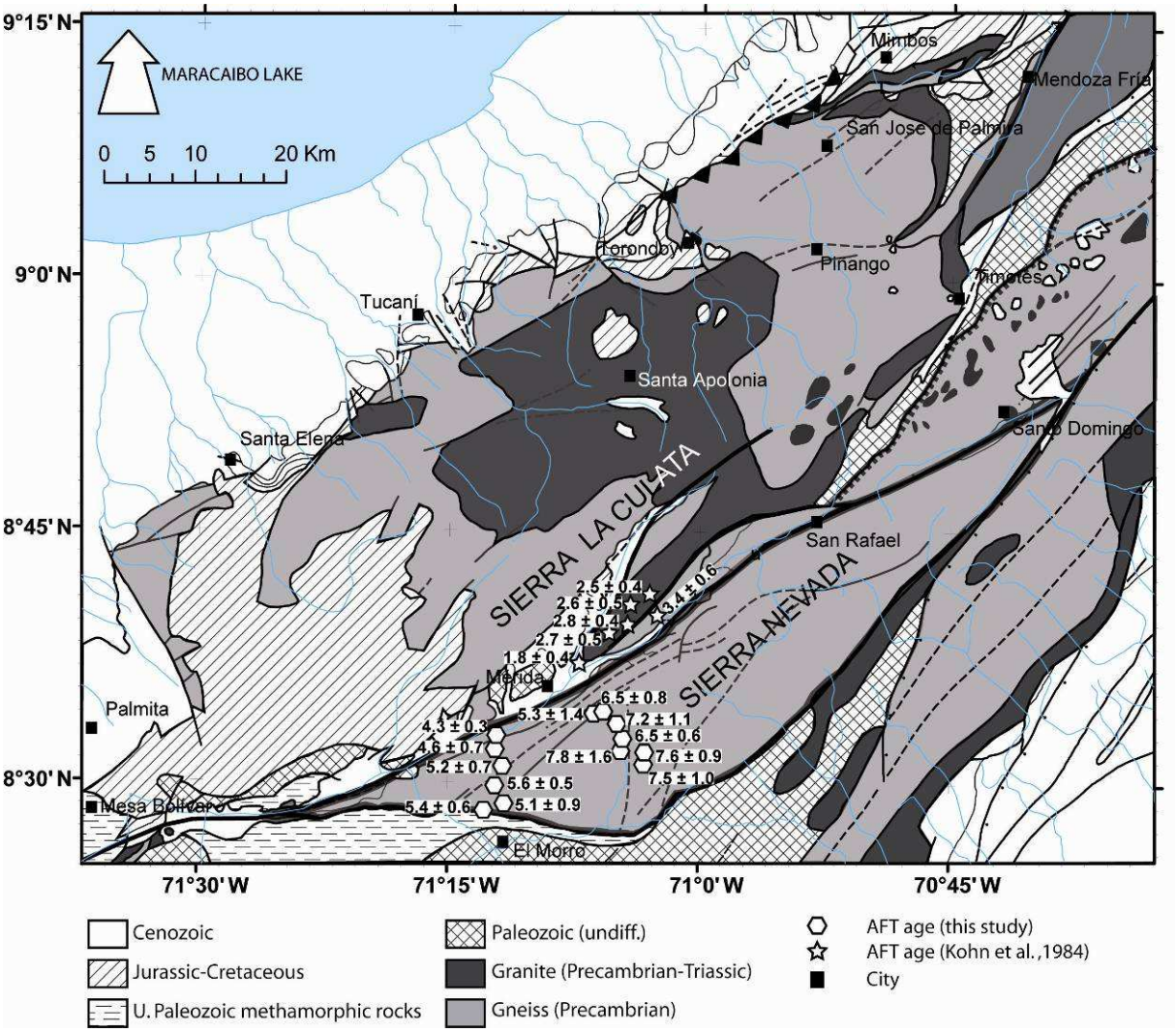

Fig. 5.2. Simplified geological map of the Mérida Andes (modified from Hackley et al. 2005) showing sample locations and AFT ages used in this study. Boconó Fault system indicated by thick lines; present-day drainage by thin grey lines.

5.3 Thermochronology data

We sampled an AFT age-elevation transect in the Sierra Nevada, containing 13 samples between 1250 m elevation in the Chama River valley SE of Mérida and 4718 m elevation at Pico Bolívar. The upper 7 samples were collected along the Teléferico de Merida cable car system, but since the Pico Bolívar slopes below ~3000 m elevation are covered by dense cloud-forest without outcrops, the lower 6 samples were collected along the Mérida-El Morro road, ~10 km to the SE (Fig. 5.2). The two age-elevation profiles overlap perfectly (Fig. 5.3A), indicating no differential exhumation between the two profiles.

5.3.1 Methods

Apatite and zircon were extracted from rock samples using standard magnetic and heavy liquid techniques. For AFT analysis, apatites were mounted in epoxy, polished and etched in a 5.5M HNO_3 solution at 20°C for 20 s. All samples were dated by the external detector method, using U-poor mica as external detector and a zeta calibration factor for Fish Canyon and Durango age standards. Samples were irradiated at the well-thermalized ORPHEE facility of the *Centre d'Etudes Nucléaires* in Saclay, France, with a nominal fluence of ~5×10^{15} neutrons/cm^2. Neutron fluences were monitored using IRMM540 dosimeter glasses. Mica detectors were etched in 48% HF at 20°C for 18 minutes. All samples were analysed by M.A. Bermúdez-Cella. Samples were counted dry with a BH-2 Olympus microscope at 1250x magnification. Separate mounts for each sample were subsequently Cf-irradiated at the University of Melbourne, Australia, in order to reveal sufficient amounts of confined tracks for length measurements. Confined track-length measurements were performed by digitizing the track ends using a drawing tube; the etch-pit width parallel to the C-axis (D_{par}) of 100 tracks crossing the etched internal surface was measured using the same digitizing technique.

Thermal history modelling was performed using HeFTy v1.3 software (Ketcham, 2005). Input data for the inversions included AFT ages, the AFT track-length distribution (uncorrected for angle to the C-axis) and D_{par} values calibrated to the values of standard samples used for deriving the annealing model (Ketcham et al. 1999). Models were constrained by the present-day surface temperature and boxes placed around the AFT ages, with box sizes of 5-15 Myr and 60-100 °C so as not to guide thermal histories (cf. Fig. 5.5). Random sub-segment spacing was used and no continuous cooling constraint was applied. "Good" and "acceptable" fits to the observations are defined following Ketcham (2005).

5.3.2 Results

AFT central ages from the Sierra Nevada profile range between 4.3±0.3 and 7.6±0.9 Ma, increasing monotonically with elevation (Table 5.1, Fig. 5.3A). Chi-square probabilities close to 100% and age dispersions (Galbraith and Laslett, 1993) close to 0 indicate that all samples contain single age populations. Fission-track etch-pit widths (D_{par}) are relatively uniform, ranging from 1.3 to 1.6 μm (Table 5.1) and indicating homogeneous apatite compositions close to fluorapatite (Carlson et al. 1999). Mean track lengths (MTL) vary between 13.9 and

14.5 μm (Table 5.1), with narrow standard deviations (0.8-1.4 μm). All samples have unimodal track-length distributions, compatible with rapid cooling since passing through the AFT closure temperature (Gallagher et al. 1998; Gleadow and Brown, 2000). We use least-square fitting of a straight line for generalized linear models (McCullagh and Nelder, 1989) to obtain a slope of the age-elevation relationship of 1.1±0.2 km/Ma (r^2 = 0.90), implying exhumation at these rates between 4 and 8 Ma in the Sierra Nevada.

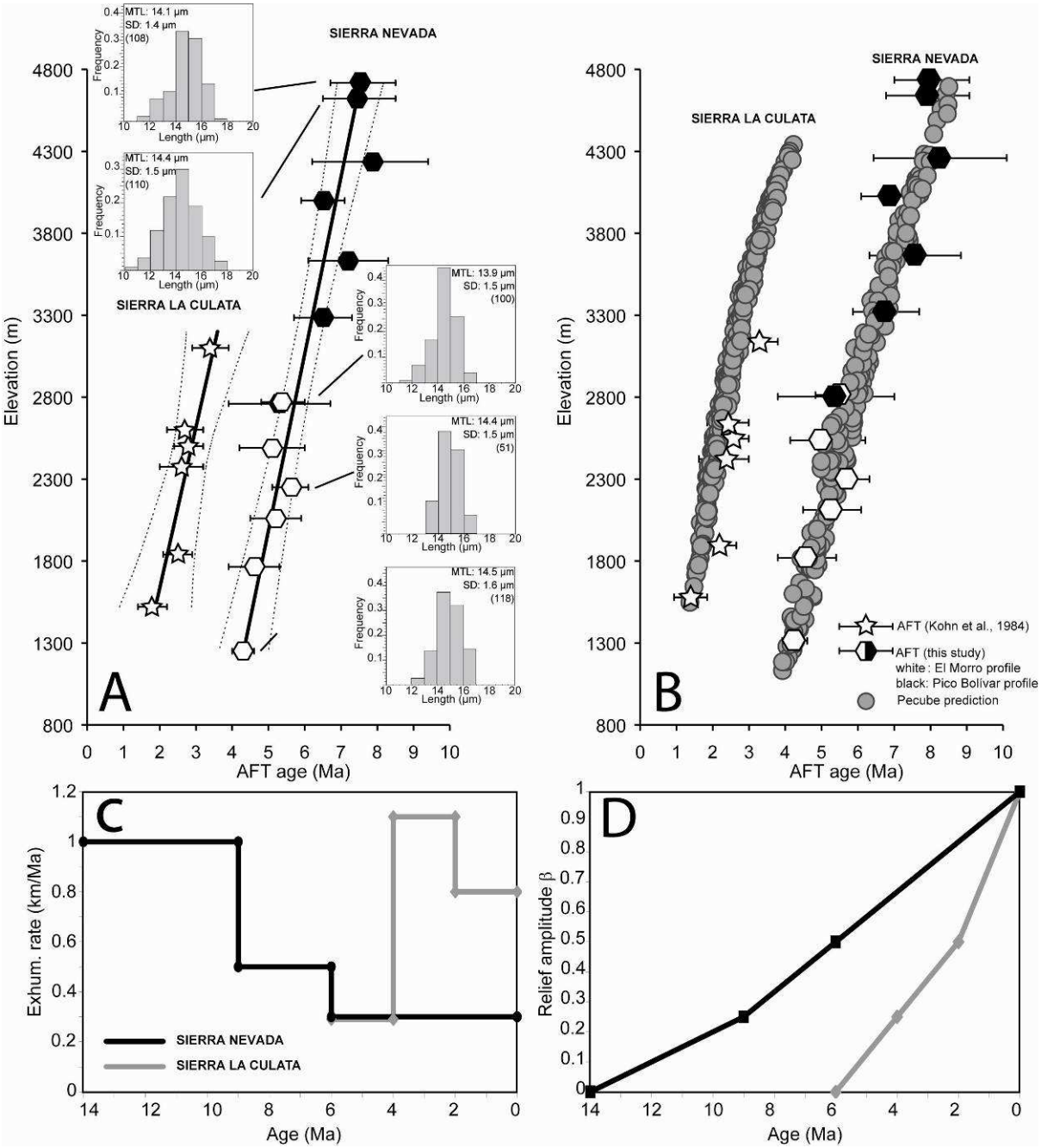

Fig. 5.3. Apatite fission-track age-elevation profiles from the Sierra Nevada and Sierra La Culata (legend for data source in B). Best-fit AER and 95% confidence curves are indicated by heavy black and thin dashed lines, respectively. Fission-track length distributions are shown for selected samples (MTL: Mean track length; SD: Standard deviation, number in parenthesis: number of track lengths measured). B) Comparison between observed data and Pecube predictions for best-fit models for the Sierra Nevada and Sierra La Culata. C) Exhumation rates through time for best-fit Pecube models (black: Sierra Nevada model; grey: Sierra La Culata model); D) Inferred relief evolution, represented by relief amplitude β (as defined by Braun, 2002) for best-fit Pecube models.

Sample	Latitude	Longitude	Elevation (m)	n	ρ_s (10^5 cm^{-2})	N_s	ρ_i (10^5 cm^{-2})	N_i	ρ_d (10^6 cm^{-2})	$P(\chi^2)$ (%)	D	Age (Ma)	± 1 σ	[U] (ppm)	MTL / SD (µm)	D_{par} / SD (µm)	Number of lengths
48	8.5317	-71.0527	4718	21	0.821	84	9.244	946	5.950	97.6	0	7.6	± 0.9	23.4	14.1 / 1.4	1.4 / 0.2	108
49	8.5273	-71.0516	4622	24	0.804	61	9.188	697	5.931	99.7	0	7.5	± 1.0	23.4	14.4 / 1.4	1.5 / 0.1	110
50	8.5332	-71.0790	4236	13	1.196	28	13.031	305	5.922	96.6	0	7.8	± 1.6	28.7	13.9 / 0.9	1.3 / 0.1	10
51	8.5437	-71.0752	3999	30	0.709	131	9.354	1729	5.912	99.6	0	6.5	± 0.6	24.7	14.1 / 1.3	1.4 / 0.1	22
52	8.5556	-71.0826	3633	21	0.709	45	8.426	535	5.902	61.8	0	7.2	± 1.1	21.3	14.4 / 1.2	1.3 / 0.1	27
53	8.5700	-71.0940	3285	28	0.381	905	4.995	905	5.893	100	0	6.5	± 0.8	14.6			
54	8.5698	-71.1055	2760	11	0.267	16	4.261	255	5.833	99.4	0	5.3	± 1.4	11.9			
65	**8.4801**	**-71.1909**	**2770**	**18**	**2.841**	**229**	**46.654**	**3760**	**5.873**	**0**	**0.38**	**5.4**	**± 0.6**	**112.9**			
66	**8.4721**	**-71.2129**	**2490**	**20**	**0.349**	**37**	**5.732**	**608**	**5.864**	**99.7**	**0**	**5.1**	**± 0.9**	**16.1**			
67	**8.4995**	**-71.2011**	**2250**	**30**	**0.865**	**174**	**13.157**	**2646**	**5.854**	**14.8**	**0.11**	**5.6**	**± 0.5**	**32.6**	**13.9 / 1.1**	**1.5 / 0.2**	**100**
68	**8.5164**	**-71.1968**	**2060**	**30**	**0.278**	**61**	**4.504**	**987**	**5.845**	**97.1**	**0**	**5.2**	**± 0.7**	**11.2**	**14.0 / 0.8**	**1.3 / 0.1**	**15**
69	**8.5355**	**-71.2015**	**1765**	**26**	**0.249**	**52**	**4.509**	**943**	**5.835**	**99.9**	**0**	**4.6**	**± 0.7**	**11.6**	**14.4 / 1.0**	**1.5 / 0.2**	**51**
70	**8.5476**	**-71.2028**	**1250**	**30**	**1.343**	**320**	**26.888**	**6405**	**5.825**	**6.7**	**0.22**	**4.3**	**± 0.3**	**69.1**	**14.5 / 1.1**	**1.6 / 0.2**	**118**

Table 5.1. Apatite fission-track data from the Sierra Nevada, central Venezuelan Andes. Note: Fission-track ages are reported as central ages (Galbraith and Laslett, 1993) , using a zeta value of 288.7 ± 5.2 (M. Bermúdez) and the IRMM 540 uranium glass standard (15 ppm U). Ages were calculated with the Trackkey program (Dunkl, 2002). Roman numbers represent samples collected along Pico Bolívar profile; bold numbers: El Morro profile. Abbreviations: n = number of grains counted; ρ_s = spontaneous track density; ρ_i = induced track density; ρ_d = dosimeter track density; N_s, N_i, N_d = number of tracks counted to determine the reported track densities. For irradiations with significant (> 3%) axial gradients in neutron fluence (as monitored by the dosimeters), ρ_d is interpolated between dosimeter values. $P(\chi^2)$ = Chi-square probability that the single grain ages represent one population; D = age dispersion; MTL = mean track length; Dpar = Etch-pit width parallel to the C-axis (Carlson et al. 1999; Barbarand et al. 2003a, b); SD = standard deviation of track-length distribution and etch-pit width measurements, respectively.

We compare our data with 7 AFT ages obtained along an age-elevation transect between 1520 and 3100 m in the Sierra La Culata by Kohn et al. (1984; Figs. 5.2 and 5.3). Although these ages were determined using the now outdated population method, several of these samples were recently recounted with the external detector method and provided identical ages (B.P. Kohn, pers. commun., 2008). AFT ages in the Sierra La Culata are significantly younger than those in the Sierra Nevada for similar elevations, ranging between 1.8±0.4 and 3.4±0.6 Ma (Fig. 5.2A). In contrast, the age-elevation relationship is similar, with best-fitting slope for the Sierra La Culata of 1.45±0.65 km/Ma (r^2 = 0.89). The offset between the two age-elevation relationships suggest a minimum of 1.9 km of relative rock uplift of the Sierra La Culata with respect to the Sierra Nevada since 4 Ma.

5.4 Numerical modeling

Age-elevation relationships are sensitive to topography and relief change (Braun, 2002) and extracting these two signals is a complex task (Valla et al. submitted). In order to test whether potential relief variations significantly affect our above estimates, we employ the numerical thermal-kinematic model *Pecube* (Braun, 2003) to test a range of exhumation rate and relief evolution scenarios. Two thousand model runs were performed for each block, systematically varying exhumation rates and relief through time. Thermal and kinematic model parameters are given in Table 5.2.

Thermal parameters	
Model crustal thickness	40 km
Number of nodes in the vertical direction	21
Thermal diffusivity	25 km^2/Ma (Braun and Robert, 2005)
Temperature at the base of the model	650 °C
Temperature at sea level	25 °C
Atmospheric lapse rate	6 °C/km
Crustal heat production	8 °C/Ma (Braun and Robert, 2005)
Erosional response time	1000 Ma
Flexural parameters	
Crustal density	2700 kg/m^3 (Gomez et al. 2005)
Sub-lithospheric mantle density	3300 kg/m^3 (Gomez et al. 2005)
Young's modulus	70 GPa (Gomez et al. 2005)
Poisson ratio	0.25 (Gomez et al. 2005)
Equivalent elastic thickness	30 km (Ojeda, 2000)

Table 5.2. Thermal and flexural parameters values for Mérida Andes used in *Pecube* modeling. References constraining parameter values are given where appropriate.

Best-fit solutions highlight the strong difference in exhumation history between the Sierra Nevada and Sierra La Culata blocks (Fig. 5.3C): whereas exhumation rates for the Sierra Nevada decrease from 1.0 km/Ma between 14 and 9 Ma to 0.3 km/Ma since 6 Ma, the Sierra La Culata block records a rapid exhumation event (1.1 km/Ma) between 4 and 2 Ma, with rates remaining at 0.8 km/Ma since that time. All solutions that fit the data require relief to increase with time (Fig. 5.3D). The fits between observed and predicted AFT ages are shown in Fig. 5.3B. Since the current mean elevations of both ranges are similar, these exhumation histories imply 2.6 km of relative rock uplift in the Sierra La Culata with respect to the Sierra Nevada since 4 Ma.

The above models were constrained with AFT ages and MTL only. In order to provide an independent check on the models, we predicted time-Temperature paths for Sierra Nevada samples with sufficiently well-documented track-length distributions using the HeFTy code (Ketcham, 2005). All samples record decreasing exhumation rates since crossing the AFT closure temperature 6 ± 2 Ma ago (Fig. 5.4) and cooled through the Partial Annealing Zone (PAZ) at rates between 16 and 40 °C/Ma. Cooling rates through the PAZ systematically increase with decreasing elevation, consistent with local denudation being at least partly controlled by relief increase, as suggested by the Pecube models. Finally, we also predicted track-length distributions for the best-fit Pecube model by importing the predicted time-temperature history into HeFTy (Fig. 5.5). Predicted track-length distributions fit the observed distributions very well, providing further support for our preferred scenario.

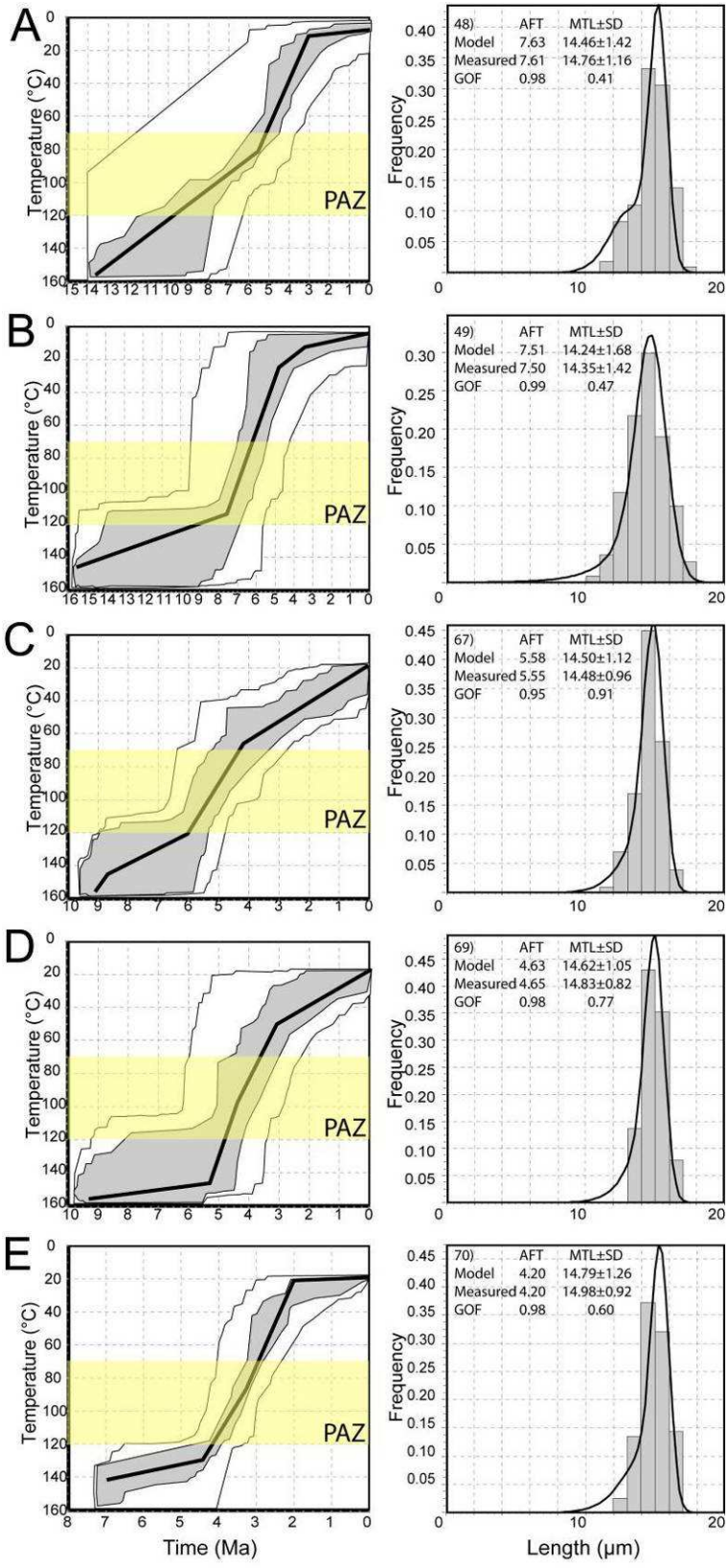

Fig. 5.4. Thermal modeling of AFT ages and track-length distributions for samples from the Sierra Nevada, obtained with the HeFTy code (Ketcham, 2005). Results are displayed as time-Temperature paths (left diagrams). Green area indicates acceptable fits; pink area indicates good fits; thick black line indicates best fit. Histogram of measured confined track lengths is overlain by a calculated probability density function for the best-fit history (right diagrams). Note that modeled t-T paths are well constrained only within the PAZ (yellow band).

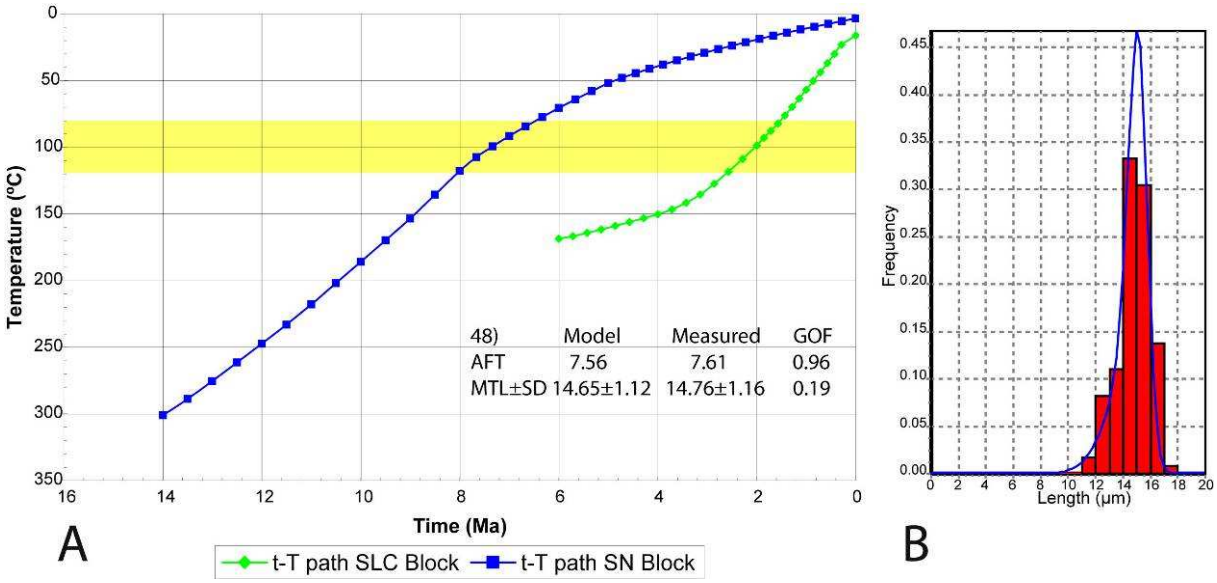

Fig. 5.5. A) Comparison of predicted and observed track-length distributions for sample 48 from Pico Bolívar (top of Sierra Nevada profile). B) Predicted track-length distributions are obtained by importing the best-fit time-temperature predicted by Pecube (Braun, 2003) into the HeFTy program (Ketcham, 2005).

5.5 Discussion and conclusions

Current tectonic models suggest that surface uplift of the VA began during the Miocene (Colletta et al. 1997; Mann et al. 2006), and that major exhumation occurred during the Pliocene (Kohn et al. 1984). Our data and numerical modelling demonstrate that Late Neogene exhumation of the VA was diachronous across the Boconó Fault. Rapid Late Miocene exhumation in the Sierra Nevada implies that crustal thickening and (oblique?) compression were well established by that time. This phase coincides with major shortening and exhumation in the Eastern Cordillera of Colombia (Gomez et al. 2005; Parra et al. 2009), possibly in response to Late Miocene accretion of the Panamá arc to the western margin of Colombia between 8-12 Ma (Cediel et al. 2003). Subsequent rapid exhumation of the Sierra La Culata in Pliocene times implies continuous oblique convergence of the Maracaibo Block and South America, contrasting with present-day tectonic escape of the block and transtension along the Boconó Fault (Backé et al. 2006).

Late Miocene uplift and exhumation of the Sierra Nevada is consistent with Late Miocene deflection of the Orinoco and Magdalena rivers (Fig. 5.1), as inferred from the Neogene sedimentary record (Hoorn et al. 1995; Díaz de Gamero, 1996). During the Late Oligocene to

early Middle Miocene the Central Cordillera of Colombia was drained to the east, while the Guyana Shield was drained to the northwest. During the Late Miocene, the northern Andes and their drainages attained their present configuration (Hoorn et al. 1995).

The structure of the VA has been interpreted as characteristic of an obliquely convergent mountain belt, in which deformation in partitioned between compression at the edges of the belt and strike-slip faulting in its core (Colletta et al. 1997). However, our data imply that the Boconó Fault also accommodates km-scale vertical offsets. Uplift and exhumation in the Mérida Andes are not obviously related to local changes in fault orientation, as the Boconó Fault segment of the central VA is transtensional rather than transpressional in the current tectonic regime (Backé et al. 2006). Instead, we suggest that temporal changes in boundary conditions, related to accretion of the Panamá arc (Cediel et al. 2003) and clockwise rotation of the Maracaibo block (Montes et al. 2005), control the spatial and temporal patterns of exhumation observed in the central VA.

5.6 Acknowledgements

This study was supported by a Consejo de Desarrollo Científico y Humanístico (CDCH-UCV) de la Universidad Central de Venezuela (UCV) PhD grant to MBC, and the French Ministery of Foreign Affairs through ECOS Nord project V08U01. We thank the Instituto Nacional de Parques (INPARQUES) de la Región Andina and the Teléferico System, Mérida-Venezuela for permission to sample in the Sierra Nevada National Park and logistical support during field work.

Chapter 6

VI. TECTONIC VERSUS CLIMATIC CONTROLS ON EXHUMATION IN THE VENEZUELAN ANDES

Mauricio A Bermúdez[a,b], Matthias Bernet[a], Peter van der Beek[a]

[a]Laboratoire de Géodynamique des Chaînes Alpines, Université Joseph Fourier, BP53, 38041 Grenoble, France (mauricio.Bermúdez-cella@e.ujf-grenoble.fr / Fax: +33 476 514058 / Phone: +33 476 635964)
[b]Laboratorios de Termocronología y Geomatemáticas, Escuela de Geología, Minas y Geofísica. Facultad de Ingeniería, Universidad Central de Venezuela, Caracas, Venezuela.

6.0 Abstract

In most orogenic systems it is not obvious if erosion and relief development are most dependent on tectonics or climate. We have studied the relationships between present day precipitation, stream-power based predictions of present-day erosion rates, seismic energy release, relief and long-term exhumation rates for the Venezuelan Andes. Apatites in modern sands collected from eight rivers draining the Venezuelan Andes were dated with the fission-track method for establishing sediment provenance and for determining catchment-averaged long-term exhumation rates. A comparison with previously published *in-situ* apatite fission-track data shows that detrital apatite fission-track thermochronology efficiently predicts exhumation patterns across the mountain belt. Catchment-averaged exhumation rates vary from <0.4 km/My to the northeast of the main mountain belt, to 0.45 km/My for large catchment draining the central Venezuelan Andes and ~0.5 km/My for small catchments draining the northwest flank of the orogen. There is no difference in catchment-wide exhumation rates on the northwest and southeast flanks of the mountain belt, despite an orographic gradient that is responsible for a threefold increase in precipitation from northwest to southeast. Long-term exhumation rates are strongly correlated to relief of the different catchments, but no or negative correlations exist with either present-day precipitation, present-day erosion indexes of the pattern of seismic energy release. Different explanations can be put forward to explain the lack of correlations including non-representativeness of the short-term precipitation and seismic records on geological timescales or insufficient spatial distribution of the samples. Alternatively, geodynamic reasons for the lack of correlation could be that

relief and exhumation in the Venezuelan Andes are decoupled from climate and that deformation leading to relief growth is mostly aseismic.

Keywords: Venezuelan Andes, detrital apatite fission-track, exhumation, erosion index, relief, climate, relations.

6.1 Introduction

The relative importance of tectonics and climate in controlling the relief development and exhumation of mountain belts remains strongly debated (e.g., Molnar and England, 1990; Burbank et al. 2003; Reiners et al. 2003; Bookhagen and Strecker, 2008; Strecker et al. 2009, Whipple, 2009). Significant problems that limit our ability to discriminate between the driving forces for topography and erosion are (1) the limited temporal precision with which variations in exhumation rate, climate and tectonics can be resolved and compared (e.g., Whipple, 2009) and (2) the different temporal scales on which these processes are resolved (Burbank et al. 2003; Reiners et al. 2003; Vernon et al. 2009): while thermochronological data record denudation on million-year timescales, seismicity (a proxy for tectonics) and precipitation (an aspect of climate) records generally do not go back more than a few tens of years. Nevertheless, the comparison of spatial patterns of long-term exhumation and short-term seismicity and precipitation may provide some first-order insights into the processes driving mountain belt erosion, even in the absence of strong spatial correlations (Dadson et al. 2003; Vernon et al. 2009; Koons, 2009).

The Andes have figured prominantly in the discussion on climate versus tectonic controls on topography and denudation of mountain belts because of the obvious link between laterally varying topographic characteristics and climatic zonation (e.g., Montgomery et al. 2001; Lamb and Davis, 2003), as well as the strong asymmetry in orographic precipitation associated with this orogen (e.g., Bookhagen and Strecker, 2008). While many previous studies have concentrated on the southern and central Andes (e.g., Strecker et al. 2007; Farías et al. 2008), attention has recently also shifted to the northern Andes. Mora et al. (2008), for instance, describe strongly asymmetric deformation and exhumation patterns in the eastern Colombian Andes, which they link to the strong NW-SE precipitation gradient across this part of the belt.

In this study, we present apatite fission-track (AFT) data from eight major river catchments in the Venezuelan Andes, the north-easternmost extension of the Andes. We compare AFT data collected from modern river sediments to available bedrock AFT data of the Venezuelan Andes (Kohn et al. 1984; Bermúdez et al. submitted) in order to test whether they faithfully record exhumation of the catchments (e.g., Ruhl and Hodges, 2005; Brewer et al. 2006) and to spatially integrate the still relatively sparse in-situ data. The purpose of this study is to determine provenance of the present day fluvial sediments, and to study the relative controls of climate, tectonics and relief on the exhumation of the Venezuelan Andes. For this purpose, the long-term exhumation rates derived from the detrital thermochronology data are compared to present-day precipitation rates, seismic energy, and relief of the individual drainages and the whole mountain belt.

Our analysis suggests that, in contrast to previous findings in the contiguous Colombian Andes (Mora et al. 2008), the strong precipitation gradient in the Venezuelan Andes does not impose a major control on long-term exhumation rates. Instead, catchments draining the highest central part of the chain, which receives little precipitation but is crosscut by the active Boconó strike-slip fault, show the highest long-term exhumation rates.

6.2 Tectonic, geomorphic and climatic setting

6.2.1 Geological evolution and exhumation history

The Venezuelan Andes were formed by oblique convergence between the continental Maracaibo block and the South American plate, driven by eastward movement of the Caribbean plate and Miocene-Pliocene closure of the Panama Arc (Fig. 6.1; Case et al. 1990). The orogen is characterized by high seismicity and spatially variable exhumation since Miocene times, as recorded by AFT thermochronology data (Kohn et al. 1984; Bermúdez et al. submitted, chapters 4 and 5 in this work). The pattern of exhumation of the Venezuelan Andes is controlled by reactivation of pre-existing faults that delineate individual tectonic blocks (Fig. 6.1). Bermúdez et al. (submitted, chapter 4 in this work) delimited at least seven tectonic blocks with contrasting exhumation and cooling histories. The most important fault systems are the right-lateral strike-slip Boconó, Central-Sur Andino and Caparo faults, and the

left-lateral strike-slip Icotea, Valera, and Carache or Burbusay fault systems (Fig. 6.1). The orogen is bounded by two seismically active thrust belts to the northwest and southeast. The Boconó fault extends from the border with Colombia for more than 500 kilometers to the northeast (Fig. 6.1). The Boconó fault zone divides the Venezuelan Andes symmetrically in its central part, where two separate chains can be distinguished: The Sierra La Culata to the northwest and the Sierra Nevada to the southeast. These two blocks cooled rapidly but diachronously during the late Miocene–Pliocene (Kohn et al. 1984; Bermúdez et al, submitted, chapter 5 in this work). In contrast, the Caparo and Valera blocks at the southwestern and northeastern terminations of the Venezuelan Andes respectively, experienced a phase of slow cooling from the late Oligocene to late Miocene. Both these blocks are dominated by Paleozoic and Mesozoic sedimentary rocks, whereas Proterozoic to Paleozoic gneisses and granites are exposed in the core of the mountain belt, in the Sierra Nevada and Sierra La Culata ranges. This crystalline basement is flanked by Cenozoic sedimentary rocks to the north and south (Fig. 6.1).

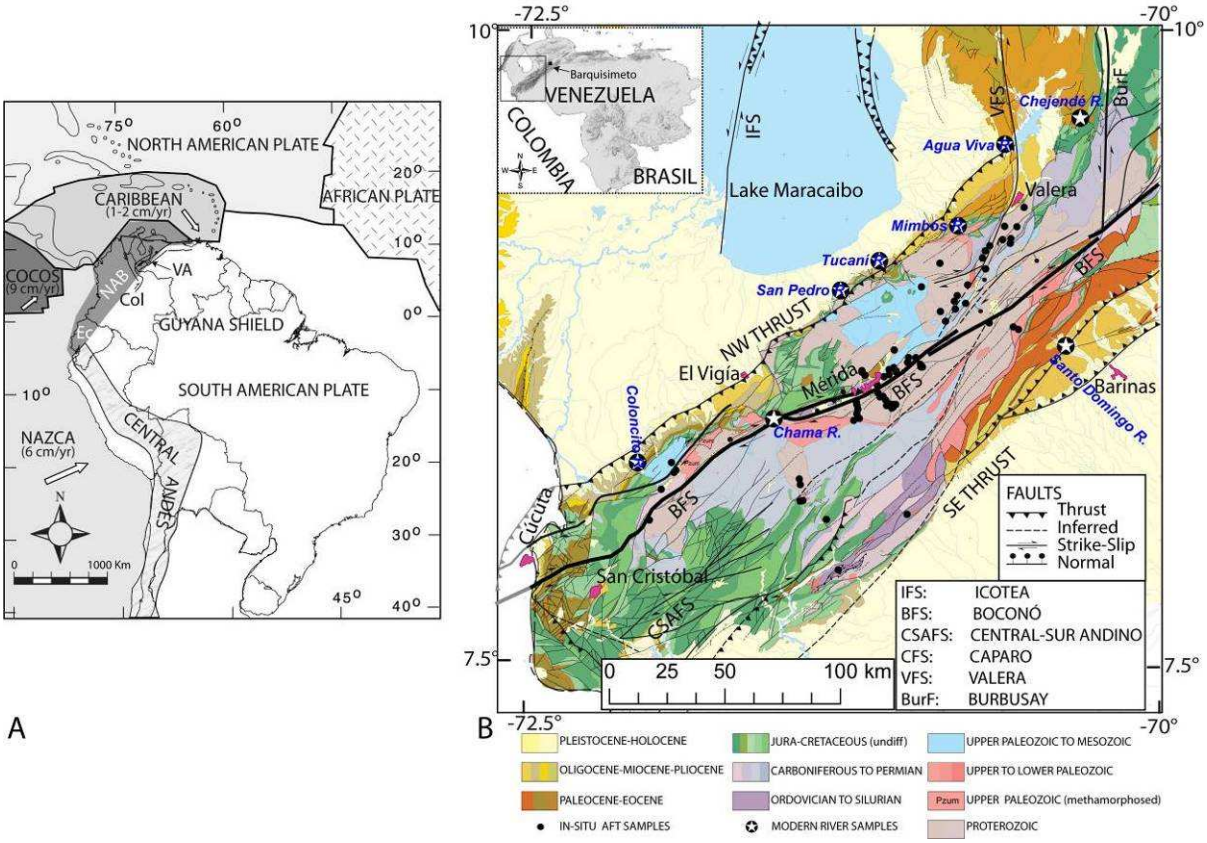

Fig. 6.1. A) Tectonic framework of northwestern South America. NAB = Northern Andean Block; VA= Venezuelan Andes; Ec, Col= Ecuador and Colombia respectively. B) Geologic, structural and drainage network map of the Venezuelan Andes (modified from Audemard et al. 2000 and Hackley et al. 2005). Stars correspond to location of detrital AFT samples; the name of the corresponding river is indicated in blue. Black points are the in-situ AFT samples of Kohn et al. (1984) and Bermúdez et al. (chapters 4 and 5 in this work). Names of major fault systems indicated in legend.

6.2.2 Relief

The relief of the Venezuelan Andes rises very rapidly (within 50 km) from sea level at Lake Maracaibo to the north of the belt and in the Barinas basin to the south, to close to 5,000 meters at Pico Bolívar in the Sierra Nevada de Mérida (Fig. 6.2). The central Sierra Nevada de Mérida and Sierra la Culata ranges count 14 and 54 peaks whose elevations surpass 4,300 meters, respectively, with the Sierra Nevada containing the 3 highest peaks in Venezuela. These highest parts of the Venezuelan Andes (mean elevation 3000-3200 m; Bermúdez et al. chapter 4 in this work) have been glaciated during the Quaternary; Last Glacial Maximum moraines occur at 3400-3600 m elevation (Schubert, 1984) and older moraines have been identified at elevations several 100 m lower. The mean elevation of the range is significantly lower outside of the central Mérida Andes and varies between 1160 and 1695 m for the tectonic blocks recognised to the southwest and northeast (Bermúdez et al. chapter 4 in this work).

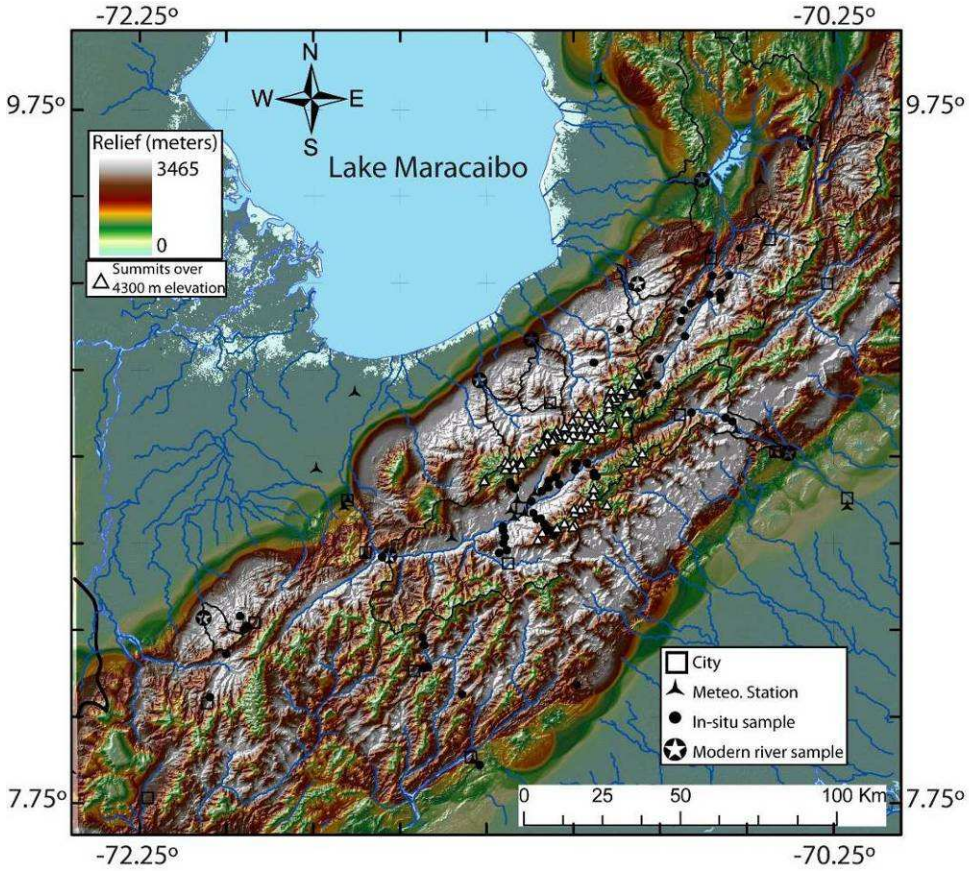

Fig. 6.2. 10-km radius relief across the Venezuelan Andes, draped over shaded relief image of topography. Peaks over 4300 m elevation in the central part of the range are indicated by triangles. Mean relief for each analyzed catchment is summarized in Table 6.2.

The relief of the Venezuelan Andes is shown in Figure 6.2; relief was calculated as the maximum elevation difference within a 10-km radius for every pixel in the digital elevation model (e.g., Montgomery and Brandon, 2002). The highest relief values (up to nearly 3500 m) are found along the central Chama River valley, which follows the Boconó Fault, and on both the northwestern and southeastern flanks of the orogen. Relief is lower both in the high central ranges (Sierra Nevada and Sierra la Culata), due to the presence of low-relief glacial erosion surfaces at high elevations, and in the tectonic blocks making up the northeastern and southwestern ends of the range.

6.2.3 Seismicity

Most of the historical and instrumental seismicity in the Venezuelan Andes is aligned with the main lineation of the Boconó fault system, while smaller events are scattered within a band several tens of kilometers wide adjacent to this fault zone, indicating that many of its branches are also active faults (Fig. 6.3A). Most of the seismicity occurs along the main trace of the fault at an average depth about 15 km. The depths tend to increase for the biggest events to the northwest (Lake Maracaibo basin) and southeast (Barinas basin) of the surface trace of the Boconó fault, reaching depths that can exceed 40 km. A seismic zone of intermediate depth (~160 km) occurs towards the southwestern boundary of the Venezuelan Andes and continuous below the Eastern Cordillera of Colombia. This significant concentration of events is known as the Bucaramanga seismic nest (Schneider et al, 1987). More scattered, but relatively large magnitude (several magnitudes >5), earthquakes are associated with the north-south oriented Icotea, Valera and Burbusay fault systems to the north of the Venezuelan Andes.

Focal mechanisms suggest predominantly right-lateral faulting along the Boconó fault, left-lateral faulting along the north-south trending faults to the north of the Venezuelan Andes, and compression along the northwest and southeast foreland fold-and-thrust belts (Colmenares and Zoback, 2003; Corredor, 2003; Cortés and Angelier, 2005). These focal mechanisms indicate compressional stress oriented approximately WNW-ESE across the central Venezuelan Andes, evolving toward a strike-slip regime with NW-SE directed compression axis to the northeast.

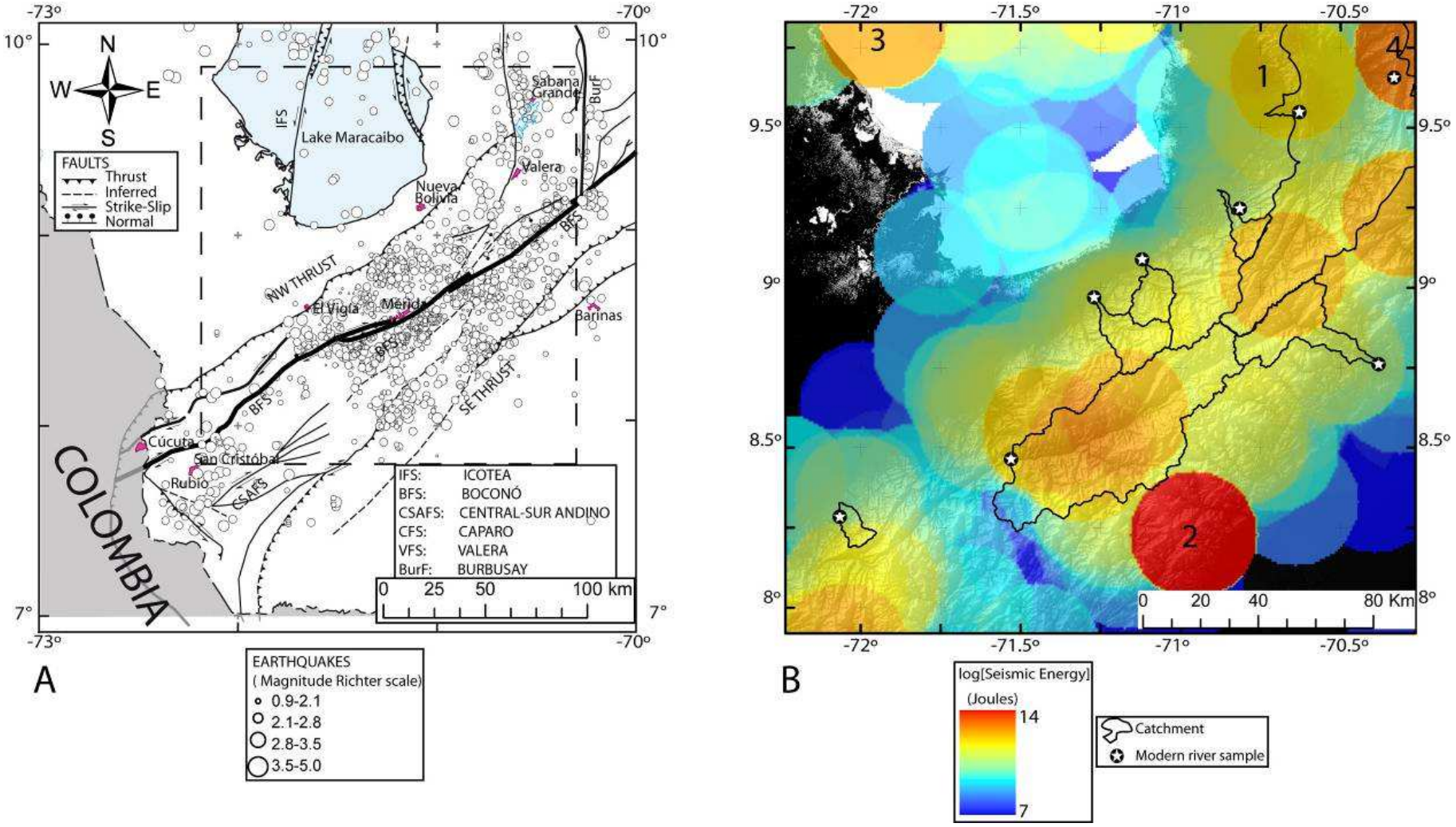

Fig. 6.3. A) Major active faults systems (modified from Audemard et al. 2000) and seimsicity database compiled for the period 1990-2009 from digital libraries at Universidad de Los Andes (http://lgula.ciens.ula.ve/) and FUNVISIS (http://www.funvisis.gob.ve). B) Cumulated seismic energy released, calculated from the earthquake database. Individual earthquakes with magnitude >5 occurring outside the Venezuelan Andes are indicated (1: 1993/12/31, 70.70 W / 9.65 N, mb=5.4; 2: 2001/12/21, 70.96 W / 8.17 N, Mw = 5.6; 3: 2006/01/03, 71.92 W /9.89 N, Mw = 5.0; 4: 2006/08/04, 70.65 W / 9.97 N, Mw = 5.2) Table 6.2 summarizes the mean cumulated seismic energy released for each analyzed catchment.

In order to quantify the effects of seismicity across the Venezuelan Andes, we compiled the seismicity record over a twenty year period (from 1990 to March 2009) using data available from the digital library of the Geophysics Laboratory of Universidad de Los Andes, Mérida (http://lgula.ciens.ula.ve/) and the Venezuelan Foundation for Seismological Investigation (FUNVISIS) website (www.funvisis.gob.ve). The data were filtered using two criteria: 1) epicenters of the earthquakes located between latitudes 72.25°W - 70.25°W and longitudes 7.75°N - 10.00°N, and 2) only data with local magnitudes M_l reported were considered. Figure 6.3A shows a summary of earthquakes that occurred in the Venezuelan Andes during the last twenty tears. We calculated the released seismic energy (*Se*) from the local magnitudes using the classical expression (Gutenberg and Richter, 1954):

$$\log(Se) = 1.5M_l + 4.8 \tag{6.1}$$

Released seismic energy values were cumulated within circles with radius of 25 km around the epicenter of each earthquake. Figure 6.3B shows the resulting map of seismic energy obtained from this procedure. The rate of seismic energy release is highest in the central Andes (Chama catchment) and decreases toward the northeast and southwest. However, the calculated pattern is strongly affected by several Mw > 5 earthquakes that occurred outside of the Venezuelan Andes themselves, notably a series of strike-slip earthquakes that occurred on the Burbusay, Valera and Icotea fault systems

6.2.4 Precipitation pattern

The topography of the Venezuelan Andes results in a well-developed orographic precipitation pattern. Moist air masses from equatorial South America in the south need to rise in order to cross the Venezuelan Andes to the north, causing heavy precipitation on the southern flank of this mountain belt whereas the centre and northern flank of the belt are semi-arid. It has been proposed that the present precipitation/drainage system of the Venezuelan Andes started developing at about 8 Ma as a response to tectonically driven surface uplift (Hoorn et al. 1995; Bermúdez et al. chapter 5 in this work). We have used precipitation data from 30 meteorological stations in and around the Venezuelan Andes to elaborate a mean annual precipitation map for the past twenty years. The database was compiled from different sources: 1) NOAA World Temperature – Precipitation dataset

(http://bonnet19.cs.qc.edu:7778/pls/rschdata/ rd_start.main), 2) Stansell et al. (2006), 3) Naranjo and Duque (2004), 4) Bio-climatic net stations of Mérida (http://www.cecalc.ula.ve/redbc/colecciones/colecciones_datos.html), and 5) Data provided by Gerard Kopp (pers. comm.) of the Institute for Meteorology and Climate Research, University of Karlsruhe (Germany) for the Mérida Atmospheric Research Station at Pico Espejo (MARS). The precipitation map shown in Figure 6.4 was compiled from these data using nearest-neighbor interpolation (Arya et al. 1998) and highlights the strong orographic gradient between the northern and southern flanks of the Venezuelan Andes, with precipitation ranging from 1.6 to 3.4 m/yr on the southern flank as opposed to 0.09-1.1 m/yr on the northern flank. A particular feature is the arid patch that expands into the orogen between El Vigía and Mérida: hot dry winds from the north exploit the Chama River valley to penetrate deep into the orogen, generating a unique arid climate in this area (Fig. 6.4).

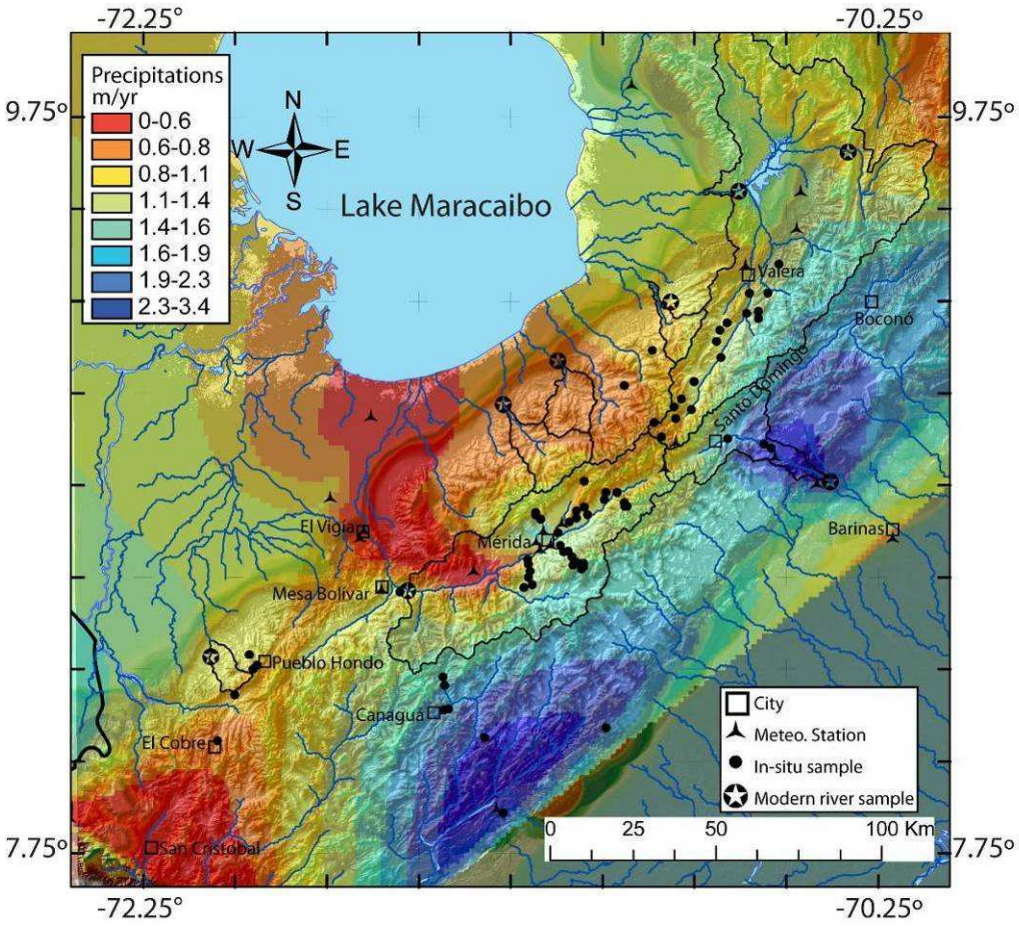

Fig. 6.4. Mean precipitation pattern (m/yr) for the last 20 years across the Venezuelan Andes, compiled from various databases (see text for details), overlain on shaded relief image of topography

6.3 Detrital apatite fission-track thermochronology

Thermochronology of detrital grains provides information on cooling rates and exhumation processes in convergent mountain belts (e.g., Garver et al. 1999; Carter, 2007). Detrital thermochronology provides a complimentary record of the erosional history of a mountain belt, with respect to local cooling paths deduced from *in-situ* samples within the orogen (Brandon and Vance, 1992). Modern river sediments integrate the recent exhumation history of the entire drainage basin and provide a spatially integrated view of exhumation, which may be the only way to characterise exhumation patterns for inaccessible areas. In addition, when source-area age signal are known in some detail, thermochronology of detrital material provides information on sediment provenance (Garver et al. 1999; Bernet and Spiegel, 2004).

6.3.1. Data collection and discrimination of age components

We collected samples for detrital AFT thermochronology from eight river catchments draining the Venezuelan Andes. The Coloncito, Chama, Tucaní, San Pedro, Agua Viva, Mimbós and Chejendé rivers drain the northern flank, and the Santo Domingo River the southern flank of this mountain belt (Figs. 6.1, 6.5). Samples were collected within active river channel bars at all sites and prepared using standard techniques (cf. Bermúdez et al. chapter 4 in this work for details). We aimed to count at least 100 grains for each sample in order to attain statistically significant AFT age populations; this objective was attained for 5 out of 8 samples (Table 6.1), the 3 others having >50 single-grain ages.

Because detrital thermochronology samples are derived from source areas with variable bedrock ages, they may contain several single-grain age populations (Brandon and Vance, 1992; Garver et al. 1999; Bernet and Spiegel, 2004). Different methods have been proposed to decompose a fission-track grain age distribution into its age components, the most popular of which is a binomial peak-fitting algorithm (Binomfit) developed by Brandon (1992, 1996). However, the binomial peak-fitting method is not ideally suited to decompose detrital AFT age distributions that include young ages, as the uranium content (and therefore the track counts on which the fit is based) are relatively low (e.g., Garver et al. 1999). Here, we employ a recently developed Poissonian peak-fitting method (the *p*-partition algorithm of Bermúdez-Cella, 2008; cf. appendix for a brief overview) to decompose the grain-age distribution of our modern river samples. Results were compared with Binomfit as well as a Bayesian method for

the age-mixture modeling using Markov Chain Monte Carlo (Jasra et al. 2006) (see appendix I).

Resulting age peaks are reported in Table 6.1 and Figure 6.5. In most samples, three age components were detected: 1) a 3-7 Ma, Late Miocene – Pliocene component, 2) a 7-13 Ma, Middle-Late Miocene component and 3) a 16-28 Ma Late Oligocene – Early Miocene component. In the Chama river sample, which drains the largest source area, a small (2%) fourth component was detected at 41 Ma (Middle Eocene), whereas in the smaller San Pedro catchment sample, the Oligocene-Miocene peak is divided into two subordinate components. The youngest age component is also the largest age population (31 up to 56%) in most river samples, with exception of the Chama and Tucaní river samples, in which the second component is largest.

Sample	River	Longitude	Latitude	Elevation (m)	No. of grains	Central Age (Ma) ± SE	$P_1 \pm SE_1$	σ_1	N_1	$P_2 \pm SE_2$	σ_2	N_2	$P_3 \pm SE_3$	σ_3	N_3	$P_4 \pm SE_4$	σ_4	N_4
0206	Santo Domingo	-70.3800	8.7600	244	100	7.8 ± 0.5	5.2 ± 0.3	2.0	56	11.8 ± 0.9	2.6	37	28.0 ± 4.6	7.5	7	—		—
0507	Chejendé	-70.3310	9.6556	575	69	8.4 ± 0.4	7.3 ± 0.5	2.7	34	12.0 ± 1.7	2.8	21	28.3 ± 7.5	8.2	14	—		—
0807	Agua Viva	-70.6285	9.5489	102	100	11.1 ± 0.8	4.6 ± 0.4	1.7	36	9.5 ± 0.6	2.3	33	21.1 ± 0.9	4.7	31	—		—
1307	Mimbós	-70.8140	9.2473	353	55	5.6 ± 0.4	4.1 ± 0.4	1.5	27	8.3 ± 0.8	1.1	21	22.0 ± 8.3	5.6	7	—		—
1607	San Pedro	-71.1202	9.0880	187	68	6.4 ± 0.5	3.6 ± 0.4	1.2	28	8.1 ± 0.8	1.6	26	14.5 ± 2.2	2.4	12	27.7 ± 12.1	3.9	2
1707	Tucaní	-71.2702	8.9697	181	105	7.0 ± 0.4	3.4 ± 0.3	1.0	34	8.0 ± 0.5	1.1	51	19.5 ± 2.3	5.5	20	—		—
1907	Chama	-71.5294	8.4638	408	105	6.9 ± 0.4	2.9 ± 0.3	1.3	33	8.2 ± 0.4	1.5	49	17.8 ± 2.3	4.1	21	41.4 ± 19.2	8.3	2
2607	Coloncito	-72.0653	8.2843	438	104	5.0 ± 0.3	3.2 ± 0.3	1.1	49	7.3 ± 0.5	1.3	42	18.2 ± 3.7	5.3	13	—		—

Table 6.1. Detrital apatite fission-track data from modern river samples in the Venezuelan Andes.

Note: Fission-track age is given as central age for each population P_i. SE is the standard fission-track error (Galbraith, 2005), σ_i corresponds to the standard deviation, and N_i to the number of grains that form the population *i*. Samples were counted with a BH-2 Olympus microscope at 1250x magnification (dry objective), using a zeta value of 288.7 ± 5.2 (M. Bermúdez) and the IRMM 540 uranium glass standard (15 ppm U). Populations were discriminated with the p-partition algorithm (Bermúdez-Cella, 2008; see text for discussion and appendix section for details on method).

Access to the southern flank of the Venezuelan Andes is extremely difficult and our dataset contains only one river draining to the south; the Santo Domingo River sample shows a similar grain-age distribution and peak age as the rivers that drain to the north (Table 6.1, Figure 6.5). The Chejendé River and Agua Viva River samples were collected above and below the Agua Viva reservoir respectively (Fig.6.1), in the Valera tectonic block to the northeast of the main mountain belt. All three peaks of the Agua Viva River sample are younger than the corresponding peak ages in the Chejendé River and the size of the age peaks in the Agua Viva sample are more even than in the Chejendé River sample (Table 6.1, Figure 6.5), suggesting mixing in of both younger and older grains.

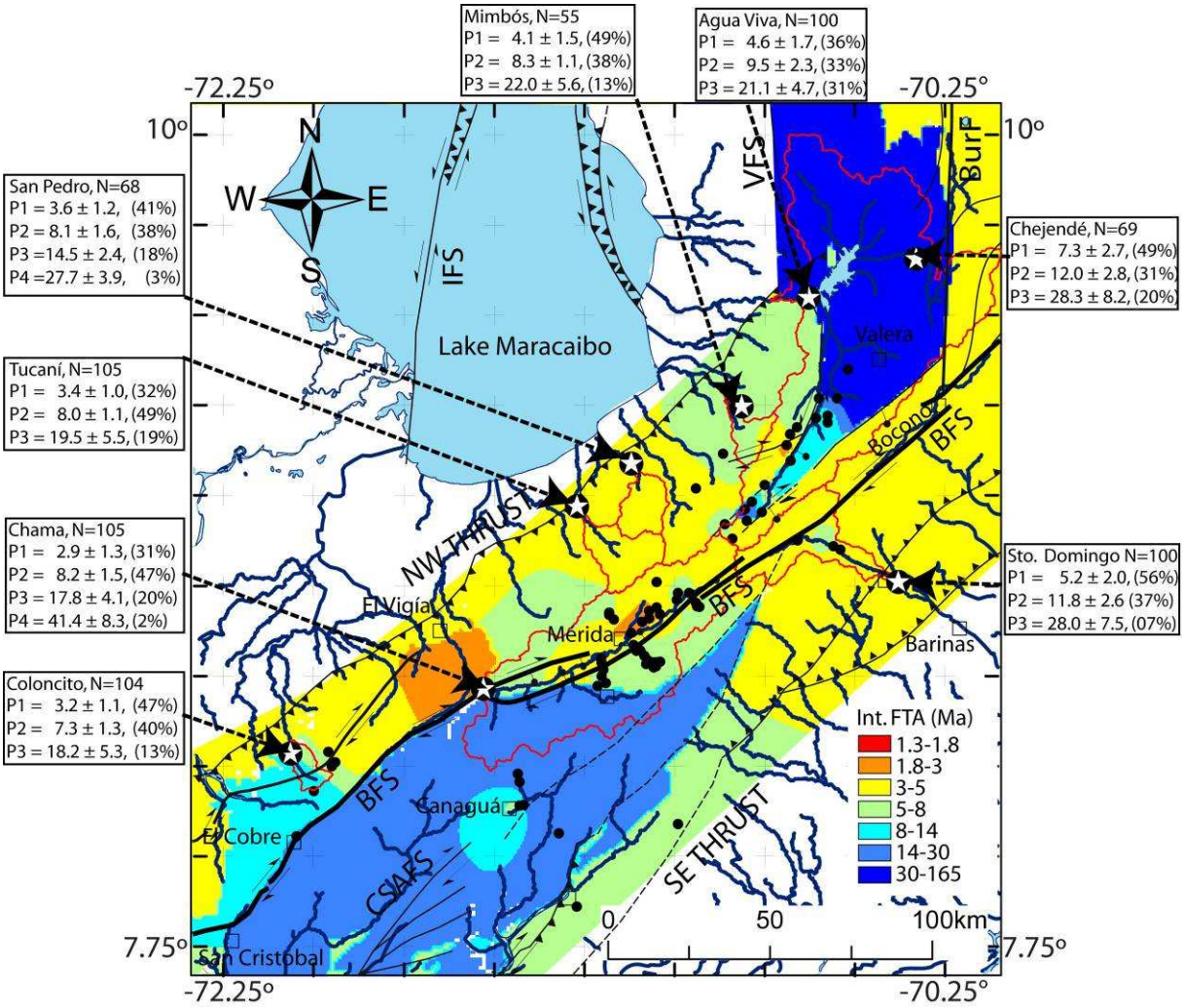

Fig. 6.5. Interpolated in-situ fission-track ages map and detrital apatite fission-track central ages for each catchment. The different populations were discriminated using the p-partition method (see Appendix). The errors reported in this figure correspond to standard deviation (σ) of the fission-track age, for each population. The quantities in the parenthesis correspond to percentage of grains that integrate each population. See Table 6.2 for more information.

A comparison of these results with predictions from other peak-fitting methods (appendix figures) suggests that our Poissonian peak-fitting method tends to subdivide the AFT grain-age distributions more finely, with the other methods predicting only 2 peaks for most samples. The Binomial peak-fitting method tends to concur with ours with respect to the younger age-peaks but generally does not discriminate the oldest (often minor) peak. The Bayesian mixture modeling approach, in contrast, has difficulties in detecting the youngest age peak. These somewhat diverging results underline that fitting age peaks to a single-age age spectrum remains a somewhat arbitrary exercise and that age components should not be taken as absolute entities.

6.3.2 Comparison of detrital and bedrock apatite FT ages

Before using the detrital AFT grain-age distributions of the modern river samples to assess potential controls on exhumation patterns throughout the Venezuelan Andes, we need to answer the question to what degree the detrital age patterns reflect source-area ages. Previous studies (Bernet and Spiegel, 2004; Ruhl and Hodges, 2005; Brewer et al. 2006) have shown that detrital thermochronology faithfully records source-area exhumation in a number of different settings. Here, we compare our detrital AFT grain-age distributions to previously published bedrock AFT ages of the Venezuelan Andes (Kohn et al. 1984; Bermúdez et al. submitted a, b). Bermúdez et al. (chapter 4 in this work) proposed a map of bedrock AFT ages for the Venezuelan Andes (Figure 6.5), constructed by interpolating the ages within different tectonic blocks using a spline with barriers method (Terzopoulos, 1988) and considering the major fault systems defining the blocks as barriers. Note, however, that the distribution of bedrock AFT ages along the Venezuelan Andes is still relatively limited, the database consisting of only 68 samples. Figure 6.6 compares the probability-density function (PDF) of selected detrital samples with that derived from the interpolated map of bedrock ages in their respective catchments. Both the detrital grain-age distributions and the modelled bedrock age distributions were decomposed into age populations using the p-partition method in order to compare the peak ages. We also show cumulative age-distributions (CDF) and calculate the Kolmogorov-Smirnov (KS) statistic between the detrital and model bedrock CDF (Conover, 1980). Note that we do not weight the model bedrock distribution according to AFT age or inferred exhumation rate, i.e. we do not suppose *a-priori* that short-term erosion rates reflect long-term denudation rates. We also do not take potential variations in apatite content for different lithologies making up the catchments into account.

The quality of the comparison between detrital and bedrock data strongly depends on the density of available bedrock ages, as shown by the four examples of the Chama, Agua Viva-Chejendé, Santo Domingo and Coloncito catchments. The Chama River (Fig. 6.6A) is the largest catchment sampled in this study. Interpolation of the 32 available bedrock AFT ages, including two age-elevation profiles (Kohn et al. 1984; Bermúdez et al. submitted, chapter 5 in this work), resulted in 1857 modelled bedrock AFT ages within the river catchment. Decomposition of the observed grain age distribution with the *p*-partition method provides four AFT age populations for the detrital sample (2.9 ± 0.3, 8.2 ± 0.4, 17.8 ± 2.3, and 41.4 ± 19.2 Ma) and three for the modelled *in-situ* AFT ages (3.0 ± 0.6, 5.7 ± 0.8 and 18.2 ± 1.7 Ma). The three youngest populations are very similar. The fourth detrital population of 41.4 Ma was not detected in the modeled bedrock ages, probably because of the limited and fairly localized dataset of bedrock AFT ages in the catchment. The comparison between CDF confirms these observations; the KS statistic of 0.26 (for a p-value of 0.5; Conover, 1980) indicates a good fit between the two CDF.

Figure 6.6B shows the comparison for the Agua Viva and Chejendé detrital samples. The data of both samples were combined and the p-partition algorithm was applied on the combined sample (169 grains) to distinguish three age peaks of 6.0 ± 0.3, 12.6 ± 0.8 and 22.2 ± 0.9 Ma. The 17 available bedrock AFT ages were used to generate 3015 modelled AFT age for the catchment. Using the p-partition method, three age populations of 5.3 ± 1.6, 8.9 ± 3.4 and 36.3 ± 3.8 Ma can be obtained from the modelled data. The two youngest age peaks for the modelled bedrock age distribution are within error of the detrital age peaks. The third age population is significantly older in the modelled bedrock age distribution than in the detrital distribution, but the detrital PDF shows that the sample may in fact contain a population older than 25 Ma. However, the comparison between CDF for this sample indicate that only the two first component of age are reproduced by the in-situ data, the KS value of 0.62 indicates large differences between the two CDF. In particular, our modelled bedrock age map predicts ages >30 Ma for a very large part of the catchment lying within the Valera block (Fig. 6.5), extrapolated from only a few ages in the south. Clearly, more data are needed toward the north of this block.

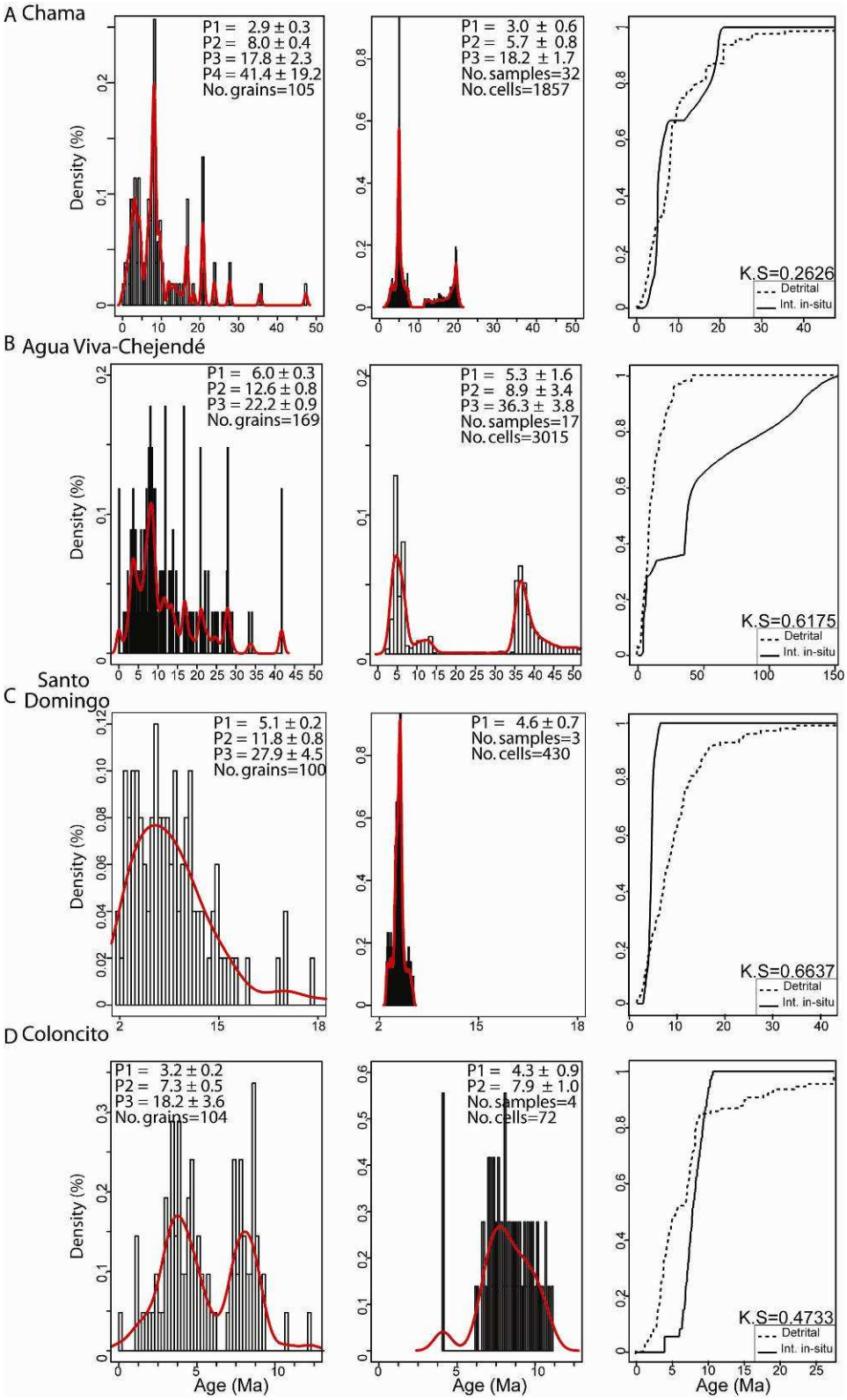

Fig. 6.6. Comparison between detrital AFT age distributions (left plots) and interpolated bedrock fission-track data (central plots) for A) Chama, B) Agua Viva-Chejendé, C) Santo Domingo and D) Coloncito rivers (cf. location on Fig. 5). Age distributions are shown as histograms and probability-density functions (PDF). Age components and standard deviations, as determined by the p-partition algorithm are indicated. The right plots show cumulative probability-density functions (CDF) for detrital and bedrock fission-track ages. The KS-value indicates the degree of fit between the distribution given by detrital (dotted line) and bedrock data. If KS $\leq$ 0.5 the null hypothesis of similarity between detrital and in-situ fission-track age distributions can be accepted.

The results for the Santo Domingo and Coloncito catchments are shown in Figures 6.6C and 6.6D respectively. For the Santo Domingo River, 100 detrital AFT ages were compared to 430 modelled bedrock AFT ages for the catchment. However, the 430 modelled ages are based on only three bedrock AFT samples, which is obviously insufficient for reproducing a good fit between the detrital and modelled bedrock AFT ages (KS = 0.66). Only the youngest age population of the detrital sample was detected with the modelled bedrock AFT ages. For the Coloncito River, only the two youngest age populations were found in the bedrock data, which is reflected in an acceptable fit (KS = 0.47) between the CDF. For both drainages, much more bedrock AFT data would be needed to produce a good fit. Nonetheless, these examples show that a comparison is feasible and underlines the coupling between detrital and bedrock AFT ages, indicating that a sample of modern river sediment reproduces the ages within the catchment. As a consequence, we can use the detrital AFT ages to infer exhumation rates in areas where none or only very few bedrock AFT ages exist, as for example in the smaller catchments of the Tucaní, Mimbós, and San Pedro rivers.

6.3.3 Implications for sediment provenance

The different age populations can be compared to the spatial distribution of bedrock AFT ages (Fig. 6.5) to determine apatite provenance (Hurford and Carter, 1991; Bernet and Spiegel, 2004; Carter, 2007). The youngest group of bedrock ages, between 1.3 and 3 Ma, is found only in the Chama River drainage. This corresponds to the youngest AFT age component of 2.9 Ma detected in the Chama River sample. A probable source for this young age component is the El Carmen block, located within two branches of the Boconó fault system and rapidly uplifted and exhumed during Pliocene times (Kohn et al. 1984; Bermúdez et al. submitted, chapter 5 in this work). A second possible source terrain could be the Mesa Bolívar granite to the south of the town of El Vigía (Figures 6.1, 6.5) that is characterised by AFT ages of ~2.5 Ma (Kohn et al. 1984; Bermúdez et al. chapter 5 in this work).

Early Pliocene AFT ages of 3-5 Ma, as well as late Miocene ages of 5-8 Ma are widespread on both flanks of the mountain belt, in the Escalante, Sierra Nevada and Sierra La Culata blocks. These age groups have been detected in the Coloncito, Tucaní, San Pedro, Mimbós, Agua Viva-Chejendé and Santo Domingo catchments, which partly or completely drain these blocks.

Detrital age populations between 8-16 Ma appear in the Tucaní, San Pedro, Mimbós, Agua Viva-Chejendé and Santo Domingo River samples. The most likely source for this AFT age population appears to be the Valera granite, exposed along the southernmost branch of the Valera fault system (Figs. 6.1 and 6.5). That this age population also appears in small north-flowing river that do not drain the Valera granite (Tucaní, San Pedro and Mimbós rivers), has three possible explanations: 1) the 8-16 Ma detrital AFT ages are related to sediment recycling from inverted foreland basin sediments, as observed in detrital deposits elsewhere (e.g., van der Beek et al. 2006). 2) These AFT ages come from local sources in the Sierra La Culata on the northern flank of the Venezuelan Andes (for instance, remnants of the Mesozoic sedimentary cover, Figure 6.1) that have not been sampled for *in-situ* AFT thermochronology. 3) The interpolated map of bedrock ages is based on sparse data in the north-central Venezuelan Andes (Figure 6.5). This uncertainty could also explain why this AFT age population appears in the Santo Domingo River sample and would suggest more widespread occurrence of Middle Miocene AFT ages in this part of the Venezuelan Andes. Middle Miocene ages have also been locally encountered in the Escalante and Caparo blocks (in particular in the Canaguá area (Figs. 6.1 and 6.5) and could be the sources for the P2 and P3 peaks encountered in the Chama and Coloncito river samples.

The oldest detrital AFT populations of 21-41 Ma can be linked to two slowly exhuming source areas where such bedrock ages have been encountered; the Caparo Block for the Chama river sample, and the Valera Block for the Mimbós, Agua Viva, Chejendé and Santo Domingo river samples.

6.4 Predicted exhumation and erosion patterns

6.4.1 Long-term exhumation rates

The detrital age distributions can also be used to provide predictions of long-term catchment-averaged exhumation rates, which can be compared to modeled short-term erosion rates as well as potential control parameters. We employ a simple 1-D steady-state thermal model developed by Brandon et al. (1998; see also Ehlers, 2005; Reiners and Brandon, 2006) to convert detrital AFT ages to exhumation rates. As this model does not take either transient thermal effects (e.g. Rahl et al. 2007) or the 3-D effects of topography (e.g., Whipp et al. in

press) into account, predicted exhumation rates should be considered first-order estimates. Parameters used for these calculations are a surface temperature of 25°C, layer thickness to constant temperature of 40 km, thermal diffusivity of 25 km^2 My^{-1}, heat production of 1 °C My^{-1} and a temperature at the base of the layer of 650 °C, implying a pre-exhumation surface geothermal gradient of 16.5 °C/km (Bermúdez et al. submitted a). The model iteratively calculates an exhumation rate ($\dot{\varepsilon}$), cooling rate, closure temperature (T_c) and -depth (z_c) from the AFT ages, using the Dodson (1973) equation to solve for the closure temperature of the thermochronometer (in this case: AFT) and a steady-state thermal structure to relate this to the closure depth. The predicted cooling age is then re-estimated as $\frac{z_c}{\dot{\varepsilon}}$.

For each detrital sample, we use the above procedure to translate single-grain detrital ages into exhumation rates, which we then combine to predict a catchment-averaged exhumation rate. In order to include the expected effect that rapidly exhuming areas of a catchment will contribute more sediment (and thus more datable apatite grains), we calculate the long-term catchment-averaged exhumation rate ($\dot{\varepsilon}_T$), as the mean of the single-grain exhumation rates, weighted by the single-grain ages:

$$\dot{\varepsilon}_T = \frac{\sum_{j=1}^{N} [\dot{\varepsilon} \times age]_j}{\sum_{j=1}^{N} (age)_j} \tag{6.2}$$

where N is the total number of grains in the sample, $\dot{\varepsilon}$ is the calculated single-grain long-term exhumation rate and *age* is the single-grain FT age. Results are shown in Table 6.2. The smaller north-draining catchments of the Tucaní, Mimbós, San Pedro and Coloncito rivers have relatively high long-term erosion rates of ~0.5 km/My, followed by the Chama and Santo Domingo River catchments with about 0.45 km/My, and the Agua Viva-Chejendé River catchment with a relatively slow long-term erosion rate of <0.4 km/My.

6.4.2 Short-term erosion patterns

The above long-term exhumation rates can be compared to model predictions of the intensity of short-term erosion using the erosion-index approach of Finlayson et al. (2002). The erosion-index can be calculated in different ways as a function of stream power, which is the rate of potential energy expenditure by flowing water and has been used extensively in studies

of erosion, sediment transport, and geomorphology as a measure of the erosive power of rivers and streams (Wilson and Gallant, 2000). The analysis is based on a prediction of bedrock incision rate as a function of stream power (Finlayson et al. 2002; Tucker and Whipple, 2002):

$$\dot{e} = k \ A_s^{\,m} S^n \tag{6.3}$$

where $\dot{e}$ is the local incision rate, A_s is upstream drainage area (used as a proxy of discharge), S is local slope, and m, n and k are constants. The parameter k is mainly related to bedrock erodibility. Considering the similar geologic and geographic conditions of the studied catchments and the lack of information on relative erodibility of the different lithologies outcropping in the Venezuelan Andes, we take k to be uniform throughout the study area. Setting k to unity, the predicted $\dot{e}$ is the erosion index in the case of uniform precipitation.

With the purpose of incorporating spatial variations in precipitation P and studying their influence on the erosion index we also applied the following prediction for $\dot{e}$:

$$\dot{e}_p = \sum \left(A_p P\right)^m S^n \tag{6.4}$$

where A_p is the pixel area and the summation sign implies summing the precipitation over each pixel within the catchment. We term $\dot{e}_p$ the precipitation erosion index.

Different m and n values can be employed in equations (6.3) and (6.4), depending on the control of river incision rates by total stream power, stream power per unit channel width or shear stress (Finlayson et al. 2002; Tucker and Whipple, 2002): in the case where incision is controlled by total stream power (TSP), m=1, n=1; for incision controlled by stream power per unit channel width (USP), $m = \frac{1}{2}$, n=1; if incision is controlled by fluvial shear stress (SSP), $m = \frac{1}{3}$, $n = \frac{2}{3}$.

Normalized erosion index maps for the Venezuelan Andes, predicted by the six possible models (TSP, USP, SSP, uniform or spatially variable precipitation) are shown in Figure 6.7. These maps emphasize distinct zones of high erosion potential associated with the steepest terrain and largest discharge of the main rivers. If uniform precipitation is considered, the most important zones of high erosion potential of the Venezuelan Andes are located in the central Chama and Santo Domingo valleys, with secondary regions of high erosion potential

on both the northern and southern flanks. Consequently, under this assumption the Chama and Santo Domingo rivers, together with the small catchments (Tucaní, San Pedro, Mimbós) on the northwest flank of the orogen, have high relative erosion indexes (whether considering TSP, USP or SSP) with the peripheral Coloncito and Agua Viva-Chejendé river catchments showing lower erosion indexes (Table 6.2).

When the precipitation data are incorporated in the erosion index predictions, the results differ significantly due to the strong orographic effect (Figure 6.4), which would imply that the southeast flank of the orogen should erode more rapidly than the northwest (Figure 6.7). In particular, the predicted high relative erosion index in the central Chama valley disappears when precipitation is taken into account, due to the pronounced aridity of this valley. Consequently, the southeast-draining Santo Domingo catchment is predicted to have the highest relative erosion index (whether considering TSP, USP or SSP), followed by the Chama River catchment. Incorporating spatially variable precipitation lowers the relative erosion index values for the small north-western Tucaní, San Pedro and Mimbós catchments, which become indistinguishable from those for the peripheral Agua Viva-Chejendé and Coloncito catchments (Table 6.2).

Catchment	$\dot{\varepsilon}_T$ (km/My)	P (m/y)	Seismic Energy[1] ($\times 10^{12}$ J)	Seismic Energy[2] (J/m^2)	Relief (m)	TSP	USP	SSP	TSP Prec	USP Prec	SSP Prec
Santo Domingo	0.44	1.91	1.21	381	1285	0.75	0.77	0.86	0.70	0.70	0.76
Agua Viva-Chejendé	0.37	1.11	1.72	506	1058	0.72	0.68	0.74	0.66	0.59	0.62
Mimbós	0.50	0.90	1.43	482	1663	0.73	0.75	0.84	0.65	0.65	0.70
San Pedro	0.50	0.77	0.65	422	1861	0.73	0.78	0.88	0.62	0.64	0.69
Tucaní	0.47	0.80	1.00	632	1591	0.75	0.81	0.91	0.63	0.66	0.72
Chama	0.44	1.15	2.12	1786	1386	0.76	0.79	0.88	0.67	0.66	0.71
Coloncito	0.53	0.98	0.49	154	1817	0.72	0.73	0.81	0.65	0.62	0.68

Table 6.2. Measures of long-term exhumation and potential control parameters for each catchment.

Note: The Agua Viva-Chejendé catchment results were combined for this analysis. $\dot{\varepsilon}_T$ is catchment-averaged long-term exhumation rate determined from detrital AFT data (cf. Section 4.1). P is mean annual precipitation for the past twenty years from NOAA World Temperature and Precipitation Dataset (http://bonnet19.cs.qc.edu:7778/pls/rschdata/rd_start.main), Stansell et al. (2006), Naranjo and Duque, (2004), bio-climatic net stations of Mérida (www.cecalc.ula.ve/redbc/colecciones/colecciones_datos.html) and data provided by Gerard Kopp (pers. comm.). Seismic energy represents the cumulative seismic energy released during the last 19 years after data from Universidad de Los Andes (http://lgula.ciens.ula.ve/) and FUNVISIS (www.funvisis.gob.ve) and estimated for each catchment (1) from the map of cumulated seismic energy release within 25-km radius windows around each earthquake (Figure 6.3B) and (2) by summing the seismic energy released by earthquakes occurring within each catchment and dividing by catchment area. Relief was calculated using a 10 km radius after Montgomery and Brandon (2002). The Total Stream Power (TSP), Shear Stress (SSP) and Uniform Stream Power (USP) are used as predictors of short-term erosion rates (Wilson and Gallant, 2000; Finlayson et al. 2002; Tucker and Whipple, 2002) and calculated as explained in Section 6.4.2 assuming spatially constant precipitation. TSPprec, SSPprec, and USPprec are the same erosion indexes but taking spatially variable precipitation into account. Erosion indexes are given as log-normalised values.

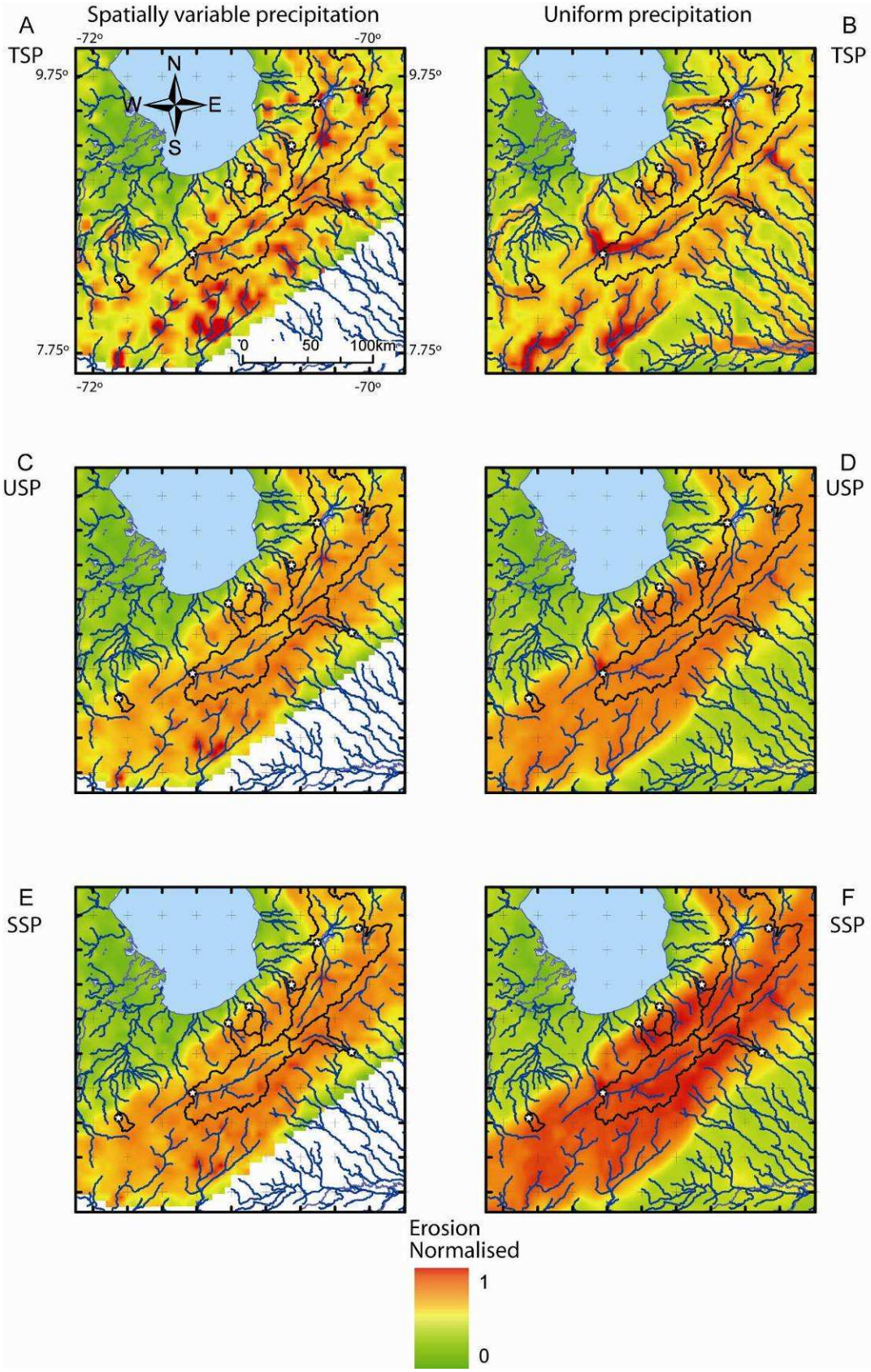

Fig. 6.7. Normalized stream power index map across the Venezuelan Andes. Left columns (A, C and E) take spatially variable precipitation into account (stream power calculated following equation 3); right columns (B, D, F) assume spatially constant precipitation (stream power calculated following equation 2): A, B) Total Stream Power (TSP; $m = n = 1$ in equations 6.2, 6.3); C, D) Unit Stream Power (USP; $m = 0.5$; $n = 1$); E, F) Shear Stress (SSP; $m = 0.33$; $n = 0.67$).

6.5 Discussion

6.5.1 Relations between tectonics, climate and erosion in the VA

Whether long-term exhumation rates in mountain belts are controlled to a first degree by tectonic or climatic factors remains a matter of debate. Some authors have argued for strong coupling between long-term exhumation and precipitation, for instance for the Central Andes (Montgomery et al. 2001) or the Washington Cascades (Reiners et al. 2003), while others argued for decoupling between long-term exhumation and precipitation, such as in the central Himalaya (Burbank et al. 2003) or in the European Alps (Vernon et al. 2009). Recently, Mora et al. (2009) have argued for coupling between precipitation and exhumation rates in the Eastern Cordillera of Colombia, which is contiguous to the Venezuelan Andes. Are long-term exhumation rates in the Venezuelan Andes controlled by present-day precipitation rates? If they are uncorrelated with precipitation, what could be the controlling factor driving exhumation? The underlying question is, how strongly are tectonic and climatic processes coupled and on which timescales? Table 6.2 summarizes our observations on long-term exhumation, predicted relative short-term erosion and potential controlling factors for the eight studied catchments in the Venezuelan Andes. The challenge lies in comparing exhumation rates over several million years, derived from AFT ages, with present-day precipitation or seismicity data that was collected over the past 100 years in the best cases.

In order to gain insight into the potential controls on erosion and exhumation rates in the Venezuelan Andes, we have calculated Pearsonian correlation coefficients between each of the measures reported in Table 6.2. Table 6.3 summarizes the results of this analysis. Given that we compare all variables for 7 catchments, correlations are statistically significant (at a 95% confidence level) for a Pearson correlation coefficient ≥ 0.7.

Variable	$\dot{\varepsilon}_T$ (km/My)	P (m/y)	Seismic Energy[1] ($\times 10^{12}$ J)	Seismic Energy[2] (J/m^2)	Relief (m)	TSP	USP	SSP	TSP Prec	USP Prec	SSP Prec
$\dot{\varepsilon}_T$ (km/My)	1										
Precipitation (m/y)	-0.39	1									
Seismic Energy[1] ($\times 10^{12}$ J)	**-0.70**	0.26	1								
Seismic Energy[2] (J/m^2)	-0.32	0.01	**(0.76)**	1							
Relief (m)	**0.95**	-0.58	**-0.74**	-0.29	1						
TSP	-0.16	0.36	0.43	0.70	-0.21	1					
USP	0.38	-0.07	-0.10	0.39	0.40	**(0.78)**	1				
SSP	0.43	-0.10	-0.16	0.33	0.46	**(0.74)**	**(1.00)**	1			
TSP Prec	-0.46	**(0.94)**	0.48	0.19	-0.66	0.35	-0.18	-0.22	1		
USP Prec	0.17	0.54	0.04	0.21	0.05	**(0.79)**	**(0.75)**	**(0.75)**	0.43	1	
SSP Prec	0.31	0.48	-0.10	0.13	0.18	**(0.74)**	**(0.78)**	**(0.78)**	0.35	**(0.98)**	1

Table 6.3. Pearsonian correlation coefficients between measures of Table 6.2 for all catchments.
Note: All variables calculated as in Table 6.2. Values in bold represent statistically significant correlations at the 95% confidence level (according to a test for zero correlation based on t-statistics with n-2 degrees of freedom; Conover, 1980). Values shown in parentheses indicate trivial correlations, because the linear dependence of the two compared variables is expected.

Figure 6.8 shows how long-term exhumation rates in the Venezuelan Andes correlate with different potential control parameters (relief, seismic energy release, precipitation, present-day stream power). A first observation is the very strong positive correlation (r = 0.95) between long-term exhumation rates and relief, implying that the present-day relief of the Venezuelan Andes is adapted to the long-term exhumation rates. The correlation we find here is much stronger than that reported, for instance, in the European Alps (Wittmann et al. 2007; Vernon et al. 2009) or in the San Bernardino Mountains of California (Binnie et al. 2007). The reason for this is probably the comparably lower exhumation rates and relief values in the Venezuelan Andes, so that bedrock landsliding on threshold slopes, which tends to decouple relief and exhumation rates (Montgomery and Brandon, 2002) is less important with respect to these other mountain belts. In effect, a large proportion of slopes close to the threshold for landsliding is only encountered in the central Sierra Nevada and Sierra la Culata blocks of the Venezuelan Andes (Bermúdez et al. chapter 5 in this work).

In contrast, long-term exhumation rates appear to be decoupled from present-day precipitation rates; they appear even (weakly) negatively correlated with present-day precipitation (i.e. highest exhumation rates occur on the dry northwest flank of the orogen). Also, whereas short-term erosion indexes (i.e. TSP, SSP or USP) are only weakly correlated to long-term exhumation rates, the correlations become even weaker or negative when spatially variable precipitation rates are taken into account in the calculation of these measures (TSP Prec, SSP Prec or USP Prec). The lack of correlations suggests that the present-day precipitation pattern does not strongly control long-term exhumation rates in the Venezuelan Andes, in contrast to what has been inferred for the contiguous Eastern Cordillera of Colombie (Mora et al. 2009). Two caveats need, however, to be recalled before concluding from this data that climate and exhumation are decoupled in the Venezuelan Andes: first the relatively limited spatial extent of our sampled catchments, for which the wet southern flank is clearly under-represented and second the timescale problem already mentioned previously. Considering the first, it is clear that our dataset would benefit from inclusion of more remote south-flank catchments. As for the problem of comparing measurements on strongly varying timescales, whereas we obviously acknowledge that we cannot readily extrapolate the present-day precipitation measurements several million years in the past, we do note that (1) the Neogene sedimentary record of northern South America suggests that the topographic relief of the Venezuelan Andes and, therefore, its associated orographic imprint, has been in place since Late Miocene times (Hoorn et al. 1995; Diaz de Gamero, 1996); and (2) Quaternary glaciations, which may

strongly modify erosion patterns in some mountain belts (e.g., Burbank et al. 2003; Vernon et al. 2009) have been relatively limited in the Venezuelan Andes (Schubert, 1984; Stansell et al. 2006).

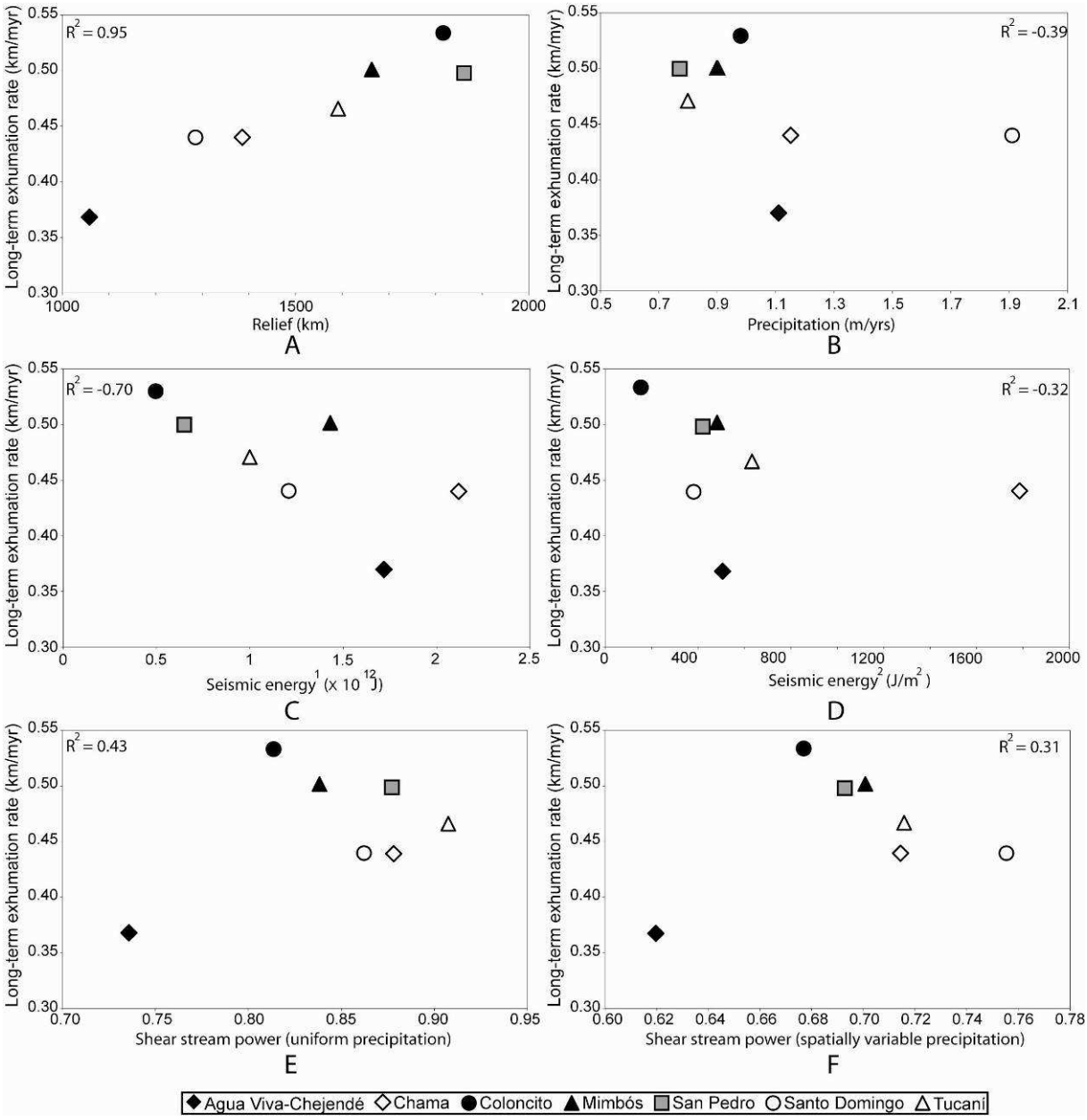

Fig. 6.8. Correlation plots for: A) relief versus exhumation rate, B) present-day precipitation versus exhumation rate, C) seismic energy calculated in a radius of 25 km versus exhumation rate, D) seismic energy in the catchment divides by the area of catchment versus exhumation rate, E) erosion index (Shear Stress or SSP; m = 0.33; n = 0.67) with uniform precipitation (equation 6.2) versus exhumation rate, and F) erosion index (Shear Stress or SSP; m = 0.33; n = 0.67) with spatially variable precipitation precipitation (equation 6.3) versus exhumation rate (For more detailed information see the Table 6.3).

If precipitation does not strongly control long-term exhumation rates in the Venezuelan Andes, what about a tectonic control? To answer this question, we use cumulative seismic

energy release as a proxy for tectonic forcing. We estimate the cumulative seismic energy released within the different catchment in two different ways: by averaging the values of Figure 3B within each catchment, or by simply summing the seismic energy released by each earthquake within the catchment boundaries and normalising by catchment area. The difference between the two methods is the extent to which earthquakes occurring outside the catchment boundaries are taken into account. Somewhat surprisingly, the predicted correlations between seismic energy release and both long-term exhumation rates and relief are negative, suggesting that low seismicity areas are associated with rapid exhumation and strong relief. We can propose several explanations for this surprising result: firstly, as for the precipitation data, the short time-scale seismicity data may not be representative of tectonic forcing over geological timescales. However, there is very little correlation between measures of seismic energy release and stream-power based erosion indexes, suggesting that short-term erosion rates (if these are correctly predicted by the stream-power models) are also decoupled from seismic energy. Secondly, as noted previously, the seismic energy release pattern is strongly controlled by large (Mw > 5) strike-slip earthquakes located outside the Venezuelan Andes, which contribute significantly to accumulated seismic energy in the low-exhumation Agua Viva-Chejendé catchment for instance. However, correlations on the central Andean catchments only (i.e. excluding the Agua Viva-Chejendé and Coloncito catchments) do not lead to significantly different results. Thus, we believe the reason for the lack of positive correlation between seismicity on the one hand, and relief and exhumation rates on the other, is twofold: first, many large earthquakes have strike-slip mechanisms (Colmenares and Zoback, 2003; Corredor, 2003; Cortés and Angelier, 2005) and thus do not contribute directly to relief growth; second, a significant part (up to 90%) of the deformation in the Venezuelan Andes may be aseismic (Corredor, 2003) and the seismicity thus does not capture the true tectonic deformation field, this means that the seismicity has changed over geologic time.

6.6 Conclusions

Detrital AFT analysis of modern river sediment is an important tool for studying sediment provenance and long-term exhumation rates in complex areas with difficult access, such as in the Venezuelan Andes. We have shown that the technique efficiently records catchment-wide long-term exhumation rates when compared to *in-situ* samples. The detrital AFT ages of seven river drainages of the Venezuelan Andes reproduce and extrapolate the exhumation

patterns reported by Bermúdez et al. (chapter 4 in this work) and can thus be used to infer exhumation rates in areas where *in-situ* data is absent.

Catchment-averaged long-term exhumation rates in the Venezuelan Andes vary between 0.37 and 0.53 km/My, with small rivers draining the northwest flank of the orogen recording the highest rates (~0.5 km/My), large central catchments recording rates of ~0.45 km/My and the large Agua Viva – Chejendé catchment located to the northeast of the belt the lowest rate (0.37 km /My). These long-term exhumation rates correlate very well with relief of the catchments, but correlations with the patterns of stream-power based predictions of short-term erosion rates, precipitation and seismic energy release are weak or negative.

The lack of correlation between long-term exhumation rates and relief on one hand and precipitation on the other suggests that either precipitation is not the main controlling factor for driving exhumation and relief development in the Venezuelan Andes, or that the short-term record of present-day precipitation is not representative of long-term average values. A similar lack of correlation with seismic energy release is likewise attributed to the different timescales of observation between long-term exhumation rates and the short-term seismicity record, together with the fact that many large earthquakes have strike slip mechanisms and thus do not contribute directly to relief growth and that much of the deformation of the Venezuelan Andes is aseismic. In order to better comprehend the potential control of climate on exhumation of the Venezuelan Andes, it is necessary to obtain more data for their remote southern flank.

6.7 Acknowledgements

This study was supported by the CDCH de la Universidad Central de Venezuela (UCV), Project Number PI 08-00-6219-2006 and ECOS-Nord project V08U01. We thank Juan Flores and Antonio León for support during field work. We acknowledge Dr. Gerhard Kopp of the Institute for Meteorology and Climate Research, University of Karlsruhe, Germany, for providing the meteorological data of the Mérida Atmospheric Research Station for Pico Espejo (MARS). We are also thankful to María Elena Naranjo of the Universidad de Los Andes (ULA) for providing precipitation data of the following stations: Páramo de Mucuchies, Páramo Pico El Aguila, Los Plantíos, Mucubají, Valle Grande and Tabay.

Chapter 7

VII. STRATIGRAPHY AND PROVENANCE OF THE MÉRIDA ANDES PRO- AND RETRO-SIDE FORELAND BASIN DEPOSITS: INSIGHTS FROM DETRITAL APATITE FISSION-TRACK THERMOCHRONOLOGY, PALYNOLOGY, AND SEDIMENT PETROLOGY.

This chapter will be submitted for publication in the next months once all sediment petrologic and palynological samples haven been prepared and analyzed. Field work information and preliminary results are presented in this chapter

7.0 Abstract

The foreland basins on the pro- and retro-side of the Mérida Andes are filled with Mio-Pliocene synorogenic sediments. Proximal deposits have been uplifted and tilted since the late Pliocene and are now exposed on the northern and southern flanks of the orogen. Stratigraphic, thermochronologic, palynological, and petrologic analyses of these sedimentary rocks provide information on basin evolution, sediment provenance, and exhumation of sediment source areas. In this study we present detrital apatite fission-track (AFT) ages of seven sandstones samples collected from the Betijoque Formation on the northern flank, and eight samples from the Río Yuca and Parángula formations on the southern flank of the Mérida Andes. Furthermore, 27 pollen samples from the Río Yuca and Betijoque formations were successfully analyzed, in addition to Rock-Eval analysis of 7 samples of organic material from the same formations. The palynological data suggest Pliocene depositional ages for the Betijoque and upper Río Yuca formations. This observation is supported by detrital AFT data. The Rock-Eval analyses indicate that the Río Yuca and Betijoque formations never reached burial depths sufficient for hydrocarbon production and therefore temperatures in these parts of the two basins were not sufficient for resetting AFT ages. The pollen and AFT data indicate that the Parángula Formation is possibly of middle Miocene age. All Neogene sediments deposited in these two basins were derived from erosion of Mérida Andes crystalline bedrocks and recycling of sedimentary cover units. The observed detrital AFT ages confirm the episodic nature of exhumation of different tectonic blocks in the crystalline core of the Mérida Andes.

Keywords: Mérida Andes, exhumation, apatite fission-track analysis, foreland basin, stratigraphy, palynology.

7.1 Introduction

The Mérida Andes in northwestern Venezuela are the result of oblique convergence between the Maracaibo continental block and the South America plate (Fig. 7.1A; Colleta et al. 1997; Bermúdez et al. submitted, chapter 5 in this work). This convergence started in the late Paleogene, resulting in major surface uplift of the Mérida Andes during the Late Miocene (Hoorn et al. 1995). The growth of the Mérida Andes caused the separation of the Maracaibo and Barinas-Apure basins (Guzmán and Fisher, 2006), which used to form a continuous basin bounded by the northern Andes in Columbia to the NW and W and the Guyana Shield to the SE (Fig. 7.1A).

The Mio-Pliocene pro-side foreland basin on the northern flank of the doubly vergent Mérida Andes contains molasse deposits that are divided into the Palmar, Isnotú and Betijoque formations (James, 2000a, b). In the retro-side foreland basin the Mio-Pliocene deposits include the Parángula and Río Yuca formations. All these formations consist of fluvial mudstones, sandstones and conglomerates, derived from erosion of the uplifting Mérida Andes. The synorogenic sedimentary rocks preserve the record of Mio-Pliocene erosional exhumation of the Mérida Andes and are therefore important for understanding the long-term evolution of this mountain belt.

Detailed stratigraphic age information on these formations is difficult to obtain, partly because these units are poor in fossil content and difficult to date with magnetostratigraphy due to discontinuous outcrops, strong secondary magnetization in some parts, and coarse grained lithologies. The objective of this paper is to improve the stratigraphic information on the Betijoque, Parángula and Río Yuca formations by a) using detrital apatite fission-track (AFT) ages and pollen samples to determine maximum depositional ages and the exhumation history of the Mérida Andes, and b) to determine provenance from sediment petrology and detrital thermochronology.

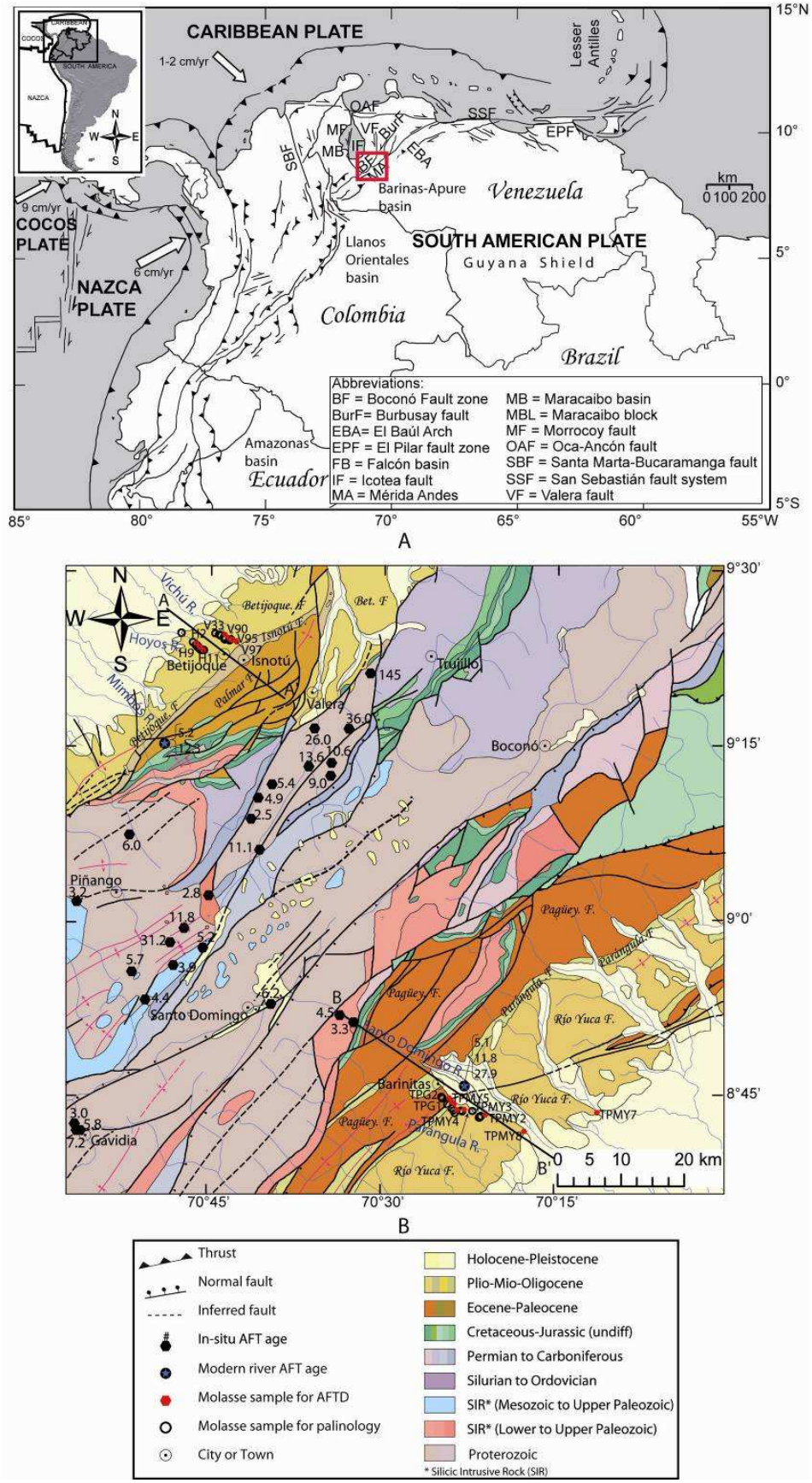

Fig. 7.1. A) Major tectonic features of northern South America (after Colmenares and Zoback, 2003). B) Geologic map of the study area in the Mérida Andes (modified after Hackley et al. 2005). Red points mark the location of AFT samples in the foreland basins. Black points correspond to palynological samples.

7.2 Geologic setting

Basin formation in north-western South America started in the late Jurassic with development of rift grabens during Atlantic rifting. These rift grabens were filled with red clastic sedimentary rocks of the La Quinta Formation. With continuous rifting a passive margin developed during the Early Cretaceous to Paleocene, leading to deposition of the La Luna Formation, a calcareous shale unit which is the source rock of 98% of all oil in the Maracaibo basin today (Escalona and Mann, 2006). The La Luna Formation is overlain by Late Cretaceous rocks of the Colon Formation and the Paleocene Guasare Formation. The tectonic style of the Maracaibo basin changed from a passive margin to a foreland basin setting in the late Paleocene because of oblique convergence between the Caribbean and South American plates (Lugo and Mann, 1995). Deformation and surface uplift in the Colombian Andes increased erosion and clastic sediments were transported to the Maracaibo basin, resulting in deposition of the Eocene shallow-marine/deltaic Misoa Formation, with the basin depocenter being located in the western part of the Maracaibo basin. The mainly quartz-arenitic Misoa Formation is one of the two main reservoir rocks of the Maracaibo basin (Escalona and Mann, 2006). The reservoir is sealed by a regional late Eocene/Oligocene unconformity, which indicates uplift and partial erosion of the basin deposits during the Late Eocene. Subsidence recommenced in the southern Maracaibo basin in the Early-Middle Miocene with deposition of the shallow marine clastic La Rosa/Palmar Formation, followed by the fluvial Late Miocene Isnotú and Pliocene Betijoque formations. The depocenter of this second foreland basin phase formed because of Mio-Pliocene crustal loading of the Maracaibo block during oblique collision of the Maracaibo block with the South American plate (De Toni and Kellogg, 1993). This collision was driven by Maracaibo block clockwise rotation (Montes et al. 2005), and collision of the Panamá Arc with the northern Andes in Colombia (Kohn et al. 1984; Coletta et al. 1997). The Mérida Andes pro-side foreland basin reaches a maximum burial depth of about 6 km (De Toni and Kellogg, 1993). Proximal parts of the Palmar, Isnotú and Betijoque formations have been tilted and exposed along the northern flank of the Mérida Andes since the Late Pliocene-Pleistocene (Fig 7.2A).

The Barinas basin is located on the southern flank of the Mérida Andes. This basin is limited in the southeast by the Guyana shield, in the west by the Colombian Andes, and in the northeast by the El Baúl Arch (Fig. 7.1A). During the Late Cretaceous passive margin and the Eocene foreland basin phase this basin was connected to the Maracaibo basin (Zambrano et al.

1972; Roure et al. 1997; James 2000a, b; Guzmán and Fisher 2006). Middle Eocene marine sediments of the Gobernador and Pagüey formations in the Barinas basin reach a thickness of up to 1 km. These rocks are partly time-equivalent with the Misoa Formation in the Maracaibo basin. In contrast to most parts of the Maracaibo basin, the central part of the Barinas-Apure basin was affected by subsidence during the Oligocene, leading to deposition of the Carbonera Formation. This formation is not preserved in the proximal basin units, which are tilted and exposed along the southern flank of the Mérida Andes today (Fig. 7.2B). Therefore, the Eocene Pagüey Formation is in direct contact with the fluvial Miocene Parángula Formation, which is overlain by the fluvial late Miocene to Pliocene Río Yuca Formation. In contrast to the northern pro-side foreland basin, the Mio-Pliocene southern retro-side foreland basin reaches a maximum thickness of only 2-3 km (De Toni and Kellogg, 1993; Chacín et al. 2005; Jácome and Chacín, 2008).

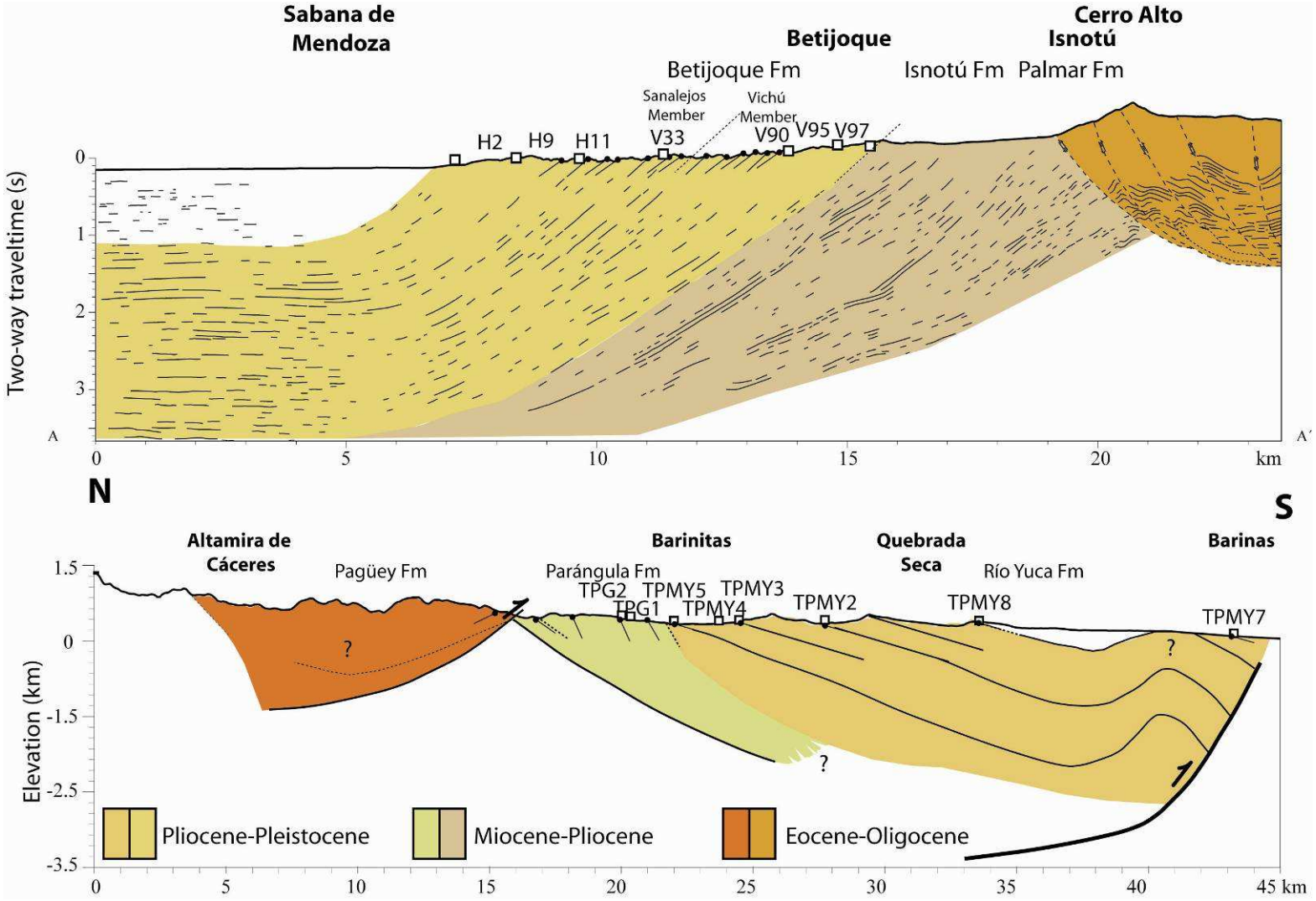

Fig. 7.2. A) Cross-section on the northern flank of the Mérida Andes, showing approximate sample locations along the Río Hoyos and Río Vichú sections. The seismic profile was obtained from seismic lines provided for PDVSA to Jorge Mora of the Central University of Venezuela. B) Topographic profile of the Barinas basin along Parángula River section near Barinitas on the southern flank of the Mérida Andes.

7.3 Stratigraphic analysis and sample collection

For gaining a better understanding of Mio-Pliocene stratigraphy of the pro- and retro-side foreland basin of the Mérida Andes we studied sedimentary rock outcrops on both flanks of the mountain belt. Two complementary sections were mapped and sampled along the Río Hoyos and Río Vichú near the city of Betijoque on the northern flank of the Mérida Andes (Fig. 7.1B), focusing on the Betijoque Formation. The Parángula and Río Yuca formations were studied along the Parángula River to the west and south of Barinitas on the southern flank of the Mérida Andes (Fig. 7.1B).

For detrital AFT analysis a total of 15 samples, ~5-15 kg each, were collected from medium to coarse grained sandstones. On the northern flank, three samples (H2, H9 and H11) were collect from the Sanalejos member of the Betijoque Formation along the Río Hoyos section. One sample (V33) collected in the Río Vichú section also belongs to the Sanalejos member. The others 3 samples (V90, V95 and V97) collected along the Río Vichú section belong to the Vichú Member (Figs. 7.2A, 7.3). On the southern flank, two samples (TPG-1, TPG-2) were collected from the Parángula Formation and six samples (TPMY-2, TPMY-3, TPMY-4, TPMY-5, TPMY-7 and TPMY-8) from the Río Yuca Formation along the Parángula River section (Figs. 7.2B, 7.4).

A total of 125 pollen samples were collected from mudstone deposits, 52 along the Río Hoyos section and 73 along the Parángula River section (Fig. 7.3). For Rock-Eval analyses, seven samples of organic material were taken from all three sections. In addition, sandstone samples were collected for thin section analysis, 9 along the Río Hoyos and Río Vichú sections, and 17 along the Parángula River section (Fig. 7.4).

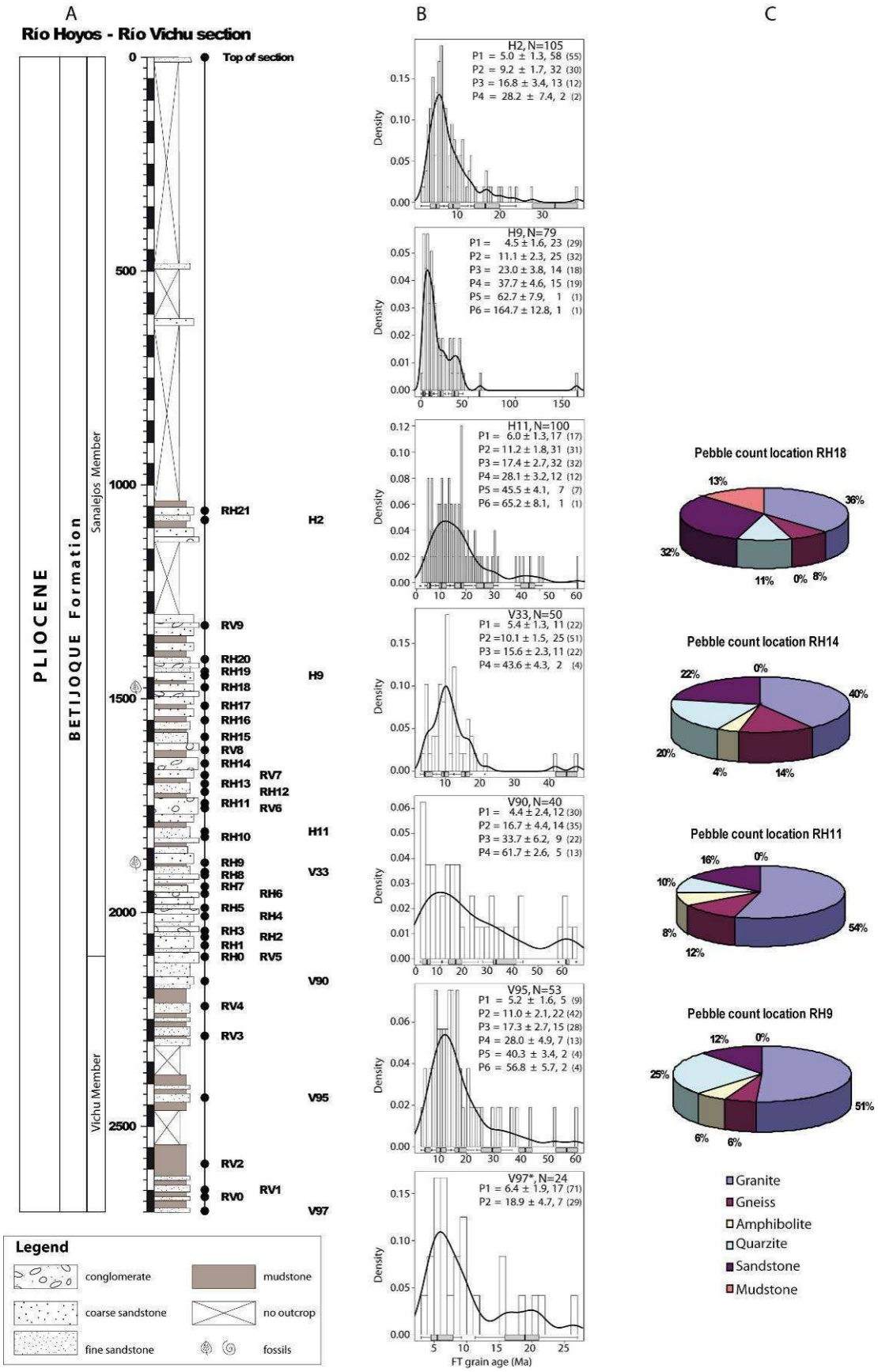

Fig. 7.3. A) Generalized stratigraphic section of the Betijoque Formation on the northern flank of the Mérida Andes. Also are shown are the stratigraphic positions of samples collected for palynological, AFT, petrologic and Rock-Eval analyses. See text for detailed description. B) Plot Density Functions (PDF) of AFT grain-age distributions with histograms. At the base of each plot box-plots results of p-partition discriminations are shown. *The populations discriminated for this sample is not statistically significant, because the numbers of grains counted are lower to 40 grains. C) Pebble-count plots obtained from counting in the field.

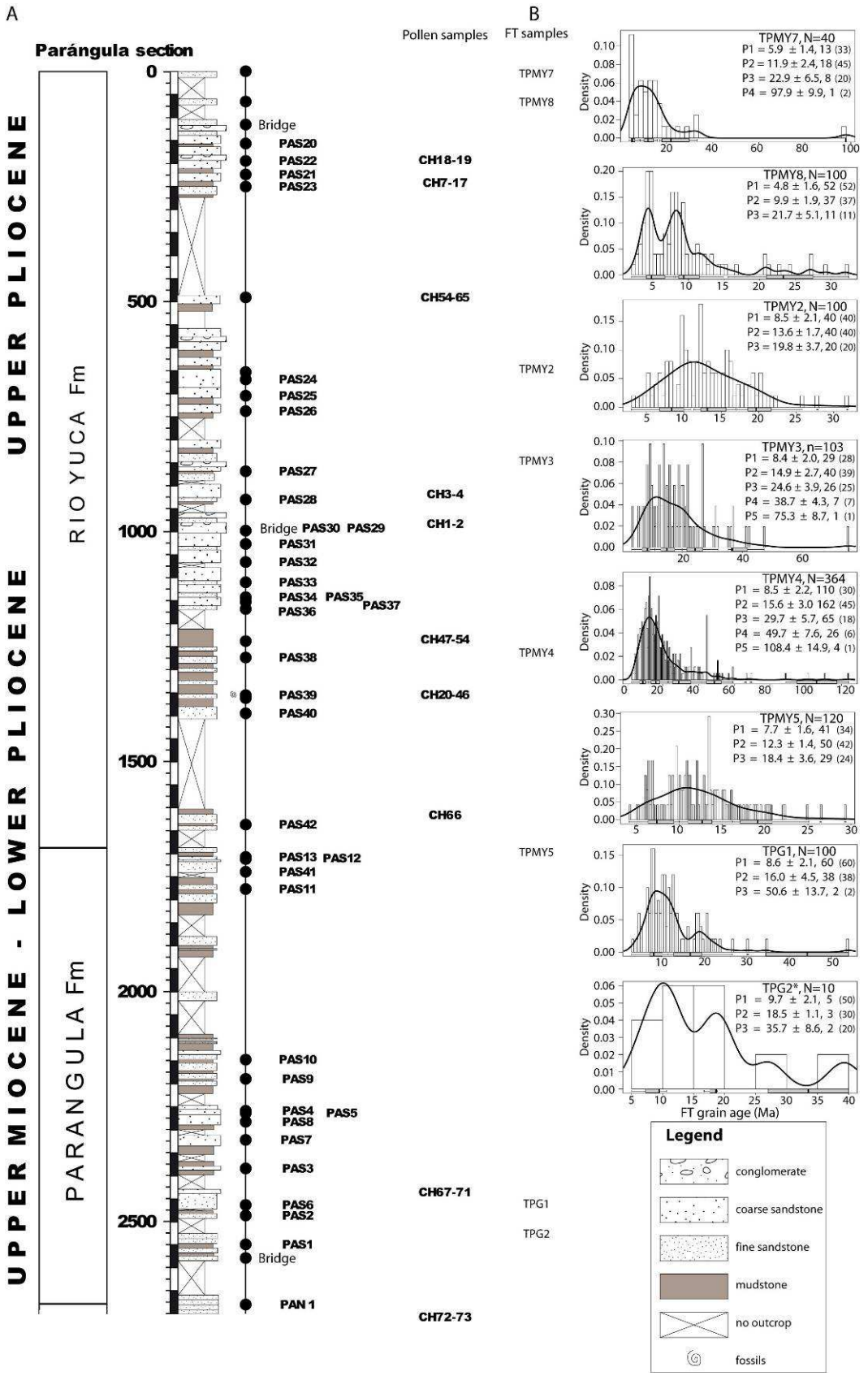

Fig. 7.4. A) Generalized stratigraphic section of the Río Yuca and Parángula formations on the southern flank of the Mérida Andes. Also are shown are the stratigraphic positions of samples collected for palynological, AFT, petrography and Rock-Eval analysis. See text for detailed description. B) Plot Density Functions (PDF) of AFT grain-age distributions with histograms. At the base of each plot box-plots results of p-partition discriminations are shown. *The populations discriminated for this sample is not statistically significant, because the numbers of grains counted are lower to 40 grains.

7.4 Methods

7.4.1 Detrital apatite fission-track thermochronology

For detrital AFT analysis apatites were separated from whole-rock samples using standard crushing, sieving, heavy liquid, and magnetic separation techniques. Apatite aliquots were mounted in epoxy resin and polished to expose internal grain surfaces. Mounts were etched for 20 seconds in 5.5 M HNO_3 at 20°C. Eleven samples were irradiated together with Fish Canyon Tuff and Durango apatite age standards and IRMM-540 uranium glass standards at the Orphée reactor, Centre d'Etudes Nucléaires de Saclay, Gif-sur-Yvette, France. The other four samples were irradiated at the Oregon State University reactor, along with CN1 glass standards, Fish Canyon Tuff and Durango apatite standards.

During mounting we assured that 500-800 grains were randomly distributed within the mounts. This helps avoiding sampling bias during counting, given the variety of apatites in a detrital sample with respect to their cooling age and uranium content. Randomly selected grains were counted at 1250× (dry) using an Olympus BH-2 microscope. Our goal was to date about 100 grains per sample, to achieve the required level of statistical adequacy for provenance studies (Vermeesch, 2004). However, not for all samples was it possible to find that many countable grains because of inclusions, dislocations and poor apatite quality caused by alteration (Table 7.1).

Observed fission-track grain-age distributions are commonly presented in probability density functions (PDF). These PDFs can be decomposed into major grain-age components (e.g. Brandon, 1992). For discriminating a PDF grain-age spectrum into main-age components we used the p-partition method of Bermúdez-Cella (2008) and Bermúdez et al. (submitted, chapter 6 in this work). This method has the advantage that it is not affected by grains with low uranium concentrations. The results were compared with results obtained using commercial peak-fitting software (PeakFit 4.12 of Aspire International Software™) and the BINOMFIT software of Brandon (see Ehlers, 2005). In almost all cases there are no differences between the results given by different software.

7.4.2 Palynological analysis

All palynological samples were processed following the standard procedures of the Hugo de Vries-Laboratory, University of Amsterdam. One cm^3 of sample material was taken from each sample and sieved (250 μm mesh size). Organic-rich clays and silts were treated with a 10% sodium pyrophosphate ($Na_4P_2O_7.10H_2O$). Lignites were oxidized with a so-called Schulze mixture ($2HNO_3$, 60%; $KClO_3$, 7%). Bromoform with a density of 2.0 gs/cm^3 was used to separate the organic/inorganic fraction and the organic residue was mounted in glycerine and sealed with paraffin. Sporomorphs were counted by Carina Hoorn, taking a minimum pollen sum of 300 angiosperms. In exceptional cases, when pollen concentration was very low, a minimum of 100 angiosperms was counted.

7.4.3 Characterization of organic matter

For Rock-Eval, total carbon and calcium concentration analysis, all organic matter samples were crushed for obtaining an average fins grain size of 5 μm. All the samples were analyzed at the Institut des Sciences de la Terre, Université Pierre et Marie Curie by François Baudin.

7.4.3.1 Characterization by Rock-Eval pyrolysis

An *Oil Show Analyzer* (OSA) was used for Rock-Eval pyrolysis. The methodology for this technique has been described in detail by Espitalié et al. (1985, 1986). The method requires heating of about 100 mg of sample material. The sample is heated at a rate of 25°C/min to 300°C. During the first heating interval (20-300°C in a helium atmosphere) free hydrocarbons in the rock sample are volatilized (peak S1). During the second heating interval (300-600°C at about 43°C/min) heavy hydrocarbon substances ($>C_{40}$) are volatilized (peak S2). Subsequently the pyrolysed sample is introduced into an oxidization oven, using an automated system. During this phase the sample is heated for 45 min to 600°C under an air current. The CO_2 produced during this heating interval is detected by measuring the thermal conductivity (peak S4). This cycle of analysis provides the following parameters:

1. The quantity of hydrocarbons (gas and oil) content in the rock. This is given by peak S1 and is expressed in mg/g of rock.

2. The amount of hydrocarbon products from kerogen cracking. This corresponds to peak S2 and represents the total quantity of oil that the kerogen can provide
3. The Tmax is the temperature when peak S2 reached its maximum. This parameter is an indicator of the degree of maturation of the organic matter.
4. The content of residual organic carbon, measured by oxidization, corresponds to peak S4.

With these parameters the following information is calculated:

1. The quantity of total organic carbon (TOC) in percent.
2. The petroleum potential (PP) of the rock: PP = S_1+S_2 (mg hydrocarbons (HC)/g of rock).
3. The hydrogen Index, HI = S_2/TOC x 100 (mg HC/g TOC), which is roughly equivalent to the H/C of the organic matter.

The HI/Tmax diagram allows the characterization of the degree of thermal maturation of organic matter in sedimentary rocks. With this type of plot it is possible to discriminate four different types of organic matter:

- Type I corresponds to algal organic matter that has been altered by bacteria.
- Type II corresponds to marine phytoplankton organic matter.
- Type III corresponds to plant fragments in sediments.
- Type IV corresponds to altered organic matter of undetermined biological source.

7.4.3.2 Determination of total carbon content by elementary analysis (LECO)

For this analysis part of the sample is oxidized at high temperatures (1100°C). The CO_2 produced during the combustion is detected with and infra-red analyzer, providing the pondered percentage of total carbon (Ctot) of the sample with a precision of ± 0.2%. This measure is made twice. The organic carbon content (Corg) is estimated by subtracting from Ctot the mineral carbon content (Cmin), assuming that this is present only as calcite:

$$Corg = Ctot - Cmin$$

or

$$Corg = Ctot - (CaCO_3/8.33)$$

7.4.3.3 Calcimetric measure

Measuring the $CaCO_3$ concentration was only possible for two of the seven samples. One hundred mg of crushed rock sample were attacked with 1N HCl, and the amount of released CO_2 was measured.

7.4.4 Sediment petrology

Descriptions of sediment petrology and sedimentary facies from field observations from the pro- and retro-side foreland basins are presented further below. Microscopic sediment petrologic analyses have not been done yet, because thin section preparation of 29 samples was delayed but is currently under way at the thin section preparation lab in St. Etienne. Preliminary sediment petrologic results are presented here for a set of thin sections of the Isnotú and Betijoque formations. These sections were made by students of the Central University at Caracas in connection with a geologic mapping exercise by Jorge Mora in the 1990's. Even if the exact sample location and stratigraphic position of the samples is unknown, they provide a first inside in the petrology of the pro-side foreland basin. The thin sections were point-counted using a BX41 Olympus petrographic microscope, using 10 – 100x magnification.

7.5 Results

7.5.1 Detrital apatite fission-track thermochronology

The age range of dated grains and fitted peaks, using the p-partition method, of all fifteen samples are given in Table 7.1, and in the Figs. 7.3B, 7.4B. All samples failed the χ^2 test, indicating that grains were derived from various sources. The discrimination made on the samples (TPG-2 and V97) that have less than 40 grains is not statistically significant. However, these samples are displayed here (Table 7.1, Figs. 7.3B, 7.4B.) with the purpose of studying the sample tendency. Therefore, all the samples are characterized by multiple age populations (Table 7.1). No indications for partial resetting of fission tracks in apatites from the Pliocene Betijoque and upper Río Yuca formations were found. For two samples of the Parángula Formation (TPG1-2), some individual grains have FT ages close to their

supposedly early Miocene depositional age (Stratigraphic Code of Venezuelan Petroleum Basins www.pdvsa.com/lexico), but no indications were found for partial resetting of apatite in this formation. The stratigraphic position and PDF plots with central AFT ages and standard deviation of dated sandstones samples are given in Figures 7.3 and 7.4 for the Maracaibo and Barinas basin respectively. For samples with more than 40 dated grains more than four age populations were found. Age populations P4, P5 and P6 tend to be much older than the depositional ages, and in many cases these populations are defined by only a few grains.

On the northern flank, the samples from the Betijoque Formation provide the following age patterns (Fig. 7.3B). All samples contain Early Pliocene to Late Miocene age components. The first age component (P1) of all samples ranges between 4 and 6 Ma. All samples also contain a Late to Middle Miocene age component of 9 to16 Ma. In addition, a Middle Eocene to Late Oligocene age component can be discriminated in almost all the samples (Table 7.1).

The detrital AFT age pattern of samples collected from the Barinas basin is slightly different (Fig. 7.4). Only samples TMPY7 and TPMY8, from the top of the studied section, have young peaks between about 5 and 6 Ma (Table 7.1), comparable to the northern flank samples. All samples, including the two from the Parángula Formation, have a Late to Middle Miocene age component of 9 to16 Ma. Furthermore, Early Miocene age peaks (16 to 23 Ma) are present in all samples. Eocene-Oligocene AFT age components are poorly discriminated in the samples of the southern flank. Only sample TPMY4, for which 364 individuals grains were dated, has such an old peak (Table 7.1).

Northern Flank																										
FT samples	**N-Lat.**	**W-Long.**	**Elevation (m)**	**Strat. Depth**	**Central age ± SE**	***N***	**P_1±SE$_1$**	**σ_1**	**N_1**	**P_2±SE$_2$**	**σ_2**	**N_2**	**P_3±SE$_3$**	**σ_3**	**N_3**	**P_4±SE$_4$**	**σ_4**	**N_4**	**P_5±SE$_5$**	**σ_5**	**N_5**	**P_6±SE$_6$**	**σ_6**	**N_6**	**Formation**
H2	9.3919	-70.776	279	1082	7.8 ± 0.5	105	5.0±0.3	1.3	58	9.2±0.6	1.7	32	16.8±1.4	3.4	13	28.2±4.0	7.4	2							Betijoque
H9	9.3883	-70.7707	252	1446	15.3 ± 1.5	79	4.5±0.5	1.6	23	11.1±0.8	2.3	25	23.0±1.6	3.8	14	37.7±2.7	4.6	15	62.7±0.2	7.9	1	164.0±0.4	12.8	1	Betijoque
H11	9.3839	-70.7661	306	1811	15.4 ± 0.9	100	6.0±0.7	1.3	17	11.2±0.7	1.8	31	17.4±1.0	2.7	32	28.1±2.4	3.2	12	45.5±5.4	4.1	7	65.2±0.6	8.1	1	Betijoque
V33	9.4012	-70.7355	203	1906	10.4 ± 0.6	49	5.4±0.5	1.3	11	10.1±0.5	1.5	25	15.6±1.1	2.3	11	43.6±13.4	4.25	2							Betijoque
V90	9.399	-70.7321	449	2160	16.6 ± 2.1	40	4.4±0.5	2.4	12	16.7±1.7	4.4	14	33.7±5.8	6.2	9	61.7±16.5	2.6	5							Betijoque
V95	9.3976	-70.7274	251	2433	13.8 ± 1.0	53	5.2±1.2	1.6	5	11.0±0.8	2.1	22	17.3±1.8	2.7	15	28.0±4.6	4.9	7	40.3±19.9	3.4	2	56.8±18.9	5.7	2	Betijoque
V97*	9.3956	-70.7233	238	2698	7.3 ± 0.7	24	6.4±0.7	1.9	17	18.9±4.3	4.7	7													Betijoque
Southern Flank																										
TPMY-7	8.7207	-70.1757	191	0	12.2 ± 1.3	40	5.9±0.8	1.4	13	11.9±0.9	2.4	18	22.9±3.8	6.5	8	97.9±0.3	9.9	1							Rio Yuca
TPMY-8	8.6919	-70.3037	301	66	7.3 ± 0.4	100	4.8±0.2	1.6	52	9.9±0.6	1.9	37	21.7±2.8	5.1	11										Rio Yuca
TPMY-2	8.7183	-70.3528	300	656	12.6 ± 0.5	100	8.5±0.6	2.1	40	13.6±0.7	1.7	40	19.8±1.4	3.7	20										Rio Yuca
TPMY-3	8.7247	-70.3822	320	850	15.6 ± 0.8	103	8.4±0.5	2.0	29	14.9±0.7	2.7	40	24.6±1.5	3.9	26	38.7±5.4	4.3	7	75.3±0.6	8.7	1				Rio Yuca
TPMY-4	8.7248	-70.3937	360	1275	15.6 ± 0.5	364	8.5±0.3	2.2	110	15.6±0.4	3.0	162	29.7±1.4	5.7	65	49.7±5.0	7.6	23	108.4±34.5	14.9	4				Rio Yuca
TPMY-5	8.7382	-70.4052	340	1708	12.2 ± 0.5	120	7.7±0.5	1.6	41	12.3±0.5	1.4	50	18.4±0.8	3.6	29										Rio Yuca
TPG1	8.7444	-70.4106	390	2475	11.4 ± 0.5	100	8.6±0.3	2.1	60	16.0±0.7	4.5	38	50.6±15.5	13.7	2										Parangula
TPG2*	8.7448	-70.4111	390	2538	14.3 ± 1.9	10	9.7±1.7	2.1	5	18.5±2.8	1.1	3	35.7±12.8	8.6	2										Parangula

Table 7.1. Detrital apatite fission-track results of samples from the Betijoque, Río Yuca and Parángula formations.

Note: N is the total number of grains counted; the age given in Ma represent the central age for each population P_i discriminated by the p-partition algorithm; errors of peak ages are given ±1 SE; N_i is the number of grains counted belong to the population P_i, and σ is the standard deviation in a specific population. All samples were counted at 1250x dry (100x objective, 1.25 tube factor, 10 oculars) by M. Bermúdez using a zeta (CN-1) of 129.82 ± 5.03 (±1 SE) for samples with an asterisk. The rest of the samples were dated by the same person using a zeta (IRRM-540R) of 288.66 ± 5.23 (±1 SE). *The populations discriminated for this sample is not statistically significant, because the numbers of grains counted are lower to 40 grains. See Figures 7.3 and 7.4.

7.5.2 Palynological analysis

Out of the 125 pollen samples collected in the field, only twenty four samples of the Betijoque Formation and three of the Río Yuca Formation were analyzed so far (Table 7.2 and 7.3). The quantity of pollen was not very abundant. The objective was to discriminate Pliocene and Miocene biostratigraphic marker species. In Tables 7.2 and 7.3 Pliocene species are given in yellow, and Late Miocene-Pliocene species are marked in blue. Reworked Eocene pollen and dinoflagellates are shown at the bottom of the tables. Taxonomic references are shown in Table 7.4. The taxa shown in Tables 7.2 and 7.3 are presented in order of first appearance. The pollen species *Azolla sp., Botryococcus sp.* and marine palynomorphs (foraminifera/ acritarchs/dinoflagellates) were excluded from the total. Almost all counted taxa were included in the pollen sum because when dealing with pre-Pleistocene material, it is often uncertain whether local or regional elements are involved.

Only few and poorly preserved dinoflagellate cysts are present in the samples from the Río Yuca section in the Barinas basin. *Polysphaeridium* spp. is the most frequent dinoflagellate, followed by *Spiniferites* spp. Rare or single occurrences include *Areoligera sp*., *Homotryblium* sp. and a questionable specimen of *Diphyes colligerum*. According to Roel Verreusel (Comm. Pers., 2009) the *Polysphaeridium* specimens bear numerous slender processes, which is more typical for the “older”, Eocene or Oligocene types. The presence of *Areoligera sp*. and the questionable specimen of *Diphyes colligerum*, would indicate an Eocene age, but the poor preservation and the scattered occurrences suggest reworking.

BETIJOQUE FORMATION/SAMPLES & COUNTS	CH105	CH100	CH110
POLLEN, MORPHOLOGICAL TAXA			
Clavainaperturites microclavatus	9	2	
Cyperaceaepollis sp.	1		
Echitricolporites mcneilly	1	1	
Echitricolporites spinosus	13	11	
Ericipites sp.	8		
Heterocolpites incomptus	1	1	
Ilexpollenites sp.	1	2	
Perisyncolporites pokornyi	1		
Monoporites annulatus	70	69	
Podocarpidites sp.	2		
Proteacidites sp.	1		
Psilamonocolpites sp.		1	
Psilaperiporites minimus	1		
Psilatricolporites crassus		2	
Psilatricolporites operculatus	1	2	
Retimonocolpites sp.			2
Retitricolporites irregularis		1	
EXTANT TAXA			
Clusiaceae spp.	1		
Draba		1	
Iridaceae?		2	
Hibiscus	1		1
Myrtaceae spp.	1		
Oropanax (Araliaceae)	1		
Plantago?		1	
Rubiaceae spp.		1	
Rutaceae spp.	1		
Sapotaceae spp.		2	
Symplocos (Apocynaceae)	1		1
cf. Tiliaceae spp.	1		
Valeriana	1		
Weinmannia?	5	1	
REWORKED			
Gemmamonocolpites		1	
SUM	123	101	4
PTERIDOPHYTES			
Cingulatisporites sp.	2		
Cyatheacidites annulatus (Lophosoria)	4	13	
Echitriletes muelleri		1	
Kuylisporites waterbolkii		2	
Magnastriatites grandiousus		1	
Psilate, monolete	84	21	2
Psilate, trilete (Cyatheaceae)	80	21	6
Psilate, trilete (small)		2	
Verrucatotriletes bullatus	24	22	1
Verrucatotriletes sp.	14	4	5
Verrucatosporites usmensis		12	
Verrucatosporites spp.	4	9	4
EXTANT TAXA			
Hemitelia		1	1
Jamesonia	16	2	
Lycopodium foveolate (cf. Camarozonisporites sp.)	6	1	3
Lycopodium jussiaei	1		
Pityrogramma	2	19	

Table 7.2. Palynological counts for Betijoque Formation.

RIO YUCA FORMATION/SAMPLES & COUNTS	CH20	CH21	CH26	CH28	CH29	CH30	CH31	CH31	CH33	CH37	CH38	CH40	CH44	CH48	CH49	CH50	CH51	CH52	CH53	CH54	CH56	CH57	CH 60	CH63
POLLEN, MORPHOLOGICAL TAXA																								
Annutriporites iversenii			1									1												
Bombacacidites baumfalkii					1		1				1	2	1	4		1								
Bombacacidites brevis							1					1										1		
Bombacacidites sp.																2								
Clavainaperturites microclavatus							1					4				1				2				
Corsinipollenites oculusnoctis					1		1					1												
Crassiectoapertites columbianus												1									1			
Crototricolpites annemariae												2										1		
Echitricolporites mcneillyi			3																				1	
Echitricolporites spinosus			3				1					2								1	1		1	
Echitriporites trianguliformis																				1				
Fenestrites spinosus			1																					
Grimsdalea magnaclavata											1					1					1			
Heterocolpites incomptus														2										
Jandufouria saemrogiformis														2		1		1			1			
Mauritiidites franciscoi			2	1							3	2	1	1						3		2		
Monoporites annulatus	1										3	2						2		4		1		
Podocarpidites sp.												3								1			2	
Psilastephanocolporites fissilis																							1	
Proteacidites triangulatus											1	1				1								
Psilamonocolpites sp.							1									1		2	2		2		1	
Psilamonocolpites rinconii							5				3				2					1				
Perisyncolporites pokornyi			1				1		1		2					1			1					1
Psilaperiporites minimus				1			1					1												
Psilaperiporites robustus				1								1												
Psilatricolpites acerbus																2								
Psilatricolporites caribbiensis?			1																					
Psilatricolporites crassus (reworked?)			3	7	1	4	54	15	6	4	35	22	1	16	4	25	4	12	1	5	29	24	9	2
Psilatricolporites cyamus									1															
Psilatricolporites divisus			2			1	1																	
Psilatricolporites labiatus			1				1		1		1	1				1					1	1	1	
Psilatricolporites operculatus							4				1	2							1	1	1	1		
Psilatricolporites schneiderii												3												
Psilatricolporites transversalis							1															1		
Psilatricolporites varius					1		1								1									
Retibrevitricolpites sp.			1				3		1		2	13											1	
Retimonocolpites longicolpatus			1			1																		
Retimonocolpites sp.											2	2				2								
Retitricolporites simplex																1								
Retitricolporites hispidus											2	1			1									
Retitricolporites guianensis																						1		
Retitricolporites irregularis							1				1			1		1			1		2			
Retistephanocolpites angelicus																1								
Spirosyncolpites spiralis					1		1				1						1	1				2	1	
Stephanocolpites evansii			2								1					1								
Striatricolpites catatumbus											2	1						2						
Striasyncolpites zwaardii							1																	

Table 7.3. Palynological counts for Río Yuca Formation

RIO YUCA FORMATION/SAMPLES & COUNTS	CH20	CH21	CH26	CH28	CH29	CH30	CH31	CH31	CH33	CH37	CH38	CH40	CH44	CH48	CH49	CH50	CH51	CH52	CH53	CH54	CH56	CH57	CH 60	CH63
Zonocostites ramonae							2					3		1	1									
EXTANT GENERA																								
Apocynaceae spp.																						1		
Myrica?	1											1										1		
Myrtaceae							1													2				
Sapotaceae							1							1							6			
Rubiaceae																				5	1	1		
Rutaceae									1															
Symplocos			1									1									2			
Hibiscus			3				1					1										1		
Weinmannia?	1																							
REWORKED																								
Middle Miocene																								
Crassoretitriletes vanraadshoovenii							1					1								1				
Paleogene																								
Cicatricosisporites dorongensis						2	9				7	4		3		9		2		2	2	1	1	
Gemmamonocolpites amicus											2					1								
Retitricolporites saturum											1					2								
Spinozonocolpites sp.										1						2					1			
Unnamed type 953 (Maraven)							1				2	1										1		
very large psilate, trilete (Gonzalez 1967)							1				1					2							2	
DINOFLAGELLATES					1	1	2				6	4		2		7	1	2		2	1	5		
FORAMINIFERA				1			1				1		1	1		1		1			1	1		
Cretaceous																								
Elaterate pollen																1								
Palaeozoic																								
Megaspores and gymnosperms			1												1									
SUM	3	0	27	11	6	9	101	15	11	5	82	85	4	34	10	68	6	25	6	31	53	47	21	3
PTERIDOPHYTES																								
Cyatheacidites annulatus (Lophosoria)		1													1									
Echitriletes muelleri			9			5		1			1	1					1						5	
Magnastriatites grandiosus																1					1		1	
Psilate, trilete (Cyatheaceae)	12		6	1		2	1	1	2		4	17	1	2	1	8		7	1		13	9	2	10
Psilate, trilete (small)					1						1	1												
Psilate, monolete	4		7	1			1				5	8				2		1		2	2	5		
Verrucatosporites sp.	7		4				2		3		1	5		1		6		2		1	3	1	1	
Verrucatotriletes cf. bullatus																1								
Verrucatotriletes spp.	7		3				2				3	2		2	4	2					3	1		1
Extant taxa																								
Lycopodium foveolate (cf. Camarozonisporites sp.)	2		3									1												
Hemitelia											1													
Pityrogramma			2									9	1	1				1			3	3	6	
BRIOPHYTES	5	1	44	1	16	46		64	1			1												

Table 7.3 (cont). Palynological counts for Río Yuca Formation

Pollen & Spores (Río Yuca, Parángula, Betijoque Fms.)	Author
Annutriporites iversenii	Van der Hammen, 1956; González-Guzmán 1967
Bombacacidites baumfalkii	Lorente 1986
Bombacacidites brevis	Dueñas 1979
Bombacacidites spp.	Couper 1960
Camarozonisporites sp. *(Lycopodium foveolate)*	Germeraad et al. 1968
Cicatricosisporites dorongensis	Potonie & Gelletich, 1933
Cingulatisporites sp.	Thomson, in Thomson & Pflug 1953
Clavainaperturites microclavatus	Hoorn 1994b
Corsinipollenites oculusnoctis	(Thiergart 1940); Nakoman 1965
Crassiectoapertites columbianus	Dueñas 1980
Crassoretitriletes vanraadshoovenii	Germeraad et al. 1968
Crototricolpites annemariae	Leidelmeyer 1966
Cyatheacidites annulatus (Lophosoria)	Cookson, 1947
Cyperaceaepollis sp.	Krutzsch 1970
Echitricolporites mcneillyi	Germeraad et al. 1968
Echitricolporites spinosus	Van der Hammen 1956 ex Germeraad et al. 1968
Echitriletes cf. *muelleri*	Regali et al. 1974
Echitriporites trianguliformis	Van Hoeken-Klinkenberg 1964
Ericipites sp.	Wodehouse, 1933
Fenestrites spinosus	Van der Hammen 1956 ex Lorente, 1986
Gemmamonocolpites amicus	Gonzalez-Guzman 1967
Grimsdalea magnaclavata	Germeraad et al. 1968
Heterocolpites incomptus	Van der Hammen 1956 ex Hoorn 1993
Ilexpollenites sp.	Thiergart 1937 ex Potonie 1960
Jandufouria saemrogiformis	Germeraad et al. 1968
Kuylisporites waterbolkii	Potonie 1956
Magnastriatites grandiosus	(Kedves & Sole de Porta 1963); Dueñas 1980
Mauritidiites franciscoi	(Van der Hammen 1956); Van Hoeken-Klinkenberg 1964
Monoporopollenites annulatus (also Monoporites annulatus)	(Van der Hammen, 1954); Jaramillo & Dilcher, 2001
Perisyncolporites pokornyi	Germeraad et al. 1968
Podocarpidites sp.	Cookson 1947 ex Couper 1953
Proteacidites cf. *triangulatus*	Lorente 1986
Psilamonocolpites sp.	Van der Hammen & Garcia, 1965
Psilamonocolpites rinconii	Dueñas 1986
Psilaperiporites minimus	Regali et al. 1974
Psilaperiporites robustus	Regali et al. 1974
Psilastephanocolporites fissilis	Leidelmeyer 1966
Psilastephanocolporites schneideri	Hoorn 1993
Psilatricolpites acerbus	Gonzalez-Guzman 1967
Psilatricolporites caribbiensis	Muller et al. 1987
Psilatricolporites cyamus	Van der Hammen & Wijmstra 1964
Psilatricolporites aff. *Sapotaceae*	Van der Hammen 1956 ex Van der Hammen & Wijmstra 1964
Lanagiopollis crassa (also Psilatricolporites crassus)	(Van der Hammen & Wymstra, 1964); Frederiksen, 1988
Psilatricolporites divisus	Regali et al. 1974
Psilatricolporites labiatus	Hoorn 1993
Ranunculacidites operculatus (also Psilatricolporites operculatus)	(Van der Hammen & Wymstra, 1964); Jaramillo & Dilcher 2001

Table 7.4. Taxonomic references used for palynological analysis.

Pollen & Spores (Río Yuca, Parángula, Betijoque Fms.)	Author
Tetracolporopollenites transversalis (also Psilatricolporites transversalis)	(Dueñas, 1980); Jaramillo & Dilcher 2001
Psilatricolporites varius	Dueñas 1983
Retibrevitricolpites sp.	Van Hoeken-Klinkenberg, 1964
Retimonocolpites sp.	Pierce, 1961
Retimonocolpites longicolpatus	Lorente 1986
Retitricolpites simplex	Gonzalez-Guzman 1967
Retitricolporites saturum	Gonzalez-Guzman 1967
Rhoipites guianensis (also Retitricolporites guianensis)	(Van der Hammen & Wymstra, 1964); Jaramillo & Dilcher, 2001
Rhoipites hispidus (also Retitricolporites hispidus)	(Van der Hammen & Wymstra, 1964); Jaramillo & Dilcher, 2001
Retitrescolpites? irregularis (also Retitricolporites irregularis)	(Van der Hammen & Wymstra, 1964); Jaramillo & Dilcher, 2001
Retistephanoporites angelicus	Gonzalez-Guzman 1967
Stephanocolpites evansii	Muller et al. 1987
Spinozonocolpites sp.	Muller, 1968
Spirosyncolpites spiralis	Gonzalez-Guzman 1967
Striatopollis catatumbus (also Striatricolpites catatumbus)	(Gonzalez, 1967); Takahashi and Jux, 1989
Striasyncolpites zwaardii	Germeraad et al. 1968
Verrucatosporites spp.	Pflug 1952 ex Potonie 1956
Verrucatosporites usmensis	(Van der Hammen 1956); Germeraad et al. 1968
Verrucatotriletes cf. *bullatus*	Van Hoeken-Klinkenberg 1964
Zonocostites ramonae	Dueñas 1980

Table 7.4 (cont). Taxonomic references used for palynological analysis.

7.5.3 Characterization of organic matter content

TOC levels of the seven analyzed samples range between 0 and 51%. Samples RH5 and PAS39 can be considered as non-organic matter, with TOC% levels <0.1%, which is the detection limit of the Rock-Eval analysis. The TOC measurements confirm the LECO Ctot contents determined for samples CH52 (1), RH3, RH5, RV1 and PAS39. There was, however, a significant difference between the percentages of TOC and Ctot for the samples CH52 (2) and RV3. For these two samples calcimetric analyses were performed. These analyses show $CaCO_3$ concentrations of 38.5% and 0% for samples CH52 (2) and RV3 respectively (Table 7.5). Thus the percentage of Corg calculated for sample CH52 (2) is very close to the TOC%. In contrast, a 10% difference is found in sample RV3, which is poor in calcite (Table 7.5). This difference cannot be physically explained. Samples RV1 and RV3 have significant TOC, in the range of coal (Baudin et al. 2007).

All analyzed samples have a TOC% higher than 0.2, and a peak value of S2 greater than 0.1 mg/g. Tmax values between 389°C and 424°C were determinate only for 4 of the 7 samples for which the measurement of this parameter was reliable (Fig. 7.5; Table 7.5). The measured values HI range from 9 to 268 mg HC/g of TOC in 4 of the 7 samples (Table 7.5).

Sample	CaCO3 (%)	Tmax (°C)	S1 (mg/g)	S2 (mg/g)	TOC (%)	Ctot LECO (%) 1	Ctot LECO (%) 2	Corg LECO (%)	HI (OSA) mg HC/g TOC	HI (LECO) mg HC/g TOC
CH52 (2)	NA	424	1.2	0.1	1	1	1	NA	12	11
CH52 (1)1	38.5	389	0.9	0.4	4.7	8.9	9.3	4.5	9	9
RH3	NA	NA	0	0	0.1	0.1	0.1	NA	NA	NA
RH5	NA	NA	0	0	0	0	0	NA	NA	NA
RV1	NA	400	3.2	16.5	51	50.9	53.3	NA	32	32
RV3	0	397	11.3	100.3	37.4	46.1	48.5	46.1	268	212
PAS39	NA	NA	0.8	0.1	0.1	0	0	NA	NA	NA

Table 7.4. Results of Carbonate content (CaCO3) and Rock-Eval analysis. Note: NA indicates measure not available; Tmax is the maximum temperature; S1 indicates hydrocarbons concentration (gas and oil) present in the rock; S2 indicates the amount of hydrocarbon produced from kerogen cracking. TOC is the weighted concentration of Carbon Organic Total expressed in percentage; Ctot 1 and 2 correspond to the two measures of the weighted total carbon in percentage; Corg is the content of carbon organic; HI (OSA) and HI (LECO) are measures of the Hydrogen Index.

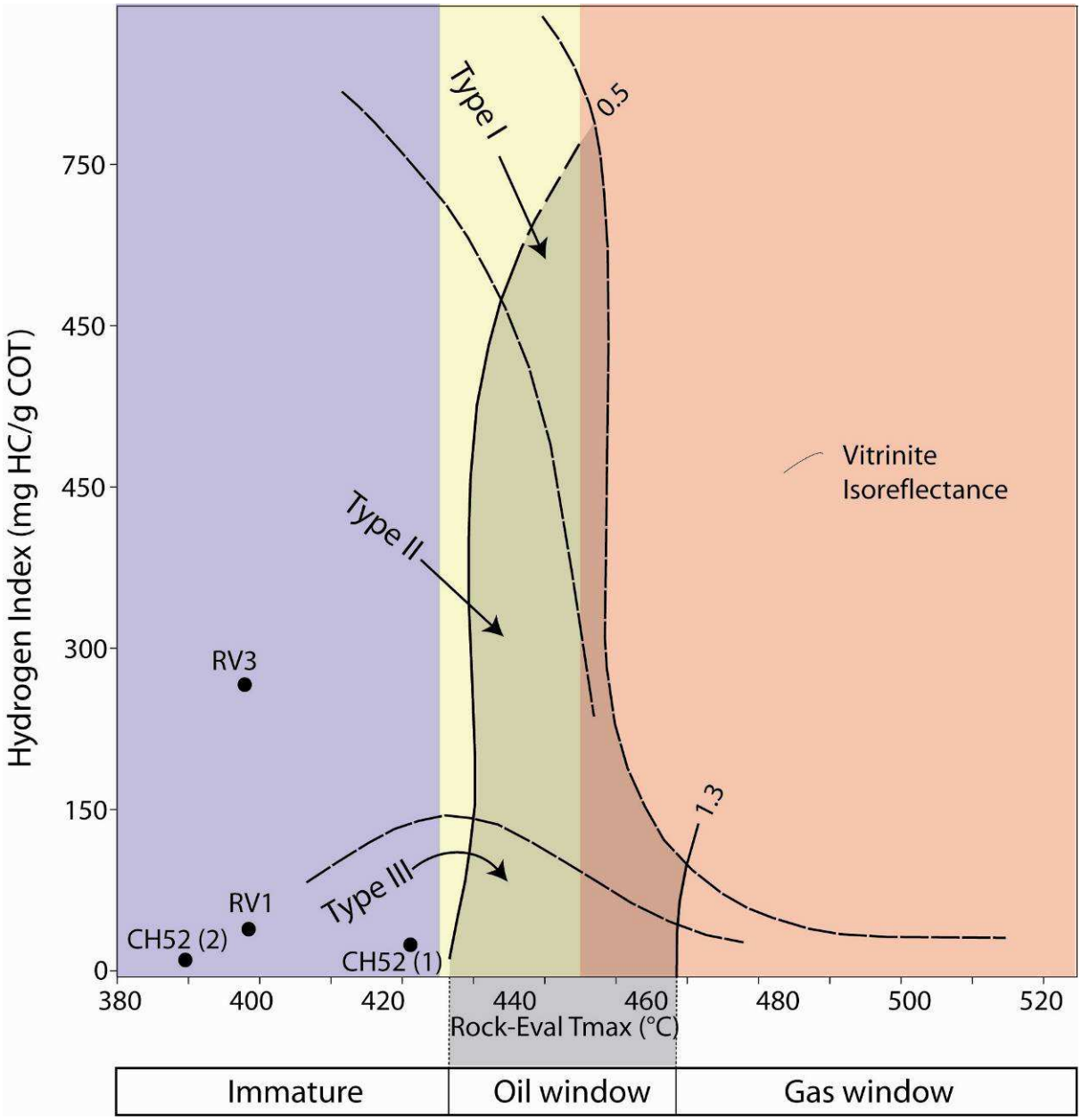

Fig. 7.5. Hydrogen Index (HI) versus Temperature maximum (Tmax) plot, shown for samples CH52 1 and 2 from the Río Yuca Formation and samples RV1 and RV2 from the Betijoque Formation. All four samples were not sufficient heated during burial to reach kerogen maturation.

7.5.4 Sediment petrology

Point counting results of thin sections available from the Isnotú and Betijoque formations are given in Table 7.6 (Mehrkian, 2009) and presented in Figure 7.6. The sandstones of the Betijoque and Isnotú formations can be classified as sub-litharenite and litharenites in the QFL diagram after McBride (1963) (Fig. 7.6A). For comparison point-count data of the Eocene Misoa Formation is shown in Figure 7.6B as well (Housiau, 2009).

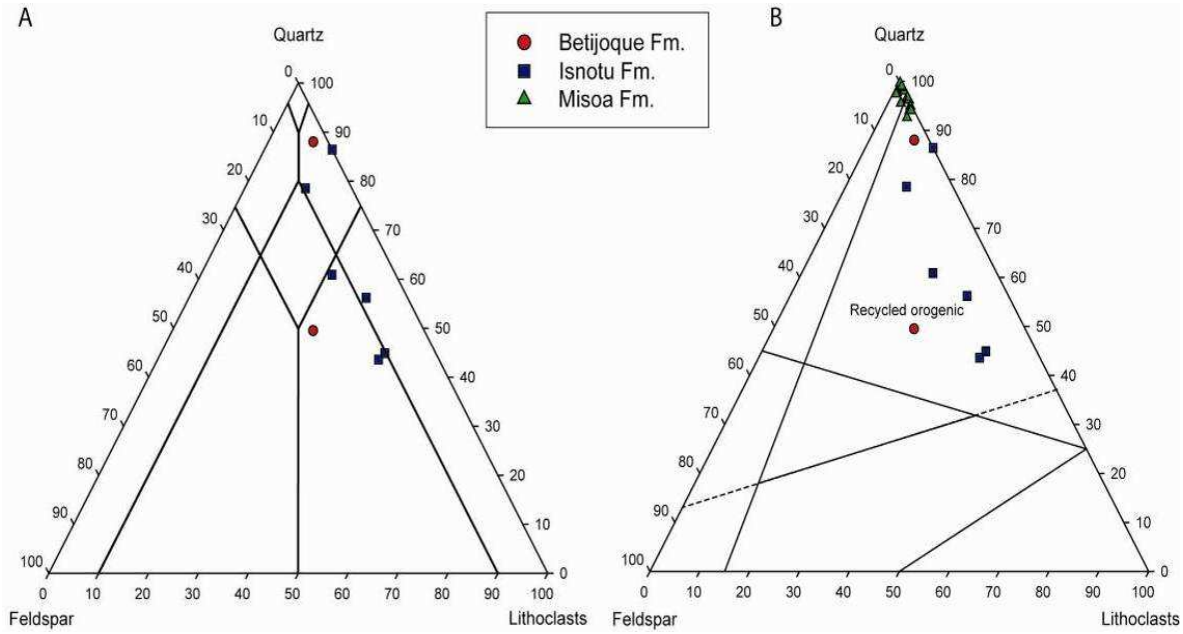

Fig. 7.6. A) The analyzed samples can be classified as sub-litharenite and litharenites classified after McBride (1963). B) All samples of the Isnotú and Betijoque formations fall into the "recycled orogenic" field on the QFL diagram after Dickinson et al. (1985). For comparison point-counting results of the Eocene Misoa Formation are shown.

Sample	Quartz	Feldspar	Lithoclast
Isnotu and Betijoque Fm			
B-113	88.0	3.0	9.0
B-306	49.5	22.3	28.2
I-324	43.6	12.1	44.3
I-325	78.5	9.3	12.2
I-331	44.9	10.2	44.9
I-333	56.2	8.3	35.5
I-128	60.9	12.8	26.3
I-157	86.4	0.0	13.6
Misoa Fm			
S5	96.5	0.3	3.2
S6	98.0	0.3	1.7
S7	98.0	0.0	2.0
S8	96.2	0	3.8
S9	94.9	0.3	4.8
S10	95.5	1.9	2.6
S11	97.7	1.6	0.7
S12	97.4	1.9	0.7
S13	94.0	1.0	5.0
S14	94.0	0.6	1.4
S15	98.7	0.0	1.3
S16	96.8	0.0	3.2
S17	99.7	0.0	0.3
S18	92.6	2.2	5.2
S19	99.0	0.0	1.0
S20	96.8	0.0	3.2

Table 7.5. Point count results of the Isnotu, Betijoque and Misoa formations. Results have been normalized to 100%. Up to 300 points were counted per thin-section. Point-counting results of the Isnotú and Betijoque formations are from Mehrkian (2009), while Misoa Formation results are from Housiau (2009).

7.5.5 The Río Hoyos-Río Vichú stratigraphic section

The Pliocene Betijoque Formation of the Maracaibo basin was studied along two river profiles, the Río Hoyos and Río Vichú, to the north of the village Betijoque, in the state of Trujillo. Because of limited accessibility and poor outcrop conditions, our field work was focused on the upper part of the Vichú member and most of the Sanalejos member of the Betijoque Formation. The total section that we analyzed has a thickness of about 2700 m (Figs. 7.2A, 7.3). For most of the section the strata strike and dip consistently at about N58° NW35°, except at the top of the section where the dip rapidly becomes sub-horizontal to the NW (Fig. 7.2A). While the upper part of the Vichú member contains several meter thick alternating fine sandstone and mudstone deposits (Fig. 7.7A), the Sanalejos member is marked by 1 to 2 m thick, mainly matrix supported polymict conglomerate layers, alternating with sandstone and mudstone layers (Fig. 7.7B and C). Conglomerate clasts of the Sanalejos member include gneiss, granite, amphibolites, sandstone, mudstone and vein quartz pebbles (Fig. 7.3C). Sedimentary structures observed in sandstone layers of the Betijoque Formation include cross-bedding with climbing ripples (Fig. 7.7D) or flame structures (Fig. 7.7E). Certain mudstone layers contain fossil leaf fragments and imprints (Fig. 7.8).

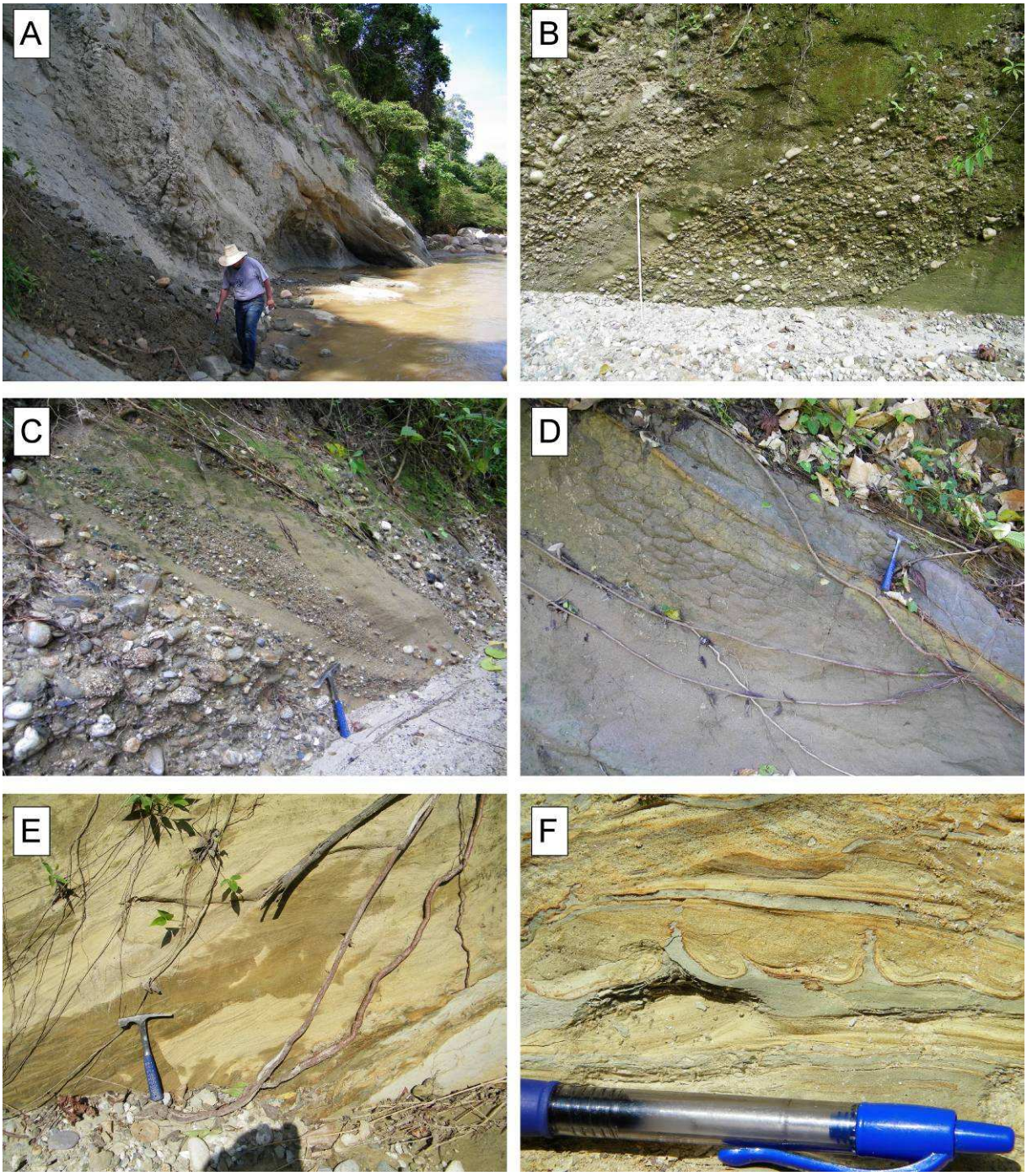

Fig. 7.7. A) Alternating fine sandstone and mudstone deposits of the Vichú member. B-D) The Sanalejos member is marked by 1 to 2 m thick, mainly matrix supported polymict conglomerate layers, alternating with sandstone and mudstone layers. E) Sedimentary structures observed in sandstone layers of the Betijoque Formation include cross-bedding with climbing ripples or F) flame structures.

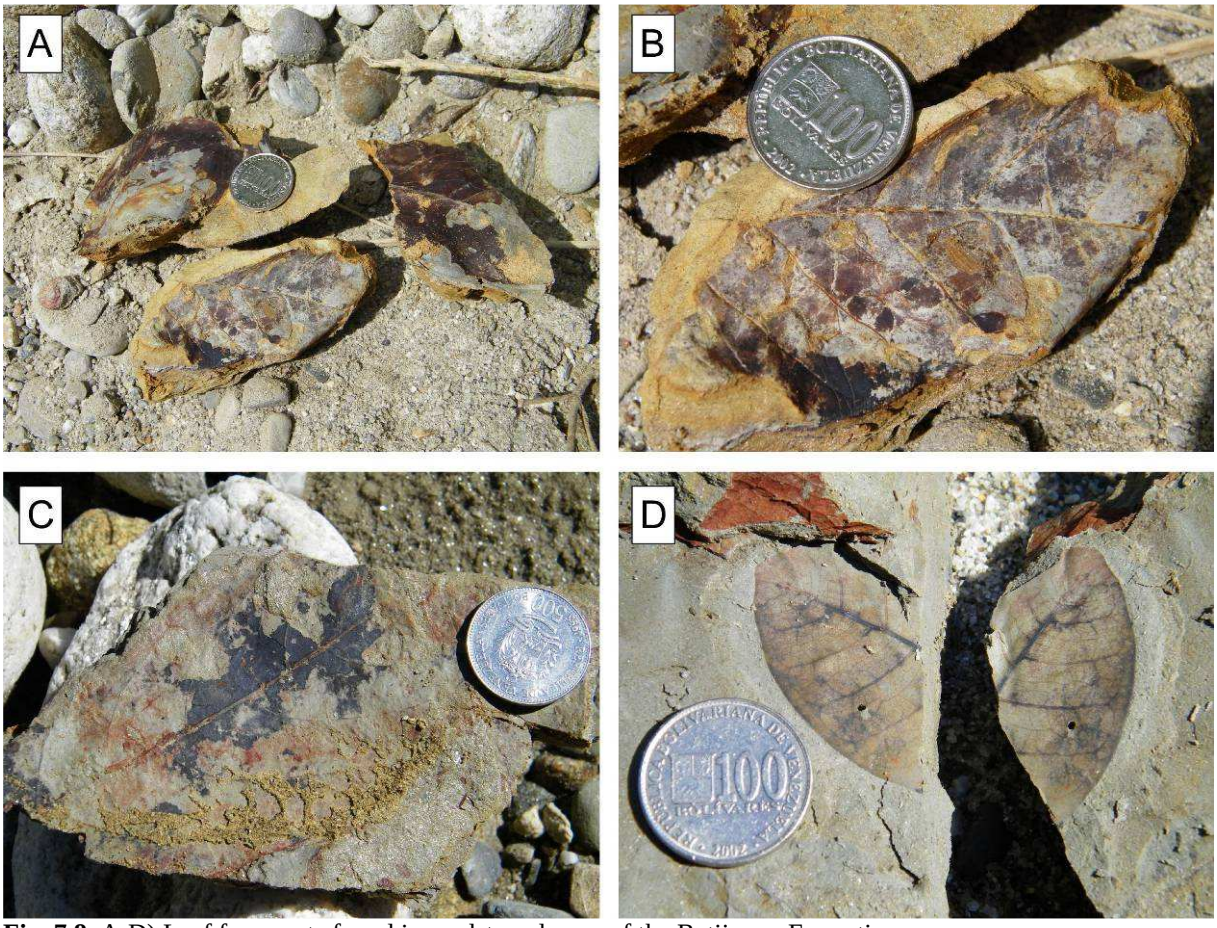

Fig. 7.8. A-D) Leaf fragments found in mudstone layers of the Betijoque Formation.

7.5.6 Parángula River stratigraphic section

The Parángula Rivers section was studied along the Parángula River to the west, southwest, and south of Barinitas in the state of Barinas on the southern flank of the Mérida Andes. The total thickness of the section we studied is about 2700 m (Fig. 7.4). Near the base of the studied section is the contact to the Eocene Pagüey Formation. The strata of the Pagüey Formation are gently folded and the southern limb of the anticline strikes and dips N50° SE37° (Fig. 7.2B). The overlaying Parángula Formation has a strike and dip of N45° SE44° near the contact, but the dip angles increases to on average to SE60° upsection. Unfortunately the contact is not exposed. More apparent is the difference in lithology between shallow marine, thin bedded quartz rich sandstone layers and the red fluvial sand and mudstones of the Parángula Formation (Fig. 7.9A and B). The contact between the Parángula Formation and the overlying Río Yuca Formation is not exposed along the Parángula River, but is marked by a lithologic change to several dm to m thick, beige, mudstone and fine to coarse grained sandstone of the Río Yuca Formation (Fig. 7.9C and D). From about the middle of the Río Yuca Formation on first matrix supported polymict conglomerate layers appear. These layers

are more frequent to the top of the section (Fig. 7.9E and F). Similar to the Betijoque Formation the conglomerates include gneiss, granite, sandstone, and vein quartz clasts. Some mudstone outcrops of the Río Yuca Formation yielded leaf fragments and a *Hemisinus* fossil (Fig. 7.10). This gastropod is a neotropical snail genus, whose members almost entirely live in fresh water streams and, lakes (F. Wesselingh, pers. comm.).

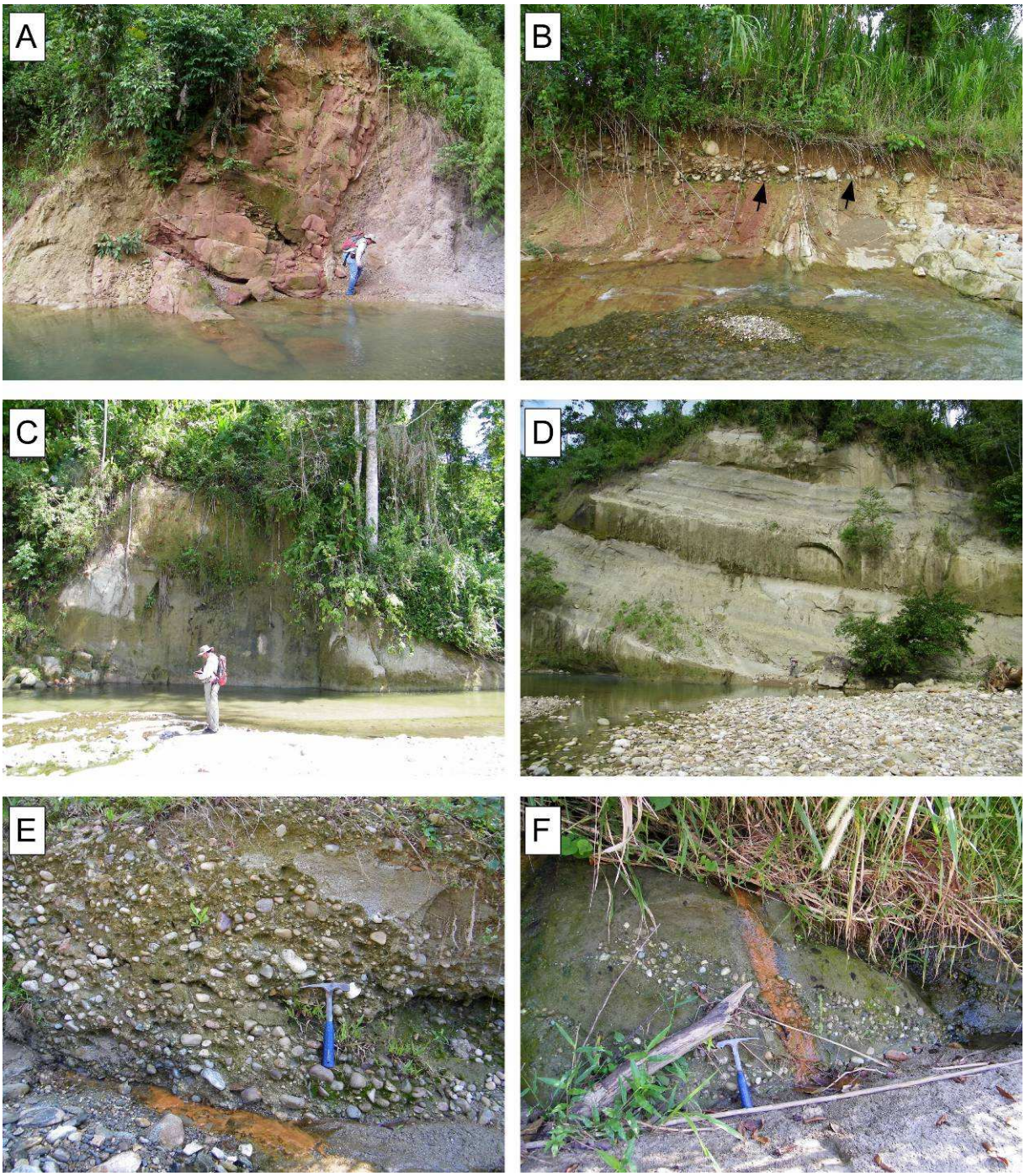

Fig. 7.9. A) Outcrop of red mudstone and sandstone of the Parángula Formation W of Barinitas. B) Angular unconformity (black arrows) between the middle Miocene Parángula Formation and Quaternary fluvial conglomerates of the Parángula River. C-D) Alternating channel and flood plain deposits of the sandy

meandering system of the Río Yuca Formation. E-F) Polymict, matrix supported conglomerate layers in the upper Río Yuca Formation**.**

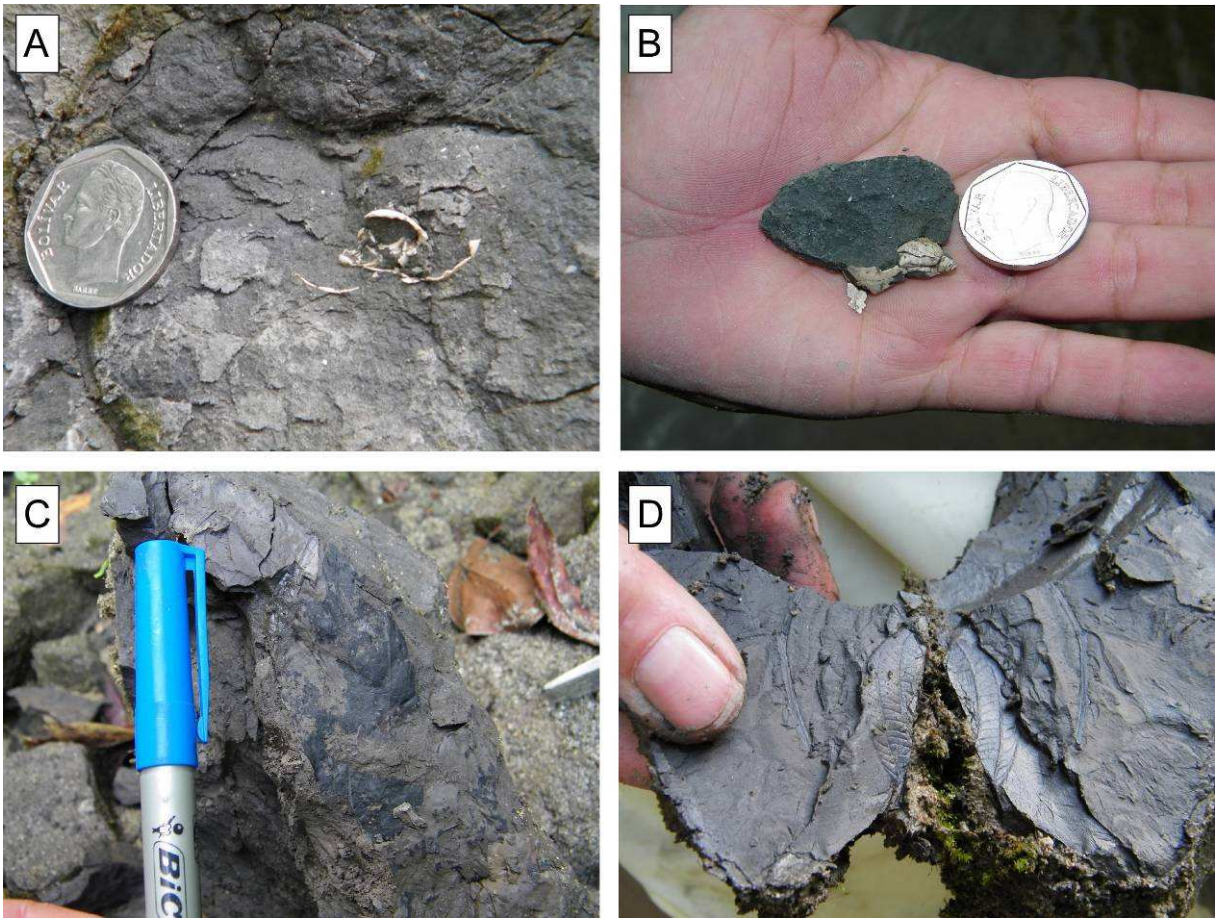

Fig. 7.10. A-B) Gastropod fossil fragments (*Hemisinus)* and C-D) leaf imprints from mudstone of the Río Yuca Formation.

7.6 Discussion

7.6.1 Stratigraphy and provenance of the two foreland basins

7.6.1.1 Depositional environments

The lithologies and sedimentary structures preserved in the Betijoque Formation can be summarized in two facies. The deposits of the upper part of the Vichú member resemble deposition in sandy meandering river system, given the thickness of relatively deep sandy channel and fine grained overbank deposits. The Sanalejos member on the other hand seems to be better characterized as a deep gravel-bed river system (Miall, 1996). This indicates an increase in transport energy either associated with an increase in slope or discharge. The litho facies preserved in the Parángula Formation resemble a fine-grained meandering river system.

Energy must have increased in the paleo-drainage system in the Late Miocene and Pliocene during deposition of the Río Yuca Formation because of a change to a sandy meandering to gravel sand meandering system. Overall the depositional style of the Río Yuca Formation strongly resembles the middle Siwaliks in Nepal and Bhutan of the Himalayan foreland basin.

7.6.1.2 Depositional ages

As mentioned above, depositional ages of the Mio-Pliocene deposits in the Maracaibo and Barinas basins, are not well constrained. Our palynological analyses do help us with establishing at least some age limits. For the Betijoque Formation, so far only two samples from the middle of the section, CH100 and CH105 have been analyzed (position RH18 and RH19 in Fig. 7.7, Table 7.2). These samples contain a Pliocene marker species, *Echitricolporites mcneillyi*. However, *Echitricolporites spinosus, Cyatheacidites annulatus and Lophosoria* indicate reworking of Late Miocene-Pliocene sediment from the lower part of the section.

For the upper Río Yuca Formation a Pliocene age is based on biostratigraphic marker species *Echitricolporites mcneillyi* (Germeraad et al. 1968) in samples CH26 and CH60, *Fenestrites spinosus* (van der Hammen 1956; Lorente, 1986) in sample CH26, *Stephanocolpites evansii* (Muller et al. 1987) in samples CH26, CH38, and CH50, and *Striasyncolpites zwaardii* (Germeraad et al. 1968) in sample CH31 (Table 7.3). The stratigraphic position of these samples is shown in Figure 7.4. Similar to the Betijoque Formation Late Miocene-Pliocene marker species *Echitricolporites spinosus* (Van der Hammen 1956, Germeraad et al. 1968), *Grimsdalea magnaclavata* (Germeraad et al. 1968) and *Cyatheacidites annulatus* or *Lophosoria* (Cookson, 1947) in samples CH21, CH26, CH31 and CH40 located in the middle of the section (location PAS39, Fig. 7.4) indicate recycling of Late Miocene sediments during deposition of the upper part of the Río Yuca Formation, which therefore has a Pliocene age. The pollen samples of the Parángula Formation have not been analyzed so far and are therefore not yet available interpretation.

In lieu of more precise biostratigraphic or magnetostratigraphic information detrital AFT ages can be used as a proxy for the depositional age, as the youngest grains or peak age in a detrital age should be the same or older than the depositional age (Kowallis et al. 1986; Bernet and Garver, 2005). In case of volcanic deposits, the (youngest) peak age is the same as the

depositional age, because of very fast cooling following an eruption. However, no volcanic layers have been observed in the Betijoque, Río Yuca or Parángula formations. Therefore the youngest peak is not directly equivalent to the depositional age, but may be close to it, given a certain lag time and error of the peak age estimate. This relation only holds if fission tracks in apatite were not reset after deposition because of burial heating. HI plotted versus Tmax presented in Figure 7.5 suggests that samples CH52 and CH55 from the Río Yuca Formation, and samples RV1 and RV2 from the Betijoque Formation never reached sufficient burial depth and heating for oil maturation (Fig 7.3, 7.4 and 7.5). The Tmax values for these 4 samples are inferior to 430-435°C, which merely corresponds to the beginning of hydrocarbon formation (Espitalié et al. 1977). Therefore, AFT ages were not reset in our samples and the young peak ages can be used as proxies for depositional ages. That the samples were not heated is not a surprise. While the thermal gradients within the Maracaibo and Barinas basins are not well known, it has been shown that foreland basins in general tend to be relatively cool, with low thermal gradients of 15-25°C/km (Allen and Allen, 2005). Assuming a mean surface temperature of 20°C and a thermal gradient of 20°C/km even the most deeply buried samples in our sections have hardly experienced the beginning of partial annealing. Therefore, samples V97 and V95 of the Betijoque Formation indicate a maximum Late Miocene – early Pliocene depositional age for the base of the section we studied (Fig. 7.3, Table 7.1). For the Parángula section a maximum middle –Late Miocene deposition age can be discerned from sample TPG2 toward the base of the studied section (Fig. 7.4, Table 7.1). It is apparent that the ages of the youngest peaks in the two sections remain fairly constant, 4-6 Ma in the Rio-Hoyos/Río Vichú section and 9-7 Ma in the Parángula River section (except for the upper to samples who have the same young peaks as found in the Betijoque Formation). This phenomenon of static peaks will be discussed below.

7.6.1.3 Sediment provenance

Sandstone petrology and pebble lithologies are good indicators of sediment provenance. On both sides of the Mérida Andes the Miocene-Pliocene foreland basin deposits received sediment from the crystalline core of the mountain belt. This is shown by gneiss and granite lithic fragments in the sandstones and gneiss, granite and amphibolite clasts in the conglomerates. The variety of observed granite clast includes micro-granular granite, and epi-granular granite with large feldspars and/or hornblende. Further petrologic work on these clasts is needed to relate them more closely to Mesozoic, Paleozoic and Proterozoic

crystalline rocks. Beside the crystalline fragments, sedimentary rock fragments and clasts are common. The appearance of sedimentary rock fragment is an indication of sediment recycling, particularly during deposition of the Pliocene Betijoque and upper Río Yuca formations. The recycled sedimentary rock fragments have three possible sources: A) Mesozoic and Paleozoic cover rocks of the Mérida Andes, B) shallow marine Eocene deposits, such as the Pagüey Formation, and C) recycling of poorly consolidated Middle to Late Miocene foreland basin deposits. Sedimentary fragments derived from Mesozoic and Paleozoic cover rocks can be recognized because they are well cemented and rounded. Our pollen analyses show significant abundance of mature (dark brown) Eocene pollen and dinoflagelates in the Pliocene samples, a clear indication for the recycling of Eocene sediments. The same is true for the Pliocene samples that contain recycled Late Miocene pollen.

A similar picture emerges when studying the detrital AFT grain age distributions and peak ages. In Figure 7.11 the AFT peak ages versus stratigraphic depth are shown. The youngest populations P1 and P2 of the Betijoque Formation samples have more or less static peaks at ~5-6, and 10-11 Ma. The exceptions are samples V90 and V97, in which the 10-11 Ma peak is missing (Fig. 7.3, 7.11A, Table 7.1). The samples of the Parángula and Río Yuca formations in the Barinas basin show a similar trend. The first two peaks of samples TPMY7 and TPMY8 are the comparable to the peak ages found in the Betijoque Formation. The stratigraphically older samples of the Parángula section have “young” peak ages of about 7-9 and 15-16 Ma. Older peak ages mainly range between 20-30 Ma (Table 7.1). The question is: What is the meaning of all these peak ages?

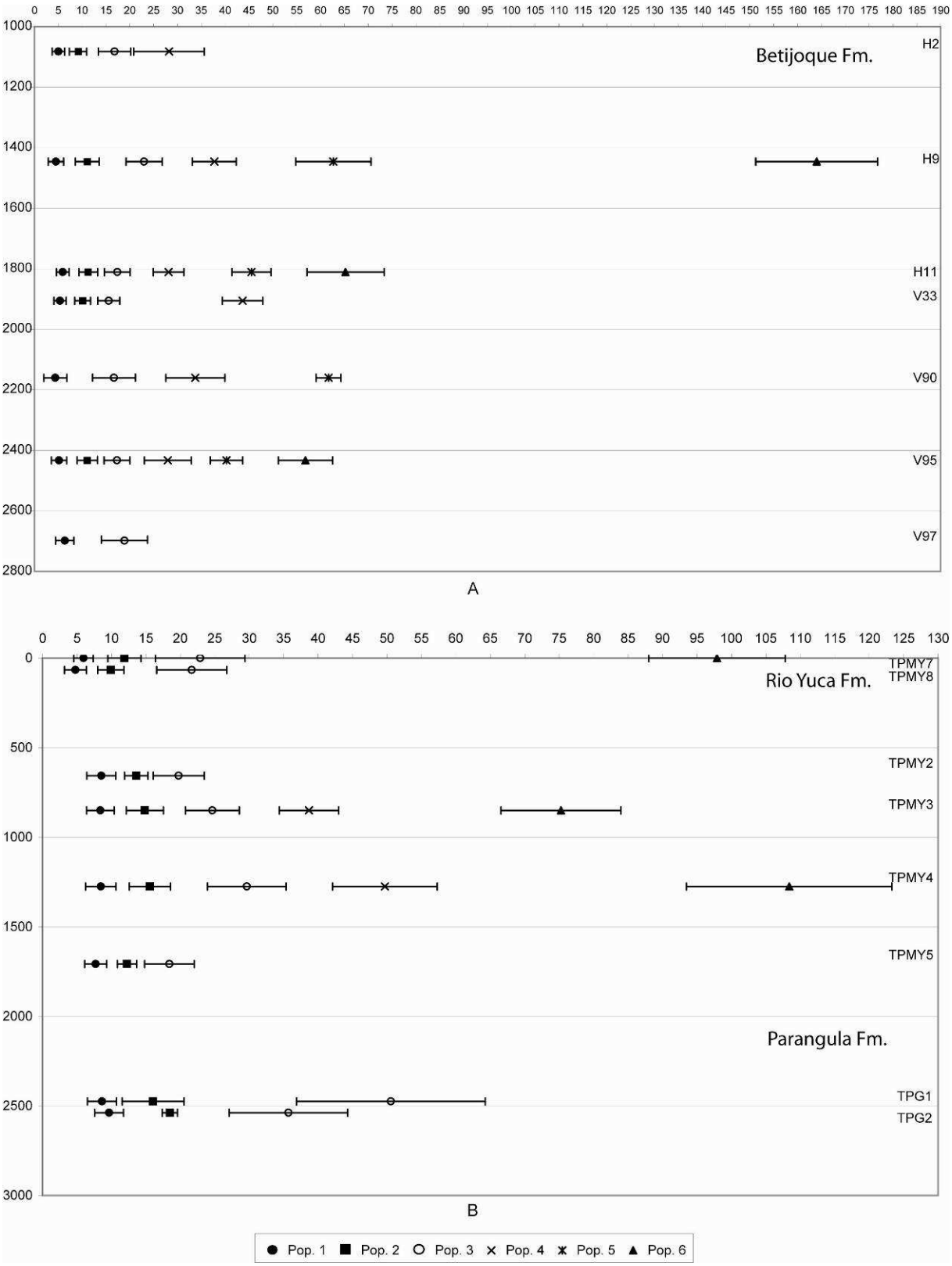

Fig. 7. 11. Up-section variation of AFT age populations: A) Betijoque Formation. B) Parángula and Río Yuca formations. Component ages were determined with the p-partition method (Bermúdez-Cella, 2008, see Appendix 1, 2) and are given considering the standard deviation (σ) on each population.

7.6.2 Neogene exhumation history of the Mérida Andes

Bedrock AFT ages of the crystalline core of the Mérida Andes have been published by Kohn et al. 1984 and Bermúdez et al. (submitted; chapters 4 and 5 in this work). The detrital AFT ages in the foreland basin on both sides of the mountains correspond closely to the published bedrock ages in the mountains. Apatites with 20-30 Ma cooling ages are originally derived from the Valera or the Caparo block (Bermúdez et al. submitted; chapters 4 and 5 in this work). The 7-11 Ma to 15-16 Ma peaks related to exhumation of the Sierra Nevada and Sierra La Culata blocks during the middle-Late Miocene (Bermúdez et al. submitted; chapters 4 and 5 in this work). The youngest peak ages at around 5 Ma are associated with exhumation of the El Carmen block (small Sierra La Culata block, Kohn et al. 1984) for apatites found in the Maracaibo basin, and exhumation of the Santo Domingo gneiss in the Barinas basin. Because the exhumation of the central tectonic blocks in the Mérida Andes was episodic, the detrital age spectra present static peaks. Sediment recycling of foreland basin sediments may reinforce the static peaks in the younger samples further up-section. The older, more slowly but continuously exhuming Valera and Caparo blocks provide a “moving” peak signal (Fig. 7.11).

7.7 Conclusions

Oblique convergence between the Maracaibo Block and the South American plate since the middle to Late Miocene resulted in major surface uplift and formation of the Mérida Andes. Because the Mérida Andes are a doubly vergent mountain belt, two foreland basins developed. The Maracaibo pro-side foreland basin was formed on the northern flank, and the Barinas retro-side foreland basin on the southern flank of the Mérida Andes orogenic wedge.

Contrary to previous estimates, the fluvial Parángula Formation in the Barinas basin seems to be of middle Miocene age, based on AFT data, because burial was insufficient for resetting of fission-tracks in apatite, as shown by Rock-Eval analysis of organic matter. Our stratigraphic, petrologic, pollen and thermochronologic analyses demonstrate that the lower Río Yuca Formation is of Late Miocene age, while the upper Río Yuca Formation in the Barinas basin and the Betijoque Formation in the Maracaibo basin were deposited during the Pliocene. The detrital AFT data presented in this work are consistent with the exhumation patterns and

tectonics of the Mérida Andes presented by Kohn et al. (1984) and Bermúdez et al. (submitted, chapters 4 and 5 in this work).

7.8 Acknowledgements

This study was supported by the Consejo de Desarrollo Científico y Humanístico (CDCH-UCV) de la Universidad Central de Venezuela (UCV), Project PI 08-00-6219-2006; Fondo Nacional de Ciencia y Tecnología (FONACIT) Project Number S1-200000636; ECOS Nord project V08U01 and the support provided by Petróleos de Venezuela, SA (PDVSA) in 1990-1995. We also thank Roel Verreusel for the detailed study of dinoflagellates of the Río Yuca Formation; and François Senebier for mineral separations.

Chapter 8

VIII. GENERAL CONCLUSIONS

8.1 Conclusions

The main conclusions of this thesis are:

1) Based on 68 *in-situ* AFT ages, thermal modelling and topographic analyses it was possible to conclude that:

- There are at least seven individual tectonic blocks in the Venezuelan Andes: the Cerro Azul, Escalante, Caparo, Valera, Sierra La Culata, El Carmen, and Sierra Nevada blocks, characterized by different topographic and exhumation patterns. The first four blocks exhibit lower values of mean elevation, between 1160 and 1695 m. High topography between ~3000-3200 m characterizes the blocks located in the central part of the Venezuelan Andes.
- Youngest AFT ages (1-3 Ma) and longest mean tracks lengths (MTL; ~14-15 μm) are found close to the Boconó fault, specifically in samples from the El Carmen block and at the limit between the Sierra La Culata and Escalante blocks. AFT ages between 4-8 Ma are concentrated in the central part of the Venezuelan Andes, in the Sierra La Culata and Sierra Nevada blocks, and on both flanks of the chain in the Escalante block and the Cerro Azul thrust block. The MTL results are compatible with rapid cooling through the apatite PAZ, followed by residence at shallower depths of these blocks.
- Older AFT ages and shorter MTL (~12-13 μm) were found in the Caparo block with ages between 7-30 Ma, which are clearly younger than the depositional ages of the Triassic-Jurassic La Quinta formation (Hargraves and Shagam, 1969) from which they were collected. The Valera block is characterized by a wide range of AFT ages and short MTL (~12-13 μm), increasing from 8 Ma at its southeastern limit to 145 Ma in the north.
- The temporal changes in boundary conditions, related to collision of the Caribbean plate, accretion of the Panamá arc (Cediel et al. 2003) and clockwise rotation of the Maracaibo block (Montes et al. 2005) have caused reactivation of pre-existing fault zones that currently function as right-lateral strike-slip (Boconó, Central Sur Andino and Caparo fault systems), left-lateral strike-slip (Valera and Burbusay faults system),

and thrusts faults. These structures exert the primary control on exhumation patterns found across the Venezuelan Andes.

- The exhumation patterns are consistent with the tectonic assembly of the Northern Andes.

2) Based on two AFT age-elevation profiles in the Sierra Nevada and Sierra La Culata, blocks of the Venezuelan Andes, the data and numerical modelling demonstrate the following:

- Late Neogene exhumation of the Venezuelan Andes was diachronous across the Boconó fault. The data imply that the Boconó Fault also accommodates km-scale vertical offsets.
- Rapid Late Miocene exhumation in the Sierra Nevada implies that crustal thickening and (oblique?) compression were well established by that time, possibly as a response to Late Miocene accretion of the Panamá arc to the western margin of Colombia during this period.
- Subsequent rapid exhumation of the Sierra La Culata in Pliocene times implies continuous oblique convergence of the Maracaibo Block and South America.
- The maximum surface uplift of the Sierra Nevada is consistent with Late Miocene deflection of the Orinoco and Magdalena rivers, as inferred from the Neogene sedimentary record (Hoorn et al. 1995; Díaz de Gamero, 1996).

3) Comparison of the in-situ AFT age database and the integration of eight detrital AFT ages from modern river sediments with short-term climatic and tectonic records (precipitation, seismic energy release, and erosion index calculations) permit to conclude that:

- The detrital AFT ages of eight river catchments of the Venezuelan Andes reproduce and confirm in an efficient way the exhumation patterns discriminated by in-situ AFT data.
- Detrital AFT thermochronology is an important tool for studying sediment provenance and long-term erosion in complex areas with difficult access, such as in the Venezuelan Andes, exhibiting high resolution along the catchments.
- Exhumation rates are strongly correlated to relief in the catchments, suggesting a strong topographic control on erosion.
- There is no strong correlation between long-term exhumation rates and present-day precipitation patterns. In particular, the north-western flank of the belt appears to be

exhumed more rapidly than the south-eastern flank, despite a threefold increase in precipitation from north to south due to the orographic effect.

4) AFT analysis on synorogenic sediments permits to conclude that:

- The Pliocene-Pleistocene Betijoque and Late Miocene-Pliocene Río Yuca formations located in the northern and southern foothills, respectively, contain the same record of exhumation as shown by in-situ AFT data.
- Older populations inside the molasse sediments (Betijoque, Río Yuca and Parángula) provide evidence to support the reactivation of inherited structures and the Eocene-Oligocene origin of the chain.
- Five different geodynamic events are preserved in these sediments: three static peaks at 5 Ma, 9 Ma and 15 Ma could indicate the beginning of tectonic reorganization and surface uplift in the Venezuelan Andes as suggested by Hoorn et al. (1995) and Montes et al. (2005), which finished with the closure of Panamá Isthmus; a moving peak at 25 Ma could be related to rotation and accretion of the Eastern Cordillera of Colombia; and a continuous supply of apatites of Paleocene-Eocene age could correspond to recycling of sediments or a Pre-Andean structure.
- Although the depositional ages of the sedimentary rocks sampled in the Maracaibo and Barinas basins are not well known, important constraints were obtained by the other methods used in this work: Palynology and Rock-Eval analysis. The first suggests a Late Miocene-Pliocene limit for the Betijoque and Río Yuca formations, and the presence of reworked material of Eocene age. The Rock-Eval analyses indicate that the Mio-Pliocene sediments of Río Yuca and Betijoque in these basins have not been buried deeply enough to allow significant thermal resetting of fission-tracks. Thus, young AFT age peaks in the observed grain-age distributions can be used as a minimum proxy for the depositional age.
- The young AFT ages (9-10 Ma) found in the Parángula Formation imply that this formation is probably much younger than generally believed (Middle Miocene).
- The Pliocene Betijoque Formation in the north and the upper part of the Río Yuca Formation in the south were deposited at about the same time.

The results obtained in this study are support a geological model of the Venezuelan Andes, in which the chain is partitioned into several tectonic blocks bounded by major fault systems.

These blocks are exhumed at different times and rates. New exhumation erases the record of previous exhumation periods. This makes it difficult to discriminate between existing geodynamic models: 1) flower structure model or 2) orogenic float model. Which model is more appropiate? To better discriminate between the two models other low temperature thermochronometeric data is needed in addition to seismic analysis of deep structure beneath the Venezuelan Andes. It is absolutely necessary to know the structures at depth and to consider the possible rotation and translation of individual tectonic blocks.

8.2 Synthesis

In spite of difficulties and limitations characteristic of any research project, this dissertation has contributed to the following elements of our understanding of the origin and evolution of the Venezuelan Andes in the regional context:

1. I contributed with new in-situ, modern river, and synorogenic AFT data to the reconstruction of the Cenozoic to recent kinematics of this orogen.
2. I demonstrated the partitioning of the chain in different blocks that respond in different ways to the deformation caused by the triple convergence of tectonic plates.
3. I presented a possible tectonic reconstruction, which includes at least one part of the Northern Andes (Colombia), and relates the different cooling phases associated with regional tectonic events, as recorded in AFT ages across the Venezuelan Andes
4. I showed that the long-term exhumation is controlled by tectonically driven surface-uplift and erosion, and less by climate.

8.3 Future perspectives

Being the responsible faculty of a fully functional fission-track laboratory at the Universidad Central de Venezuela in Caracas, allows me to continue my work and develop new projects in Venezuela and beyond when I return to Caracas. This work will include national and international collaboration. In the future, much research remains to be done, for example:

1. Increase the database of apatite fission-track ages of in-situ, synorogenic, and modern rivers samples with the purpose of understanding tectonic processes in more detail in certain key areas, in particular the remote southern flank of the orogen.
2. Include higher-temperature zircon fission-track or (U-Th)/He data in order to better constrain the total exhumation of different blocks in the Venezuelan Andes.
3. Apply new low-temperature thermochronometers, such as (U-Th)/He, or ^{3}He-^{4}He, which are more sensitive to surface processes and permit explaining topographic changes.
4. Incorporate the entire existing database into new 3-D thermal modelling using Pecube and test different tectonic models.
5. Extend this work to the rest of the Northern Andes and develop geodynamic models that take the regional tectonics and surface processes into account.

Chapter 8

VIII. CONCLUSIONS GÉNÉRALES

8.1 Conclusions

Les principales conclusions de cette thèse sont:

1) Sur la base de 68 nouveaux âges AFT *in-situ*, couplés à la modélisation thermique et des analyses topographiques, il a été possible de conclure que :
   - Il est possible de discriminer sept blocs tectoniques distincts: Cerro Azul, Escalante, Caparo, Valera, Sierra Culata, El Carmen, et Sierra Nevada. Ces blocs sont caractérisés par des caractéristiques topographiques et des histoires d'exhumation différentes. Les quatre premiers blocs présentent des valeurs d'altitude moyenne relativement faibles, entre 1160 et 1695m. Une topographie moyenne entre ~3000-3200 m caractérise les blocs situés dans la partie centrale des Andes vénézuéliennes.
   - Des âges jeunes (1-3 Ma) et des traces de fission longues (~14-15 µm) ont été trouvés à proximité de la faille de Boconó, dans le bloc d'El Carmen et à la limite entre la Sierra La Culata et le bloc El Escalante. Des âges AFT entre 4 et 8 Ma sont concentrés dans la partie centrale des Andes vénézuéliennes, dans les blocs de la Sierra Culata et la Sierra Nevada, ainsi que sur les deux flancs de la chaîne, dans le bloc Escalante au nord et le bloc Cerro Azul au sud. L'analyse des longueurs de traces est compatible avec un refroidissement rapide à travers la zone de recuit partiel ou "Partial Annealing Zone" (PAZ) suivi d'une résidence à des profondeurs moindres pour ces blocs.
   - Des âges anciens et de faibles longueurs de traces de fission (~12-13 µm) ont été trouvés dans le bloc Caparo, au sud-ouest de la chaîne. Ici, les âges varient entre 7 et 30 Ma, clairement plus jeunes que les âges de dépôt de la Formation La Quinta (Hargraves et Shagam, 1969) d'où les échantillons ont été recueillis. Le bloc de Valera, au nord-est, est caractérisé par une grande variété d'âges AFT et des longueurs comparables à celles du bloc Caparo. Un âge de 145 Ma a été trouvé au nord du bloc de Valera. Les faibles longueurs de traces dans ces deux blocs indiquent un refroidissement relativement lent, avec une résidence dans la PAZ plus étendue.
   - Les changements temporels dans les conditions aux limites de la plaque Amérique du Sud, liées à la collision de la plaque Caraïbe, l'accrétion de l'Arc de Panama (Cediel et al. 2003) et la rotation horaire du bloc de Maracaibo (Montes et al. 2005) ont réactivé plusieurs paléo-structures. Les plus importantes sont les systèmes de failles

décrochantes dextres de Boconó, Central Sur-Andino et Caparo, ainsi que les systèmes nord-sud de failles décrochantes sénestres de Valera et Burbusay et les chevauchements sur les deux flancs des Andes. Toutes ces structures sont compatibles avec l'ensemble tectonique des Andes du Nord de l'Amérique du Sud, et contrôlent la variabilité de l'exhumation à travers les Andes vénézuéliennes.

2) La modélisation numérique des données récoltées le long de deux profils altitudinaux dans les blocs de la Sierra Nevada et de la Sierra La Culata, situés dans la partie centrale des Andes vénézuéliennes, démontre que :
   - L'exhumation Néogène des Andes vénézuéliennes a été diachronique à travers la faille de Boconó. Les données impliquent que cette faille accommode également des mouvements verticaux d'échelle kilométrique.
   - L'exhumation de la Sierra Nevada de Mérida a été rapide pendant le Miocène tardif ; cela implique l'épaississement de la croûte et donc de la convergence (oblique ?) pendant cette époque. Cette convergence peut être une réponse à l'accrétion de l'arc de Panama à la marge occidentale de la Colombie.
   - L'exhumation rapide de la Sierra La Culata pendant le Pliocène implique une convergence oblique continue entre le bloc de Maracaibo et l'Amérique du Sud jusqu'à au moins cette période.
   - Un soulèvement maximal de la surface de la Sierra Nevada au Miocène est compatible avec la déviation Miocène tardive de paléo-rivières au sud et à l'ouest : l'Orénoque et Magdalena, qui a été déduite de l'enregistrement sédimentaire Néogène (Hoorn et al. 1995, Diaz de Gamero, 1996).

3) La comparaison entre les résultats de thermochronologie *in-situ* et détritique dans les sédiments actuels de 8 rivières, combinée avec une base de données de contrôles potentiels sur l'exhumation comme les précipitations, la sismicité et des indices du taux d'érosion a permis de conclure que :
   - Les résultats sur les sédiments corroborent et reproduisent efficacement le schéma d'exhumation observé sur les données *in-situ*.
   - La thermochronologie détritique est un outil efficace pour étudier la provenance et les effets de l'érosion à grande échelle, sur des zones d'accès difficile comme les Andes

vénézuéliennes. Les résultats présentés dans ce travail indiquent que cet outil a une résolution comparable à la thermochronologie *in-situ*.

- Les taux d'exhumation dans les bassins-versants étudiés sont fortement corrélés avec le relief, ce qui suggère un fort contrôle topographique sur l'érosion.
- Il n'y a pas de forte corrélation entre les taux d'exhumation à long terme et la distribution actuelle des précipitations. En particulier, le flanc nord-ouest de la chaîne semble être exhumé plus rapidement que le flanc sud-est, malgré l'augmentation des précipitations du nord au sud comme conséquence de l'effet orographique.

4) L'analyse par traces de fission des apatites provenant des sédiments syn-orogéniques a permis de conclure que :
   - La Formation Pliocène-Pléistocène de Betijoque sur le flanc nord, et la Formation Miocène-Pliocène de Río Yuca située au sud, montrent des variations d'exhumation qui réflètent celles enregistrées par les données in-situ.
   - Des populations d'âges anciennes, trouvées dans les sédiments molassiques (Betijoque, Río Yuca et Parángula) renforcent l'hypothèse de la réactivation de structures héritées et l'origine Eocène-Oligocène des Andes vénézuéliennes.
   - Cinq événements géodynamiques différents sont enregistrés dans ces sédiments: trois pics statiques à 5, 9, et 15 Ma pourraient indiquer le début de la réorganisation tectonique rapportée par divers auteurs (Hoorn et al. 1995; Montes et al. 2005) qui se termine avec la fermeture de l'arc de Panamá entre 2 et 3 Ma. Un pic mobile à 25 Ma pourrait être liée à la rotation et l'accrétion de la Cordillère Orientale colombienne, et un approvisionnement continu d'apatites d'âge Paléocène-Eocène pourrait correspondre au recyclage des sédiments ou à la présence d'une structure préandine.
   - Les âges de dépôt des séries molassiques ne sont pas bien contraints jusqu'à présent. L'intégration de la thermochronologie avec d'autres méthodes comme la palynologie et le Rock-Eval suggère que les formations Betijoque et Isnotú n'ont jamais atteint une profondeur d'enfouissement suffisante pour recuire les traces de fission dans les apatites. Ainsi, les composantes d'âges les plus jeunes discriminés dans la distribution d'âges AFT peuvent être considérées comme une estimation maximale de l'âge de dépôt.

- Des âges AFT jeunes (9-10 Ma) ont été trouvés dans la Formation Parángula et impliquent que cette formation est probablement beaucoup plus jeune (Miocène moyen) que précédemment admis.

Les résultats obtenus dans cette étude soutiennent un modèle géologique des Andes du Venezuela, dont la chaîne est partitionnée en plusieurs blocs tectoniques délimitée par des principaux systèmes de faille. Ces blocs sont exhumés à des moments et taux d'exhumation différents. Les dernières exhumations effacent le record de l'exhumation des périodes précédentes. Il est donc difficile de discriminer entre les deux modèles géodynamique existants: 1) modèle de structure en fleur ou 2) le modèle de orogéniques flottant. Quel modèle est le plus approprié? Afin de mieux distinguer entre les deux modèles, est nécessaire plus de données thermochronologiques, en plus de l'analyse sismique de la structure profonde sous les Andes vénézuéliennes. Il est absolument nécessaire de connaître les structures en profondeur et d'examiner la possible rotation et la traslation des blocs tectoniques individuels.

8.2 Synthèse

Malgré les difficultés et contraintes propres à tout projet de recherche scientifique, cette thèse a contribué aux éléments suivants qui sont nécessaires pour comprendre l'origine et l'évolution des Andes du Venezuela dans leur contexte régional:

1. J'ai rapporté de nouvelles données de thermochronologie par traces de fission sur apatites collectés *in-situ* dans les roches du socle, ainsi que dans des sédiments de rivière actuels et des sédiments synorogéniques. Ces données peuvent être utilisées dans l'avenir pour des reconstructions géodynamiques de cet orogène au Cénozoïque.
2. J'ai démontré le découpage de la chaîne en différents blocs qui répondent de façon diverse à la déformation causée par la triple convergence de plaques.
3. J'ai proposé une reconstruction tectonique qui comprend au moins une partie de la Cordillère des Andes du Nord, correspondant à la limite entre Les Andes vénézuéliennes et la Cordillère Oriental colombienne. J'ai essayé d'associer les différentes phases de refroidissement avec des événements tectoniques régionaux importants.

4. J'ai montré que l'exhumation à long-terme est contrôlée par la tectonique, laquelle contrôle le soulèvement de surface et l'érosion, et que le climat n'exerce pas de contrôle important sur les variations spatiale des taux d'exhumation.

8.3 Perspectives et avenir

Étant responsable scientifique d'un laboratoire de thermochronologie par traces de fission (installé et à pleine capacité) au sein de mon université au Venezuela me permettra à mon retour à Caracas de développer de nouveaux projets dans la région. Mon expérience acquise pendant la thèse me donne en plus la possibilité de travailler en collaboration avec d'autres chercheurs au niveau national et international. Dans l'avenir, il reste encore beaucoup de recherche à faire, par exemple :

1. Augmenter la base de données d'âges traces de fission sur apatites dans les roches *in-situ*, sur les dépôts sédimentaires syn-orogéniques et les sables de rivières actuels dans le but de comprendre les processus tectoniques plus en détail dans certains domaines clés, en particulier sur le lointain flanc sud de l'orogène.
2. Inclure des données thermochronologiques de plus haute température (traces de fission et/ou (U-Th)/He sur zircon) afin de mieux contraindre l'exhumation totale de différents blocs dans les Andes vénézuéliennes.
3. Appliquer de nouvelles méthodes thermochronologiques de basse température (U-Th/He sur apatite), qui sont plus sensibles aux processus superficiels et peuvent expliquer les changements de relief.
4. Incorporer la base de données existante dans de nouveaux modèles thermique 3-D utilisant Pecube et tester différents modèles tectoniques.
5. Prolonger ce travail au reste des Andes du Nord, avec le but de proposer des modèles géodynamiques qui prennent en considération la tectonique régionale et les processus de surface.

Capítulo 8

VIII. CONCLUSIONES GENERALES

8.1 Conclusiones

Las principales conclusiones de esta tesis son:

1) Basado sobre las 68 edades in-situ, el modelado numérico termal y el análisis topográfico indican lo siguiente:

- Al menos siete bloques tectónicos: Cerro Azul, Escalante, Caparo, Valera, Sierra La Culata, El Carmen, y Sierra Nevada, tienen características topográficas y patrones de exhumación diferentes. Los primeros cuatro bloques exhiben los valores más bajos de elevación promedio entre 1160 y 1695 m. En contraste, valores altos de topografía promedio entre ~3000-3200 m son encontrados en el resto de los bloques localizados en la parte central de Los Andes Venezolanos.
- Edades jóvenes (1-3 Ma) por de trazas de fisión en apatitos y largas medidas de longitudes de trazas (MTL; ~14-15 μm): son encontradas muy cerca de la zona de fallas de Boconó, específicamente en el bloque El Carmen y en los límites entre la Sierra la Culata y el bloque El Escalante. Edades de trazas de fisión en apatitos entre 4-8 Ma son concentradas en la parte central de Los Andes Venezolanos, en el bloque El Escalante y el bloque constituido por los cabalgamientos de Cerro Azul. Las medidas de longitudes de trazas de fisión para las muestras en esos bloques son compatibles con rápido enfriamiento o "cooling" a través de la zona de desvanecimiento parcial de trazas de fisión o "Partial Annealing Zone (PAZ)".
- Edades antiguas y cortas longitudes (~12-13 μm) proporcionadas por el método de trazas de fisión en apatitos fueron encontradas en los bloques de Caparo entre 7-30 Ma, las cuales son más jóvenes que la edad Triásica-Jurásica de la Formación La Quinta (Hargraves y Shagam, 1969) del cual fueron colectadas las muestras. El bloque de Valera está caracterizado por un amplio rango de edades incrementándose desde 8 Ma en el límite suroeste hasta 145 Ma al norte de este bloque, análogamente se encontraron cortas longitudes de trazas de fisión (~12-13 μm) lo cual indica un enfriamiento más lento para estos bloques y una mayor residencia en la PAZ.
- Los cambios temporales en las condiciones de bordes, relacionadas a la colisión de la Placa del Caribe, acreción del Arco de Panamá (Cediel et al. 2003) y rotación horaria

del bloque de Maracaibo (Montes et al. 2005) reactivaron diversas paleo-estructuras que actualmente han evolucionado como los sistema de fallas destrales Boconó, Central Sur Andino y Caparo; sinestrales: Valera y Burbusay, así como los corrimientos situados a ambos flancos andinos. Todas esas estructuras controlan los patrones de exhumación a lo largo de Los Andes.

- Los diversos patrones de exhumación encontrados son consistentes con el ensamble tectónico de Los Andes Nortes.

2) Basado en los dos perfiles verticales a lo largo de los bloques de Sierra Nevada y la Sierra Las Culata, los datos y la interpretación de éstos mediante modelado numérico demuestra lo siguiente:

- La exhumación durante el Neógeno tardío de Los Andes de Venezuela fue diacrónica a través del sistema de fallas de Boconó. Los resultados sugieren que este sistema de fallas acomoda gran parte de la transpresión en forma de movimientos verticales.
- La rápida exhumación ocurrida durante el Mioceno tardío en la Sierra Nevada de Mérida implica que el adelgazamiento de la litosfera y la compresión (¿oblicua?) estuvieron relacionadas durante ese tiempo. Posiblemente como respuesta a la acreción del Arco de Panamá contra la parte occidental de la Placa Suramericana durante ese período.
- La exhumación rápida y consecuente de la Sierra La Culata durante el Plioceno implica una convergencia continua entre el bloque de Maracaibo y Suramérica.
- La máxima elevación superficial de la Sierra Nevada de Mérida es consistente con la deflexión de los paleo-ríos Orinoco y Magdalena, la cual fue inferida de los registros sedimentarios Neógenos (Hoorn et al. 1995; Díaz de Gamero, 1996).

3) La comparación entre los resultados de termocronología in-situ y de sedimentos de 8 ríos actuales, en conjunto con datos de procesos a corta escala temporal como precipitación, sísmica y erosión permiten concluir que:

- Las edades de trazas de fisión en apatitos detríticos encontrados en las 7 cuencas de los 8 ríos estudiados (Coloncito, Chejendé, Chama, Mimbós, San Pedro, Tucaní, Santo Domingo, y Agua Viva) reproducen y corroboran de una manera eficiente los patrones de exhumación discriminados en las muestras in-situ.

- La termocronología detrítica constituye una importante herramienta para estudiar la proveniencia sedimentaria y los procesos de erosión a gran escala, en áreas de difícil acceso como Los Andes Venezolanos. Los resultados presentados en este trabajo indican que esta herramienta tiene una resolución mayor que la termocronología in-situ.
- No existe correlación entre las tasas de exhumación a largo plazo y los patrones de precipitación actuales. En particular, aunque el flanco norte de la cadena pareciera ser exhumado mucho más rápido que el flanco sur, este último se caracteriza por presentar el triple de los valores de tasas de precipitaciones promedio observados en el flanco norte debido al efecto orográfico.

4) Los análisis mediante termocronología de trazas de fisión en apatitos pertenecientes a los sedimentos sinorogénicos de las cuencas de Maracaibo y Barinas permiten concluir lo siguiente:

- La formación de edad Pliocena-Pleistocena Betijoque y Mioceno tardío a Pliocena Río Yuca localizadas en los flancos norte y sur de Los Andes, muestran patrones de exhumación similares a los observados mediante termocronología in-situ.
- El conjunto de edades antiguas dentro de los sedimentos sinorogénicos (Betijoque, Río Yuca y Parángula) proporcionan evidencias suficientes que fundamentan la reactivación de estructuras heredadas tectónicamente y el origen Eoceno-Oligoceno de esta cadena montañosa.
- Cinco eventos geodinámicos diferentes pueden ser discriminados en los sedimentos de las Formaciones Parángula, Río Yuca y Betijoque: tres picos estáticos a 5 Ma; 9 Ma; y 15 Ma podrían indicar diferentes fases del período de reorganización tectónica reportado por diversos autores (Hoorn et al. 1995; Montes et al. 2005) que finaliza con el cierre del Arco de Panamá; un pico móvil hace 25 Ma podría estar relacionado con la rotación y acreción de la Cordillera Oriental de Colombia y por último un continuo aporte de edades Paleocenas-Eocenas podrían ser concordante con el reciclaje de sedimentos o indican la presencia de una estructura preandina.
- Aunque las edades de las formaciones estudiadas no son bien conocidas por la inexistencia de marcadores bioestratigráficos, los análisis palinológicos proporcionan un límite Mioceno tardío-Plioceno para las formaciones Betijoque y Río Yuca. Los análisis de materia orgánica (Rock-Eval) sugieren que esas formaciones no alcanzaron

la suficiente profundidad para soterrar los apatitos dentro de la PAZ. De esta manera, la primera componente discriminada en las edades de los granos pueden ser consideradas como una aproximación para la edad depositacional de tales formaciones.

- Edades jóvenes de trazas de fisión sobre apatitos (9-11 Ma; Tortonianas) encontradas en la Formación Parángula implica que esta formación es probablemente mucho más joven que lo que actualmente se creía (Mioceno Medio).
- La Formación Betijoque de edad Pliocena ubicada en el flanco norte es correlacionable con la parte superior de la Formación Río Yuca, en el flanco sur.

Los resultados obtenidos en este estudio apoyan un modelo geológico de los Andes de Venezuela, cuya cadena está particionada en varios bloques tectónicos limitados por importantes sistemas de fallas. Estos bloques se exhuman a diferentes intervalos de tiempo y contrastantes velocidades de exhumación. Las exhumaciones recientes borran el registro de la exhumación de los períodos anteriores. Por tanto, es difícil discriminar entre los dos modelos geodinámicos existentes: 1) el modelo de estructura en flor, o 2) el modelo de orogéno flotante. ¿Qué modelo es el más apropiado? Para distinguir mejor entre los dos modelos es necesario incluis más datos termocronológicos, además de los análisis sísmicos de la estructura profunda en los Andes venezolanos. Esto último y los fenómenos de rotación y traslación de los distintos bloques tectónicos son de vital importancia para el planteamiento de nuevos modelos geodinámicos que expliquen el origen y evolución en el tiempo de Los Andes de Venezuela.

8.2 Síntesis

A pesar de las dificultades y limitaciones características de cualquier investigación científica, esta tesis también contribuyó con los siguientes elementos necesarios para entender el origen y evolución de Los Andes venezolanos en el contexto regional:

1. Contribuyo con nuevas edades mediante termocronología por trazas de fisión en apatitos in-situ, en sedimentos sinorogénicos y en sedimentos actuales transportados por los ríos modernos. Esta base de datos refleja la cinemática reciente de este orógeno y podrá ser utilizada a futuro para la elaboración de nuevos modelos tectónicos.

2. Demuestro la partición de la cadena en diferentes bloques que responden de diversas formas a la deformación causada por la triple convergencia de placas.
3. Presento una posible reconstrucción tectónica, la cual incluye al menos una parte de Los Andes del Norte de Suramérica (La Cordillera Oriental de Colombia y la Sierra de Santa Marta-Bucaramanga), y trato de relacionar las diferentes edades de enfriamiento encontradas en los datos termocronológicos de Los Andes de Venezuela con eventos tectónicos regionales.
4. Demuestro que la exhumación a largo plazo está controlada principalmente por los procesos tectónicos y que el posible control que pueda ejercer el clima sobre los patrones de exhumación es despreciable.

8.3 Perspectivas a futuro

El hecho de formar parte del personal de investigación del Laboratorio de Termocronología de la Universidad Central de Venezuela (ya instalado y a plena capacidad) me permitirá al regresar a Venezuela la oportunidad de desarrollar nuevos proyectos de investigación en el área, además de trabajar en colaboración con otros investigadores e instituciones a nivel nacional e internacional. Este trabajo puede ser extendido en el futuro mediante:

1. Incrementar la base de datos termocronológicos de trazas de fisión en apatitos, pertenecientes a rocas in-situ, sedimentos detríticos y sinorogénicos con el propósito de comprender los procesos tectónicos con mayor detalle en ciertas áreas claves de Los Andes Venezolanos, en particular en el flanco sur.
2. Incluir termocronómetros de alta temperatura, como trazas de fisión sobre circón o U-Th/He sobre este mineral, con el propósito de comprender aún más la exhumación total de los diferentes bloques en Los Andes Venezolanos.
3. Aplicar nuevos termocronómetros de baja temperatura como (U-Th)/He, ó ^{3}He-^{4}He, los cuales son más sensibles a los procesos superficiales y permiten explicar los cambios en la topografía.
4. Utilizar todos los datos termocronológicos existentes y los que se recolecten a futuro en modelos numéricos 3D como Pecube y probar diferentes modelos tectónicos para estudiar la sensibilidad de los datos a dichos modelos.
5. Extender este trabajo al resto de Los Andes del Norte de Suramérica y desarrollar modelos geológicos que tomen en cuenta los procesos tectónicos y superficiales a escala regional.

6. Realizar estudios interdisciplinarios que acoplados con los métodos termocronológicos de baja temperatura permitan estudiar en el tiempo la evolución de Los Andes del Norte de Suramérica.

REFERENCES

Aggarwal, Y., 1983, Seismic slip rates and earthquake rupture zones in the southern Caribbean: implications for plate motions and earthquake hazard in this region, paper presented at X Caribbean Geological Conference, Instituto Nacional de Investigaciones Geologico Mineras de Colombia, p.14-22.

Aleman, A., Ramos, V., 2000, Northern Andes. In: Cordani et al. (Eds.), Tectonic Evolution of South America. XXXI International Geological Congress, Brasil, p. 453-480.

Allen, P.A., Allen, J.R., 2005, Basin Analysis: Principles and Applications, 2nd ed., Blackwell Publishing, p. 549.

Amortegui Vera, A.E, 2007, Nature et Evolution Methamorphique des terrains oceanic en Ecuateur; consecuences possibles sur la genese des magmas adakitiques. Theses de Doctorat de l'Université Joseph Fourier, p.194.

Armstrong, P.A., 2005, Thermochronometers in Sedimentary Basins. Reviews in Mineralogy & Geochemistry, v. 58, p. 499-525.

Arya, S., Mount, D.M., Netanyahu, N.S., Silverman, R., Wu, A.Y., 1998, An Optimal Algorithm for Approximate Nearest Neighbor Searching in Fixed Dimensions. Journal of the ACM., v. 45 (6), p. 891-923.

Aspden, J.A., Litherland, M., Duque, P., Salazar, E., Bermudéz, R., Viteri, F., 1987a, Un nuevo cinturón ofiolítico en la Cordillera Real, Ecuador, y su posible significación regional. Politécnica, Monografía de Geología, v. 5 (12), p.81-93.

Aspden, J.A., McCourt, W.J., Brook, M., 1987 b, Geometrical Control of Subduction- Related Magmatism: The Mesozoic and Cenozoic Plutonic History of Western Colombia. Jour. Geol. Soc. London, v. 144, p. 893-905.

Aspden, J.A., Harrison, S.H., Rundle, C.C., 1992 b, New geochronological control for the tectono- Magmatic evolution of the metamorphic basement, Cordillera Real and El Oro province of Ecuador. Jour. South American Earth Sci., v. 6 (1-2), p.77-96.

Aspden, J.A., McCourt, W.J., 2002, Late Cretaceous to Tertiary events in the Western Cordillera of Ecuador. V ISAG, Tolouse, France, Extended Abstracts, p.45-48.

Audemard, F. A., 1993. Néotectonique, Sismotectonique et Aléa Sismique du Nordouest du Vénézuéla (Système de failles d'Oca-Ancón). PhD thesis, Université Montpellier II, France, p.369.

Audemard, F.A., 1996, Late Quaternary Marine deposits of the Paraguana Peninsula State of Falcón northwestern Venezuela-preliminary geological observation and neotectonic implications. Quaternary International, v.31, p.5-11.

Audemard, F.A., 2003, Geomorphic and geologic evidence of ongoing uplift and deformation in the Mérida Andes, Venezuela. Quaternary International, v.101-102, p. 43-65.

Audemard, F.E., 1991, Tectonic of western Venezuela PhD Thesis, Rice University Houston/Texas, p.245.

Audemard, F.E., Audemard F.A., 2002, Structure of the Mérida Andes, Venezuela: relations with the South America-Caribbean geodynamic interaction. Tectonophysics, v. 345, p. 299-327.

Audemard, F.A., Machette, M.N., Cox, J.W., Dart, R.L., Haller, K.M., 2000, Map and Database of Quaternary Faults in Venezuela and its Offshore Regions. U.S Geological Survey. Open-File Report 00-018 (paper edition).

Audemard, F.E., Singer A., Soulas J.P., 2006, Quaternary faults and stress regime of Venezuela. Revista de la Asociación Geológica Argentina, v.61 (4), p.480-491.

Avé-Lallemant, H.G., 1997, Transpression, Displacement Partitioning, And Exhumation In The Eastern Caribbean/South American Plate Boundary Zone. Tectonics, v.16 (2), p. 272-289.

Backé, G., Dhont, D., Hervouët, Y., 2006, Spatial and temporal relationships between compression, strike-slip and extension in the Central Venezuelan Andes: Clues for Plio-Quaternary tectonic escape. Tectonophysics, v. 425, p. 25-53.

Ball, M.M., Harrison, C.G.A., Supko, P.R., 1969, Atlantic opening and the origin of the Caribbean. Nature, v. 223, p.167-168.

Ball, M.M., Harrison, C.G.A., Supko, P.R., Bock, W., Maloney, N.J., 1971, Marine Geophysical measurements on the southern boundary of the Caribbean Sea. Geol. Soc. America Mem, v.130, p.1-33.

Barbarand, J., Carter, A., Hurford, A.J., Wood, I.G., 2003a, Compositional and structural control of fission-track annealing in apatite. Chemical Geology, v.198 (1-2) , p.107-137.

Barbarand, J., Hurford, T., Carter, A., 2003b, Variation in apatite fission-track length measurement: implications for thermal history modelling. Chemical Geology, v.198 (1-2), p.77-106.

Baudin F., Tribovillard N., Trichet J., 2007, Géologie de la Matière Organique. – Ed. Vuibert, Collection Interactions, p.263.

Bayona, G., Silva, C., Jiménez, G., 2008, Nuevos datos paleomagnéticos de Panamá y la Sierra Nevada de Santa Marta en Colombia; inferencias preliminares de rotaciones y traslaciones de terrenos. XIV Congreso Venezolano de Geofísica.

Bell, J.S., 1971, Tectonic evolution of the central part of the Venezuelan Coast Ranges. Geol. Soc. America. Mem., v.130, p.107-118.

Bell, J.S., 1972, Geotectonic evolution of the southern Caribbean area. Geological Society of America, Memoir, v.132, p.369-386.

Beltrán, C., 1994, Trazas activas y síntesis neotectónica de Venezuela a escala 1:2.000.000. VII Congreso Venezolano de Geofísica, Caracas. Sociedad Venezolana de Ingenieros Geofísicos, p. 541- 547.

Beltrán, C.,Giraldo, C., 1989, Aspectos geotectónicos de la región nororiental de Venezuela Proceedings. VII Congreso Geológico Venezolano, v, 3, p.1000-1021.

Bermúdez-Cella, M., 2008, Detection of Poisson mixtures by p-Partition. Divulgaciones Matemáticas, v.16 (1), p.73-86.

Bernet, M., Brandon, M., Garver, J., Balestrieri, M.L., Ventura, B., Zattin, M., 2009, Exhuming the Alps through time: clues from detrital zircon fission-track thermochronology, Basin Res., in press (doi: 10.1111/j.1365-2117. 2009.00400.x).

Bernet, M., Garver, J.I., 2005, Fission-track analysis of detrital zircon. Reviews in Mineralogy and Geochemistry, v.58, p.205-237.

Bernet, M., Spiegel, C., 2004, Introduction: Detrital thermochronology. Geological Society of America, Special Paper, v. 378, p.1-6.

Binnie, S.A., Phillips, W.M., Summerfield, M.A., Fifield, L.K., 2007, Tectonic uplift, threshold hillslopes, and denudation rates in a developing mountain range. Geology, v.35, p.743-746.

Blythe, A.E., Burbank, D.W., Farley, K.A., Fielding, E.J., 2000, Structural and topographic evolution of the central Transverses Ranges, California, from apatite fission-track, (U-Th)/He and digital elevation model analyses. Basin Research, v.12, p. 97-114.

Blythe, A.E., House, M.A., Spotila, J.A., 2002, Low-temperature thermochronology of the San Gabriel and San Bernardino Mountains, southern California: Constraining structural evolution. Geological Society of America Special Paper, v. 365, p. 231-250.

Boesi, T., Galea, F.A., Rojas, G., Lorente, M.A., Durán, I., Velásquez M., 1988, Estudio estratigráfico del Flanco Norandino en el sector Lobatera–El Vigía. III Simposio Bolivariano, Exploración Petrolera de las Cuencas Subandinas, Caracas, Memoria, Tomo I, p.1-41.

Bookhagen, B., Strecker, M.R., 2008. Orographic barriers, high-resolution TRMM rainfall, and relief variations along the eastern Andes. Geophys. Res. Lett., v.35: L06403, doi:10.1029/2007GL032011.

Brandon, M.T., 1992, Decomposition of fission-track grain-age distributions. Am. J. Sci., v. 292, p.535-564.

Brandon, M.T., 1996, Probability density plots for fission-track grain age distributions. Radiation Measurements, v.26, p.663-676.

Brandon, M. T., 2005, Programs for illustrating closure, partial retention and the response of cooling ages to erosion: CLOSURE, AGE2EDOT, and RESPTIME, in Reiners, P. W., and Ehlers, T. A., editors. Thermochronology: Reviews in Mineralogy and Geochemistry, p. 602-610.

Brandon, M.T., Roden-Tice, M.K., Garver, J.I., 1998, Late Cenozoic exhumation of the Cascadia accretionary wedge in the Olympic Mountains, northwest Washington State. GSA Bulletin, v. 110 (8), p.985-1009. DOI: 10.1130/0016-7606.

Brandon, M.T., Vance, J.A., 1992, Tectonic evolution of the Cenozoic Olympic subduction complex, Washington State, as deduced from fission track ages for detrital zircons. American Journal of Science, v. 292, p. 565-636.

Braun, J., 2002, Quantifying the effect of recent relief changes on age-elevation relationships. Earth and Planetary Science Letters, vol. 200, p. 331-343.

Braun, J., 2003, Pecube: A new finite element code to solve the heat transport equation in three dimensions in the Earth's crust including the effects of a time-varying, finite amplitude surface topography. Computers and Geosciences, v.29, p.787-794.

Braun, J., Beaumont, C., 1995, Three-dimensional numerical experiments of strain partitioning at oblique plate boundaries: Implications for contrasting tectonic styles in the southern Coast Ranges, California, and central South Island, New Zealand. Journal of Geophysical Research, v.100, p.18059-18074.

Braun, J., Robert, X., 2005, Constraints on the rate of post-orogenic erosional decay from low-temperature thermochronological data: application to the Dabie Shan, China. Earth Surface Processes and Landforms, v. 30, p. 1203-1225.

Braun, J., van der Beek, P.A., Batt, G., 2006, Quantitative Thermochronology: Numerical Methods for the Interpretation of Thermochronological Data, 258 pp., Cambridge University Press, Cambridge, New York.

Brewer, I.D., Burbank, D.W., Hodges, K.V., 2006. Downstream development of a detrital cooling-age signal: Insights from 40Ar/39Ar muscovite thermochronology in the Nepalese Himalaya. In: S.D. Willett, N. Hovius, M.T. Brandon and D.M. Fisher (Editors), Tectonics, Climate, and Landscape Evolution. Geological Society of America Special Paper, v.398, p.321-338.

Bucher, W.H., 1952, Geologic structure and orogenic history of Venezuela. Geol. Soc. America Mem., v. 49, p.1-113.

Burbank, D.W., Blythe, A.E., Putkonen, J., Pratt-Sitaula, B., Gabet, E., Oskin, M., Barros, A., Ojha, T.P., 2003, Decopling of erosion and precipitation in the Himalayas. Nature, v.426, p.652-655.

Burbidge, D.R., Braun, J., 1998, Analogue models of obliquely convergent continental plate boundaries. Journal of Geophysical Research, v. 103, p.15221-15237.

Burchart, J., 1981, Evaluation of uncertainties in fission track dating: Some statistical and geochemical problems. Nucl. Tracks, v. 5, p.87-92.

Burke, K., Dewey, J. F., Cooper, C., Mann, P., Pindell, J. L., 1984, Caribbean tectonics and relative plate motions, Geological Society of America, Memoir, v.162, p. 31-63.

Burtner, R. L., Nigrini, A., Donelick, R.A, 1994, Thermochronology of lower Cretaceous source rocks in the Idaho-Wyoming thrust belt. Am. Assoc. Petrol. Geol. Bull., v.78, p.1613-1636.

Carlson, W.D., Ketcham, R.A., Donelick, R.A., 1999, Variability of apatite fission-track annealing kinetics: III. Extrapolation to geological time scales. Am. Mineral., v.84, p.1235-1255.

Carter, A., 2007, Heavy Minerals and detrital fission-track thermochronology. Developments in Sedimentology, v. 58, p. 851-868.

Case, J.E., Durán, L.G., López, R.A., Moore, W.R., 1971, Tectonic investigations in western Colombia and eastern Panamá. Geological Society of America Bulletin, v.82 (10), p.2685- 2712.

Case, J.E., Shagam, R., Giegengack, R.F., 1990, Geology of the northern Andes: An overview. Geological Society of America, The Geology of North, p.177-200.

Castillo, J., Gose, W.A., Perarnau, A., 1991, Paleomagnetic results from Mesozoic strata in the Mérida Andes, Venezuela. Journal of Geophysical Research, v.96, p.6011- 6022.

Cediel, F., Shaw, R.P., Cáceres, C., 2003, Tectonic assembly of the Northern Andean Block, in C. Bartolini, R.T. Buffler, and J. Blickwede, eds., The Circum-Gulf of Mexico and the Caribbean: Hydrocarbon habitats, basin formation, and plate tectonics. Am. Assoc. Petrol. Geol., Memoir, v. 79, p. 815-848.

Chacín, L., Jácome, M.I., Izarra, C., 2005, Flexural and gravity modelling of the Mérida Andes and Barinas-Apure Basin, Western Venezuela. Tectonophysics, v.405, p.155-167.

Chambers, J.M., Cleveland, W.S., Kleiner, B., Tukey, P.A., 1983, Graphical Methods for Data Analysis. Chapman & Hall, p.395.

Chicangana, G., 2005, The Romeral fault system: a shear and deformed extinct subduction zone between oceanic and continental lithospheres in northwestern South America. Earth Sci. Res. J., vol.9 (1), p.50-64.

Coates, A.G., Collins, L.S., Aubry, M.P., Berggren, W.A., 2004, The Geology of the Darien, Panama, and the late Miocene-Pliocene collision of the Panama arc with northwestern South America. Geological Society of America Bulletin, v.116, p.1327-1344.

Colletta, B., Roure, F., De Toni, B., Loureiro, D., Passalacqua, H., Gou, Y., 1997, Tectonic inheritance, crustal architecture, and contrasting structural styles in the Venezuelan Andes. Tectonics, v.16 (5), p.777-794.

Colmenares, L., Zoback, M.D, 2003, Stress field and seismotectonics of northern South America. Geology, v. 31, p.721-724.

Conover, W. J., 1980, Practical Nonparametric Statistics. 2nd. Ed. New York: Wiley.

Cookson, I. C., 1947, Plant microfossils from the lignites of Kerguelen archipelago. Proceedings of the Linnean Society of New South Wales, v.72, p.127-142.

Cooper, M.A., Addison, F.T., Alvarez, R., Coral, M., Graham, R.H., Hayward, A.B., Howe, S., Martinez, J., Naar, J., Peñas, R., Pulham, A.J., Taborda, A., 1995, Basin Development and Tectonic History of the Llanos Basin, Eastern Cordillera, and Middle Magdalena Valley, Colombia. AAPG Bulletin, v.79 (10), p.1421-1443.

Corredor, F., 2003, Eastward extent of the Late Eocene-Early Oligocene onset of deformation across the northern Andes: constraints from the northern portion of the Eastern Cordillera fold belt, Colombia. Journal of South American Earth Sciences, v.16, p.445-457.

Cortés, M., Angelier, J., 2005, Current states of stress in the northern Andes as indicated by focal mechanisms of earthquakes. Tectonophysics, v.403, p.29-58.

Cortés, M., Colletta, B., Angelier, J., 2006, Structure and tectonics of the central segment of the Eastern Cordillera of Colombia. Journal of South American Earth Sciences, v.21, p.437-465.

Crowley, K.D., Naeser, C.W., Naeser, N.D., 1989, Fission track analysis: Theory and applications. Short course manual. Geological Society of America Annual Meeting St. Louis, Missouri. USA.

Cruz, L., Fayon, A., Teyssier, C., Weber, J., 2007, Exhumation and deformation processes in transpressional orogens: The Venezuelan Paria peninsula, SE Caribbean-South American plate boundary. Geological Society of America, Special Paper, v. 434, p. 149-165.

Dadson, S.J., Hovius, N., Chen, H., Dade, W.B., Hsieh, M.L., Willett, S.D., Hu, J.C., Horng, M.J., Chen, M.C., Stark, C.P., Lague, D., Lin, J.C ., 2003, Links between erosion, runoff variability and seismicity in the Taiwan orogen. Nature, v.426, p.648-651.

Daly, M. C., 1989, Correlations between Nazca/Farallon plate kinematics and forearc basin evolution in Ecuador. Tectonics, v.8, p.769-790.

Davison, A. C., Hinkley, D., 2006, Bootstrap Methods and their Applications (8th ed.). Cambridge: Series in Statistical and Probabilistic Mathematics.

De Cizancourt, H., 1933, Tectonic structure of Northern Andes in Colombia and Venezuela. American Association of Petroleum Geologists Bulletin, v.17,3, p.211-228.

Deratmiroff, G.N., 1971, Late Cenozoic imbricate thrusting in the Venezuelan Andes. American Association of Petroleum Geologist Bulletin, v.58 (8), p.1336-1355.

De Toni, B., Kellogg, J., 1993, Seismic evidence for blind thrusting of the Northwestern flank of the Venezuelan Andes. Tectonics, v.12, p.1393-1409.

Dewey, J.W.,1972, Seismicity and tectonics of western Venezuela. Bull. Seism. Soc. America, v.62, p.1711-1751.

Dhont, D., Backé, G., Hervouët, Y., 2005, Plio-Quaternary extension in the Venezuelan Andes: Mapping from SAR JERS imagery. Tectonophysics, v. 399, p. 293-312.

Díaz de Gamero, M.L., 1996, The changing course of the Orinoco River during the Neogene: a review. Palaeogeography, Palaeoclimatology, Palaeoecology, v.123, p. 385-402.

Dickinson, W.R., 1985, Interpreting provenance relations from detrital modes of sandstones, in Zuffa, G.G., ed., Provenance of Arenites: Series C. Mathematical and Physical Science, v. 148, p.333-361.

Diebold, J., Driscoll, N., 1999, New Insights on the Formation of the Caribbean Basalt Province revealed by Multichannel Seismic Images of Volcanic Structures in the Venezuelan Basin. In: Caribbean Basins.

Sedimentary Basins of the World, 4, Ed. by Paul Mann (Series Editor, K.J. Hsü). Elsevier Science B.V., Amsterdam, Chapter 19, p. 561-589.

Dodson, M.H., 1973. Closure temperature in cooling geochronological and petrological systems.Contrib. Mineral. Petrol., v.40, p.259-74.

Dodson, M.H., Compston, W., Williams, I.S., Wilson, J.F., 1988, A search for ancient detrital zircons in Zimbabwean sediments. J. Geol. Soc. (London), v.145 (6), p.977- 983.

Donelick, R.A., O'Sullivan, P.B., Ketcham, R.A., 2005, Apatite Fission-Track Analysis. Reviews in Mineralogy and Geochemistry, v. 58, p. 49-94.

Donnelly, T.W., 1973, Late cretaceous basalts from the Caribbean, a possible flood basalt province of bast sizes. EOS Transaction, American Geophysical Union, v.54, p.1004.

Donnelly, T. W., Beets, D., Carr, M.J., Jackson, T., Klaver, G., Lewis, J. ,Maury, R., Schellekens, H., Smith, A.L., Wadge, G., Westercamp, D., 1990, History and tectonic setting of Caribbean magmatism, in G. Dengo, and J. E. Case, eds., The Caribbean Region. The Geology of North America, p. 339-374.

Driscoll, N., Diebold, J., 1999, Tectonic and Stratigraphic Development of the Eastern Caribbean Region: New Constraints from Multichannel Seismic Data. In: Caribbean Basins. Sedimentary Basins of the World, 4, Ed. by Paul Mann (Series Editor, K.J. Hsü). Elsevier Science B.V., Amsterdam, Chapter 20, p. 591-627.

Duerto, L., Escalona, A., Mann, P., 2006, Deep structure of the Mérida Andes and Sierra de Perijá mountain fronts, Maracaibo Basin, Venezuela. Am. Assoc. Petrol. Geol. Bull., v.90, p.505-528.

Dunkl, I., 2002, Trackkey: a Windows program for calculation and graphical presentation of fission track data. Computers & Geosciences, v.28 (1), p.3-12.

Duque- Caro,H., 1980, Geotectónica y Evolución de la región Noroccidental Colombiana. Ingeominas, Bol. Geol., v.23 (3), p.3-37.

Duque-Caro, H., 1984, Estilo Estructural, Diapirismo y episodios de Acrecimiento del Terreno sinu- San Jacinto en el Noroccidente de Colombia. Ingeominas, Bol. Geol., v.27 (2), p.1-29.

Duque-Caro, H., 1990, The Choco Block in the northwestern corner of South America: structural, tectonostratigraphic, and paleogeographic implications. Journal of South American Earth Sciences, v. 3(1), p. 71-84.

Dunkl, I., 2002, Trackkey: a Windows program for calculation and graphical presentation of fission track data. Computers & Geosciences, v. 28 (1), p.3-12.

Ehlers, T. A., 2005, Crustal thermal processes and the interpretation of thermochronometer data, in Low Temperature Thermochronometry: Techniques, Interpretations, and Applications, Rev. Mineral. Geochem., vol. 58, edited by T. Ehlers and P. W. Reiners, p.315-350. Mineral. Soc. of Am., Washington, D. C.

England, P., Molnar, P., 1990, Surface uplift of rocks, and exhumation of rocks. Geology, v.18, p. 1173-1177.

Espitalié, J., Deroo, G., Marquis F., 1985-1986, La pyrolyse Rock Eval et ses applications. Revue Institut français du Pétrole, 40/5, 563 579; 40/6, 755 784 & 41/1, 73 89.

Espitalié, J., Laporte, L., Madec, J.L., Marquis, M., Leplat, F., Paulet, J., Boutefeu, A., 1977, Méthode rapide de caractérisation des roches mères, de leur potentiel pétrolier et de leur degré d'évolution. Oil & Gas Science and Technology - Rev. IFP, v. 32 (1), p.23-42.

Escalona, A., 2003, Regional Tectonics, Sequence Stratigraphy and Reservoir Properties of Eocene Clastic Sedimentation, Maracaibo Basin, Venezuela. PhD Thesis, University of Texas at Austin., p.222.

Escalona, A., Mann, P., 2006, An overview of the petroleum system of Maracaibo Basin. AAPG Bulletin, v. 90 (4), p. 657-678.

Farías, M., Charrier, R., Carretier, S., Martinod, J., Fock, A., Campbell, D., Cáceres, J., Comte, D., 2008, Late Miocene high and rapid surface uplift and its erosional response in the Andes of central Chile (33°–35°S). Tectonics, v.27: TC1005, doi:10.1029/2006TC002046.

Faure, G., 1986, Principles of isotope geology, Wiley. New York. US, p.589.

Finlayson, D.P., Montgomery, D.R., Hallet, B., 2002, Spatial coincidence of rapid inferred erosion with toung metamorphic massifs in the Himalayas. Geology, v. 30 (3), p.219-222.

Fitzgerald, P.G., Muñoz, J.A., Coney, P.J., Baldwin, S.L., 1999, Asymmetric exhumation across the Pyrenean orogen: implications for the tectonic evolution of a collisional orogen. Earth and Planetary Sciences Letters, v.173, p.157-170.

Fitzgerald, P.G., Sorkhabi, R.B., Redfield, T.F., Stump, E., 1995, Uplift and denudation of the central Alaska Range: a case study in the use of apatite fission-track thermochronology to determine absolute uplift parameters. Journal of Geophysical Research, v. 100, p. 20175-20191.

Fleischer, R.L., Hart., H.R., 1972, Fission-track dating techniques and problems. In Bishop, W., Miller, J., and Colle, S., (Eds.).Calibration of Hominoit Evolution. Scottish Academic Press, p.135-170.

Fleischer, R.L., Price, P.B., Walker, R.M., 1975, Nuclear tracks in solids – principles and applications: Berkeley, CA, University of California Press, p.605.

Foster, D.A., Gleadow, A., Mortimer, G., 1994, Rapid Pliocene exhumation in the karakoram (Pakistan), revealed by fission-track thermochronology of the K2 gneiss. Geology, v. 22, p. 19-22.

Freymueller, J.T., Kellogg, J.N., Vega, V., 1993, Plate motions in the North Andean region. Journal of Geophysical Research, v. 98 (12), p. 21,853- 21,863.

Furlong, K.P., 2007, Locating the deep extent of the plate boundary along the Alpine Fault zone, New Zealand: Implications for patterns of exhumation in the Southern Alps. Geological Society of America Special Paper, v.434, p.1-14.

Grafë, K., Frisch, W., Villa, I.M., Meschede, M., 2002, Geodynamic evolution of southern Costa Rica related to low-angle subduction of the Cocos Ridge: constraints from thermochronology. Tectonophysics, v.348, p.187-204.

Galbraith, R.F., 1981, On statistical models for fission track counts. Mathematical Geology, v.13, p.471-488.

Galbraith, R.F., 1988, Graphical display of estimates having differing standard errors. Technometrics, v.30 (3), p.271-281.

Galbraith, R.F., 2005, Statistics for Fission Track Analysis: Boca Raton, Chapman and Hall/CRC, p.219.

Galbraith, R.F., Green, P.F., 1990, Estimating the component ages in a finite mixture. Nucl. Tracks Radiat. Meas., v.17, p.196-206.

Galbraith R.F., Laslett, G.M., 1993, Statistical models for mixed fission track ages. Nuclear Tracks, v.21, p.459-470.

Gallagher, K., Brown, R., Johnson, C., 1998, Fission Track analysis and its application to geological problems. Annual Reviews Earth Planetary Science, v.26, p.519-572.

Gallagher, K., Charvin, K., Nielsen, S., Sambridge, M., Stephenson, J., 2009, Markov chain Monte Carlo (MCMC) sampling methods to determine optimal models, model resolution and model choice for Earth Science problems. Marine and Petroleum Geology, v.26, p.525-535.

Ganssser, A., 1973, Facts and theories on the Andes. Journal of the Geological Society of London, v.129, p. 93-131.

Garver, J.I., Brandon, M.T., Roden-Tice, M., Kamp, P.J.J., 1999, Exhumation Processes : Noraml Faulting, Ductile Flow and Erosion. Chapitre Exhumation history of orogenic highlands determined by detrical fission-track thermochronology. Geological Society, p. 283-304.

Gerth, H., 1955, Der Geologgische Bau der Südamerikanischen kordillere, Berlin: Gebr. Borntraeger, p.264.

Germeraad, J. H., Hopping, C.A., Muller, J., 1968, Palynology of Tertiary sediments from tropical areas. Review of Palaeobotany and Palynology, v. 6, p. 189-348.

Ghosh, N., Hall, S.A., Casey, J.F., 1984, Sea floor spreading magnetic anomalies in the Venezuelan Basin. Geological Society of America, Memoir, v.162, p.65-80.

Giegengack, R., 1984, Late Cenozoic tectonic environments of the central Venezuelan Andes. Geological Society of America Memoir, v.162, p.343-364.

Giegengack, R., Grauch, R.I., Shagam, R., 1976, Geometry of Late Cenozoic displacement along the Boconó Fault, Venezuelan Andes. Boletín de Geología Publicación Especial 7/2, p.1201-1223.

Gleadow, A.J.W., Duddy, I.R., 1981, A Natural Long-Term Track Annealing Experiment For Apatite. Nucl. Tracks, v 5 (1/2), p. 169-174.

Gleadow, A.J.W., Duddy, I.R., Green, P.F., 1986a, Fission track lengths in the apatite annealing zone and the interpretation of mixed ages. Earth Planet. Sci. Lett., v.78, p. 245-254.

Gleadow A.J.W., Duddy, I.R., Green, P.F., 1986b, Confined fission track lengths in apatite: a diagnostic tool for thermal history analysis. Contr. Mineral. Petrology, v. 94, p.405-415.

Gleadow A.J.W., Brown R.W., 2000. Fission track thermochronology, and the long-term denudational response to tectonics. in M.J. Summerfield (Ed). Geomorphology and Global Tectonics, p.57-75.

Gleadow, A.J.W., Belton, D.X., Kohn, B.P., Brown, R. W., 2002, Fission track dating of phosphate minerals and the thermochronology of apatite. In: Kohn, M. J., Rakovan, J. & Hughes, J. M. (eds) Phosphates; Geochemical, Geobiological, and Materials Importance. Mineralogical Society of America and Geochemical Society, Washington, DC, p.579-630.

Gómez, E., Jordan, T.E., Allmendinger, R.W., Cardozo, N., 2005, Development of the Colombian foreland-basin system as a consequence of diachronous exhumation of the northern Andes. GSA Bulletin, v.117 (9), p.1272-1292.

Gonzalez de Juana, C., 1952, Introducción al estudio de la geología de Venezuela. Bol. Geol.. Venez. Dir. Geol., v.2, p.407-416.

Gose, W.A., Perarnau, A., Castillo, J., 2003, Paleomagnetic results from the Perijá Mountains, Venezuela: an example of vertical axis rotation. In: Bartolini, C., Buffler, R.T., Blickwede, J. (Eds.), The Circum-Gulf of Mexico and the Caribbean: Hydro-Carbon Habitats, Basin Formation and Plate Tectonics. Memoir 79. AAPG, p.969- 975.

Grafë, K., Frisch, W., Villa, I.M., Meschede, M., 2002, Geodynamic evolution of southern Costa Rica related to low-angle subduction of the Cocos Ridge: constraints from thermochronology. Tectonophysics, v.348, p.187-204.

Green, P.F., 1981, A new look at statistics in fission track dating. Nucl. Tracks, v.5, p.77-86.

Green, P.F., 1988, The relationship between track shortening and fission track age reduction in apatite: combined influences of inherent instability, annealing anisotropy, length bias and system calibration. Earth Planet. Sci. Lett., v.89, p.335-352.

Green P.F., Duddy, I.R., Gleadow, A.J.W., Tingate, P.R., Laslett, G.M., 1985, Fission track annealing in apatite: Track length measurements and the forms of the Arrhenius Plot. Nucl. Tracks, v.1, p.323-328.

Green, P.F., Duddy, I.R., Gleadow, A.J.W., Tingate, P.R., Laslett, G.M., 1986, Thermal annealing of fission tracks in apatite, 1. A qualitative description. Chemical Geology (Isotope Geoscience Section), v. 59, p. 237-253.

Green, P.F., Duddy, I.R., Hegarty, K.A., 2005, Comment on compositional and structural control on fission track annealing in apatite. Chemical Geology, v.214, p.351-358.

Gutenberg, B., Richter, C.F., 1954, Seismicity of the Earth and Associated Phenomena. Princeton University Press, Princeton, New Jersey, p. 245 .

Guzmán, J.I., Fisher, W.L., 2006, Early and middle Miocene depositional history of the Maracaibo Basin, western Venezuela. AAPG Bulletin, v.90 (4), p. 625-655.

Hackley, P.C., Urbani, F., Karlsen, A.W., Garrity, C.P., 2005, Geologic Shaded Relief Map of Venezuela. U.S. Geological Survey Open File Report 2005-1038.

Hammer, R. D., Young, F. J., Haithcoate, T.W., Wollenhaupt, N. C., Barney, T.L., 1995, Slope class maps from soil survey and digital elevation models. Soil Science Society of America Journal, vol. 59, p.509-519.

Hargraves, R.B., Shagam, R., 1969, Paleomagnetic study of La Quinta Formation, Venezuela. Am. Assoc. Petrol. Geol. Bull., v.53, p.537-552.

Hess, H., Maxwell, J. 1953, Caribbean Research Project. Bulletin of the Geological Society of America, v. 64 (1), p.1-6.

Hoorn, C., Guerrero, J., Sarmiento, G.A., Lorente, M.A., 1995, Andean tectonics as a cause for changing drainage patterns in Miocene northern South America. Geology, v.23 (3), p. 237-240.

Hospers, J., Van Wijnen., J., 1959, The gravity field of the Venezuelan Andes and adjacents basins. Verslag van de Gewone Vergadering van de Afdeling Natuurkunde, Koninklijke Nederlandse Akademie van Wetenschappen, v. 23 (1), p.1-95.

Housiau, M., 2009, Diagenesis and provenance of Eocene quartz arenites from the Misoa Formation (Maracaibo basin, Venezuela). Unpublished MSc thesis, Université Joseph Fourier, Grenoble, p.38.

Hurford, A.J., 1986. Cooling and uplift patterns in the Lepontine Alps South Central Switzerland and an age of vertical movement on the Insubric fault line. Contributions to Mineralogy and Petrology, v.92, p.413-427.

Hurford, A.J., Carter, A., 1991, The role of fission track dating in discrimination of provenance. Geological Society, London, Special Publications, v.57, p.67-78.

Hurford, A.J., Green, P.F., 1982, A User´s guide to fission track dating calibration. Earth and Planetary Science Letters, v.59, p.343-354.

Hurford, A.J., Green, P.F., 1983, The zeta age calibration of fission track dating. Chemical Geology (Isotope Geoscience Section), v.1, p. 285-317.

Jácome, M., 1994. Interpretación geológica, sísmica y gravimétrica de un perfil transandino. Undergraduate Thesis, Universidad Simón Bolívar, Caracas, Venezuela, p.68.

Jácome, M., Chacín, L., 2008, Subsidence history of the Barinas Apure Basin: Western Venezuela. Back to Exploration: 2008 CSPG CSEG CWLS Convention Calgary, Canadá, p.682-686.

Jacques, J.M., 2004, The influence of intraplate structural accommodation zones on delineating petroleum provinces of the Sub-Andean foreland basins. Petroleum Geoscience, v.10, p.1-19.

Jaillard, E., Soler, P., Carlier, G., Mourier, T., 1990, Geodynamic evolution of the northern and central Andes during early to middle Mesozoic times. A Tethyan model. Journal of the Geological Society of London, v.147, p. 1009-1022.

James, K. H., 1990, The Venezuelan hydrocarbon habitat, in J. Brooks, ed., Classic Petroleum Provinces. Geological Society of London Special Publication, v.50, p. 9-35.

James, K.H., 2000a, The Venezuelan hydrocarbon habitat, part 1: tectonics, structure, palaeogeography and source rocks. Journal of Petroleum Geology, v. 23(1), p. 5-53.

James, K.H., 2000b, The Venezuelan hydrocarbon habitat, part 2: hydrocarbon occurrences and generated-accumulated volumes. Journal of Petroleum Geology, v. 23(2), p. 133-164.

Jamieson, R.A., Beaumont, C., 1989, Deformation and metamorphism in convergent orogens: a model for uplift and exhumation of metamorphic terranes. In: Daly, J.S. et al. (eds.), Evolution of Metamorphic Belts. Geol. Soc. Lond. Spec. Publ., v.43, p.17-129.

Jaramillo, J.M., 1978, Determinación de las edades de algunas rocas de la Cordillera Central de Colombia por el método de huellas de fisión. II Congreso Internacional Geológico Colombiano. Resúmenes, Bogotá, p.19-20.

Jasra, A., Stephens, D.A., Gallagher, K., Holmes, C.C., 2006, Bayesian mixture modelling in geochronology via Markov Chain Monte Carlo. Mathematical Geology, v.38, p.269-300.

Jenson S.K., Domingue, J.O., 1988, Extracting topographic structure from digital elevation data for geographic information system analysis. Photogrammetric Engineering and Remote Sensing, v. 54 (11), p.1593-1600.

Kafka, A.L., Weidner, D.J., 1981, Earthquake focal mechanisms and tectonic processes along the southern boundary of the Caribbean Plate. Journal of Geophysical Research, v.86 (4), p.2877-2888.

Kaniuth, K., Drewes, H., Stuber, K., Temel, H., Hernández, J. N., Hoyer, M., Wildermann, E., Kahle, H. G. and Geiger, G., 1999, Position changes due to recent crustal deformations along the Caribbean-South American plate boundary derived from CASA GPS project. General Assembly of the International Union of Geodesy and Geophysics (IUGG), Birmingham, U.K. Poster at Symposium G1 of International Association of Geodesy.

Kellogg, J.N., 1984, Cenozoic tectonic history of the Sierra de Perija, Venezuela–Colombia, and adjacent basins. In: Bonini, W.E., Hargraves, R.B., Shagam, R. (Eds.), The Caribbean–South American Plate Boundary and Regional Tectonics. GSA Memoir 162, Boulder, CO, United States, p. 239- 261.

Kellogg, J.N., Bonini, W.E., 1982, Subduction of the Caribbean Plate and basement uplifts in the overriding South American Plate. Tectonics, v.1, p.251-276.

Kellogg, J.N., Vega, V., 1995, Tectonic development of Panama, Costa Rica, and the Colombian Andes: constraints from global positioning system geodetic studies and gravity. Geological Society of America, Special Paper, v.295, p.75-90.

Kendall, M., Stuart, A., 1958, The advanced theory of statistic, distribution theory, vol.1, Charles Griffin & Company Limited, London, p.433.

Kerr, A.C., Aspden, J.A., Tarney, J., Pilatasig, L.F., 2002, The nature and provenance of accreted oceanic terranes in western Ecuador: geochemical and tectonics constraints. Jour. Geolog. Soc. London, v.159, p.577-594.

Ketcham, R. A., Donelick, R.A., Carlson, W.D., 1999, Variability of apatite fission-track annealing kinetics: III. Extrapolation to geological time scales. Am. Mineral., v.84, p.1235- 255.

Ketcham, R.A., 2003, Observations on the relationship between crystallographic orientation and biasing in apatite fission-track measurements. Am. Mineral., v.88, p.817-829.

Ketcham, R. A., 2005, Forward and inverse modelling of low-temperature thermochronology data. Rev. Mineral. Geochem., v.58, p.275-314.

Ketcham, R.A., Carter, A., Donelick, R.A., Barbarand, J., Hurford, A.J., 2007a, Improved measurement of fission-track annealing in apatite using C-axis projection. Am. Mineral., v.92, p.789-798.

Ketcham, R.A., Carter, A., Donelick, R.A., Barbarand, J., Hurford, A.J 2007b, Improved modeling of fission-track annealing in apatite. Am. Mineral., v.92, p.799-810.

Ketcham, R.A., Donelick, R.A., Balestrieri, M.A., Zattin, M., 2009, Reproducibility of apatite fission-track length data and thermal history reconstruction. Earth and Planetary Science Letters, v.284, p. 504-515.

Kohn, B., Shagam, R., Banks, P., Burkley, L., 1984, Mesozoic–Pleistocene fission track ages on rocks of the Venezuelan Andes and their tectonic implications. Geological Society of America. Memoir, v.162, p.365- 384.

Koons, P.O., 2009, On the implications of low spatial correlation of tectonic and climate variables in the western European Alps. Geology, v.37, p.863-864.

Kowallis, B.J., Heaton, J.S., Bringhurst, K., 1986, Fission-track dating of volcanically derived sedimentary rocks. Geology, v. 14 (1), p.19-22.

Lamb, S., Davis, P., 2003, Cenozoic climate change as a possible cause for the rise of the Andes. Nature, v.425, p.792-797.

Larson, R.L.,1991, Latest pulse of Earth: Evidence for a mid-Cretaceous suyperplume. Geology, v.19, p.547-550.

Laslett, G.M., Green, P.F., Duddy, I.R., Gleadow, A.J.W., 1987, Thermal annealing of fission tracks in apatite 2. A quantitative analysis. Chem. Geol., v.65, p.1-13.

Laslett, G.M., Kendall, W.S., Gleadow, A.J.W., Duddy, I.R., 1982, Bias in measurement of fission track length distributions. Nucl. Tracks, v.6, p.79-85.

Laubscher, H.P., 1987, The kinematic puzzle of the Neogene northern Andes. In: The anatomy of Mountain Ranges, eds. Schaer, J-P. and Rogers, J., p.211-227, chapter 11. Princeton University Press.

Litherland, M., Aspden, J.A., Jemielita, R.A., 1994, The metamorphic belts of Ecuador. British Geological Survey, Overseas Memoir 11, p.147, 2 maps, Keyworth, UK.

Lindsay, J.B., 2005, The Terrain Analysis System: a tool for hydro-geomorphic applications. Hydrol. Process, v.19, p.1123-1130.

Lindsay, J.B., Creed, I.F., 2005, Removal of artifact depressions from DEMs: towards a minimum impact approach. Hydrological Processes., v.19, p.3113-3126.

Lock, J., Kelsey, H., Furlong, K., Woolace, A., 2006, Late Neogene and Quaternary landscape evolution of the northern California Coast Ranges: Evidence for Mendocino triple junction tectonics. Geological Society of America Bulletin, v. 118, p. 1232-1246, 10.1130/b25885.1.

Lorente, M.A., 1986, Palynology and palynofacies of the Upper Tertiary in Venezuela. Dissertationes Botanicae, v.99, p.222 .

Lugo, J., Mann, P., 1995, Jurassic–Eocene tectonic evolution of Maracaibo basin, 699 Venezuela, in A. J. Tankard, R. Suárez S., and H. J. Welsink, Petroleum basins of South America. Am. Assoc. Petrol. Geol., Memoir 62, p. 699-725.

Lunt, D.J., Valdes, P.J., Haywood, A., Rutt, I.C., 2008, Closure of the Panama Seaway during the Pliocene: implications for climate and Northern Hemisphere glaciation. Climate Dynamics, v.30, p.1-18.

Lutz T.M., Omar, G., 1991, An inverse method of modeling thermal histories from apatite fission-track data. Earth Planet Sci. Lett., v.104, p.181-195.

MacDonald, W.D., Opdyke, N.D., 1972, Tectonic rotations suggested by paleomagnetic results from northern Colombia.,South America. Journal of Geophysical Research,, v.77(29), p.5720-5730.

MacDonald, W.D., Opdyke, N.D., 1984, Preliminary paleomagnetic results from the Jurassic rocks of the Santa Marta Massif, Colombia. In: Bonini, W.E., Hargraves, R.B., Shagam, R. (Eds.), The Caribbean–South American Plate Boundary and Regional Tectonics. GSA Memoir, v.162, p. 295-298.

Macellari, C., 1984, Late Tertiary History of the Tachira Depression, South-Western Venezuelan Andes. In: Bonini W.E., Hargraves R.B.& Shagam R. Eds. The Caribbean-South American Plates Boundary and Regional Tectonics. Geol. Soc. Am., v.162, p.333-341.

Malfait, B.T., Dinkelman, M.G., 1972, Circum-Caribbean tectonic and igneous activity and the evolution of the Caribbean plate. Geological Society of America Bulletin, v.83 (2), p. 251-271.

Mann, P., Escalona, A., Castillo, M.V., 2006, Regional geologic and tectonic setting of the Maracaibo supergiant basin, western Venezuela. American Association of Petroleum Geologists Bulletin, v. 90, p. 445-477, 10.1306/10110505031.

Maruyama, S., 1994, Plume Tectonics. Jour. Geol. Soc. Japan, v.100 (1), p.24-49.

Maufrett, A., Leroy, S., 1997, Seismic Stratigraphy and structure of the Caribbean igneous province. Tectonophysics, v.283, p.61-104.

Maya, M., 2001, Distribución, facies y edad de las rocas metamórficas de Colombia. Ingeominas, I 2426, 57 p, mapa.

Maze, W.B., Hardgravesx, R.B., 1984, Paleomagnetic results from the Jurassic La Quinta formation in the Perijá Range and their tectonic significance, in Bonini, W.E., Hardgraves, R.B., and Shagam, R., eds., The Caribbean-South American plate boundary and regional tectonics. Geological Society of America Memoir, v.162, p.287-293.

McBride, E.F., 1963, A classification of common sandstone. Journal of Sedimentary Petrology v. 33, p. 664-669.

McCourt, W.J., Aspden, J.A., Brook, M., 1984, New geological and geochronological data from the Colombian Andes; Continental growth by multiple accretion. Geological Society of London Journal, v.141, p.831-845.

McCullagh, P., Nelder, J.A., 1989, Generalized linear models.London, Chapman & Hall, p.511.

Mehrkian, K., 2009, Provenance and diagenesis of the Isnotu and Betijogue sandstone formations (Maracaibo basin, Venezuela). Unpublished MSc thesis, Université Joseph Fourier, Grenoble p.30.

Meschede, M., 1998, The impossible Galapagos connection: geometric constraints for a near-American origin of the Caribbean plate. Geologische Rundschau, v.87 (2), p.200-205.

Meschede, M., Frisch, W., 1998, A plate-tectonic model for the Mesozoic and Early Cenozoic history of the Caribbean Plate. Tectonophysics, v. 296, p.269-291.

Miall, A.D., 1996, The Geology of Fluvial Deposits: Sedimentary Facies, Basin Analysis, and Petroleum Geology. New York, Springer, p.582 .

Minster, J.B., Jordan T.H., 1978, Presented-day plate motions. J. Geophys. Res., v.83, p.5331-5354.

Molnar, P., England, P., 1990. Late Cenozoic uplift of mountain ranges and global climate change: chicken or egg?. Nature, v.346, p.29-34.

Molnar, P., Sykes, L., 1969, Tectonics of the Caribbean and middle America regions from focal mechanisms and seismicity. Geological Society of America Bulletin, v.80, p.1639- 1684.

Montes, C., Hatcher, R.D., Restrepo-Pace, P., 2005, Tectonic reconstruction of the Northern Andean blocks: oblique convergence and rotations derived from the kinematics of the Piedras-Girardot area, Colombia. Tectonophysics, v.399, p.221-250.

Monsalve, O., 1988, Estilo tectónico del flanco Norandino de Venezuela (Afiche-Poster), paper presented at Simposio Bolivariano, Exploración petrolera de las Cuencas Subandinas III, Sociedad Venezolana de Geólogos, Caracas- Venezuela, p.13-16.

Monod, B., Dhont, D., Hervouet, Y., 2008, Orogenic Float Model: an Explanation for the Dynamics of the Venezuelan Andes, American Geophysical Union, Fall Meeting 2008, abstract #T23B-2028.

Montgomery, D.R., Balco, G., Willett, S.D., 2001, Climate, tectonics, and the morphology of the Andes. Geology, v. 29 (7), p. 579-582.

Montgomery, D.R., Brandon, M.T., 2002, Topographic controls on erosion rates in tectonically active mountain ranges. Earth Planet. Sci. Lett., v.201, p.481-489.

Moore, M.A., England, P.C., 2001, On the inference of denudation rates from cooling ages of minerals. Earth and Planetary Science Letters, v.185, p.265-284.

Mora, J., Loureiro, D., Ostos, M., 1993, Pre-Mesozoic rectangular network of crustal discontinuities: One of the main controlling factors of the tectonic evolution of northern South America. Abstract, AAPG/SVG International Congress and Exhibition, Caracas, 58.

Mora, A., Parra, M., Strecker, M.R., Sobel, E.R., Hooghiemstra, H., Torres, V., Jaramillo, J.V.., 2008, Climatic forcing of asymmetric orogenic evolution in the Eastern Cordillera of Colombia. Geol. Soc. Am. Bull., v.120, p.930-949.

Mora, A., Gaona T., Kley, J., Montoya, D., Parra, M., Quiroz, L.I., Reyes, G., Strecker, M.R., 2009, The role of inherited extensional fault segmentation and linkage in contractional orogenesis: a reconstruction of Lower Cretaceous inverted rift basins in the Eastern Cordillera of Colombia, Basin Res., v.21, p.111-137.

Muessig, K.W., 1984, Structure and Cenozoic tectonics of the Falcón Basin, Venezuela, and adjacent areas. In: Bonini, W.E., Hargraves, R.B., Shagam, R. (Eds.), The Caribbean–South American Plate Boundary and Regional Tectonics. GSA Memoir 162, Boulder, Colorado, p. 217-230.

Muller, J., Di Giacomo, E., Van Erve, A.W., 1987, A palynological zonation for the Cretaceous, Tertiary, and Quaternary of Northern South America. American Association of Stratigraphical Palynologists Contributions Series, v. 19, p. 7-76.

Murdock, T.Q., Weaver, A.J, Fanning, A.F., 1997, Paleoclimatic response of the closing of the Isthmus of Panama in a coupled ocean-atmosphere model. Geophys. Res. Lett., v.24 (3), p.253-256.

Naeser, C.W., 1978, Fission track dating: U.S. Geological Survey Open-File Report 76–190, p.87.

Naeser, C.W., 1979, Fission-track dating and geologic annealing of fission tracks, in Jager, E., and Hunziker, J.C., eds., Lectures in Isotope Geology: Springer-Verlag, New York, p. 54-169.

Naeser, N.D., Naeser, C.W., McCulloh, T.H., 1989, The application of fission-track dating to the depositional and thermal history of rocks in sedimentary basins.- In: N.D. NAESER & T.H. MCCULLOH (eds), Thermal history of sedimentary basins, Springer-Verlag, New York, p.157- 188.

Naranjo, M.E., Duque, R., 2004, Estimación de la oferta de agua superficial y conflictos de uso en la cuenca alta del Río Chama, Mérida, Venezuela, INCI, v.29, p.130-137.

Nivia, A., Marriner, G., Kerr, A., 1996, El Complejo Quebradagrande, una posible cuenca marginal Intracratónica del Cretáceo Inferior en la Cordillera Central de los Andes Colombianos: Santafé de Bogotá. VII Cong. Col. Geol. Mem., 3, p. 108-123.

Ojeda-German-Yury, B.K., 2000, Analysis of flexural isotasy of the Northern Andes. CP: United-States. DG: Doctoral. DI: Florida International University. Miami, FL, United States, p. 97.

Oldow, J.S., Bally, A.W., Avé Lallemant, H.G., 1990, Transpression, orogenic float, and lithospheric balance. Geology, v.18, p.991-994.

Ostos, M., Yoris, F., Lallemant, H.G.A., 2005, Overview of the Southeast Caribbean South America plate boundary zone, in Avé Lallemant, H.G., and Sisson, V.H., eds., Caribbean-South American plate interactions, Venezuela. Geological Society of America, Special Paper, v.394, p. 53-89.

O'Sullivan, P. B., Parrish, R.R., 1995, The importance of apatite composition and single-grain ages when interpreting fission track data from plutonic rocks: A case study from the Coast Ranges, British Colombia. Earth Planet. Sci. Lett., v.132, p.213-224.

Pardo-Casas, F., Molnar, P.,1987, Relative motion of the Nazca (Farallon) and South American plates since Late Cretaceous time. Tectonics, v. 6, p.233-248.

Parra, M., Mora, A., Sobel, E.R., Strecker, M.R., Jaramillo, C., González, R., 2009, Episodic orogenic-front migration in the northern Andes: constraints from low temperature thermochronology in the Eastern Cordillera, Colombia, Tectonics, in press.

Pennington, W.D., 1981, Subduction of the eastern Panamá basin and seismotectonics of northwestern South America. Journal of Geophysical Research, v. 86 (B11), p.10,753–10,770.

Pérez, O., Aggarwal, Y., 1981, Present-day tectonics of southeastern Caribbean and northeastern Venezuela. Journal of Geophysical Research, v. 86, p.10791-10805.

Pérez, O.J., Bilham, R., Bendick, R., Velandia, J.R., Hernández, N., Moncayo, C., Hoyer, M., Kozuch, M., 2001, Velocity field accross the southern Caribbean plate boundary and estimates of Caribbean/South-American plate motion using GPS geodesy 1994-2000, Geophys. Res. Lett., v.28, p.2987-2990.

Pindell, J.L., Cande, S.C., Pitman, W.C., Browley, D.B., Dewey, J.F., Labreque, J., Haxby, W., 1988, A plate-kinematic framework for models of Caribbean evolution. In Mesozoic and Cenozoic plate reconstruction, ed. C.R Scotese and W.W. Sager. Tectonophysics, v.155, p.121-138.

Pindell, J.L., Dewey, J.F., 1982, Permo-Triassic reconstruction of western Pangea and the evolution of the Gulf of Mexico/Caribbean region. Tectonics, v.2, p.179-211.

Pindell, J., Kennan, L., 2001, Kinematic evolution of the Gulf of Mexico and Caribbean, in R.H. Fillon, N.C. Rosen, and P. Weimer (Eds.), Petroleum Systems of Deep-Water Basins: Global and Gulf of Mexico Experience: GCSSEPM Foundation, XXI Annual Research Conference, Transactions, p.193-220.

Price, P.B., Walker, R.M., 1962a, Electron Microscope Observation of Etched Tracks from Spallation Recoils in Mica. Phys. Rev. Letters, v.8, p.217-219.

Price, P.B., Walker, R.M., 1962b, Chemical Etching of Charged Particle Tracks. J. Appl. Phys., v.33, p.3407-3412.

Rahl, J. M., Ehlers, T.A., van der Pluijm, V.A., 2007, Quantifying transient erosion of orogens with detrital thermochronology from syntectonic basin deposits. Earth and Planetary Science Letters, v.256, p.147-161.

Reiners, P. W., Brandon, M.T., 2006, Using thermochronology to understand orogenic erosion, Annu. Rev. Earth Planet. Sci., v.34, p.419-466, doi:10.1146/annurev.earth.34.031405.125202.

Reiners, P. W., Ehlers, T. A., Mitchell, S.G., Montgomery, D.R., 2003, Coupled spatial variations in precipitation and long-term erosion rates across the Washington Cascades. Nature, v.426, p.645-647.

Restrepo-Alvarez, J.J., 1991, Datación de algunos plutones de Antioquia por el Método de Huellas de Fisión. Boletín de Ciencias de la Tierra, v.10, p. 95-107.

Ring, U., Brandon, M. T., Willet, S.D., Lister, G. S., 1999, Exhumation processes. In: Ring, U., Brandon, M. T., Willet, S. D., Lister, G. S. (eds) Exhumation Processes: Normal Faulting, Ductile Flow, and Erosion. Geological Society, London, Special Publications, v.154, p.1-27.

Rod, E., 1956, Strike Slip Faults of Northern Venezuela. American Association of Petroleum Geologist Bulletin, v.40(3), p.457-475.

Rod, E., 1960, Comments on the gravity field of the Venezuelan andes and adjacent basins. Bol. Inf. Assoc. Venez. Geol. Min. Pet., v.3, p.170-175.

Rosencrantz, E., Ross, M.I., Sclater, J.G., 1988, Age and spreading history of the Cayman Trough as determined from depth, heat flow, and magnetic anomalies. Journal of Geophysical Research, v. 93 (3), p.2141-2157.

Roure, F., Colletta, B., De Toni, B., Loureiro, D., Passalacqua, H., Gou, Y., 1997, Within-plate deformations in the Maracaibo and East Zulia basins, western Venezuela. Marine and Petroleum Geology, v.14 (2), p.139-163.

Ruhl, K.W., Hodges, K.V., 2005, The use of detrital mineral cooling ages to evaluate steady state assumptions in active orogens: An example from the central Nepalese Himalaya. Tectonics, v.24: TC4015, doi:10.1029/2004TC001712.

Rull, V., 2005, A Middle Wisconsin interstadial in the northern Andes. Journal of South American Earth Sciences, v.19, p.173-179.

Schneider J. F., Pennington W. D., Meyer R. P., 1987, Microseismicity and focal mechanisms of the intermediate depth Bucaramanga Nest, Colombia. J. Geophys. Res., v.92, p.13913-13926.

Shagam, R., 1972, Evolución tectónica de los andes Venezolanos. IV Congr. Geol.. Venez., Mem., v. 2, p.1201-1258.

Shagam, R., Kohn, B., Banks, P., Dasch, L., Vargas, R., Rodríguez, G., Pimentel, N., 1984, Tectonic implications of Cretaceous–Pliocene fission track ages from rocks of the circum-Maracaibo Basin region of western Venezuela and eastern Colombia. Geological Society of America. Memoir , v .162, p.385- 412.

Shubert, C., 1969, Geologic structure of a part the Barinas mountain front, Venezuelan Andes. Bull, Geol. Soc. Am., v.80, p.443-458.

Schubert, C., 1974, Late Pleistocene Mérida glaciation, Venezuelan Andes. Boreas, v.3, p.147-152.

Shubert, C., 1979, El Pilar fault zone, northeastern Venezuela brief review. Tectonophysics, v.52 (1-4), p. 447-455.

Schubert, C., 1980a, Late-Cenozoic pull-apart basins, Boconó fault zone, Venezuelan Andes. Journal of Structural Geology, v.2 (4), p. 463-468.

Schuber, C., 1980b, Morfología neotectónica de una falla rumbo-deslizante e informe preliminar sobre la falla de Boconó, Andes Merideños. Acta Científica Venezolana, v.31 (2), p.98-111.

Schubert, C., 1981, Are the Venezuelan fault systems part of the southern Caribbean plate boundary?. Geologische Rundschau, v.70, p.542-551.

Schubert, C., 1982, Neotectonics of Boconó Fault, Western Venezuela. Tectonophysics, v.85, p. 205-220.

Shubert, C., 1984, Basin formation along the Boconó-Morón-El Pilar fault system Venezuela. Journal of Geophysical Research B, v.89 (7), p.5711-5718.

Schubert, C.,1985, Comments on "Subduction of the Caribbean Plate and basement uplifts in the overriding South American Plate". Tectonics, v.4 (7), p.781-783.

Schubert, C., Clapperton, C.M., 1990, Quaternary glaciations in the northern Andes (Venezuela, Colombia and Ecuador), Quat. Sci. Rev., v.9, p.123-135.

Schubert, C., Valastro, S., 1980, Quaternary Esnujaque Formation, Venezuelan Andes: Preliminary Alluvial Chronology in a Tropical Mountain Range. Z. dt. Geol. Ges., v.131, p.927-947.

Singer, A., Audemard, F. A., 1997, Aportes de Funvisis al desarrollo de la geología de fallas activas y de la paleosismología para los estudios de amenaza y riesgo sísmico. Academia de las Ciencias Naturales, Matemáticas y Físicas. Publicación Especial, v.3, p.25-38.

Skerlec, G.M., Hargraves, R.B., 1980, Tectonic significance of paleomagnetic data from northern Venezuela. Journal of Geophysical Research, v. 85 (B10), p.5303- 5315.

Small, E.E., Anderson, R.S., 1998, Pleistocene relief production in Laramide mountain ranges, western United States. Geology, v.26 (2), p.123-126.

Soulas, J. P., 1983, Tectónica cuaternaria de la mitad Sur de los Andes Venezolanos-Grandes Rasgos. Simposio de Neotectónica, Sismicidad y Riesgo Geológico en Venezuela y el Caribe, XXXIII Conv. AsoVAC, Caracas, Acta Cient.Venezolana, v.34, 525 (Resumen).

Soulas, J.P., 1986, Neotectónica y tectónica activa en Venezuela y regiones vecinas. VI Congreso Geológico Venezolano Memorias, Septiembre-Octubre, Tomo X, p. 6639-6656.

Spiegel, C., Kohn, B., Raza, A., Rainer, T., Gleadow, A., 2007, The effect of long-term low-temperature exposure on apatite fission track stability: a natural annealing experiment in the deep ocean. Geochimica et Cosmochimica Acta, v. 71, p. 4512-4537.

Spotila, J.A, House, M.A., Blythe, A.E., Niemi, N.A., Bank, G.C., 2002, Controls on the erosion and geomorphic evolution of the San Bernardino and San Gabriel Mountains, southern California. Geological Society of America, Special Paper v.365, p.205-230.

Spotila, J.A., House, M.A., Niemi, N.A., Brady, R.C., Oskin, M., Buscher, J.T., 2007a, Patterns of bedrock uplift along the San Andreas fault and implications for mechanisms of transpression. Geological Society of America, Special Paper, v.434, p.15-33.

Spotila, J.A., Niemi, N., Brady, R., House, M., Buscher, J., 2007b, Long-term continental deformation associated with transpressive plate motion: The San Andreas fault. Geology, v.35 (11), p.967-970., doi: 10.1130/G23816A.1.

Stansell, N.D., Polyssar, P.J., Abbott, M.B., 2006, Last glacial maximum equilibrium-line altitude and paleo-temperature reconstructions for the Cordillera de Mérida, Venezuelan Andes. Quaternary Research, v.67, p.115-127.

Stephan, J.F., 1982, Evolution geodynamique du domaine caraibe Andes et chaines caraibe sur la transversele de Barquisimeto, Venézuéla.Ph.D. Thesis , Universitè Pierre et Marie Curie, Paris, 1 and 2, p.512.

Stephenson, J., Gallagher, K., Holmes, C.C., 2006, A Bayesian approach to calibrating apatite fission track annealing models for laboratory and geological timescales. Geochimica Cosmochimica Acta, v. 70, p. 5183-5200.

Stewart, R.J., Brandon, M.T., 2004, Detrital zircon fission-track ages for the "Hoh Formation": Implications for late Cenozoic evolution of the Cascadia subduction wedge. Geological Society of America Bulletin, v. 116, p. 60-75.

Strecker, M.R., Alonso, R.N., Bookhagen, B., Carrapa, B., Hilley, G.E., Sobel, E.R., Trauth, M.H ., 2007, Tectonics and climate of the southern central Andes. Ann. Rev. Earth Planet. Sci., v 35, p.747-787.

Strecker, M., Alonso, R., Bookhagen, B., Carrapa, B., Coutand, I., Hain, M.P., Hilley, G.E., Mortimer, E., Schoenbohm, L., Sobel, E.R., 2009, Does the topographic distribution of the central Andean Puna Plateau result from climatic or geodynamic processes?. Geology, v.37, p.643-646.

Sykes, L., McCann, W., Kafka, A., 1982, Motion of Caribbean Plate during last 7 million years and implications for earlier Cenozoic movements. Journal of Geophysical Research, v.87(B13), p.10656-10676.

Sylvester, A., 1988, Strike-slip faults. Geological Society of America Bulletin, v.100, p.1666-1703.

Taboada, A., Rivera, L.A., Fuenzalida, A., Cisternas, A., Philip, H., Bijwaard, H., Olaya, J., Rivera, C., 2000, Geodynamic of the northern Andes: Subductions and intracontinental deformation (Colombia). Tectonics, v.19(5), p.787-813.

Tagami, T., O'Sullivan, P.B., 2005, Fundamentals of Fission-Track Thermochronology. Reviews in Mineralogy & Geochemistry, v.58, p.19-47.

Terzopoulos, D., 1988, The computation of visible-surface representations. Institute of Electrical and Electronics Engineers Transactions on Pattern Analysis and Machine Intelligence, v.10(4), p. 417-438.

Toro, M., Steel, J. R., 2002, A high-frequency sequence study: A Miocene deltaic and estuarine succession in the eastern Maracaibo composite foreland basin, western Venezuela. Bulletin of Canadian Petroleum Geology, v. 50(1), p. 3-30.

Toussaint, J-F, 1978, Grandes rasgos geológicos de la parte septentrional del Occidente Colombiano. Boletín de Ciencias de la Tierra, Universidad Nacional de Colombia, Medellín, v.3, p.231.

Toussaint, J-F., Restrepo, J.J, 1982, Magmatic evolution of the northwestern Andes of Colombia. Earth Science Reviews, v.18, p. 205-213.

Trenkamp, R., Kellogg, J., Freymueller, J., Mora, H., 2002, Wide plate margin deformation, southern Central America and northwestern South America, CASA GPS observations. Journal of South American Earth Sciences, v. 15, p. 157-171.

Tschanz, C.M., Marvin, R.F., Cruz, B.J., Mehnert, H.H., Cebula, G.T., 1974, Geologic Evolution of the Sierra Nevada de Santa Marta, Northeastern Colombia. Geol. Soc. Am. Bull., v.85, p.273-284.

Tucker, G.E., Whipple, K.X., 2002, Topographic outcomes predicted by stream erosion models: Sensitivity analysis and intermodel comparison. Journal of Geophysical Research, 107 (B9), 2179, doi:10.1029/2001JB000162.

Valla, P.G., Herman, F., van der Beek, P.A., Braun, J., submitted, Inversion of thermochronological age-elevation profiles to extract independent estimates of denudation and relief history – I: Theory and conceptual model. Earth and Planetary Science Letters.

van der Beek, P.A, 1995, Tectonic evolution of continental rifts. PhD thesis, Faculty of Earth Sciences, Free University, Amsterdam.

van der Beek, P.A., Robert, X., Mugnier, J.L., Bernet, M., Huyghe, P., Labrin, E., 2006, Late Miocene: Recent exhumation of the central Himalaya and recycling in the foreland basin assessed by apatite fission-track thermochronology of Siwalik sediments, Nepal. Basin Research, v.18, p. 413-434.

van der Hammen, T., 1956, A palynological systematic nomenclature. Bol. Geol., Bogota v.4 (2-3), p. 63-101.

VanMelle J., Vilema W., Faure-Brac B., Ordoñez M., Lapierre H., Jiménez N., Jaillard E.,García M., 2008, Pre-accretion evolution of the Piñón oceanic terrane of SW Ecuador. Stratigraphy and geochemistry of the «Calentura Formation». Bulletin de la Societé Géologique de France, v.179(5) , p.433-443.

Vauchez, A., Barruol, G., Tommasi, A., 1997, Why do continents break-up parallel to ancient orogenic belts?. Terra Nova, v.9 (2), p. 62-66.

Vermeesch, P., 2004, How many grains are needed for a provenance study?. Earth and Planetary Science Letters, v. 224, p.441-451.

Vernon, A.J., van der Beek, P.A., Sinclair, H., 2009, Spatial correlation between long-term exhumation rates and present-day forcing parameters in the western European Alps. Geology, v.37(9), p.859-862.

Villamil, T., 1999, Campanian–Miocene tectonostratigraphy, depocenter evolution and basin development of Colombia and western Venezuela. Palaeogeography, Palaeoclimatology, Palaeoecology, v. 153, p. 239-275.

Villamil, T., Pindell, J.L., 1998, Mesozoic paleogeographic evolution of northern South America: Foundations for sequence stratigraphic studies in passive margin strata deposited during non-glacial times, in J. L. Pindell, and C. Drake, eds., Paleogeographic Evolution and Non-glacial Eustacy: Northern South America: SEPM Special Publication, p. 283-318.

Von Estorff, F.E., 1946, Tectonic framework of northwestern South America. AAPG Bulletin, v.30 (4), p. 581-590.

Wadge, G., Burke, K., 1983, Neogene Caribbean plate rotation and associated Central American tectonic evolution. Tectonics, v.2 (6), p. 633-643.

Wagner, G.A., Reimer, G.M., 1972, Fission track tectonics: The tectonic interpretation of fission track apatite ages. Earth and Planetary Science Letters, v.14, p.263-268.

Wagner, G., Van den Haute, P., 1992, Fission track dating; Netherlands: Solid Earth Sciences Library, Kluwer Academic Publishers, p.285.

Weber, J.C., Dixon, T.H., DeMets, C., Ambeh, W.B., Jansma, P., Mattioli, G., Saleh, J., Sella, G., Bilham, R., Perez, O., 2001, GPS estimate of relative motion between the Caribbean and South American plates, and geologic implications for Trinidad and Venezuela. Geology, v.29, p.75-78.

Whipp, D.M., Ehlers, T.A., 2007, Influence of groundwater flow on thermochronometerderived exhumation rates in the central Nepalese Himalaya. Geology, v.35, p.851-854.

Whipp, Jr., D. M., Ehlers, T.A., Braun, J., Spath, C.D., Effects of exhumation kinematics and topographic evolution on detrital thermochronometer data. Journal of Geophysical Research, Earth Surface, (in review).

Whipple, K.X., 2009, The influence of climate on the tectonic evolution of mountain belts. Nature Geosci., v.2, p.97-104.

White, C., 1985, Patron structural y prospectividad del frente norandino entre la Fría y el Vigía. VI Congreso Geológico Venezolano, p.5397-5416.

Wilk, M.B., Gnanadesikan, R., 1968, Probability plotting methods for the analysis of data. Biometrika, v.55, p.1-17.

Willet, S., Beaumount, C., Fullsack, P., 1993, Mechanical models for the tectonics of doubly vergent compressional orogens. Geology, v.21, p. 371-374.

Wilson, J.P., Gallant, J.C., 2000, Terrain Analysis: Principles and Applications. John Wiley & Sons, Inc., p.479.

Wilson, J.T., 1965, Submarine fracture zones, aseismic ridges, and the international council of scientific unions line: proposed western margin of the East Pacific Rigdes. Nature, v.207, p. 907-911.

Wittmann, H., von Blanckenburg, F., Kruesmann, T., Norton, K.P., Kubik, P.W., 2007, The relation between rock uplift and denudation from cosmogenic nuclides in river sediment in the Central Alps of Switzerland. J. Geophys. Res., v.112: F04010, doi:10.1029/2006JF000729.

Wolf, R.A., Farley, K.A., Kass, D.M., 1998, Modeling of the temperature sensitivity of the apatite (U-Th)/He thermochronometer. Chemical Geology, v.148, p.105-114.

Yoris, F., Ostos, M., 1997, Well Evaluation Conference, edited by Schlumberger Oilfield Services, Caracas, Venezuela, p.1-40.

Ysaccis, R., Cabrera, E., Del Castillo, H.,2000, El sistema petrolífero de la Blanquilla, costa afuera Venezuela. VII Congreso Bolivariano Exploración Petrolera en las Cuencas Subandinas, Proceedings, p. 411-425.

Zambrano, E., Vasquez, E., Duval, B., Latreille, M., Coffinières, M., 1972, Paleogeographic and Petroleum Synthesis of Western Venezuela. Editions Technip, p.59.

Zhang, W., Montgomery, D.R., 1994, Digital elevation model grid size, landscape representation, and hydrologic simulations, Water Resour. Res., v.30 (4), p.1019-1028.

APPENDIX

1. Bermúdez, M.A, Alson, P., Glotzbach, C., New Poissonian Method for determining fission-track ages, to be submitted to *Mathematical Geology*
2. Bermúdez-Cella, M., 2008, Detección de mezclas Poisson por p-Partición. *Divulgaciones Matemáticas*, 16, 1, 73-86.
3. Bermúdez-Cella, M., López, A., Bálcazar-García, M., Zarazúa-Ortega, G., Bona, R., 2009, Caracterización de Cristales de Apatito y Circón del Estándar Internacional Fish Canyon Tuff para su uso en un Laboratorio de Termocronología, *Interciencia*, vol. 34, No. 4, p. 240-246.
4. Table A1. Individuals and global values of ξ used in this thesis.
5. Figure A1. Spatial distribution of available samples collected for this thesis to study the exhumation history of the Venezuelan Andes.
6. Table A2. Prepared or processed fission track samples. (D) dated, (GBQ) grains of poor quality, (ND) not dated and D(0) samples with a zero fission-track age, see Figure A1 for geographical location.
7. Figure A2. Probability density and radial plots of in-situ fission-track samples (see Table A2).
8. Figure A3. Decomposition into significant ages populations using Binomfit and p-partition. Radial plots of modern river fission-track samples (see Table A2).
9. Figure A4. Decomposition into significant ages populations using Binomfit and p-partition. Radial plots of synorogenic sediments fission-track samples (see Table A2).
10. Figure A5. Decomposition into significant ages populations using BayesQt of modern river and synorogenic sediments (see Table A2).
11. Taxa references used to document the palinologycal analysis.

APPENDIX 1

A new Poissonian method for the determination of fission-track ages

Mauricio Bermúdez[1,2], Pedro Alson[3], Christoph Glotzbach[1]

[1]Laboratoire de Géodynamique des Chaînes Alpines, Université Joseph Fourier, BP53, 38041 Grenoble, France (mauricio.bermudez-cella@e.ujf-grenoble.fr / Fax: +33 476 514058 / Phone: +33 476 635964)
[2]Laboratorios de Termocronología y Geomatemáticas, Escuela de Geología, Minas y Geofísica. Facultad de Ingeniería, Universidad Central de Venezuela, Caracas, Venezuela
[3]Escuela de Matemáticas, Facultad de Ciencias, Universidad Central de Venezuela.

Abstract

Fission-track (FT) thermochronology has been widely used since the 1970's to constrain the rock low-temperature thermal history in numerous geological settings. Statistical problems associated with this method have been addressed since the 1980's. Today, with the improvements brought to the technique, new questions arise which require the adaptation of previously established statistical methods. Samples used for FT thermochronology are typically composed of minerals (e.g. apatite, zircon) with a wide variability in Uranium (U) concentration. Previous methods, however, suppose that all counted grains have the same U concentrations. This implies that fission-track counts can be modelled by a unique Poisson distribution whose mean is a function of the mean U concentration. This amounts to a simplification of the problem when samples are characterised by grains with strongly varying U concentrations. In this case, the age-dispersion test used for recognising homogeneous grain-age distributions is not applicable. The existing literature does not indicate in strict terms what statistic method should be applied in such cases. We propose a new statistical methodology called p-partition to solve this specific problem. The methodology is applied to FT standards, in-situ and detrital samples. For standards, the determined age is closer to the independently determined age.

Keywords: fission-track age, U concentration, homogeneity, age dispersion, Poisson distribution, mixtures.

1. Introduction

The fission track (FT) thermochronology is a radiometric dating method that differs from other techniques mainly because the 'daughter' product of the radioactive process that is measured to obtain the age is a structural defect in heavy minerals (apatite, zircon, sphene, etc) rather than a daughter isotope (Fleischer, Price and Walker, 1975). Uranium-238 (U-238) undergoes spontaneous fission decay at a known rate and is the only isotope with a decay rate that is relevant to the significant production of natural fission tracks on geological time scales. The fragments emitted by this fission process leave trails of damage (fossil tracks) in the crystal structure of the accessory mineral.

Among the methods that utilize those fission tracks to estimate the age of a rock, the external-detector method (Wagner and van den Haute, 1992), is one of the most frequently used. In this method, induced tracks are produced by thermal neutron irradiation of half of the sample to reveal the concentration of the parent isotope (U-238). The numbers of spontaneous and induced tracks, N_s and N_i, present within the same area A of a polished grain surface and the corresponding surface of a mica (external detector), are used to estimate ρ_s , ρ_i and R , where R is the ratio between spontaneous and induced track density ($R=\rho_s/\rho_i$). R is necessary to calculate the unknown fission-track age (t_u), which is obtained by using the following fission-track age equation (Wagner and van den Haute, 1992):

$$t_u = \lambda^{-1} \ln\left(1 + \frac{\lambda}{2} \zeta \rho_d R\right) \quad (1)$$

where: λ is the alpha decay constant for U-238 ($\lambda=1.55125\times10^{-10}$ y^{-1}); ζ is the zeta-calibration constant (Hurford and Green, 1983), which is calculated from an analysis of 'age standards'; ρ_d is the track density for the fluence monitor.

The ratio (R) between spontaneous and induced tracks is proportional to the age. Thus, the statistical problem of determining a sample age is reduced to how to combine the individual

56 determinations of R_j for j=1,…,n grains into a meaningful estimator for the sample. In the
57 past, many authors (Burchart, 1981; Green, 1981; Galbraith and Laslett, 1985; Galbraith and
58 Laslett, 1993; Galbraith, 2005) have proposed different estimators for R, known as isochrones,
59 mean ratio, pooled and central age estimators.
60 Currently, the most commonly used statistical procedures to estimate fission-track ages
61 (Galbraith, 1981; Galbraith, 2005) are based on the simplifying hypothesis that the data
62 samples two Poissonian distributions, one for spontaneous (N_s) and an other for induced (N_i)
63 fission-track counts. Assuming that all grains have the same U concentration, there should be
64 a strong correlation between spontaneous and induced tracks. Thus, the FT counts can be
65 modelled by a unique Poisson distribution whose mean is given by the average U
66 concentration (Poissonian models, Galbraith, 1981).
67 A standard statistical protocol is used for the determination of fission-track ages and
68 associated errors (Galbraith, 1981; Galbraith and Laslett, 1993; Galbraith 2005). The first step
69 in this protocol is to test the homogeneity of the age in the fission-track data (to test whether
70 there is a single population of ages, or, equivalently, to test whether the relation between
71 spontaneous and induced fission tracks is linear), using the dispersion in the radial plot
72 (Galbraith, 1990; 2005) and the so-called ‘Galbraith test’ (Galbraith, 1981; Galbraith 2005),
73 which is based on a chi-square distribution (Galbraith, 2005). In cases where the fission-track
74 data fails the Galbraith test, no alternative methodology exists and the age is considered as
75 statistically unreliable. When the data pass the Galbraith test, the pooled age and its standard
76 error are calculated, from which the central age and dispersion may be obtained.
77 However, in some cases, the dispersion of N_s and N_i is significantly larger than predicted by a
78 unique Poissonian distribution, for these case the data fails the Galbraith test, and,
79 consequently, this affects considerably the quality of the age estimate (Green, 1981). At
80 present, this problem has not been solved, and the common treatment is to discard ‘outlier‘

observations based on personal criteria (e.g., Haack, 1973; Burchart, 1981; Bigazzi et al., 1986), until the Galbraith test indicates homogeneity in age.

In this paper, we will be concerned with presenting a statistical technique which performs better in those unconventional situations. It is based on a new Poissonian mixture discrimination that we call a 'p-partition'. Both, p-partitions and p-patterns are explained in detail. We present a table, constructed from a wide range of simulations that can be used to apply the technique in most practical situations. Finally, an assessment of the method is presented by using it in some real unconventional data cases.

2. Poisson mixtures discrimination by p-partition algorithm

In a rapidly cooled sample with homogenous U concentration, fission-track data should show a positive correlation between spontaneous and induced tracks. In natural samples, the U-concentration varies in both apatite and zircon crystals, which renders meaningless the assumption of a single Poisson population for spontaneous and induced tracks. In this case, we suggest to use the p-partition algorithm, which is explained in the following section.

2.1. Construction and definition of the p-partition

The construction of the p-partition is explained in the flowchart in Figure 1. Let's consider a group of natural numbers (or of data) *D*; in the particular case of fission-track data, this set is given by the induced fission-track counts of a sample. In the first step (step 1 in Figure 1) the minimum value of data *D* (*min(D)*) is taken, and the first Poisson quantile (*q*) is generated (Mendenhall et al., 1981; Hyndman and Fan, 1996): $q(p, \min(D))$ using the significance level *p*. Thus, we construct the intersection of this first interval with the data *D*, giving the first cover of the data: $C_1 = [\min(D), q(p, \min(D))]$. In the second step the first value greater than the minimum value of the data C_1 is used as the minimum value of the subset D_1, as $D_1 = \{x \in D / x \geq \max(C_1)\}$ or $D_1 = D - C_1$ (step 2 in the Figure 1). The $\min(D_1)$ is used to

generate the second Poisson quantile with the same value of p, yielding: $C_2 = [q(1-p, \min(D_1)), q(p, \min(D_1))]$. Thus for C_2, we begin with the $q(1-p, \min(D_1))$ in order to create a symmetrical interval.

When there are elements in the intersection of two continuous intervals (step 3, Figure 1), we apply a decision rule based on the highest Poisson probability that a certain element x_i is in one of the two subsets. After this discrimination of intersected elements, subset D_2 is constructed as $D_2 = \{x \in D / x \geq \max(C_2)\}$ or $D_2 = D - \bigcup_{j=1}^{2} C_j$, taking into account the minimum value of D_2 min(D_2). Repeating the previous process, we generate a Poisson quantile obtained from the interval C_3, given by $C_3 = [q(1-p, \min(D_2)), q(p, \min(D_2))]$.

The step 3 (Figure 1) should be repeated n times until all the data D is contained or equal to the union of intervals C_j for j=1,…,n.

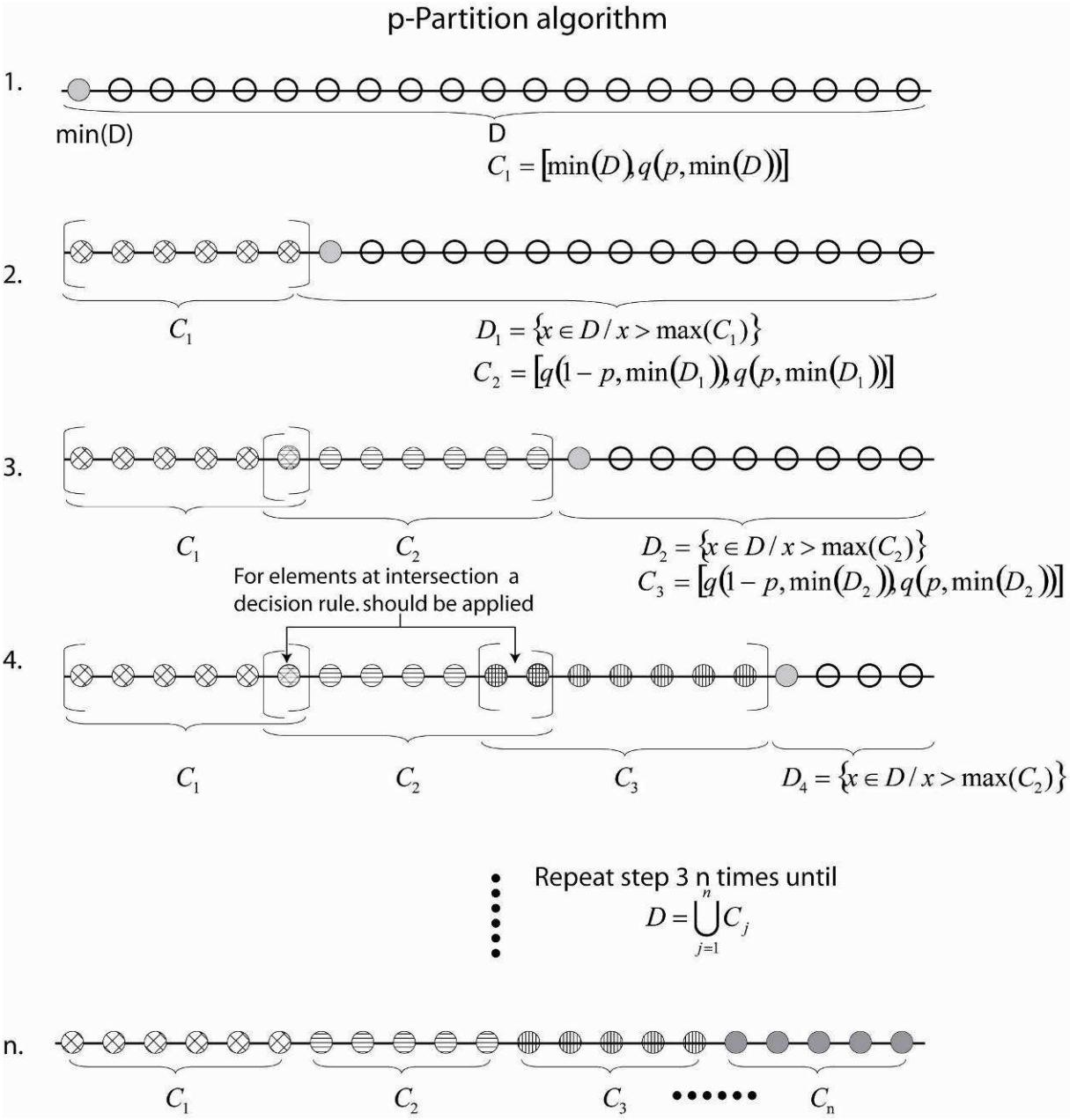

Figure 1. Flowchart showing the implementation of the p-partition algorithm.

In this work we have implemented the p-partition starting with the minimum of the set *D*, however, no significant differences were found when starting with the maximum of *D*. In the next section the p-partition algorithm is defined mathematically.

2.1.1 Definition of the p-partition

A Poisson ball (B_P) of centre *m* and radius *p*, is a set of natural numbers given by:

$$B_P(m,p)=\{x\in N\,|\,P(X=x)\geq p\}.$$

where *X* is a random variable obtained from a Poisson distribution with mean *m*. For a given finite set *D* of natural numbers, we define $D_1=D$, $m_i=\min(D_i)$, $D_{i+1}=D_i-B_P(m_i,p)$ for $i=1,...K-1$. The number *K* has to be chosen big enough to ensure that $D\subseteq\bigcup_{i=1}^{K-1}B_P(m_i,p)$ is satisfied. Let $\max(D)=m_K$. For *p* small enough, there exists for each $i=1,...K-1$, at least an n_i, with $m_i<n_i<m_{i+1}$ and $P_i(X=x)>P_{i+1}(X=x)$, if and only if $x<n_i$, where P_i is the probability Poisson distribution of mean m_i. Then if $C_i=\{n\in D\,|\,n_i<n\leq n_{i+1}\}$ for $i=2,..,K-1$, $C_1=\{n\in D\,|\,n\leq n_1\}$ and $C_K=\{n\in D\,|\,n_{K-1}<n\}$, $\{C_i\}$ is a partition of *D*. This partition, which depends on the value *p*, will be called a p-partition of *D*. (Bermúdez-Cella, 2008). Finally, we define the mean of the i^{th} Poisson subpopulation of the sample set *D*, as λ_i =integer part of (average (C_i)).

A fixed value of 0.95 for *p* is used, keeping in mind that the precision of the discrimination made by the p-partition algorithm depends on the separation among the means of the Poisson sub-populations. When the distance among the means increases, the p-value must be taken closer to 1, and reciprocally. In Table 1 we summarize our recommended a-priori for the p selection, based on the study of simulations; this value will be optimized using the p-partition algorithm as an hypothesis test. To know the distance between the means is thus very important before the p-partition can be applied, and, for this reason, we used a variation to the

p-partition algorithm, in which we use 100 Poisson random numbers for the creation of C_i, rather than quantiles.

Now, for each interval or sub-population C_i we calculate the mean and the average difference among all means of the intervals, using Table 1 for the selection of the initial p-value.

Average distance (δ) among Poissonians sub-populations using the a-priori algorithm	*Interval a-priori for p*
$\delta > 20$ *(far)*	[0.99,1]
$15 \leq \delta \leq 20$ (*intermediate*)	(0.96,0.99)
$10 \leq \delta < 15$ (*near*)	(0.94,0.96]
$\delta < 10$ (*very near*)	(0.9,0.94]

Table 1. Summary of a-priori p-values to use with the p-partition algorithm, these values depend on the average distance among means of sub-populations giving by the a-priori algorithm.

Later, the p-value is optimized using a statistical hypothesis test based on the p-partition, which allows for the analysis of the quality of the separation, and for the detection of the optimum p-value.

2.1.2 p-partition and statistical hypothesis tests.

The use of p-partition as hypothesis test allows optimize the value of p to use for the p-partition algorithm. This hypothesis test is based on the statistical method known as 'bootstrapping' (Diaconis and Efron, 1983). For more details on this test, the reader is referred to Bermúdez-Cella (2008). The optimized value of p is compared with all different p-values; in this way we can test the resolution of the optimized p-value. The separation of fission-track data by the p-partition algorithm implies that, to calculate the fission-track mean age in the equation (1), a new statistical estimator for R needs to be defined.

3. New statistical estimator for the fission-track age

The number of spontaneous N_{sj} and induced N_{ij} fission-tracks in a grain *j*, can be modelled in the following way (Galbraith, 1981):

168
$$N_{sj} = m_{sj} + \varepsilon_j = \lambda_s U_j + \varepsilon_j$$
$$N_{ij} = m_{ij} + \xi_j = \lambda_i U_j + \xi_j \quad (2)$$

169 where ε_j, ξ_j, U_j, λ_i and λ_s are random variables representing, respectively, the errors on the
170 spontaneous (ε_j) and induced (ξ_j) fission track numbers, the U concentration (U_j), and
171 appropriate parameters (λ_s and λ_i). m_{sj}, m_{ij} are the means of the U concentration. For apatite
172 or zircon grains, these values depend on the initial U concentration and on the age; for the
173 mica they depend only on the U concentration.

174 Extracting U_j from equations (2) results in the following relationships:

175
$$U_j = \frac{1}{\lambda_s}\left(N_{sj} - \varepsilon_j\right)$$
$$U_j = \frac{1}{\lambda_i}\left(N_{ij} - \xi_j\right) \quad (3)$$

176 which yields:

177
$$N_{sj} = \frac{\lambda_s}{\lambda_i} N_{ij} - \frac{\lambda_s}{\lambda_i}\xi_j + \varepsilon_j, \ \forall j = 1, \cdots, n. \quad (4)$$

178 Renaming $\frac{\lambda_s}{\lambda_i}$ by *R*, in equation (4) results in:

179
$$N_{sj} = RN_{ij} - R\xi_j + \varepsilon_j, \ \forall j = 1, \cdots, n. \quad (5)$$

180

181 Summing over *j* gives:

182

183
$$\sum_{j=1}^{n} N_{sj} = R\left[\sum_{j=1}^{n} N_{ij}\right] + \sum_{j=1}^{n}\left[-R\xi_j + \varepsilon_j\right]. \quad (6)$$

184

185 In the ideal case, the expected fission-track error is small or negligible:

$$E\left(\sum_{j=1}^{n}\left[-R\xi_j+\varepsilon_j\right]\right)=0 \quad (7)$$

which yields a reasonable estimator for *R*:

$$\overline{R}=\frac{\sum_{j=1}^{n}N_{sj}}{\sum_{j=1}^{n}N_{ij}} \quad (8)$$

This estimator is known as the "*Pooled mean*" (Burchart, 1981; Green, 1981; Galbraith, 2005). Note that to find this estimator, equation (2) assumes that the number of spontaneous fission-tracks depends only on the U concentration; however, this number also depends on the age. Galbraith (2005) suggested that the pooled estimator (8) is the maximum-likelihood estimator; however, we show in the appendix section that, this estimator is only an approximation of the maximum-likelihood (Kendall and Stuart, 1958). We show that this pooled estimator was obtained by supposing that all grains have the same U concentration. We now consider an alternate estimator if this is not the case.

3.1 The p-pooled estimator

The estimator that we propose is similar to the pooled estimator, but it does not suppose similar U concentration in all the grains. Instead of using equation (5), we suggest to use a more general equation given by:

$$\hat{N}_{sg}=R\hat{N}_{ig}-R\xi_g+\varepsilon_g \text{, where } g = 1,\ldots,m \quad (9)$$

in which *g* denotes a group that is provided by the same Poisson distribution; *m* is the number of discriminated populations; $\hat{N}_{sg}$, $\hat{N}_{ig}$ are estimates of the mean number of spontaneous and

induced tracks (N_s and N_i) in the grains belonging to group g. Combining with equation (9), separating R and neglecting the errors on fission-track counts we obtain:

$$\overline{R}_p = \frac{\sum_{g=1}^{m} \hat{N}_{sj}}{\sum_{g=1}^{m} \hat{N}_{ij}} \quad (10)$$

Note that the 'pooled estimator' (8) is a particular case of $\overline{R}_p$ when there is only one group. $\overline{R}_p$ is called the *p-pooled* estimator because it depends on the p-partition.

In the next sections we present a comparison between the p-pooled and traditional age estimators (isochrona, mean ratio, pooled and central age) applied to fission-track age standards.

3.2 Numerical implementation

The use of equation (10) assumes that the data is separated into different Poissonian populations, using the p-partition algorithm. The numerical implementation of p-pooled requires some assumptions:

1. Dimensionless. Defining A as the mean area for all grains $j = 1,\ldots,n$, the $N_{s,}$ N_i can be defined as dimensionless quantities according to:

$$\overline{N}_{s,i} = round\left(N_{s,i} \cdot \frac{A_j}{A} \right)$$

   where A_j is the area of the j-th grain and the 'round' refers to rounding to the nearest integer. Note that the choice of a particular rounding rule has little effect on the value of the estimator. This is done to prevent fission-track counts from being affected by the size of the counting area.

2. Hypothesis test and optimization. We use the p-partition hypothesis test and the optimization of the p-value (section 2.1).

3. Estimation of the age. We calculate the p-pooled estimate (10) and the corresponding fission-track age (1) from the original data.

4. p-patterns concept

Applying the p-partition algorithm to a sample *D*, we can plot the resulting means of N_{sg} and N_{ig} for each group. This provides us with a polygonal line that we call *p-pattern.* Because spontaneous and induced fission-tracks are related to the U concentration (according to equation 2), we expect the 'ideal' p-pattern to increase linearly. Figure 2 shows the p-patterns we found for 142 standard samples provided by different researchers (see acknowledgements). Figure 2A represents an 'ideal' p-pattern, Figure 2B-F represents anomalous p-patterns that take many different forms. The 5 anomalous patterns shown here indicate either some kind of problem in the determination of spontaneous fission-track numbers, (e.g., problems arising from the irradiation, sample preparation, poor contact between the mica and the sample, among many possibilities) or grains of different chemical compositions which have responded differently to annealing (e.g. Green et al. 1986, Barbarand et al., 2003a,b).

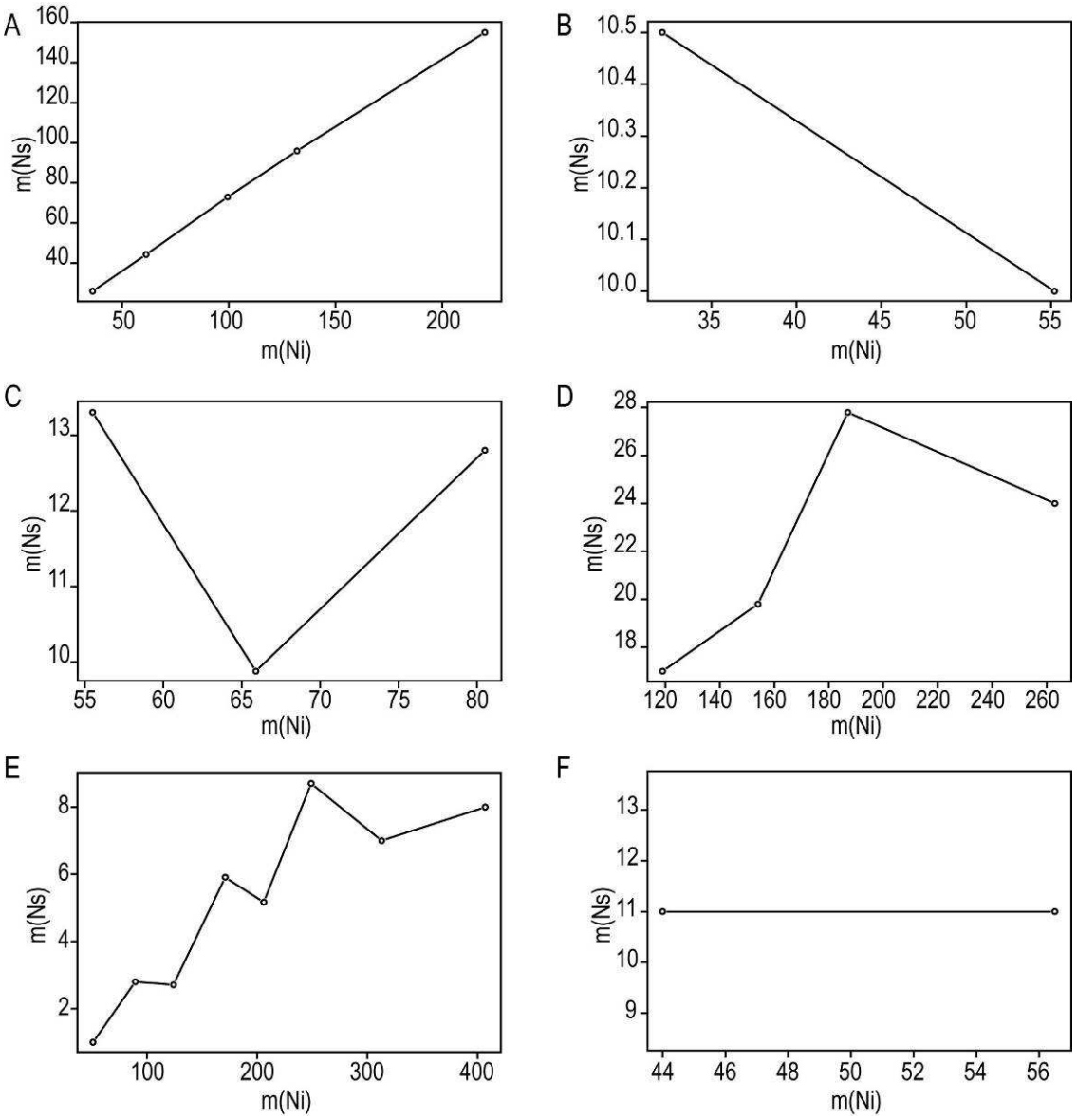

Figure 2. Different p-patterns that can be observed in fission-track data. A) Represent the 'ideal' case. The p-patterns in B to F are anomalous patterns.

5. Applications

5.1 Fission-track age standards

We have used a database of fission-track age standards (Table 3.3, p. 93, in Wagner and van den Haute, 1992) formed by 142 standards processed with the external detector technique: 32 samples of Durango apatite with a K-Ar age of 31.4 ± 0.6 Ma; 27 and 20 samples of Fish Canyon Tuff apatite and zircon with a K-Ar age of 27.8 ± 0.5 Ma; 11 samples of Buluk Member zircon with a K-Ar age of 16.4 ± 0.2 Ma; 25 and 14 samples of Dromedary

Mountains apatite and zircon with a Rb-Sr (biotite) age of 98.8 ± 0.6 Ma; 8 samples of Tardree Rhyolite zircon with a K-Ar age of 58.7 ± 1.1 Ma, and 5 samples of Bishop Tuff zircon with a $^{40}Ar/^{39}Ar$ age: of 0.734 ± 0.024 Ma.

5.1.1 Classification in p-patterns

Table 2 summarizes the character of the computed p-patterns for the entire database. Taking a fixed p=0.99, 119 dataset have 'ideal' p-patterns (cf. Figure 2A). The remaining 23 cases show anomalous p-patterns, classified according to Figure 2 in: 6 type (b), 6 type (c), 5 type (d), 4 type (e), and 2 type (f).

Classification in p-pattern. p fixed (0.99)								
Data	**Total**	**Increasing 'ideal'**	**Anomalous**	**(b)**	**(c)**	**(d)**	**(e)**	**(f)**
Durango apatite	32	27	5	3	0	0	0	2
Fish Canyon Tuff apatite	27	22	5	1	1	1	2	0
Fish Canyon Tuff zircon	20	17	3	0	1	1	1	0
Buluk Member zircon	11	9	2	0	1	1	0	0
Tardree Rhyolite zircon	8	6	2	0	0	2	0	0
Dromedary Mt. apatite	25	21	4	2	0	0	2	0
Dromedary Mt. zircon	14	12	2	0	2	0	0	0
Bishop Tuff zircon	5	5	0	0	0	0	0	0
Total	142	119	23	6	5	5	5	2

Table 2. Classification of standards database in p-patterns. A fixed p-value (0.99) was used to simplify the calculations.

5.1.2 Numerical resolution of the age provided by the different estimators

For the database given in Table 2, we calculated the age given by equation (1) using the different estimators of R (isochrona, mean ratio, pooled, central and p-pooled). To demonstrate the accuracy of the estimated age, we used the relative error given by the following equation:

$$\text{Rel. Error} = \frac{\left|\hat{t} - t_{K-Ar}\right|}{t_{K-Ar}} \qquad (11)$$

In which $\hat{t}$ and t_{K-Ar} represent the estimated and the K-Ar age for the standard samples, respectively. We calculated the average relative error for the 119 'ideal' p-patterns (Table 3). It shows that there is no significant difference among the different *R* estimators. For the 23 'anomalous' patterns, the results are shown in Table 4.

Relative Error	**Isochrona**	**Mean ratio**	**Pooled**	**Central**	**p-pooled**
Durango apatite	0.3117	0.3403	0.3171	0.3172	0.3037
Fish Canyon Tuff apatite	0.2030	0.2297	0.2093	0.2100	0.1873
Fish Canyon Tuff zircon	0.0484	0.0337	0.0370	0.0337	0.0351
Buluk Member zircon	0.4203	0.4019	0.4101	0.4077	0.4075
Tardree Rhyolite zircon	0.0181	0.0170	0.0033	0.0041	0.0033
Dromedary Mt. apatite	0.0120	0.0152	0.0021	0.0028	0.0023
Dromedary Mt. zircon	0.0110	0.0245	0.0067	0.0070	0.0069
Bishop tuff zircon	0.0312	0.0529	0.0061	0.0079	0.0048
Average	**0.1320**	**0.1394**	**0.1240**	**0.1238**	**0.1189**

Table 3. Average errors for the 119 data with 'ideal' p-patterns.

Relative Error	**Isochrona**	**Mean ratio**	**Pooled**	**Central**	**p-pooled**
Durango apatite	0.2856	0.3233	0.2966	0.2959	0.2739
Fish Canyon Tuff apatite	0.0537	0.0811	0.0237	0.0300	0.0103
Fish Canyon Tuff zircon	0.0323	0.3813	0.0625	0.0962	0.0625
Buluk Member zircon	0.5507	0.4642	0.5152	0.4964	0.5130
Tardree Rhyolite zircon	0.0134	0.0106	0.0001	0.0040	0.0001
Dromedary Mt. apatite	0.1678	0.3608	0.2487	0.2789	0.1245
Dromedary Mt. zircon	0.0191	0.0696	0.0382	0.0389	0.0382
Average	**0.1604**	**0.2416**	**0.1693**	**0.1772**	**0.1461**

Table 4. Average errors for the 23 data with 'anomalous' p-patterns.

We conclude that for the 119 data with 'ideal' p-patterns any of the age estimators can be used (Table 3). In contrast, for data with 'anomalous' p-patterns, differences among the estimators are important, while the p-pooled estimator yields the best estimation of the age.

5.2 Samples of unknown age

Applying our method to fission-track age standard samples indicates that it has certain advantages in comparison with the conventional methods. We now present results obtained

with the method for samples of unknown fission-track age. We compare our results with those obtained with the isochrona, mean ratio, pooled and central estimators.

5.2.1 Vertical profile in the Venezuelan Andes

We first applied the methodology proposed in this work to thirteen in-situ apatite fission-track samples of Bermúdez (2009). They were collected from the Sierra Nevada of Mérida along an age-elevation profile from 1.2 to 4.9 km elevation, located in the highest part of the Venezuelan Andes near Pico Bolívar. More detailed information about these samples is given in Bermúdez (2009). Table 5 shows the comparison among the different fission-track age estimations. Note that the central and pooled age converges to the same value, and that the ages obtained with all estimations, including the p-pooled estimator, are very similar. For the p-pooled estimation a fixed p-value of 0.9999 was used.

Sample	Elevation (m)	Isochrona	Error	Mean R	Error	Pooled	Error	Central	Error	p-pooled	Error	Poisson Pop.	p-pattern
48	4718	7.5	0.9	8.3	0.9	7.6	0.9	7.6	0.9	7.5	0.9	2	increasing
49	4622	6.8	0.9	8.5	1.1	7.5	1.0	7.5	1.0	7.7	1.0	2	increasing
50	4236	6.0	1.2	10.3	2.0	7.8	1.6	7.8	1.6	6.3	1.3	3	increasing
51	3999	5.8	0.5	7.1	0.7	6.5	0.6	6.5	0.6	6.2	0.6	4	increasing
52	3633	5.7	0.9	11.2	1.7	7.2	1.1	7.2	1.1	6.7	1.0	3	increasing
53	3285	7.0	0.9	5.7	0.7	6.5	0.8	6.5	0.8	7.1	0.9	4	increasing
65*	2770	4.9	0.3	6.2	0.4	5.2	0.4	5.4	0.6	4.9	0.3	4	increasing
54	2760	5.5	1.4	5.0	1.3	5.3	1.4	5.3	1.4	5.2	1.3	2	increasing
66	2490	5.0	0.8	5.3	0.9	5.1	0.9	5.1	0.9	4.9	0.8	4	increasing
67	2250	5.1	0.4	5.9	0.5	5.6	0.4	5.6	0.4	6.1	0.5	4	increasing
68	2060	4.9	0.7	5.8	0.8	5.2	0.7	5.2	0.7	5.1	0.7	3	d
69	1765	4.4	0.6	4.9	0.7	4.6	0.7	4.6	0.7	4.7	0.7	2	increasing
70	1250	3.8	0.2	4.2	0.2	4.2	0.2	4.3	0.3	3.3	0.2	7	d

Table 5. Comparison among different estimations of fission-track ages for in-situ samples of the Sierra Nevada, Venezuelan Andes (Bermúdez et al., 2009a). * Fail the Galbraith test

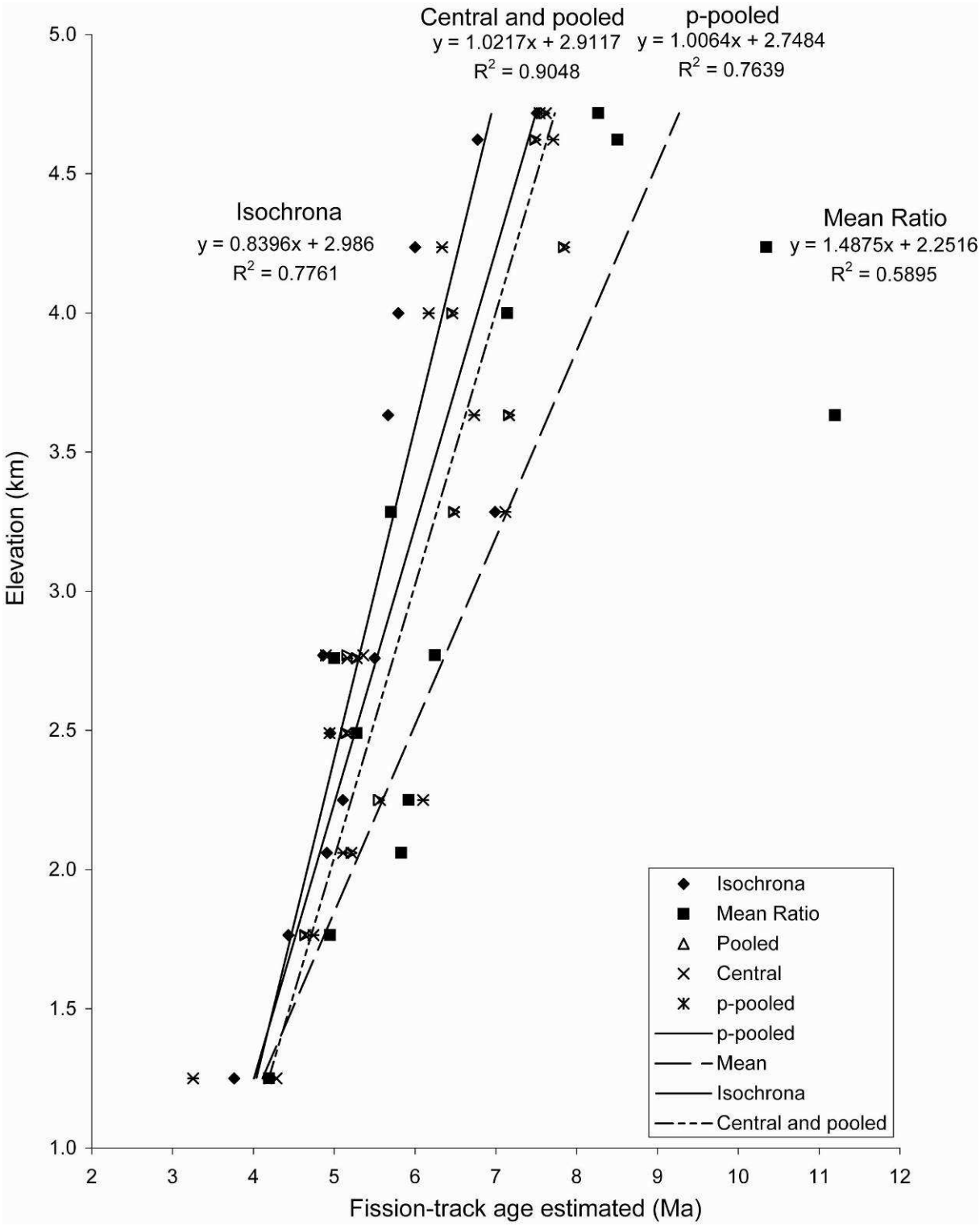

Figure 3. Comparison of age-elevations relationships given by the different fission-track age estimations

Figure 3 shows the corresponding age-elevation relationships derived from the ages along the Sierra Nevada vertical profile. The slope of each line can be used to estimate the exhumation rate. Results show that (1) the slope obtained by the central and pooled estimators are

316 concordant, and (2) the pooled family of estimators (central, pooled and p-pooled) give very
317 similar age-elevation relationships. The different estimation could be used for establishing
318 confidence intervals on exhumation rate. Thus, for the Sierra Nevada block the exhumation
319 rate lies between 0.8 and 1.5 km/Ma. Values from the pooled family suggest an exhumation
320 rate of ~1 km/Ma.
321

322 5.2.2 Modern rivers samples

323 The objective of this section is to show how the p-partition algorithm can be used to better
324 decompose mixed data of unknown populations. There are numerous approaches to
325 discriminate components of mixed data; some were specifically developed for use in
326 geochronology (Galbraith and Green, 1990; Brandon, 1992; Brandon, 1996; Richardson and
327 Green, 1997; Brandon et al., 1998; Sambridge and Compston, 1999; Viallefont et al., 2002;
328 Ehlers, 2005; Veermesch, 2007; Gallagher et al., 2009). We applied the p-partition algorithm
329 to identify the number and age of populations from detrital samples, i.e. collected in a river
330 sand. Based on this decomposition, pooled ages and standard errors are calculated for each
331 population. The results are shown using box-and-whisker diagrams (or 'boxplots'; Tukey,
332 1977; Frigge et al., 1989), located at the bottom of the probability density function (PDF, Fig.
333 4D).
334 We applied our new method (using p=0.995 as determined automatically from the
335 optimization routine), to a detrital apatite fission-track sample from the Coloncito River in the
336 Venezuelan Andes (Bermúdez, 2009). The sample is characterized by low U concentration,
337 which makes the discrimination of populations difficult with conventional methods (Carter,
338 2007). We compare our results with (1) the binomial peak-fit method (Galbraith and Green,
339 1990) using the BINOMFIT code (Brandon, 1992; Brandon, 1996; Brandon et al., 1998;
340 Ehlers, 2005), and (2) the Bayesian method for age-mixture modeling (BayesQtMix code) that

uses the Markov Chain Monte Carlo approach (Jasra et al., 2006). A comparison of the results obtained with the different methods is shown in Figure 4. BINOMFIT and BayesQtMix discriminate only two populations of age 4.1 ± 2.3 and 6.2 ± 4.6 Ma, and 5.1± 1.2 and 18.1 ± 5.0 Ma, respectively (Figures 4A, B). Figure 4C shows the results of the p-partition decomposing the data into three populations: 3.2 ± 1.1, 7.3 ± 1.3, and 18.2 ± 5.3 Ma, formed by 49, 42, and 13 grains, respectively. These values represent central age and standards errors, from each group discriminated by the p-partition algorithm. In the central part of Figure 4, the corresponding radial plot is shown (Galbraith, 1994; 2005), which shows the dispersion of the data. Finally, when the spontaneous and induced fission-track numbers are arbitrarily multiplied by a factor of 10, the binomial peak-fit method yields results that are markedly different to those shown in Figure 4A, indicating the strong dependence of U concentration on the BINOMFIT results.

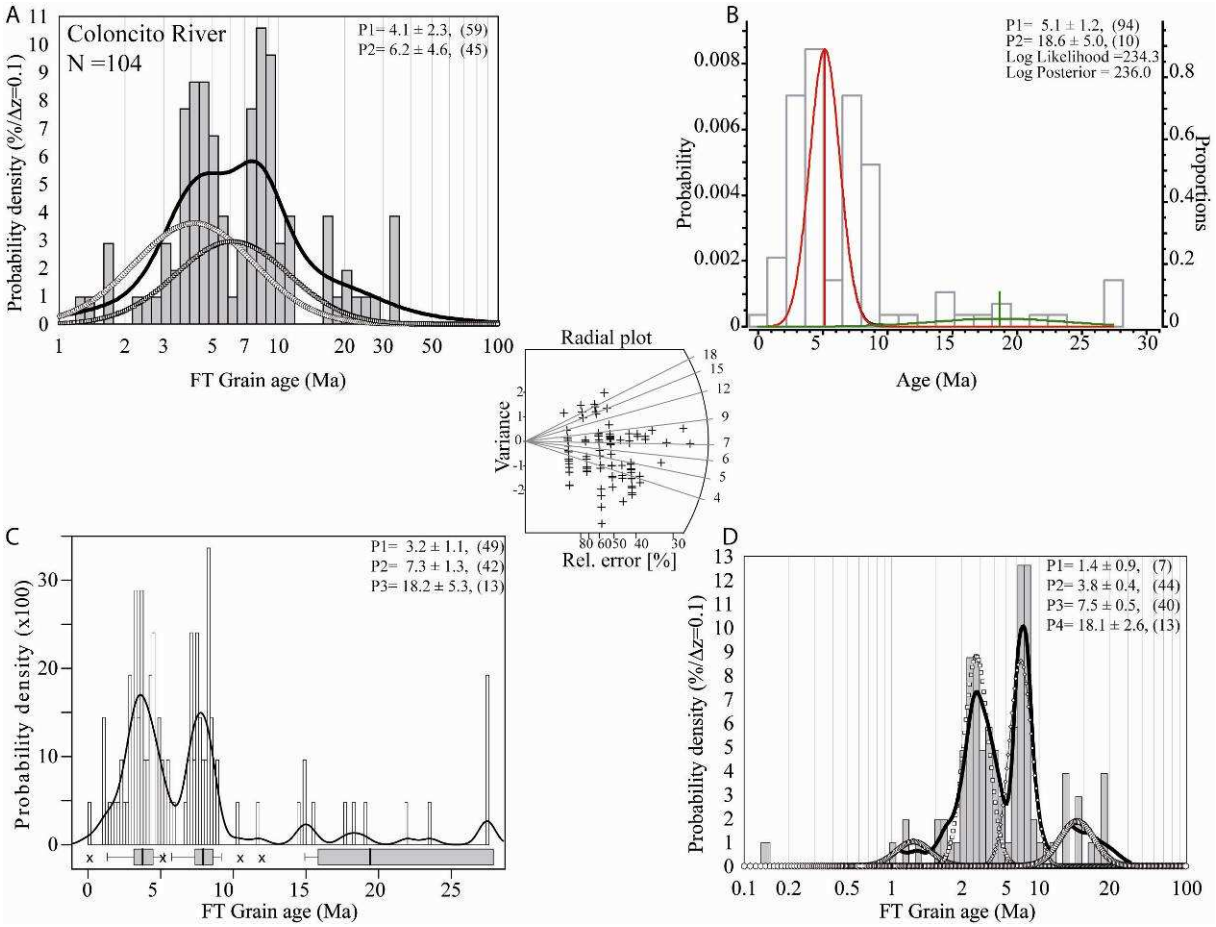

Figure 4. Results for the Coloncito River sample from the Venezuelan Andes. A) Probability Density Functions (PDF) with binomial peak-fit results using BINOMFIT software (Brandon, 1992). B) Populations discriminated with the Bayesian Method using Markov Chain (BayesQtMix, Jasra et al., 2006). C) PDF with boxplots from the p-partition algorithm using p=0.995. and D) BINOMFIT results when fission-tracks count are multiplied by a factor of 10. In the central part of this figure the radial-plot after Galbraith (1994) is shown. The numbers between parentheses correspond to numbers of elements that form the population.

6. Recommendations and Conclusions

The p-partition method we present here can be used to verify the quality of samples and to identify possible mixed age compositions, regardless of whether the data has passed the Galbraith test. We can thus recommend not discarding any observation. Instead our new method can be used to generate p-patterns, which give a reliable estimate of the quality of the data. Once the homogeneity or dispersion of the sample is tested (modified Galbraith test), and problems related to low fission-tracks counts and/or partial annealed of grains are taken into account, the second step is to calculate the different estimators of fission-track age, considering the following situations:

a) In the case of ‘ideal’ p-patterns, age estimator is independent of the estimator used.

b) In the case where p-patterns are formed by a single point, any pooled estimator give a good estimation of the age.

c) In the case of anomalous p-patterns, it is recommended to use the p-pooled or the isochrona estimator.

Where the p-pattern does not show a simple increase and yields different fission-track ages for Poissonian populations could be an indication that analyzed grains are characterized by differences in annealing kinetics, which requires the measurement of kinetic parameters (e.g. Dpar or Cl/F concentration). In addition, the method presented here statistically evaluates the probability that the sample is composed of more than one age group, which can then be decomposed using the algorithm. In samples with low U concentration, we suggest to apply the p-partition method.

7. Acknowledgments

To CDCH-UCV (and project PI-08.00.6219.2006) for permit us present this work in 23th International Nuclear Tracks Society (INTS), Beijing-China. We also thank INTS for awarding us the ‘Wladymir Perelygin’ prize; Paul Green, Charles Naeser, John Garver, Jorge Mora, and Matthias Bernet for providing us with data for the standard database; Rex Galbraith, Mark Brandon, Matthias Bernet, Peter van der Beek, Kerry Gallagher, Jean Braun, and Richard Ketcham for their suggestions and explanations; Udo Haack for send us a copy of his work. All routines used in this work are available as commented scripts with example data Splus (4, 2000 and 8) of Insightful Corporation and R software (R Development Core Team, 2009).

Appendix

Is the pooled estimator the maximum likelihood estimator (MLE)?

Consider $N_{s1}^{*},...,N_{sn}^{*}$ and $N_{i1}^{*},...,N_{in}^{*}$ the counts for a unit area of spontaneous and induced fission track respectively, of a random sample of *n* grains, obtained by external detector method. Suppose that these grains were irradiated at the same time and their fission tracks were counted by a single investigator. Under these suppositions, N_{sj}^{*} and N_{ij}^{*} for $j = 1,\ldots n$, have independent Poisson distributions with means given for the parameters λ_s, λ_i of the equation (3), thus:

$$\begin{aligned} E\left(N_{sj}^{*}\right) &= \lambda_s = \kappa\lambda_i \\ E\left(N_{ij}^{*}\right) &= \lambda_i \end{aligned} \tag{12}$$

To simplify the equations the asterisks will be omitted (*) from now on. The likelihood function *L* is proportional to the combined probability to have the counts about their observed values, or the product of the separate Poisson probabilities for each count. In this situation, *L* is given by:

$$L\left(N_{sj},\lambda_s;N_{ij},\lambda_i\right)=\frac{\lambda_s^{\sum_{j=1}^{n}N_{sj}}e^{-n\lambda_s}}{\prod_{j=1}^{n}\left(N_{sj}\right)!}\cdot\frac{\lambda_i^{\sum_{j=1}^{n}N_{ij}}e^{-n\lambda_i}}{\prod_{j=1}^{n}\left(N_{ij}\right)!}=\frac{\lambda_s^{\sum_{j=1}^{n}N_{sj}}\lambda_i^{\sum_{j=1}^{n}N_{ij}}e^{-n\left(\lambda_s+\lambda_i\right)}}{\prod_{j=1}^{n}\left(N_{sj}!\right)\left(N_{ij}!\right)} \tag{13}$$

Calculating the logarithm of that function yields:

$$\ln\left(L\right)=\sum_{j=1}^{n}N_{sj}\ln\left(\lambda_s\right)+\sum_{j=1}^{n}N_{ij}\ln\left(\lambda_i\right)-n\left(\lambda_s+\lambda_i\right)+Const. \tag{14}$$

and substituting λ_s by $\kappa\lambda_i$ we obtain:

$$\ln\left(L\right)=\sum_{j=1}^{n}N_{sj}\ln\left(\kappa\lambda_i\right)+\sum_{j=1}^{n}N_{ij}\ln\left(\lambda_i\right)-n\left(\kappa\lambda_i+\lambda_i\right)+Const. \tag{15}$$

The derivative of this last equation with respect to κ yields:

$$\frac{\partial\ln\left(L\right)}{\partial\kappa}=\sum_{j=1}^{n}\frac{N_{sj}\lambda_i}{\kappa\lambda_i}-n\lambda_i+0\,.$$

and, after simplifying, we obtain:

$$\frac{\partial \ln(L)}{\partial \kappa} = \frac{\sum_{j=1}^{n} N_{sj}}{\kappa} - n\lambda_i .$$

Equating to zero (to obtain the maximum likelihood) yields:

$$\frac{\sum_{j=1}^{n} N_{sj}}{\kappa} = n\lambda_i .$$

which leads to the following value for κ :

$$\overline{\kappa} = \frac{\sum_{j=1}^{n} N_{sj}}{n\lambda_i} \tag{16}$$

However, λ_i is an unknown Poisson mean, which cannot estimated. Thus, to be able to obtain $\overline{\kappa}$ from (16) it is necessary to estimate or approximate λ_i by its maximum likelihood estimator, which, in this case, is given by its arithmetic mean. Thus:

$$\overline{\lambda_i} = \frac{1}{n}\sum_{j=1}^{n} N_{ij} \tag{17}$$

and:

$$\overline{\kappa} = \frac{\sum_{j=1}^{n} N_{sj}}{\sum_{j=1}^{n} N_{ij}} = \frac{N_s}{N_i} \tag{18}$$

This coincides with the pooled value given in the first section of this article. In the literature (Galbraith. 2005) refers to this as the maximum likelihood estimator for the ratio *R* of the equation (1). Thus we demonstrate that the pooled is only an approximation of maximum likelihood estimator. It is thus clear that there exist other estimators that can be used to determinate the ratio R and might provide better results.

References

Bermúdez M. 2009, Cenozoic exhumation patterns across the Venezuelan Andes: insights from fission-track thermochronology: PhD doctoral dissertation, Joseph Fourier University, France, 305 p.

Bermúdez-Cella MA (2008) Detection of Poisson mixtures by p-partition. Divulgaciones Matemáticas 16:73-86.

Bigazzi G, Bonnadonna F, Hadler JC (1986) Contribution to Statistics in Fission Track Counting. Nucl. Tracks 11:123-136.

Brandon MT (1992) Decomposition of fission-track grain-age distributions, Am. J. Sci. 292:535-564.

Brandon MT (1996) Probability density plots for fission-track grain age distributions. Radiation Measurements 26:663-676.

Brandon MT, Roden-Tice MK, Garver JI (1998) Late Cenozoic exhumation of the Cascadia accretionary wedge in the Olympic Mountains, northwest Washington State. Geological Society of America Bulletin 110:985-1009.

Burchart J (1981) Evaluation of uncertainties in fission track dating: Some statistical and geochemical problems. Nucl. Tracks 5:87-92.

Carter A (2007) Heavy Minerals and detrital fission-track thermochronology. Developments in Sedimentology 58:851-868.

Diaconis P, Efron B (1983) Computer-intensive methods in statistics, Scientific American 96:116-130.

Ehlers TA (2005) Crustal thermal processes and the interpretation of thermochronometer data, in Low Temperature Thermochronometry: Techniques, Interpretations, and Applications, Rev. Mineral. Geochem., vol. 58, edited by T. Ehlers and P. W. Reiners, Mineral. Soc. of Am.: 315-350.

Fleischer RL, Price PB, Walker RM (1975) Nuclear Tracks in Solids: Principles and Techniques. University of California Press, Berkeley.

Frigge M, Hoaglin DC, Iglewicz B (1989) Some Implementations of the Boxplot. The American Statistician 43:50-54.

Jasra A, Stephens DA, Gallagher K, Holmes CC (2006) Bayesian mixture modelling in geochronology via Markov Chain Monte Carlo. Mathematical Geology 38:269-300.

Galbraith RF (1981) On statisticals models for fission-track counts. Journal of Mathematical Geology 13:471-478.

Galbraith RF (1990) The radial plot: graphical assessment of spread in ages. Nucl. Tracks Radiat. Meas. 17:207-214.

Galbraith, R.F., (2005), Statistics for Fission Track Analysis, Interdisciplinary Statistics Chapman & Hall, 219 p.

Galbraith RF, Green PF (1990) Estimating the component ages in a finite mixture. Nucl. Tracks Radiat. Meas. 17:197-206.

Galbraith RF, Laslett GM (1985) Some remarks on statistical estimation in fission-track dating. Nucl. Tracks Radiat. Meas. 10:361-363.

Galbraith RF, Laslett GM (1993) Statistical models for mixed fission track ages. Nucl. Tracks. Radiat. Meas. 21:459-470.

Gallagher K, Brown R, Johnson C (1998) Fission Track analysis and its application to geological problems. Annual Reviews Earth Planetary Science 26:519-572.

Gallagher K, Charvin K, Nielsen S, Sambridge M, Stephenson J (2009) Markov chain Monte Carlo (MCMC) sampling methods to determine optimal models, model resolution and model choice for Earth Science problems. Marine and Petroleum Geology 26:525-535.

Green PF (1981) A new look at statistics in fission track dating. Nucl. Tracks 5:77-86.

Haack U (1973) The influence of the uranium distribution on the error of fission track ages of garnets. Abstr. Geochronol. Isotope Geol. (3rd. Europ. Colloq. Geocronol. Cosmochronol. Isotope Geol. Oxford) 9.

Hurford AJ, Green PF (1983) The zeta age calibration of fission-track dating. Chem. Geol. Isot. Geosci. 41:285-312.

Hyndman RJ, Fan Y (1996) Sample quantiles in statistical packages. The American Statistician 50:361-365.

Kendall M, Stuart A (1958) The advanced theory of statistic, distribution theory, vol.1, Charles Griffin & Company Limited, London, 433 p.

Mendenhall W, Sheaffer R Wackerly D (1981) Mathematical Statistics with Applications, second edition, Duxbury Press, Boston-Massachusetts. 686 p.

McGee VE, Johnson NM (1979) Statistical treatment of experimental errors in the fission track dating method. Math. Geol. 11: 255-268.

R Development Core Team (2009), R: A language and environment for statistical computing. R Foundation for Statistical Computing, Vienna, Austria. ISBN 3-900051-07-0, URL http://www.R-project.org.

Richardson S, Green PJ (1997) On Bayesian analysis of mixtures with an unknown number of components. Journal of the Royal Statistical Society, Series B (Methodological) 59: 731-792.

Sambridge MS, Compston W (1994) Mixture modeling of multi-component data sets with applications to ion-probe zircon ages. Earth and Planetary Sciences Letters 128: 373-390.

Sewards D, Rhoades DA (1986) A clustering technique for fission-track dating of fully to partially annealed minerals and other non-unique populations. Nucl. Tracks Radiat. Meas., 11:25-268.

Tukey J (1977) Exploratory Data Analysis. Addison-Wesley, Reading, MA-USA.

Vermeesch P (2007) Quantitative geomorphology of the White Mountains (California), using detrital apatite fission track thermochronology. Journal of Geophysical Research 112: F03004 doi:10.1029/2006JF000671.

Viallefont V, Richardson S, Green PJ (2002) Bayesian analysis of Poisson Mixtures. Nonparametric Statistics 14:181-202.

Wagner G, Van den Haute P (1992) Fission Track Dating. Solid Earth Sciences Library, Kluwer Academic Publishers, Netherlands, 285 p.

APPENDIX 2

Divulgaciones Matemáticas Vol. 16 No. 1(2008), pp. 73–86

Detección de mezclas Poisson por p-Partición

Detection of Poisson mixtures by p-Partition

Mauricio A. Bermúdez-Cella
(mbermude@euler.ciens.ucv.ve,maberce@yahoo.com.)
Laboratorios de Termocronología y Geomatemáticas, Escuela de Geología, Minas y Geofísica.Facultad de Ingeniería, Universidad Central de Venezuela, 1053. Ciudad Universitaria, Caracas-Venezuela.

Resumen

En este artículo se exponen los resultados de aplicar el proceso de p-Partición a mezclas simuladas de Poisson. Se explora la p-Partición como estimador del número de subpoblaciones presentes en la mezcla y como test para decidir si una muestra tiene una o más poblaciones.
Palabras y frases clave: distribución de Poisson, mezclas, p-partición, cubrimiento por intervalos, cubrimiento por conjuntos discretos, pruebas de hipótesis, huellas de fisión, edad.

Abstract

In this paper we apply a p-partitions methodology to simulated Poisson mixtures. The p-partitions are explored as a mean of estimating the number of suppopulations in the mixture and as a test for deciding whether the sample has one or more subpopulations.
Key words and phrases: Poisson distribution, mixtures, p-partition, coverage by intervals, coverage by discrete sets, hypothesis tests, fission tracks, age.

1 Introducción

Una huella de fisión [3] es una traza que se produce al ocurrir una fisión de los átomos de uranio-238 presentes en minerales accesorios constituyentes de rocas como el apatito, circón, etc. El número o contaje de huellas de fisión

Recibido 2006/02/28. Revisado 2006/07/03. Aceptado 2006/07/15.
MSC (2000): Primary 62H30; Secondary 62H12.

de un grano de roca, es considerado una variable aleatoria de Poisson cuya media depende de la densidad de uranio del grano en que se hace el contaje. El método del detector externo para la determinación de la antiguedad de una roca, utiliza el contaje de las huellas de fisión, sobre varios granos de la roca ([6]). El hecho de que la densidad de uranio en los granos de una misma roca no sea constante hace que sea poco realista considerar siempre, los contajes hechos como provenientes de una sola población de Poisson. Además, el hecho de que provengan de diversas poblaciones de Poisson puede afectar la calidad del estimado del tiempo. Por ello se han desarrollado métodos estadísticos que toman en cuenta la posible variación de densidades de uranio ([1]). Esto ha llevado, de manera natural, a considerar el problema de separación de poblaciones en mezclas de Poisson. Al menos en la literatura matemática de geología durante el desarrollo de esta investigación no se encontró trabajos en esa dirección. En este artículo se presentan algunos resultados iniciales de separación de mezclas. El concepto clave es el de p-Partición. Se explora dicho concepto como estimador del número de poblaciones de una mezcla y como test para discriminar entre muestras unipoblacionales y muestras bipoblacionales.

2 Definición de una p-Partición

Considérese p un número entre 0 y 1, y sea:

$$cuantil(p,k) = \inf_q \{q \in \mathbb{N} / P(x \leq q) \geq p\},$$

donde x es una variable aleatoria Poisson de media k. Dado $0 \leq p \leq 1$, la p-Partición de un conjunto finito de números enteros positivos D se hace en dos etapas. En primer lugar se define un p-Cubrimiento, luego se "disjuntiza.^{es}e p-Cubrimiento para obtener la p-Partición.

Ahora bien, para construir el p-Cubrimiento, se considera:

$$k_i = \text{mín}\,\{D_i\},$$

y se define el intervalo o clase C_i como:

$$C_i = [k_i; max(k_i, cuantil(p, k_i))]$$

Tomando:

$$D_{i+1} = D_i - C_i,$$

y:

$$D_1 = D.$$

Se obtiene el p-Cubrimiento $\{H_i\}$ de D al considerar:

$$H_i = C_i \bigcap D.$$

Se designa con m_i el promedio empírico de las observaciones en C_i y $P_{m_i}(x)$ la probabilidad de que la variable de Poisson X de media m_i valga x.

La sucesión dada por los m_i es creciente entre $min(D)$ y $max(D)$. En virtud de que los $\{H_i\}$ no necesariamente son disjuntos, se establece la siguiente regla de decisión:

$$\begin{aligned} S_i &= \{x \in H_i / (x \notin H_j, i \neq j)\} \\ &\quad \cup \left\{x \in H_{i+1} \cap H_i / P_{m_i}(x) > P_{m_{i+1}}(x)\right\} \\ &\quad \cup \left\{x \in H_{i-1} \cap H_i / P_{m_i}(x) > P_{m_{i-1}}(x)\right\} \\ &\quad \cup \left\{x \in H_{i+1} - H_i / P_{m_i}(x) = P_{m_{i+1}}(x)\right\} \end{aligned}$$

3 Estudio de la p-Partición como estimación del número de subpoblaciones de una mezcla de Poisson

Utilizando el paquete estadístico S^+ se realizaron diversas simulaciones con la finalidad de estudiar la capacidad de la p-Partición para estimar el número de subpoblaciones presentes en una mezcla Poisson. Se simularon N poblaciones Poisson $\{G_i\}_{i=1,...,N}$, cada una con medias m_i respectivamente para $N = 2; 3; ...; 7; 9$. Los resultados que se exponen a continuación son el producto de más de 500 corridas, este número resultó ser estable después de haber probado con 20, 100, 500 y 1000 corridas. La cercanía de las medias de las subpoblaciones afecta, en general, la calidad de los algoritmos de separación de muestras. En el caso de las distribuciones de Poisson la incidencia de este factor se complica por el hecho de que la varianza de la distribución está siempre relacionada con la media.

Las simulaciones fueron realizadas asumiendo que la separación entre dos medias consecutivas es constante. Esto reduce considerablemente el espectro de simulaciones. Se hicieron algunas simulaciones con variantes de esta condición y los resultados que se obtienen no se diferencian de aquellos obtenidos con esta condición restrictiva. Considérese delta (δ) la separación entre dos medias consecutivas, a continuación se presentan los resultados de las simulaciones para dos casos: medias separadas y cercanas.

El objetivo de estas simulaciones al igual que el de las dos secciones siguientes es establecer un rango de probabilidades p o una tabla de valores de p ideales que pueda ser usada por los futuros usuarios de este método con el fin de hacer una discriminación efectiva de las diferentes subpoblaciones existentes en un conjunto de datos provenientes de una mezcla de varias distribuciones Poisson.

3.1 Primer Caso: Medias separadas ($\delta \geq 20$).

Medias separadas significa distancia entre dos medias consecutivas ≥ 20. Los parámetros para la primera simulación son los siguientes:

- Media inicial: $m_1 = 10$.
- Número de subpoblaciones consideradas a priori: $N = 3$.
- Número de elementos en cada grupo: $n_i = 10$.
- El valor de probabilidad a priori: $p = 0{,}90$.

Al considerar valores a priori de probabilidad $p < 0{,}90$ se observó que no existían coincidencias entre la cantidad de subpoblaciones supuestas a priori ($N = 3$) y las estimadas por la p-Partición, es decir, al fijar un valor $p < 0{,}90$ la p-Partición estimaba más de 3 subpoblaciones. Los resultados para este caso en particular y para valores de p de 0.95, 0.99 y 0.9999 son mostrados en la tabla 1. En esta última se aprecia que a medida que el nivel p es incrementado aumenta el porcentaje de coincidencias entre el número de subpoblaciones consideradas a priori y las discriminadas por la p-Partición. Para $p = 0{,}95, 0{,}99$ y $0{,}9999$, los porcentajes de coincidencias son: 6.2, 51 y 98.2 % respectivamente.

p	**%Coinc.**
0.90	0.8
0.95	6.2
0.99	51
0.9999	98.2

Cuadro 1: Porcentaje de coincidencia entre las subpoblaciones supuestas ($N = 3$) y el número de grupos de la p-Partición para diferentes valores de p en el caso de medias separadas.

Al incrementar el número de subpoblaciones a $N = 4{,}5{,}6$, y 7 los resultados son similares a los expuestos en la tabla 1 para N=3. Estos resultados

son resumidos en la figura 1 considerando valores de p entre 0.90 y 0.9999. Mientras mayor es el número de poblaciones que conforman la mezcla, en el caso de que la media de cada población esté bastante alejada con respecto a la otra población se observa que el valor máximo de coincidencia es cuando se selecciona una probabilidad de 0.9999.

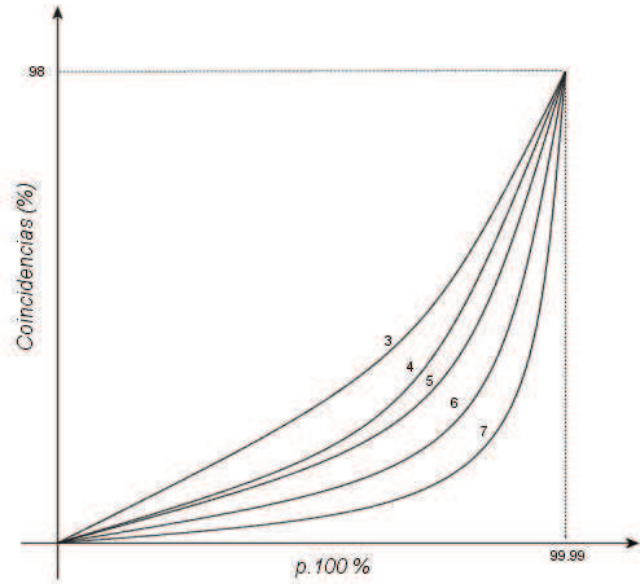

Figura 1: Porcentaje de coincidencias entre el número de subconjuntos generados por simulación y el número de poblaciones separadas por la p-Partición en el caso de medias distantes.

3.2 Segundo Caso: Medias cercanas ($\delta < 20$).

Dos subgrupos se dicen que tienen medias cercanas cuando $\delta \leq 20$. En este caso particular se tomó $\delta = 10$. En analogía con el caso anterior se asumió que m_1=10 y n_i=10. Obteniéndose para el caso en que el número de grupos considerados a priori es $N = 3$, los resultados mostrados en la tabla 2. En esta última se aprecia que cuando las medias de los 3 subgrupos están muy cercanas la probabilidad necesaria para separar "correctamente" es menor, situándose su valor entre 0.95 y 0.98.

p	**%Coinc.**
0.90	21
0.95	74.8
0.96	80.4
0.97	81.6
0.98	69.4
0.99	43
0.9999	0

Cuadro 2: Porcentaje de coincidencia entre las subpoblaciones supuestas ($N = 3$) y el número de grupos de la p-Partición para diferentes valores de p en el caso de medias cercanas.

Cuando la población está conformada por N=5 se obtuvieron los resultados mostrados en la tabla 3.

p	**%Coinc.**
0.90	41.4
0.91	54.8
0.92	64.6
0.93	72.8
0.94	71.2
0.95	51.8
0.96	31.8
0.97	15
0.98	5.6
0.99	0.4
0.9999	0

Cuadro 3: Porcentaje de coincidencia entre las subpoblaciones supuestas ($N = 5$) y el número de grupos de la p-Partición para diferentes valores de p en el caso de medias cercanas.

Como se puede apreciar en la tabla 3, en el caso de que existan 5 subgrupos, el valor de p ha descendido al rango comprendido entre 0.93 y 0.95. Este rango se mantuvo para un número de simulaciones de $20, 50, 100$ y 1000.

En el caso que existan 7 subpoblaciones en la tabla 4 se muestran los resultados obtenidos, para un número de 1000 corridas. Puede observarse que cuando el número de subgrupos que conforman la mezcla es 7, el rango óptimo de separación es alcanzado para p entre 0.90 y 0.93.

p	**%Coinc.**
0.90	60.6
0.91	66.2
0.92	62.3
0.93	47.4
0.94	27.1
0.95	10
0.96	2.7
0.97	0.3
0.98	0
0.99	0
0.9999	0

Cuadro 4: Porcentaje de coincidencia entre el número de subpoblaciones supuestas ($N = 7$) y el número de grupos de la p-Partición para diferentes valores de p en el caso de medias cercanas.

Los resultados para todas estas simulaciones 20,50,100,500 y 1000 corridas cuando las medias de cada una de las poblaciones $N = 3, 4, 5, 6,$ y 7 están poco separadas pueden ser resumidas en la figura 2.

Observando la figura 2, se concluye que cuando las poblaciones tienen medias muy cercanas entre sí, para que coincidan el número de poblaciones separadas por la p-Partición con el número de subpoblaciones utilizadas para las simulaciones es necesario disminuir el valor de p. También se aprecia que a medida que la cantidad de poblaciones aumenta el porcentaje de coincidencia disminuye. Por ejemplo, cuando $N = 4$, el máximo de coincidencias entre las poblaciones supuestas a priori y las discriminadas por la p-Partición es 86 % y se alcanza en $p = 0{,}948$ mientras que si $N = 7$, el máximo de coincidencias es 61 % y se alcanza en $p = 0{,}905$.

Todas las simulaciones realizadas considerando diferentes números de subpoblaciones: $N = 3, 4, 5, 6,$ y 7, junto con las figuras 1 y 2 permiten tener una idea del intervalo donde se encuentra el valor p a utilizar, dependiendo únicamente del grado de separación entre las medias de las subpoblaciones. Esta intervalo donde se encuentra p se denominará el rango de probabilidades p. A partir de la gran cantidad de simulaciones realizadas en esta investigación, puede establecerse un posible rango de probabilidades p de manera que el porcentaje de coincidencia entre el número de subpoblaciones supuestas a priori y las separadas por la p-Partición sea máximo, estos rangos son mostrados en la tabla 5. En la tabla 6 se resumen las observaciones antes realizadas, esta tabla

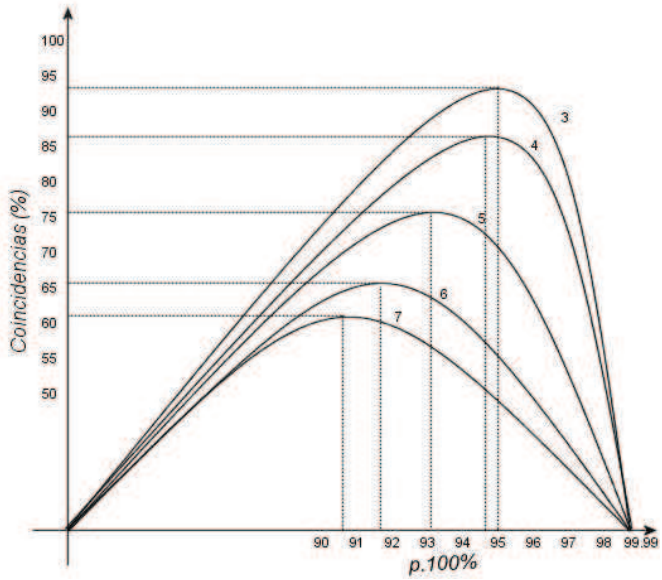

Figura 2: Porcentaje de coincidencias entre el número de subconjuntos generados por simulación y el número de poblaciones separadas por la p-Partición en el caso de medias cercanas.

proporciona una orientación precisa al momento de realizar las aplicaciones, pero es necesario tener una "idea.º conocimiento a priori acerca del grado de se-paración entre las medias de los subgrupos.

4 Pruebas de hipótesis aplicadas a la p-Partición de una población

Al aplicar la p-Partición a una población se puede no separar una muestra en dos subpoblaciones a pesar de que esta esté compuesta por observaciones que provienen de dos poblaciones poissonianas diferentes. O bien se puede separar una muestra en dos subpoblaciones a pesar de que la muestra provenga de una sola distribución de Poisson. Esta sección muestra estimados de las probabilidades de cada uno de los dos posibles errores señalados, obtenidos

# de Pob.	**Int.Prob.**p
3	$\approx (0{,}95, 0{,}97)$
5	$\approx (0{,}93, 0{,}95)$
7	$\approx (0{,}90, 0{,}93)$

Cuadro 5: Rango de confiabilidad para mezclas formadas por 3, 5 y 7 subpoblaciones con medias cercanas.

Distancia entre poblaciones: δ	**Niveles óptimos de** p
$\delta > 20$ (lejanas)	$0{,}99 \leq p < 1$
$15 \leq \delta \leq 20$ (intermedias)	$0{,}96 < p < 0{,}99$
$10 \leq \delta < 15$ (cercanas)	$0{,}94 < p \leq 0{,}96$
$5 < \delta < 10$ (muy cercanas)	$0{,}9 < p \leq 0{,}94$

Cuadro 6: Resumen de los valores óptimos a usar en la p-Partición según la distancia entre medias de subpoblaciones para diferentes valores de m_1.

mediante simulaciones.

La significancia de este test guarda relación con el p de la p-Partición. Antes de definir el test estadístico construido para esta situación, lo primero que se realizó fue buscar el valor óptimo de p, para el cual al introducir una población proveniente de una sola Distribución de Poisson no fuese dividido por en dos poblaciones, siendo este $p = 0.999999$, muy cercano a 1.

4.1 La p-Partición utilizada como test de hipótesis de que la muestra tiene una o más de una población.

Al aplicar la p-Partición como un test de hipótesis se conservan las características de las pruebas de hipótesis ([5]), con la diferencia que en lugar de discriminar parámetros de una población como la media y la varianza, discrimina hasta que punto al introducir la unión de dos grupos provenientes de dos distribuciones de Poisson distintas, la p-Partición en realidad separe estas poblaciones en una o dos. El buen ajuste del test depende del nivel de significancia p.

Para definir los parámetros que la p-Partición utilizada como test de hipótesis debe discriminar, se considera la siguiente matríz:

Sea:

$$M = \begin{pmatrix} x_{11} & x_{12} \\ x_{21} & x_{22} \end{pmatrix}$$

donde:

$x_{11} + x_{12}$ es el número de veces que se genera una muestra de Poisson con dos poblaciones diferentes .

$x_{21} + x_{22}$ es el número de veces que se genera una segunda población de Poisson.

En esta matriz:

x_{11} indica el número de veces que al aplicar la p-Partición esta constó de un sólo grupo (el número de veces que no coincide con el número de poblaciones de la muestra).

x_{12} indica el número de veces que la p-Partición indica que hay más de un grupo.

x_{21} indica el número de veces que la p-Partición indica que hay un sólo grupo y

x_{22} indica el número de veces que la p-Partición indica que hay dos grupos (el número de veces que no coincide con el número de poblaciones de la muestra).

Lo que se desea al utilizar la p-Partición como test de hipótesis es que los valores de x_{12} y x_{21} sean máximos y al compararlos entre sí se pueda tomar una decisión sobre si las muestras están formadas por una sola población o por más de una población de acuerdo al significado de las componentes de la matriz M dado anteriormente. Por ejemplo, supóngase que se generan 100 muestras Poisson (es decir: $x_{11} + x_{12}$=100 y $x_{21} + x_{22}$=100) y que la matríz M está dada por:

$$M = \begin{pmatrix} 10 & 90 \\ 90 & 10 \end{pmatrix}$$

Como x_{12}=90 esto significa que con un 90 % de probabilidad cuando se introdujo una muestra formada por varios subgrupos Poisson, la p-Partición detectó una mezcla de poblaciones. Ahora bien, la otra componente x_{21}=90, indica que cuando se introdujo la muestra como una sóla población la p-Partición identifica en un 90 % que no hay mezclas de poblaciones. Para formalizar esto, es necesario pensar el número de subgrupos dados por una p-Partición, en términos de test de hipótesis y asumiendo que:

H_0: la muestra está constituida por dos subpoblaciones.

H_1: la muestra está constituida por una subpoblación.

Así:

$$\frac{x_{11}}{x_{11} + x_{12}}$$

es un estimado de la probabilidad del error de Tipo I del test y

$$\frac{x_{22}}{x_{21} + x_{22}}$$

es un estimado de la probabilidad del error de Tipo II del test.

Un modo de optimizar el test es maximizando la función:

$$f(M) = (x_{12} + x_{21}) - (x_{11} + x_{22})$$

Se probó optimizar con otras funciones y los resultados varían muy poco.

4.2 Resultados de las simulaciones

A lo largo de las simulaciones, se procedió generando siempre muestras de 20 elementos. En el caso de que la muestra conste de dos subpoblaciones, cada una de las subpoblaciones generadas tenía 10 elementos. Además se consideró:

$$x_{11} + x_{12} = x_{21} + x_{22} = 100.$$

Los resultados de este test, son mostrados según el grado de separación entre las distancias de las medias de las subpoblaciones. En el caso de que las medias (Poisson) de las subpoblaciones están muy cercanas, es decir, medias de 8 y 10 respectivamente, el intervalo donde se encuentra el nivel p-óptimo es el (0.995,0.996), la función de maximización establece un p-óptimo de 0.995611, obteniéndose que el 58 % de las veces en que hay dos grupos, el test discrimina 2 grupos, mientras que el 67 % de las veces en que hay un sólo grupo el test discrimina un sólo grupo. En este caso el error de tipo II es 0.33 y el error de tipo I es 0.42. Todas estas observaciones son resumidas en la tabla 7. En estas situaciones de separación de medias tan cercanas el test tiene un desempeño pobre.

Media de G_1	m_1=8
Media de G_2	m_2=10
Intervalo donde se encuentra el p-óptimo	[0,995, 0,996]
p-óptimo	0.995611
Matriz M	$\begin{pmatrix} 42 & 58 \\ 67 & 33 \end{pmatrix}$
Valor de la función $f(M)$	50

Cuadro 7: Resultados de la p-Partición como test de hipótesis en el caso de m_1=8 y m_2=10

Fijando m_1=8 y tomando m_2 =10;12;...;20, se estudiaron 6 casos, el último de ellos es resumido en la tabla 8. En este caso, el intervalo donde se alcanza el máximo está entre [0.998, 0.99999], el nivel p-óptimo es de 0.999777. Para

este caso particular, si se observa los valores estadísticos de los errores de tipo I y II se aprecia que la probabilidad de que ocurran estos errores es pequeña: 1 %, en ambos casos. El valor de la función donde el máximo es alcanzado es de 196, lo cual representa una buena aproximación.

Media de G_1	m_1=8
Media de G_2	m_2=20
Intervalo donde se encuentra el p-óptimo	[0,998, 0,9999]
p-óptimo	0.999777
Matriz M	$\begin{pmatrix} 1 & 99 \\ 99 & 1 \end{pmatrix}$
Valor de la función $f(x)$	196

Cuadro 8: Resultados de la p-Partición como test de hipótesis en el caso de m_1=8 y m_2=20

Análogamente, se hicieron otras pruebas tomando medias mayores, con los siguientes criterios: se tomaba como media del primer subgrupo m_1, y $m_2 = m_1 + 2i$ con $i = 1 \ldots n$ hasta que m_2 fuera el doble de m_1. En la figura 3, se resumen los 8 casos considerados, con medias m_1 de 8, 14, 18, 20, 30, 40, 50 y 60. El eje x representa la distancias entre las dos medias de las dos poblaciones consideradas, el eje y representa la altura del valor de $f(M)$ obtenido con el p-óptimo. Mientras más cerca estén las medias el valor del p-óptimo será más cercano a 0.99, mientras que a mayor distancia entre las medias el valor de p se acerca mucho a 1, es decir, p=0.999999. La noción de cercanía y lejanía para medias grandes cambia con respecto a medias pequeñas.

En la mayoría de las simulaciones se observó que al aumentar considerablemente m_1, debido a que la varianza de una Distribución de Poisson esta relacionada con su media $\overline{m}$ mediante:

$$\theta^2(m) = \overline{m}$$

esta varianza también se incrementaba, y la p-Partición tiende a no separar eficazmente poblaciones con medias çercanas". Esto es cierto para el caso en que $m_1 > 100$.

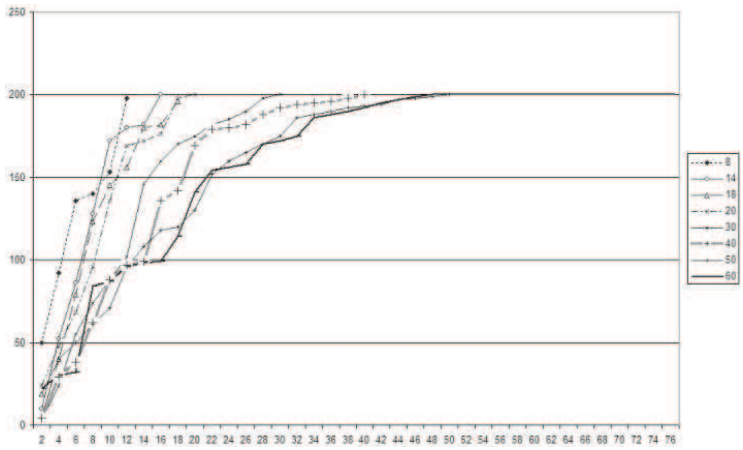

Figura 3: Resultados de la p-Partición para diferentes distancias entre medias.

5 Agradecimientos

Este artículo es parte de [1] y [2], trabajos dirigidos por Pedro Alson a quien le agradezco sus comentarios y sugerencias para la versión final de este artículo.

6 Conclusiones

El algoritmo descrito en este artículo fue aplicado a varios de los conjuntos de datos que motivaron este estudio. Esto permitió:

1) Hacer un estudio más detallado sobre la estructura de ciertos datos y compararlos con los resultados que se obtienen con el test de Galbraith ([4]). Se pudo constatar ([1], [2]), que en numerosos casos el test de Galbraith es inefectivo, mientras que el test, basado en la p-Partición, sí detecta distanciamiento de la hipótesis nula.

2) Mostrar que el problema físico de tener varias concentraciones de uranio en muestras si afecta la calidad del estimado en la edad proporcionada por el método de huellas de fisión y que la influencia de una distribución heterogénea de uranio no había sido resuelto por la técnica del detector externo como se pensó desde 1981 (ver [6]).

3) La aplicación de la p-Partición a los datos de huellas de fisión lleva a la

noción de p-Patrones ([2]) que permite mejorar la calidad de la estimación de la edad de las rocas para los casos de datos en donde la distribución heterogénea del uranio afecta la calidad de la estimación de la edad.

4) Permitió definir un nuevo estimador ([1], [2]) de la edad proporcionada por el método de huellas de fisión que es mucho más eficiente que los estimadores convencionales para este fin.

Las rutinas de S^+ que sirvieron para este estudio pueden ser suministradas por el autor si le son solicitadas.

Referencias

[1] Bermúdez C., Mauricio A. *Estudio de métodos estadísticos para la datación de material rocoso utilizando huellas de Fisión.* Tesis de Maestría, Escuela de Matemáticas, Universidad Central de Venezuela, 92 p., 2002.

[2] Bermúdez C., Mauricio A. *Aspectos estadísticos de la datación de eventos tectotérmicos por el método de huellas de Fisión.* Trabajo de Ascenso, Escuela de Geología, Minas y Geofísica, Universidad Central de Venezuela, 124 p., 2005.

[3] Bermúdez, M., Alson, P., y Mora, J. *Ecuación Fundamental de la Edad para la datación de minerales y su adaptación a la ecuación práctica para el método de huellas de fisión.* Revista de la Facultad de Ingeniería, 2005, Volumen 20, N° 2. Caracas, Venezuela.

[4] Galbraith, R.F. *On Statistical Models for Fission Track Counts.* Math. Geol., 1981, Vol. 13, No. 6, USA.

[5] Mendenhall, W., Scheaffer, R., and Wackerly, D. *Mathematical Statistics with Applications.* Second Edition, Duxbury Press, Boston-Massachusetts, 686 p., 1981.

[6] Wagner G. and Van Den Haute P. *Fission Track Dating.* Solid Earth Sciences Library, Kluwer Academic Publishers. Netherlands, 285 p., 1992.

APPENDIX 3

CARACTERIZACIÓN DE CRISTALES DE APATITO Y CIRCÓN DEL ESTÁNDAR INTERNACIONAL *FISH CANYON TUFF* PARA SU USO EN UN LABORATORIO DE TERMOCRONOLOGÍA

MAURICIO BERMÚDEZ-CELLA, ARTURO LÓPEZ, MIGUEL BALCÁZAR-GARCÍA, GRACIELA ZARAZÚA-ORTEGA y ROMMEL BONA

RESUMEN

*Cristales de apatito y circón del estándar internacional FCT (*Fish Canyon Tuff*, Montañas San Juan de Colorado, EEUU) para el método de huellas de fisión fueron caracterizadas usando difracción y fluorescencia de rayos X, microscopía electrónica de barrido de bajo y alto vacío, y petrografía de secciones finas, para identificar la disposición de estos minerales en la matriz de la muestra. Un total de 19 cristales de apatitos fueron fechados mediante esta técnica de datación arrojando una edad de 27,2 ±0,2Ma, la cual esta en concordancia con la edad K-Ar (27,8 ±0,5Ma). El estudio realizado permitió reconocer la existencia de diferentes especies cristalinas de circones y apatitos, así como la validación de cada uno de los procedimientos para la datación de apatitos en el Laboratorio de Termocronología de la Universidad Central de Venezuela.*

Los minerales pesados (apatito y circón) de la toba volcánica de *Fish Canyon Tuff* (FCT) en las Montañas de San Juan de Colorado, EEUU, son un estándar internacional para el fechado de muestras de edad desconocida por el método de huellas de fisión (MHF; Fleischer *et al*., 1975; Hurford y Green, 1982, 1983; Wagner y van den Haute, 1992), el evento geológico asociado a la formación de estos minerales, fue una extrusión volcánica violenta ocurrida hace 27,8 ±0,5Ma según el método de datación potasio-argón (K-Ar), (Lipman, 1975).

El uso de estándares en los métodos de datación radiométrica (Faure, 1986) es importante por dos razones; la primera porque permite calibrar los procedimientos de laboratorios y la segunda porque a través de ellos se deducen parámetros necesarios en la ecuación de edad proveniente del decaimiento radioactivo de isótopos inestables. En el caso de la termocronología por huellas de fisión, el FCT es utilizado con este mismo doble propósito. En este caso los parámetros a obtener son el factor Z y/o, la fluencia de neutrones aplicada en el reactor nuclear, para luego incorporar éstos en la ecuación de edad práctica del MHF (Wagner y van den Haute, 1992) y posteriormente fechar otras muestras de edad desconocida.

El objetivo principal de este trabajo fue llevar a cabo la caracterización de los granos de apatito y circón del FCT por fluorescencia (FRX) y difracción (DRX) de rayos x, microscopía electrónica de barrido (MEB) de alto y bajo vacío, y análisis petrográfico de secciones delgadas, con el fin de validar cada una de las etapas realizadas en el Laboratorio de Termocronología de la Universidad Central de Venezuela (UCV) y fechar cristales de apatitos por el MHF.

Marco Geológico

La toba volcánica FCT es el producto de la expulsión de lava

PALABRAS CLAVE / Apatito / Circón / Difracción / Fluorescencia / Huellas de Fisión / Microscopía Electrónica de Barrido / Minerales Pesados /

Recibido: 07/04/2008. Modificado: 05/04/2009. Aceptado: 08/04/2009.

Mauricio Bermúdez-Cella. M.Sc. en Matemáticas, Universidad Central de Venezuela (UCV). Estudiante de Doctorado, Université Joseph Fourier, Francia. Docente-Investigador, UCV, Venezuela. Dirección: Laboratorios de Termocronología y Geomatemáticas, Escuela de Geología, Minas y Geofísica, UCV, Venezuela. e-mail: maberce@gmail.com

Arturo López. Químico, M.Sc. en Química Nuclear, Universidad Nacional Autónoma de México (UNAM), Científico, Departamento de Estudios del Ambiente, Instituto Nacional de Investigaciones Nucleares (ININ), México.

Miguel Balcázar. Ph.D. en Física, Birmingham University, UK. Líder de Proyecto, Departamento de Estudios del Ambiente, ININ, México.

Graciela Zarazúa-Ortega. Doctora en Ingeniería. Universidad Autónoma del Estado de México, Científica, Departamento de Estudios del Ambiente, ININ, México.

Rommel Bona. Ingeniero Geólogo, UCV. Estudiante de Doctorado, UNEFA, Venezuela.

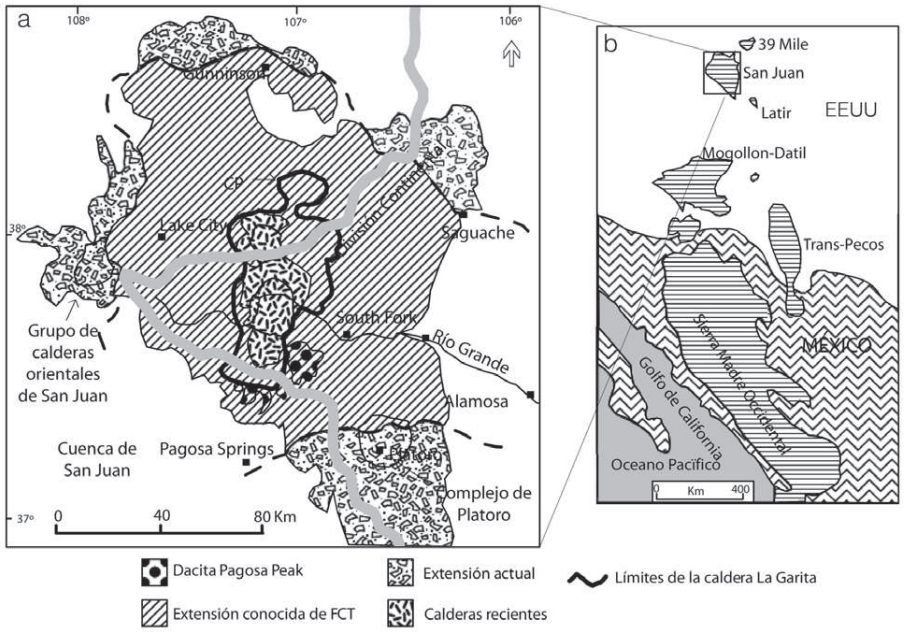

Figura 1. a: Mapa de ubicación del campo volcánico de San Juan y distribución aproximada del FCT. b: Orientación de los campos volcánicos del Terciario Medio al momento de la subducción de la Sierra Madre Oriental (Modificada de Bachmann *et al*., 2002).

ocurrida durante el Terciario a través de la Caldera Garita y otras fisuras en el Parque Nacional Black Canyon, localizado en el río Gunnison, a ~7 millas al NO de Montrose, Colorado. Este parque nacional está formado por un conjunto de campos volcánicos extintos (Figura 1) y el cañón actual es el resultado de la erosión de estructuras preexistentes (Charlier *et al*., 2007).

Estos campos volcánicos, de acuerdo a Bachmann *et al*. (2002) están relacionados a los procesos de magmatismo ocurridos durante la extensión causada por la subducción de la Sierra Madre Occidental al campo volcánico San Juan. En la Figura 1b puede observarse la orientación de los campos volcánicos del Terciario Medio al momento de la subducción de la Sierra Madre Oriental.

La Caldera Garita, según diversos autores (Lipman, 2000; Bachmann *et al*., 2002) es una larga caldera volcánica localizada en el campo de San Juan, en las montañas del mismo nombre al suroeste de Colorado, EEUU (Figura 1). Esta es una de las numerosas calderas formadas durante un proceso masivo de litificación de flujos de cenizas o depósitos piroclásticos en Colorado, Utah y Nevada en el intervalo 40–25Ma. La Garita fue probablemente el sitio donde hubo una mayor cantidad de erupciones entre 26 a 28Ma (Oligoceno). El depósito resultante de este vulcanismo es conocido como *Fish Canyon Tuff*, el cual tiene un volumen de ~5000km^3 (Charlier *et al*., 2007).

Metodología

Análisis petrográfico

Se seleccionaron cinco muestras de mano con variaciones laterales visibles de una muestra de *Fish Canyon Tuff* proporcionada por John Garver, del Union College, EEUU, a Jorge Mora, del Laboratorio de Termocronología de la UCV.

Las Figuras 2a-e representan las secciones delgadas de las muestras de FCT estudiadas. En términos generales, éstas poseen características de una roca volcánica, es decir, abundancia de vidrio en la roca y fenocristales, los cuales algunas veces se encuentran embebidos en una matriz vítrea. Así, es posible asignar una cristalinidad de tipo hipocristalina. En las muestras FCT-1, FCT-2 y FCT-3, representadas por las Figuras 2a, b y c, respectivamente, se observan: 1) inclusiones de apatito en corte transversal (delimitados por circunferencias), 2) el mismo mineral en corte basal (encerrados en cuadrados), y 3) cristales de circón (delimitados por un hexágono) en biotita. En la Figura 2b se observan áreas blancas correspondientes a cristales de plagioclasas. La Figura 2d representa la muestra FCT-4, donde se observan granos de circón con hábito prismático encerrados en hexágonos y alta figura de interferencia incluidos en biotita. Puede observarse en la Figura 2e (FCT-5) inclusiones de esfenas (encerrada en una elipse) y apatito (encerrado en circunferencia), ambas como inclusión en el fenocristal de biotita. Los resultados de este análisis

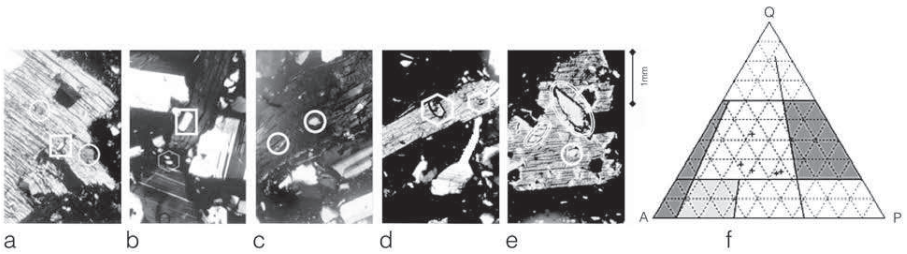

Figura 2. Fotografía de las secciones delgadas en nícoles cruzados (NX). Objetivo 0:/0,12×. Ocular: 12,5× para las secciones FCT-1 al FCT 5 (a-e); f: diagrama ternario para la clasificación de rocas volcánicas según Streckeisen (1979), elaborado en Matlab y modificado de Middleton (1999). Ver Tabla I.

TABLA I
RESULTADOS DEL ANÁLISIS PETROGRÁFICO DE LAS CINCO SECCIONES DE FCT

Mineral	FCT-1	FCT-2	FCT-3	FCT-4	FCT-5
Ortosa	6	8	5	8	6
Biotita	18	18	13	18	13
Horblenda	2	3	4	4	4
Accesorios (esfena, apatito y circón)	1	1	1	1	1
Cuarzo	20	17	25	25	28
Microclino	1	1	NC	NC	1
Albita (0-5% an)	3	5	6	10	8
Albita (5-10% an)	15	10	8	9	8
Anortoclasa	5	9	12	5	7
Oligoclasa	19	13	10	5	10
Sanidina	10	12	10	8	11
Clorita	NC	3	2	4	3
Piroxeno	NC	NC	4	3	3

Los valores están en porcentaje. Estos valores son mostrados en forma de diagrama ternario en la Figura 2f. NC: no cuantificable.

se resumen en la Tabla I, y son presentados en la Figura 2f en forma de diagrama ternario (triángulo APQ) para clasificación de rocas volcánicas según Streckeisen (1979). De esta figura se deduce que el tipo de roca volcánica es una riolita dacítica que pudo generarse como producto de la expulsión rápida del magma a la superficie.

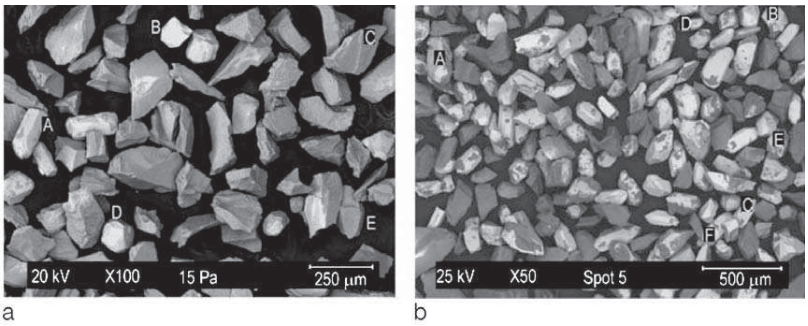

Figura 3. Vista de cristales y fragmentos de rocas en MEB de bajo vacío (a) y de alto vacío (b).

TABLA II
VALORES DEL ANÁLISIS POR FLUORESCENCIA CUANTITATIVA DEL MICROSCOPIO ELECTRÓNICO DE BAJO VACÍO PARA LOS CRISTALES A Y B*

Cristal A				Cristal B			
Elemento	Elmt %	Sigma %	Atomic %	Elemento	Elmt %	Sigma %	Atomic %
C	22,38	0,32	33,91	C	40,16	0,37	57,82
O	39,05	0,41	44,43	O	28,70	0,36	31,02
F	3,28	0,37	3,14	Na	0,48	0,05	0,36
Na	0,57	0,06	0,45	Al	1,28	0,04	0,82
Al	1,52	0,05	1,02	Si	9,25	0,10	5,70
Si	3,39	0,07	2,20	P	0,59	0,13	0,33
P	9,66	0,12	5,68	Ca	1,02	0,05	0,44
Cl	0,40	0,04	0,20	Zr	18,52	0,26	3,51
Ca	19,76	0,19	8,97				

* Ver Figura 4,

Separación de minerales pesados

Para esta separación se llevó a cabo la siguiente secuencia: 1) Concentración primaria de minerales mediante el sistema automatizado para la separación de minerales (SASMP), que además incluye el triturado y tamizado para homogeneizar la muestra en fracciones entre 0,074 y 0,250mm. 2) Separación magnética mediante el Magnet Lift. 3) Concentración mediante la técnica de líquidos pesados, discriminándose tres fracciones de diferente densidad (d), a saber: F1 (2,96≤d≤3,3), F2 (3,095≤d≤3,225) y F3 (d≥3,3).

Fluorescencia de rayos X (FRX)

La fracción F1 fue llevada al Laboratorio de Trazas de Fisión del Instituto Nacional de Investigaciones Nucleares de México (ININ) donde se dividió la muestra en dos partes; la primera mediante una separación manual de apatitos bajo lupa, a la cual se le realizó un análisis mediante FRX, y la segunda formada por el remanente de cristales.

Microscopía electrónica de barrido (MEB)

La misma fracción F1 utilizada para el análisis de fluorescencia de rayos X fue sometida a un análisis por microscopía electrónica de alto y bajo vacío, utilizando los denominados espectrómetros de energía dispersiva de rayos X (EDX).

Difracción de Rayos X (DRX)

Se realizaron tres tipos de sesiones. La primera sobre las mismas muestras de mano, la segunda sobre la muestra analizada por fluorescencia y microscopía electrónica de barrido, y la tercera sobre la fracción F2.

Método de huellas de fisión (MHF) bajo la técnica del detector externo (TDE)

Se realizó la siguiente secuencia de pasos: 1) Montado de la fracción F2 en resina epóxica y pulido de muestras. 2) Revelado de huellas de fisión espontáneas. 3) Montaje del detector externo o mica. 4) Preparación del contenedor para su irradiación en el reactor nuclear: en el contenedor se colocan dos vidrios estándares de densidad de uranio conocida (IRMM-540), dos pastillas con muestras de edad conocida como el apatito de Durango, cuya edad es de 31,4 ±0,5Ma, y entre estos dos estándares se colocan las muestras a ser fechadas. 5) Revelado de huellas de fisión inducidas sobre la mica. 6) Preparación de la sección para conteo en el microscopio. 7) Conteo y obtención de la edad en apatitos utilizando la ecuación práctica de edad por el método de huellas de fisión. (Wagner y van den Haute, 1992).

Resultados

MEB de bajo vacío con fluorescencia semicuantitativa

Este análisis fue realizado a la fracción F1, sobre un conjunto de granos discriminados previamente de acuerdo a sus características cristalográficas. La Figura 3a muestra los cristales de minerales y fragmentos de rocas a los cuales se les realizó este estudio con una presión en cámara de 15psi y una energía de 20keV. En la figura se indican (A-E) los diferentes tipos de granos observados. Aquí se presentan solamente los resultados obtenidos para los cristales A y B, que se resumen en la Tabla II, puesto que el cristal D es muy similar al B y los cristales C y E son fragmentos de roca cuya composición fue analizada con mayor detalle por MEB de alto vacío. La Figura 3b representa la imagen de la fracción estudiada por MEB de alto vacío.

En la Figura 4a puede apreciarse con mayor ampliación (500×) un cristal analizado, sobre el cual se señala con un cuadrado el área donde fue aplicado el análisis por fluorescencia de rayos X (FRX). El análisis efectuado sobre esta zona del cristal arrojó el espectro mostrado encima de la figura, donde el eje *x* representa la energía aplicada. Se observan tres picos significativos que corresponden a la presencia de Ca, P y O, mientras los picos más pequeños corresponden a Si, Al, Na, F y Cl. La concentración (%) de cada uno

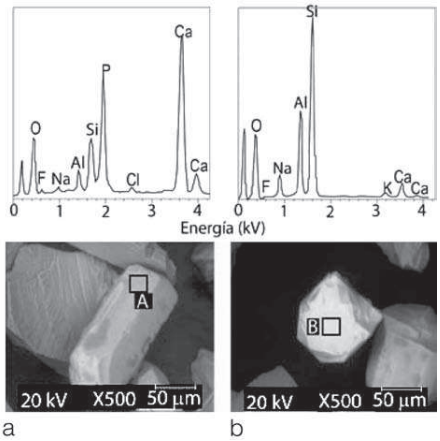

Figura 4. Espectro generado por el microscopio electrónico de bajo vacío para grano A (a) y grano B (b). Ver Tabla II.

de estos elementos es resumido en la Tabla II para este cristal. En este caso, en virtud de que la concentración del flúor es mayor que la de cloro, pareciera tratarse de un fluorapatito.

En la Figura 4b se ilustra el espectro semicuantitativo arrojado por el análisis por MEB al grano B, que aparece debajo del mismo con el señalamiento de la zona donde fue aplicada la sonda para el estudio por FRX. Aunque en este espectro no se visualizan los picos correspondientes a C y Zr, los resultados mostrados en la Tabla II para este cristal permiten aseverar que se trata de un cristal de circón. La razón por la cual no se visualizan estos elementos en el espectro es que sus concentraciones son relativamente bajas, por lo cual están por debajo del límite de detección y el "ruido" oculta sus picos, haciéndolos indistinguibles.

MEB de alto vacío con sonda dispersiva de energía por rayos X

En la Figura 3b se muestra la vista de la misma fracción F1 analizada anteriormente, a 50× bajo el microscopio de barrido electrónico de alto vacío del Instituto Nacional de Investigaciones Nucleares (ININ) de México, con una energía dispersiva de 25keV y presión de 200psi. De estos cristales se seleccionaron al azar cinco granos y se les realizó un análisis por área en la parte central de cada uno de ellos. Los granos estudiados fueron denotados con las letras A a F. A continuación se presentan los resultados de los análisis realizados sobre los granos B, C, D y F.

TABLA III
VALORES ARROJADOS POR LA SONDA EDX DEL MICROSCOPIO ELECTRÓNICO DE ALTO VACÍO APLICADO SOBRE EL CRISTAL B*

Elemento	Wt %	At %	K-Ratio
O K	35,61	67,31	0,06
SiK	15,22	16,39	0,11
ZrL	49,17	16,30	0,37

* Ver Figura 5.

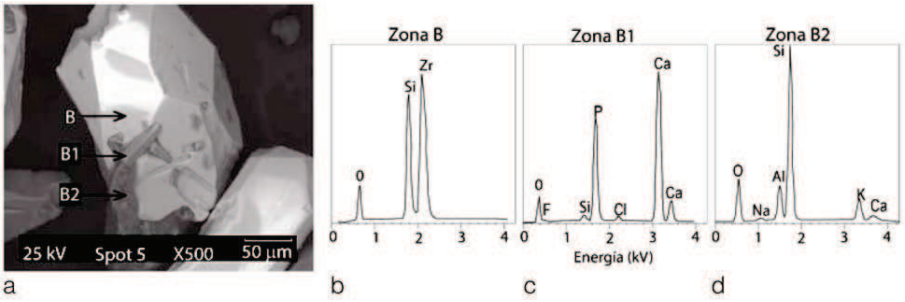

Figura 5. Grano B (en a) y las tres zonas donde se aplicó la sonda EDX del MEB. Espectro generado sobre zona B (b), inclusión B_1 (c) y zona B_2 (d). Ver Tablas III y IV.

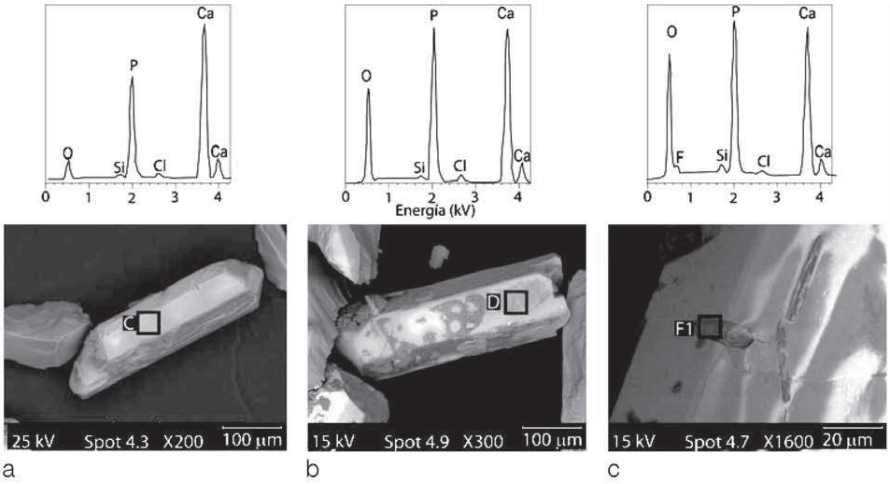

Figura 6. Espectro generado por la aplicación de la sonda EDX del MEB sobre cristal C (a), cristal D (b) y sobre la inclusión F_1 del cristal F (c). Ver Tablas V y VI.

En la Figura 5a se muestra un ejemplar del cristal B, y a la derecha tres espectros arrojados por EDX en tres diferentes zonas del grano, señalados como B, B1 y B2. En la Figura 5b se observan picos significativos de Zr sobre la capa L y de O, reconocido sobre la capa K. En la Tabla III, se muestran los valores semicuantitativos obtenidos de este estudio. Según los elementos encontrados, Zr (49,17%) y O (35,61%), se deduce que el grano analizado es un circón. Sobre el grano estudiado se observan algunas inclusiones y otro material adherido al mismo. Se seleccionaron dos zonas, una sobre la inclusión (B1) y otra zona (B2) cuyos respectivos espectros se presentan en las Figuras 5c y d. Los resultados del estudio sobre ambas zonas están resumidos en la Tabla IV. En el caso de la zona B_1 la inclusión corresponde a un cristal de apatito, por los altos valores de Ca, P y O, y como la proporción de F (2,93%) es mayor a la de Cl (0,95%) puede afirmarse que es un fluorapatito. Con respecto a la zona B_2, las concentraciones de elementos mostrada en la Tabla IV permiten inferir que se trata de restos de fragmentos de la matriz.

TABLA IV
VALORES ARROJADOS POR LA SONDA EDX DEL MICROSCOPIO ELECTRÓNICO DE ALTO VACÍO APLICADO SOBRE LAS ZONAS B_1 Y B_2 DEL CRISTAL B*

Zona B_1				Zona B_2			
Elemento	Wt %	At %	K-Ratio	Elemento	Wt %	At %	K-Ratio
O K	36,27	55,53	0,05	O K	39,82	54,44	0,09
F K	2,23	2,87	0,00	NaK	1,12	1,07	0,00
SiK	0,93	0,81	0,01	AlK	8,19	6,64	0,05
P K	20,56	16,26	0,16	SiK	42,91	33,41	0,29
ClK	0,95	0,66	0,01	K K	6,97	3,90	0,05
CaK	39,06	23,87	0,35	CaK	0,99	0,54	0,01

* Ver Figura 5.

Los cristales C y D mostrados en las Figuras 6a y b, respectivamente, fueron seleccionados de acuerdo a su geometría hexagonal, por lo cual se sospechaba que podrían ser cristales de apatitos. El análisis realizado sobre el cristal C indica y confirma dicha sospecha. En este caso no es posible la cuantificación del flúor; sin embargo, se observa en su respectivo espectro (Figura 6a) la presencia de dos picos de calcio (Ca) activados sobre la capa K y el valor de Cl (1,08%) en la Tabla V permiten aseverar que es un cristal de cloroapatito. Análogamente al caso anterior, el análisis realizado sobre el cristal D, mostrado en la Figura 6b y la Tabla V (Wt% Cl= 1,29) confirman que se trata

de un cristal de cloroapatito. En la figura 6c se aprecia la inclusión F_1 del cristal F, correspondiente a un grano de circón; la presencia de los elementos P, Ca y O revelan que la inclusión es un fluorapatito, por ser el porcentaje de F mayor que el de Cl (Tabla VI).

Fluorescencia de rayos X

Debido a que en las sesiones de microscopía electrónica de barrido se distinguieron básicamente apatitos (tipo flúor- y cloro-apatitos), circones y fragmentos de la matriz, se realizaron dos sesiones de FRX, la primera correspondiente a la matriz o granos sobrantes de la separación visual bajo una lupa 10× y la segunda perteneciente a la selección de granos estudiados por MEB.

Los resultados de la FRX del segundo grupo mostraron un espectro formado por diferentes elementos de los cuales 14 (K, Ca, Mn, Fe, Hf, As, Bi, Br, Rb, Th, U, Sr, Y y Zr) son los más significativos. La presencia de tierras raras como U y Th es completamente normal, debido a que los minerales accesorios al cristalizar introducen estos átomos dentro de su estructura; de allí la utilidad que tienen estos minerales para la datación radiométrica. La presencia del hafnio en el espectro se debe a que este elemento es un catión que determina la presencia del mineral circón, ya que en este silicato el circonio (Zr), frecuentemente se encuentra junto con el Hf y ocasionalmente con U, Th e Y. El mineral circón es parte del grupo de los silicatos y está compuesto de minerales con fórmula general XSiO4, donde X es el catión tetravalente X^{+4}. Si este catión es Zr, el mineral es circón, si el catión es Hf el mineral recibe el nombre de hafnón, en el caso del Th recibe el nombre de torita y en el caso del U es denominado cofinita.

El intercambio se favorece con el Hf debido a que el Zr y el Hf se encuentran en la misma familia de la tabla periódica de los elementos, por lo que sus propiedades químicas para formar compuestos son similares. El mineral circón, puede contener un 20% de hafnón en su estructura, y si éste excede ese porcentaje se le designa como hafnón. La presencia de estos elementos en la estructura del silicato es debida a las especies iónicas que se forman de los elementos, que permiten un fácil intercambio químico entre los átomos de Zr con los de Hf, Th o U. Por esta propiedad química los circones contienen una concentración más alta de U, situándose ésta usualmente en el rango de 100 a 1500ppm, aunque varía dependiendo del tipo de roca fuente que contiene el circón y del tamaño del cristal (Sakamoto *et al*., 1980; Duddy y Kelly, 1999).

Por su parte, la variación en la concentración de Hf depende de las condiciones fisicoquímicas del entorno donde se encuentre la muestra. Sin embargo, hasta el momento no se ha realizado un estudio de cómo influye la presencia de este elemento en la estimación de la edad proporcionada por el método de huellas de fisión.

Difracción de rayos X

El primer análisis de difracción de rayos X hecho a las muestras de mano y realizado en el Laboratorio de Difracción y Fluorescencia de Rayos X de la Escuela de Geología, Minas y Geofísica de la Universidad Central de Venezuela (UCV) indicó cuatro especies cristalinas: apatito (fluorapatito, hidroxilapatito), plagioclasas, circón y gestantita. Otro análisis realizado en la Universidad Nacional Autónoma de México (UNAM), sobre la fracción F1 arrojó la presencia de a) feldespatos: plagioclasa de composición intermedia entre albita ($NaAlSi_3O_8$) y anortita ($CaAl_2Si_2O_8$); b) piroxenos: enstatita ferrosa, (Mg, Fe) SiO_3 y c) apatitos: hidroxilapatito y fluorapatito. La última sesión del estudio se realizó en la UCV sobre la fracción F2 y proporcionó el espectro mostrado en la Figura 7.

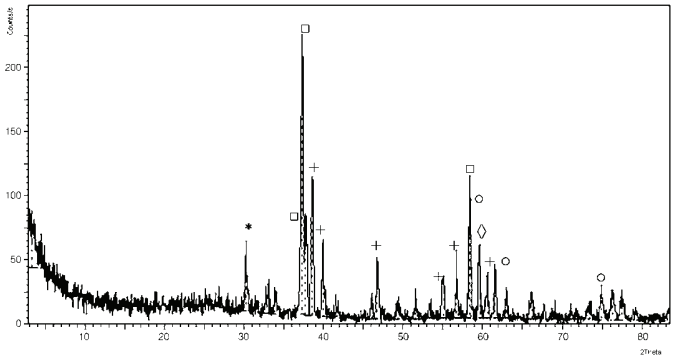

Figura 7. Espectro generado del estudio de difracción de rayos X para la muestra de FCT refinada entre 3,095 y 3,225 grs/cm^3, donde el eje x se refiere a la penetración del rayo con un ángulo de incidencia 2α, y el eje y se refiere al número de emisiones contadas por segundo (cps). Los símbolos sobre el espectro denotan la especie de apatito reconocida a partir de ese valor y están identificados en la leyenda de la Tabla VII.

Los valores máximos de la Figura 7 están resumidos en la Tabla VII. Utilizando la biblioteca de reconocimiento de especies existentes en el laboratorio fue posible discriminar las cinco especies de apatitos señalados en la leyenda de la Tabla VII e indicados con los mismos símbolos en la Figura 7.

Datación de Apatitos del FCT por MHF

La fracción F2 fue procesada completamente bajo la metodología presentada anteriormente con el fin de fechar apatitos de *Fish Canyon Tuff* (FCT) por el método de huella de fisión (MHF). Después de irradiadas las muestras, se revelaron las huellas de fisión inducidas (N_i) sobre las micas colocadas a cada una de las pastillas (resina con cristales pulidos). A continuación se calculó la densidad del flujo (ρ_m) de neutrones sobre el monitor, mediante el conteo de huellas inducidas sobre las micas colocadas sobre (o en) cada vidrio IRMM540. Posteriormente, se

TABLA V
VALORES ARROJADOS POR LA SONDA EDX DEL MICROSCOPIO ELECTRÓNICO DE ALTO VACÍO APLICADO SOBRE LOS CRISTALES C Y D *

Cristal C				Cristal D			
Elemento	Wt %	At %	K-Ratio	Elemento	Wt %	At %	K-Ratio
O K	33,19	52,99	0,04	O K	39,00	59,13	0,08
SiK	0,82	0,75	0,01	SiK	0,43	0,38	0,00
P K	21,91	18,07	0,17	P K	20,97	16,42	0,18
ClK	1,08	0,78	0,01	ClK	1,29	0,88	0,01
CaK	43,00	27,41	0,39	CaK	38,30	23,18	0,36

* Ver Figura 6.

TABLA VI
VALORES ARROJADOS POR LA SONDA EDX DEL MICROSCOPIO ELECTRÓNICO DE ALTO VACÍO APLICADA SOBRE LA INCLUSIÓN F_1 DEL CRISTAL F*

Elemento	Wt %	At %	K-Ratio
O K	55,91	71,24	0,11
F K	6,56	7,04	0,01
SiK	0,73	0,53	0,00
P K	16,41	10,80	0,12
ClK	0,41	0,24	0,00
CaK	19,98	10,16	0,18

* Ver Figura 6.

TABLA VII
RESULTADOS SEMICUANTITATIVOS PARA LA MUESTRA DE FCT REFINADA ENTRE 3,095 Y 3,225 GRS/CM^3

Espacio-d (Å)	Rel. nt. (%)	Ángulo (°2Theta)	Altura (counts/s)	Background (counts/s)	Ancho (°2Theta)	Significación
3,43 *	24,56 *	30,22 *	53,54 *	10,31 *	0,12 *	1,41 *
2,79 □	100 □	37,31 □	217,99 □	7,17 □	0,28 □	6,34 □
2,76 □	36,1 □	37,70 □	78,7 □	6,95 □	0,24 □	1,32 □
2,70 +	49,54 +	38,55 +	108 +	6,59 +	0,28 +	4,52 +
2,62 +	27,25 +	39,91 +	59,39 +	6,05 +	0,24 +	2,92 +
2,25 +	22,01 +	46,71 +	47,97 +	4,24 +	0,16 +	1,06 +
1,93 +	15,01 +	55,07 +	32,72 +	4,39 +	0,28 +	1,43 +
1,88 +	24,17 +	56,66 +	52,7 +	4,43 +	0,2 +	1,47 +
1,83 □	50,72 □	58,34 □	110,57 □	4,46 □	0,16 □	1,2 □
1,83 ○	41,81 ○	58,47 ○	91,15 ○	4,47 ○	0,1 ○	100 ○
1,79 ◊	26,44 ◊	59,61 ◊	57,63 ◊	4,49 ◊	0,28 ◊	3,14 ◊
1,77 +	15,94 +	60,59 +	34,76 +	4,51 +	0,48 +	3,03 +
1,74 ○	18,9 ○	61,50 ○	41,21 ○	4,53 ○	0,16 ○	1,04 ○
1,47 ○	12,1 ○	74,91 ○	26,37 ○	3,4 ○	0,32 ○	1,25 ○

Los símbolos al lado derecho de cada cifra denotan la especie de apatito reconocida a partir de ese valor. □: calcium chloride phosphate hydroxide (hydroxylapatite chlorian $Ca_5(PO_4)_3(OH.Cl.F)$), +: calcium fluoride phosphate (fluorapatite, $Ca_5(PO_4)_3F$), ○: calcium phosphate hydroxide (hydroxylapatite, $Ca_5(PO_4)_3(OH)$), ◊: calcium fluoride carbonate phosphate hydroxyde (carbonatefluorapatite $Ca_{10}(PO_4)_5CO_3F_{1.5}(OH)_{0.5}$) y *: calcium carbonate phosphate hydroxyde (carbonatehydroxylapatite $Ca_{10}(PO_4)_3(CO)_3(OH)_2$). Ver Figura 7.

obtuvo el Factor Z, de acuerdo a la expresión

$$Z=\frac{\exp(\lambda_\alpha t_{estándar})-1}{\frac{\lambda_\alpha}{2}\left(\frac{N_s}{N_i}\right)_k \rho_m}$$

donde N_s y N_i : número de huellas de fisión espontáneas e inducidas, respectivamente, las cuales son determinadas sobre áreas idénticas en la pastilla para N_s y sobre la mica para N_i.;λ_α=1,55125×10^{-10} año^{-1}: constante de decaimiento radioactivo por emisión de partículas α; ρ_m: densidad; y $t_{estándar}$: edad del estándar utilizado para el cálculo de Z, en este caso del apatito de Durango (31,4 ±0,5Ma).

El factor Z fue calculado a partir del conteo de N_s, N_i y A (área sobre la cual fue realizado el conteo) sobre 30 cristales del apatito de Durango, cuyo valor promedio fue

$$\overline{Z}=\frac{1}{30}\sum_{k=1}^{19} Z_k = 307{,}46\text{Ma}$$

el cual fue sustituido en la ecuación de edad práctica para el MHF (Wagner y van den Haute, 1992) para determinar la edad individual de cada cristal de la muestra del FCT, la cual para cada grano j= 1,…, m viene dada por

$$t=\frac{1}{\lambda_\alpha}\ln\left[\frac{\lambda_\alpha}{2}\left(\frac{\rho_s}{\rho_i}\right)_j Z\rho_m+1\right]$$

La Tabla VIII muestra la forma estándar (Naeser *et al*., 1979) de presentar los resultados provenientes del MHF sobre 19 cristales de apatito del FCT. Al incorporar estos valores en el programa TrackKey (Dunkl, 2002) se obtuvo una edad promedio de 27,2Ma con una desviación estándar de 0,2Ma, la cual está en concordancia con las edades encontradas mediante los métodos K-Ar, ^{40}Ar/^{39}Ar, Rb-Sr y U-Pb para el FCT (Lanphere, 2004) y para el MHF (Miller *et al*., 1985; Lim y Lee, 2000).

TABLA VIII
RESULTADOS DE LOS ANÁLISIS POR TRAZAS DE FISIÓN PARA LA MUESTRA DE FCT

ρ_s (x10^{6}cm^{-2})	N_s	ρ_i (x10^{6}cm^{-2})	N_i	Square	U ppm	t_j
0,196	13	0,738	49	80	16	27,31
0,169	14	0,639	53	100	14	27,19
0,253	21	0,952	79	100	21	27,36
0,161	12	0,589	44	90	13	28,07
0,136	9	0,512	34	80	11	27,25
0,301	12	0,115	46	48	26	26,85
0,181	9	0,683	34	60	15	27,25
0,169	7	0,675	28	50	15	25,74
0,258	15	0,981	57	70	22	27,09
0,265	22	1,010	84	100	23	26,96
0,136	9	0,482	32	80	11	28,95
0,145	12	0,566	47	100	13	26,28
0,138	8	0,516	30	70	12	27,45
0,056	3	0,189	11	70	4	28,07
0,201	10	0,763	38	60	17	27,09
0,301	7	1,200	28	28	27	25,74
0,181	9	0,663	33	60	15	28,07
0,120	8	0,452	30	80	10	27,45
0,602	5	0,229	19	100	5	27,09

ρ_s, ρ_i : densidad de huellas de fisión espontáneas (Ns) e inducidas (Ni); Square: número de celdas contadas, para 100 celdas el área es de 8,30x10^{-7}·cm^2; U: concentración de uranio en el grano en partes por millón (ppm); y t_j : edad para cada grano j. Los parámetros para el cálculo de la edad por el método de huellas de fisión fueron Z= 307,46Ma, la densidad del monitor utilizado (vidrios monitores IRMM540) ρ_m= 0,671×10^6 huellas/cm^2. La edad promedio y desviación estándar obtenida por el método de huellas de fisión para esta muestra es de 27,2 ±0,2Ma.

Conclusiones

La muestra de FCT analizada es del tipo riolita dacítica. En ésta, el contenido de tierras raras como U, Th y la presencia de Hf, permite concluir que existen varias especies de circones. Sin embargo, la resolución de los equipos aquí utilizados no permitió diferenciar las especies de este mineral. En cuanto a la disposición de los minerales pesados dentro de la matriz del FCT, los circones se encuentran en dos formas, libres en la matriz y encajados en la biotita. En cuanto a los apatitos, una parte de éstos se encuentran encajados en la biotita (cloroapatitos), otra parte libre en la matriz y el resto como inclusiones dentro de los granos de circón (fluorapatitos).

Sobre la fracción F2 (3,095-3,225 grs/cm^3) fue posible reconocer cinco tipos de apatitos diferentes: hidroxil-apatito, carbonato-flúor-apatito, carbonato-hidroxil-apatito, flúor-apatito e hidroxil-apatito clórico. La edad proporcionada por el método de huellas de fisión fue de 27,2 ±0,2Ma, la cual concuerda con la edad K-Ar (27,8 ±0,5Ma), lo cual indica una buena aplicación de los procedimientos del método de huellas de fisión bajo la técnica del detector externo en el laboratorio. No obstante, se desconoce si la presencia de cristales de apatitos con diferentes composiciones químicas afecta el estimado de la edad y el error.

Con respecto al tamaño y distribución de los cristales en la muestra, los fluorapatitos y cloroapatitos son los de mayor tamaño, aunque se necesita incrementar el tamaño de la muestra y hacer un estudio más detallado sobre la dimensión de los cristales y su composición química. Además, su distribución depende del tamaño de apertura de los tamices utilizados. Otro importante estudio futuro ha de ser el intento de datar cada una de las especies para reconocer diferencias en el estimado de la edad. El presente trabajo representa el primer esfuerzo en conjunto entre laboratorios de termocronología en Latinoamérica para estandarizar los procedimientos llevados a cabo en ambos laboratorios.

AGRADECIMIENTOS

Los autores agradecen a John Garver, Union College, Schenectady, EEUU y Jorge Mora, UCV, Venezuela, por proporcionar la muestra; al personal de microscopía electrónica de barrido de alto y bajo vacío, ININ, México; al Laboratorio de Trazas de Fisión, Departamento de Ciencias de la Tierra, UNAM, México; al Laboratorio de Difracción y Rayos X, Escuela de Geología, Minas y Geofísica, UCV, Venezuela; al International Nuclear Track Society (INTS) por habernos proporcionado el Vladimir P. Perelygin Prize; y el financiamiento del CDCH-UCV (proyecto PI. 08.00.6219.2006).

REFERENCIAS

Bachmann O, Dungan MA, Lipman PW (2002) The Fish Canyon Magma Body, San Juan Volcanic Field, Colorado: Rejuvenation and Eruption of an Upper-Crustal Batholith. *J. Petrol. 43*: 1469-1503.

Charlier BLA, Bachmann O, Davidson JP, Dungan MA, Morgan JD (2007) The Upper Crustal Evolution of a Large Silicic Magma Body: Evidence from Crystal-scale Rb-Sr Isotopic Heterogeneities in the Fish Canyon Magmatic System, Colorado. *J. Petrol. 48*: 1875-1894.

Duddy IR, Kelly PR (1999) Uranium in mineral sands: measurement and uses. *Aust. Inst. Geosci. Bull. 26*: 1-5.

Dunkl I (2002) Trackkey: a Windows program for calculation and graphical presentation of fission track data. *Comp. Geosci. 28*: pp. 3-12.

Faure G (1986) *Principles of Isotope Geology*. 2ª ed. Wiley. Nueva York, NY, EEUU. 589 pp.

Fleischer RL, Price PB, Walker RM (1975) *Nuclear Tracks in Solids. Principles and Applications*. University of California Press. Berkeley, CA, EEUU. 605 pp.

Hurford AJ, Green PF (1982) A user's guide to fission track dating calibration. *Earth Planet. Sci. Lett. 59*: 343-354.

Hurford AJ, Green PF (1983) The ζ age calibration of fission-track dating. *Isot. Geosci. 1*: 285-317.

Lanphere M (2004) Reply to comment on "Precise K–Ar, 40Ar/39Ar, Rb–Sr and U–Pb mineral ages from the 27.5 Ma Fish Canyon Tuff reference standard" by M.A. Lanphere and H. Baadsgaard. *Chem. Geol. 211*: 389-390.

Lim HS, Lee YII (2000) Fission-track dating calibration of age standards in a Korean reactor, HANARO. *Geosci. J. 4*: 251-254.

Lipman PW (1975) *Evolution of the Platoro Caldera Complex and Related Volcanic Rocks, Southeastern San Juan Mountains, Colorado:* A *Study of Relations between Ash-flow Eruptions, Lava-flow Activity, and Caldera Structure at a Mineralized Volcanic Center*. Geological Survey Professional Paper Nº 852. Govt. Print. Off. Washington, EEUU. 128 pp.

Lipman PW (2000) Central San Juan Caldera Cluster. En Bethke PM, Hay RL (Eds.) *Ancient Lake Creede: Its Volcano-Tectonic Setting, History of Sedimentation, and Relation to Mineralization in the Creede Mining District*. GSA Special Paper. 346 pp. 9-69.

Middleton GV (1999) *Data Analysis in the Earth Sciences Using Matlab*. Prentice Hall. NJ, EEUU. 260 pp.

Miller DS, Duddy IR, Green PE, Hurford AJ, Naeser CW (1985) Results of interlaboratory comparison of fission-track age standards: fission-track workshop 1984. *Nucl. Tracks 10*: 383-391.

Naeser CW, Gleadow AJW, Wagner GA (1979) Standardization of fission-track data reports: *Nucl. Tracks 3*: 133-136.

Sakamoto K, Hamajima Y, Itoh K, Yamazaki K (1980) Uranium determinations by ^{133}Xe in terrestrial zircon, apatite and chromite; comparative study of thermal releases of fissiogenic xenon from terrestrial and meteoritic minerals. *J. Radioanal. Nucl. Chem. 60*: 343-352.

Streckeisen A (1979) Classification and nomenclature of volcanic rocks, lamprophyres, carbionatites and mellitic rocks: recommendations and suggestions of the IUGS Subcommision on the Systematics of igneous Rocks. *Geology 7*: 331-335.

Wagner G, van den Haute P (1992) *Fission Track Dating in Solid*. Earth Sciences Library, Kluwer. Dordrecht, Holanda. 285 pp.

CHARACTERIZATION OF ZIRCON AND APATITE CRYSTALS FROM FISH CANYON TUFF INTERNACIONAL STANDARD FOR USE IN A THERMOCRONOLOGY LABORATORY

Mauricio Bermúdez-Cella, Arturo López, Miguel Balcázar-García, Graciela Zarazúa-Ortega and Rommel Bona

SUMMARY

Batches of apatite samples and zircons, collected from the international standard Fish Canyon Tuff (FCT) in San Juan Mountains, Colorado, USA, for fission-track dating method (FTDM) were characterized using, x-ray diffraction, x-ray fluorescence, scanning electron microscopy of low and high vacuum with energy dispersive x-ray spectrometer, apatite FTDM and thin section analysis. A total of 19 apatite crystals were dated by FTDM providing an age of 27.2 ±0.2Ma, in agreement with the K-Ar age (27.8 ±0.5Ma). The studies performed allowed recognition of the existence of different crystalline species of zircons and apatites, as well the validation of each one of the procedures for this dating method in the thermo-chronology laboratory of the Universidad Central de Venezuela.

CARACTERIZAÇÃO DE CRISTAIS DE APATITA E ZIRCÃO DO PADRÃO INTERNACIONAL *FISH CANYON TUFF* PARA SEU USO EM UM LABORATÓRIO DE TERMOCRONOLOGÍA

Mauricio Bermúdez-Cella, Arturo López, Miguel Balcázar-García, Graciela Zarazúa-Ortega e Rommel Bona

RESUMO

*Cristais de apatita e zircão de padrão internacional FCT (*Fish Canyon Tuff*, Montañas San Juan de Colorado, EEUU) para o método de traços de fissão foram caracterizadas usando difração e fluorescência de raios X, microscopia electrônica de varredura de baixo e alto vácuo, e petrografia de seções delgadas, para identificar a disposição destes minerais na matriz da amostra. Um total de 19 cristais de apatita foram datados mediante esta técnica de datação mostraram uma idade de 27,2 ±0,2Ma, a qual está em concordância con a idade K-Ar (27,8 ±0,5Ma). O estudo realizado permitiu reconhecer a existência de diferentes espécies cristalinas de zircões e apatitas, bem como a validação de cada um dos procedimentos para a datação de apatitas no Laboratório de Termocronologia da Universidade Central de Venezuela.*

APPENDIX 4

Standard	Irradiation	Monitor	Nd	ρ_m	ξ	$\pm\sigma$
Fish Canyon Tuff	2-2007	IRMM-540R	7796	6.13E+05	262.46	16.20
Durango	2-2007	IRMM-540R	7919	6.23E+05	288.50	14.20
Durango	4-2007	IRMM-540R	6431	6.32E+05	319.50	9.20
Durango	4-2007	IRMM-540R	6431	6.32E+05	308.40	9.00
Durango	8-2007	IRMM-540R	5601	6.60E+05	259.28	19.90
Fish Canyon Tuff	8-2007	IRMM-540R	4984	5.88E+05	201.86	17.90
Durango	9-2007	IRMM-540R	6626	6.65E+05	242.80	16.80
Weighted mean					**288.66**	**5.23**

Standard	Irradiation	Monitor	Nd	ρ_m	ξ	$\pm\sigma$
Fish Canyon Tuff	U1A-94	CN-1	5426	3.27E+06	128.31	8.30
Durango	U1A-94	CN-1	5771	3.48E+06	136.59	10.10
Durango	U1A-94	CN-1	6115	3.68E+06	128.33	5.80
Weighted mean					**129.82**	**5.02**

Table A1. Individuals and global values of ζ used in this thesis.

APPENDIX 5

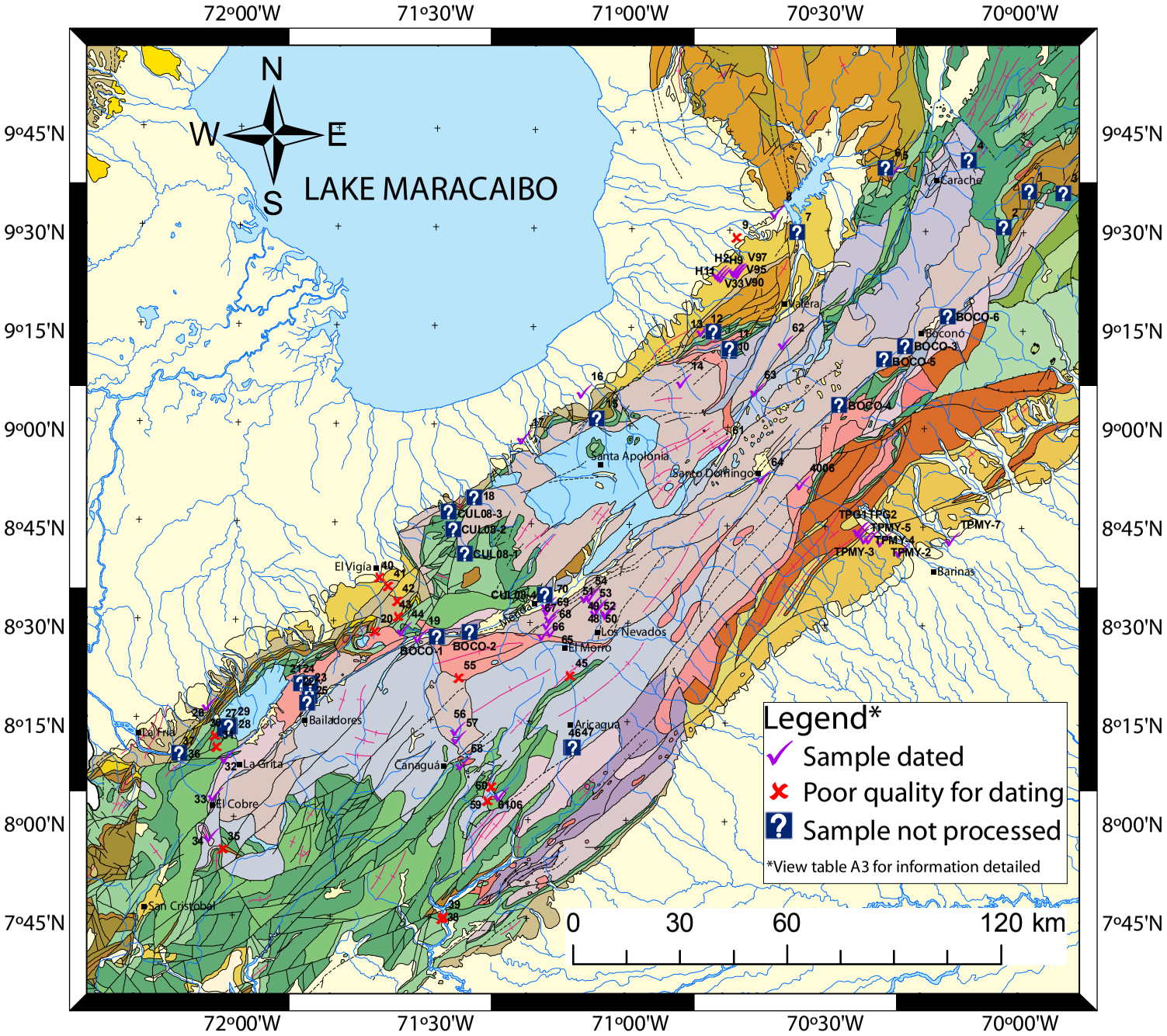

Figure A1. Spatial distribution of available samples collected for this thesis to study the exhumation history of the Venezuelan Andes

APPENDIX 6

Sample	Block	Location and lithology	Latitude (ºN)	Longitude (ºW)	Elevation (m)	Status	Thesis Position
1		Humocaro Granite	9,6057	-69,9864	1012	ND	
2		Sagua River sediments	9,5131	-70,0511	1771	ND	
3		Cantera Anzoategui sandstones	9,6007	-69,8989	1464	ND	
4		Carache Granite	9,6833	-70,1414	2373	ND	
5	Flank North	Chejendé River sediments	9,6556	-70,3310	575	D	Chapter 6
6		Puente Gómez sandstones	9,6619	-70,3532	492	ND	
7		Agua Viva-Guaimacire sandstones	9,4976	-70,5786	200	ND	
8	Flank North	Agua Viva River sediments	9,5489	-70,6285	102	D	Chapter 6
9		El Cenizo River sediments	9,4827	-70,7322	89	GPQ	
10		Monte Carmelo Intrusive rock	9,1943	-70,7501	1485	ND	
11		Monte Carmelo silic sandstones	9,1999	-70,7488	1553	ND	
12		Mimbós Granite	9,2504	-70,8154	355	ND	
13	Flank North	Mimbós River sediments	9,2473	-70,8140	353	D	Chapter 6
14	SLCB	Palmira Granite	9,1162	-70,8648	1574	D	Chapter 4
15		Santa Apolonia Granite	9,0194	-71,0841	746	ND	
16	Flank North	San Pedro River sediments	9,0880	-71,1202	187	D	Chapter 6
17	Flank North	Tucaní River sediments	8,9697	-71,2702	181	D	Chapter 6
18		Río Perdido Granite	8,8167	-71,3964	314	ND	
19	Flank North	Chama River sedimens	8,4638	-71,5294	408	D	Chapter 6
20		Mesa Bolívar Granite	8,4747	-71,6443	931	GPQ	
21		Zea Granite	8,3402	-71,8327	1067	ND	
22		Zea Bailadores Granite	8,3078	-71,8096	1973	ND	
23		Batallón-La Negra Granite	8,3238	-71,8104	2186	GPQ	
24		Mesa Sta Rita Granite	8,3400	-71,8083	1614	ND	
25		Bailadores Gneiss	8,2910	-71,8148	1588	ND	
26	Flank North	Río Coloncito sediments	8,2843	-72,0653	438	D	Chapter 6
27		El Tesoro-Umuquena Red sandstones	8,2234	-72,0248	1078	ND	
28		El Tesoro-Umuquena Amphibolite	8,2286	-72,0125	1244	ND	
29		El Tesoro-Umuquena Granite	8,2287	-72,0144	1232	ND	
30		La Grita massive sandstones	8,2059	-72,0498	1413	GPQ	
31		La Grita Granite 2	8,1765	-72,0454	1909	GPQ	
32		La Grita Granite 1	8,1509	-72,0185	1095	D (0 Ma)	
33	CB	El Cobre Granite	8,0554	-72,0474	1670	D	Chapter 4
34		Queniquea Zumbador Granite	7,9518	-72,0572	2715	D (0 Ma)	
35		Queniquea Granite	7,9190	-72,0272	1859	GPQ	
36		Las Mesas sandstones	8,1602	-72,1401	702	ND	
37		Las Mesas sandstones 2	8,1591	-72,1463	578	GPQ	
38		Caparo Granite 1	7,7461	-71,4674	266	GPQ	
39		Caparo Granite 2	7,7518	-71,4635	314	GPQ	
40		Río Chama sandstones	8,6107	-71,6340	110	GPQ	
41		El Vigía sandstones	8,5901	-71,6119	149	GPQ	
42		El Vigía quartz sandstones	8,5527	-71,5896	194	GPQ	
43		El Vigía sandstones	8,5123	-71,5845	249	GPQ	
44	EB and SLCB	Granito Tunel Caña Brava	8,4808	-71,5707	323	D (0 Ma)	
45		Vía Aricagua La Quinta Formation	8,3666	-71,1471	2405	GPQ	
46		Cañandon Quartz sandstones	8,1842	-71,1420	962	ND	
47		Cañandon Granite	8,1851	-71,1377	990	ND	
48	SNB	Pico Espejo1 Sierra Nevada Gneiss	8,5317	-71,0527	4718	D	Chapter 5
49	SNB	Pico Espejo 2 Sierra Nevada Gneiss	8,5273	-71,0516	4622	D	Chapter 5
50	SNB	Alto de la Cruz Sierra Nevada Gneiss	8,5332	-71,0790	4236	D	Chapter 5
51	SNB	Loma Redonda Sierra Nevada Gneiss	8,5437	-71,0752	3999	D	Chapter 5
52	SNB	Loma Redonda-Aguada Sierra Nevada Gneiss	8,5556	-71,0826	3633	D	Chapter 5
53	SNB	Aguada-La Montaña Sierra Nevada Gneiss	8,5700	-71,0940	3285	D	Chapter 5
54	SNB	Agua Montaña Sierra Nevada Gneiss	8,5698	-71,1055	2760	D	Chapter 5
55		Via Chacantá sandstones	8,3592	-71,4308	2720	GPQ	
56	CB	Mucutampó sandstones	8,2286	-71,4333	2000	D	Chapter 4

Table A2. Prepared or processed fission track samples. (D) dated, (GPQ) graind of poor quality, (ND) not dated and D(0) samples with a zero fission-track age.

Sample	Block	Location and lithology	Latitude (ºN)	Longitude (ºW)	Elevation (m)	Status	Thesis Position
57	CB	Mucutampó-Chacanta Gneiss	8,2062	-71,4297	1440	D	Chapter 4
58	CB	La Quinta Canagua-Mucuchachi Sandstones	8,1416	-71,4180	1276	D	Chapter 4
59		Canaguá schists	8,0467	-71,3535	1035	GPQ	
60		La Tendida La Quinta Formation	8,0838	-71,3424	920	GPQ	
61	SLCB	Chachopo Granite	8,9550	-70,7581	2306	D	Chapter 4
62	VB	La Quebrada Augengneiss	9,2155	-70,6079	749	D	Chapter 4
63	VB	Puente Vía Jajo Gneiss	9,0963	-70,6774	1174	D	Chapter 4
64	SLCB	Santo Domingo Gneiss	8,8755	-70,6594	1723	D	Chapter 4
65	SLCB	El Morro P1 Gneiss	8,4801	-71,1909	2770	D	Chapter 5
66	SLCB	El Morro P2 Gneiss	8,4721	-71,2129	2490	D	Chapter 5
67	SLCB	El Morro P3 Gneiss	8,4995	-71,2011	2250	D	Chapter 5
68	SLCB	El Morro P4 Gneiss	8,5164	-71,1968	2060	D	Chapter 5
69	SLCB	El Morro P5 Gneiss	8,5355	-71,2015	1765	D	Chapter 5
70	SLCB	El Morro P6 Gneiss	8,5476	-71,2028	1250	D	Chapter 5
02-06	Flank South	Santo Domingo River sediments	8,76	-70,38	244	D	Chapter 6
40-06	CATB	La Soledad Granite	8,8600	-70,5600	1604	D	Chapter 4
61-06	CB	Caparo Granite	8,0639	-71,3200	1278	D	Chapter 5
TPMY-7	Barinas Basin	Río Yuca Formation	8,7207	-70,1757	191	D	Chapter 7
TPMY-8	Barinas Basin	Río Yuca Formation	8,6919	-70,3037	301	D	Chapter 7
TPMY-2	Barinas Basin	Río Yuca Formation	8,7183	-70,3528	300	D	Chapter 7
TPMY-3	Barinas Basin	Río Yuca Formation	8,7247	-70,3822	320	D	Chapter 7
TPMY-4	Barinas Basin	Río Yuca Formation	8,7248	-70,3937	360	D	Chapter 7
TPMY-5	Barinas Basin	Río Yuca Formation	8,7382	-70,4052	340	D	Chapter 7
TPG1	Barinas Basin	Parángula Formation	8,7444	-70,4106	390	D	Chapter 7
TPG2	Barinas Basin	Parángula Formation	8,7448	-70,4111	390	D	Chapter 7
H2	Maracaibo Basi	Betijoque Formation Vichú member	9,3919	-70,7760	279	D	Chapter 7
H9	Maracaibo Basi	Betijoque Formation Vichú member	9,3883	-70,7707	252	D	Chapter 7
H11	Maracaibo Basi	Betijoque Formation Vichú member	9,3839	-70,7661	306	D	Chapter 7
V33	Maracaibo Basi	Betijoque Formation Vichú member	9,4012	-70,7355	203	D	Chapter 7
V90	Maracaibo Basi	Betijoque Formation Isnotú member	9,3990	-70,7321	449	D	Chapter 7
V95	Maracaibo Basi	Betijoque Formation Isnotú member	9,3976	-70,7274	251	D	Chapter 7
V97	Maracaibo Basi	Betijoque Formation Isnotú member	9,3956	-70,7233	238	D	Chapter 7
BOCO-1	SNB	Sierra Nevada Gneiss	8,4616	-71,4859	465	ND	
BOCO-2	SNB	Sierra Nevada Gneiss	8,4754	-71,4049	712	ND	
BOCO-3	SNB	Sierra Nevada Gneiss	9,2109	-70,3007	1240	ND	
BOCO-4	SNB	Sierra Nevada Gneiss	9,0597	-70,4675	2178	ND	
BOCO-5	SNB	Sierra Nevada Gneiss	9,1765	-70,3540	1315	ND	
BOCO-6	SNB	Sierra Nevada Gneiss	9,2870	-70,1930	1738	ND	
CUL08-1	SLCB	Sierra La Culata Gneiss	8,6745	-71,4176	1900	ND	
CUL08-2	SLCB	Sierra La Culata Gneiss	8,7351	-71,4484	910	ND	
CUL08-3	SLCB	Sierra La Culata Gneiss	8,7800	-71,4616	372	ND	
CUL08-4	SLCB	Sierra La Culata Gneiss	8,5719	-71,2124	1512	ND	

Table A2. Prepared or processed fission track samples. (D) dated, (GPQ) graind of poor quality, (ND) not dated and D(0) samples with a zero fission-track age.

APPENDIX 7

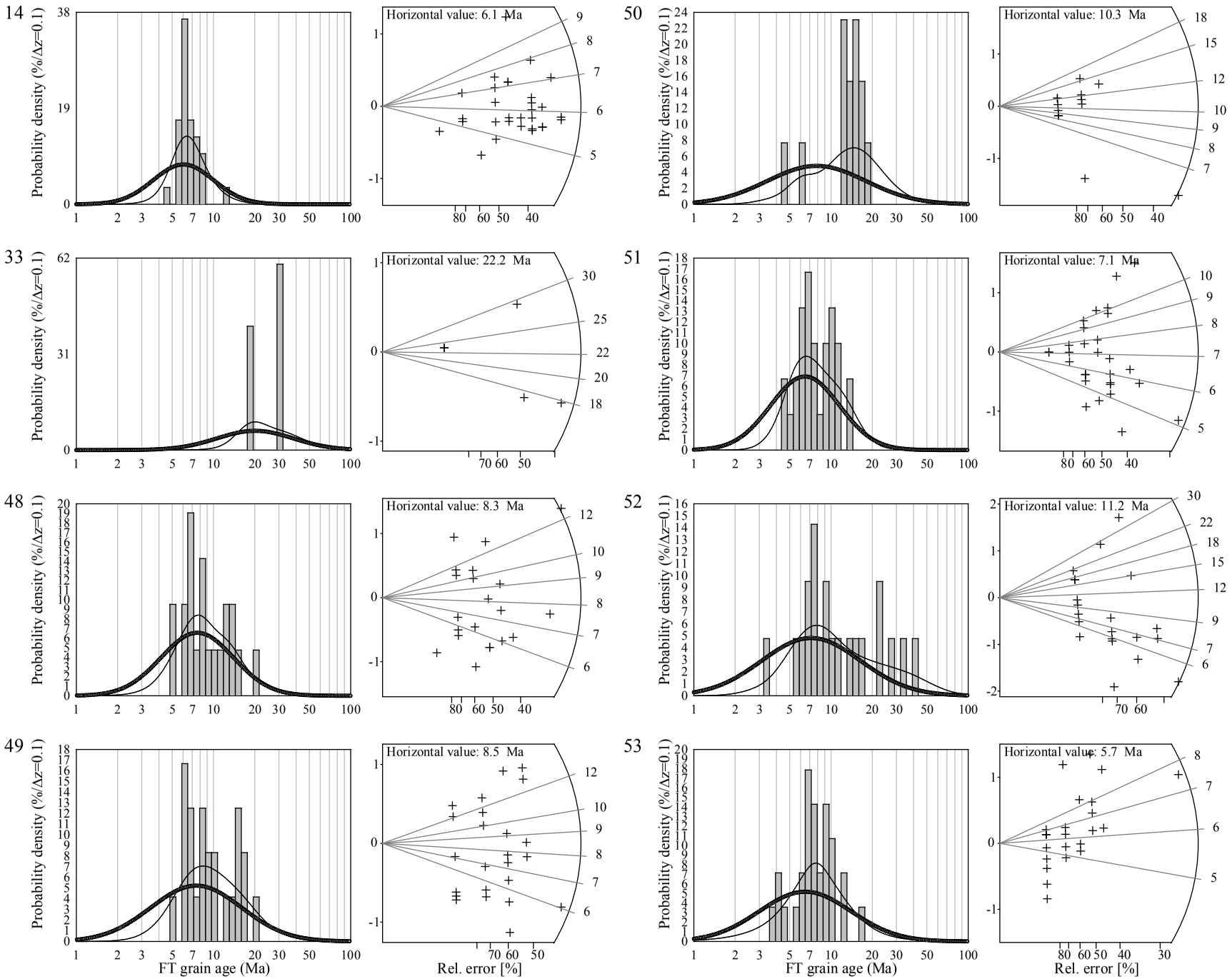

Figure A2. Probability density and radial plots of in-situ fission-track samples (see Table A2).

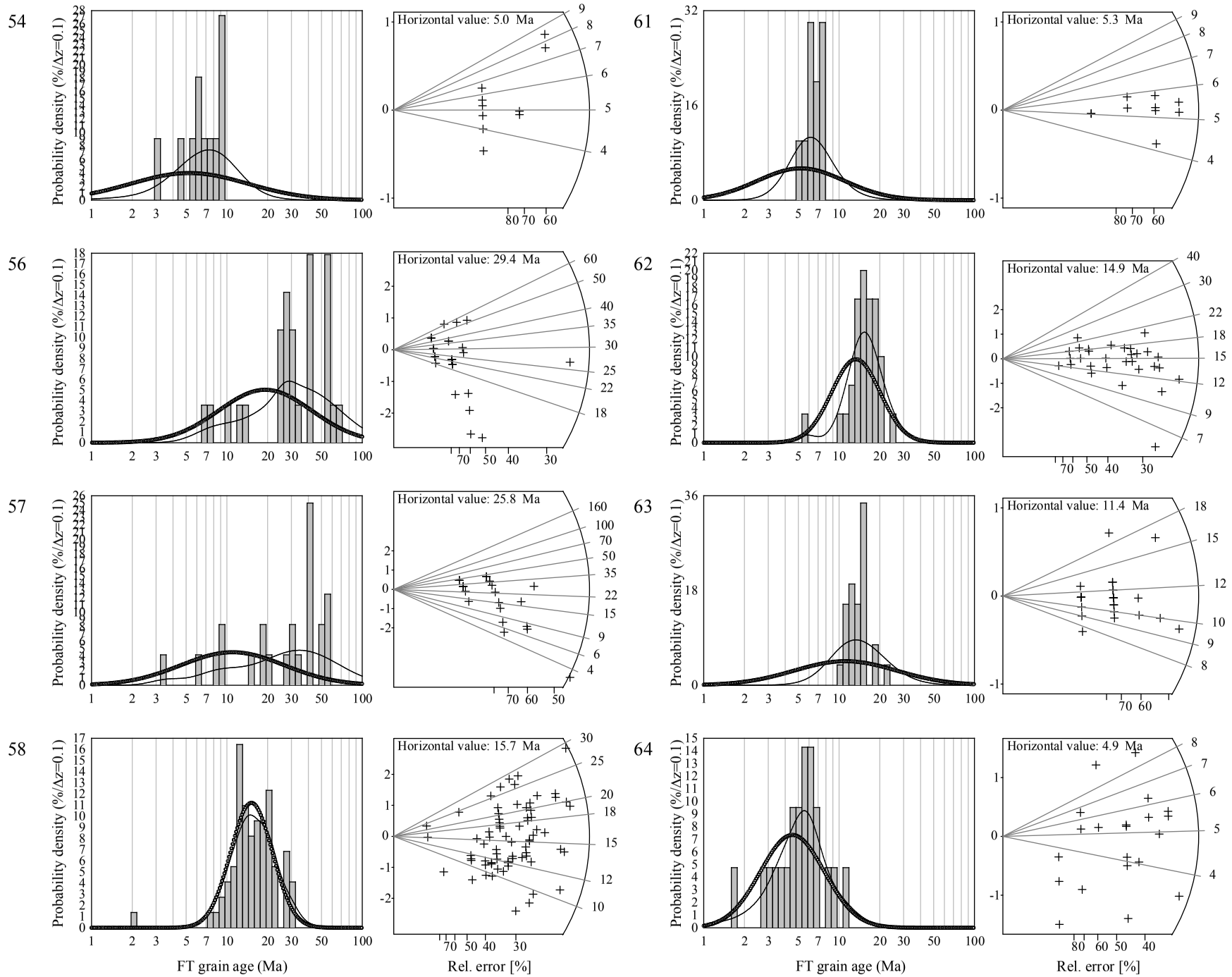

Figure A2 (cont.). Probability density and radial plots of in-situ fission-track samples (see Table A2).

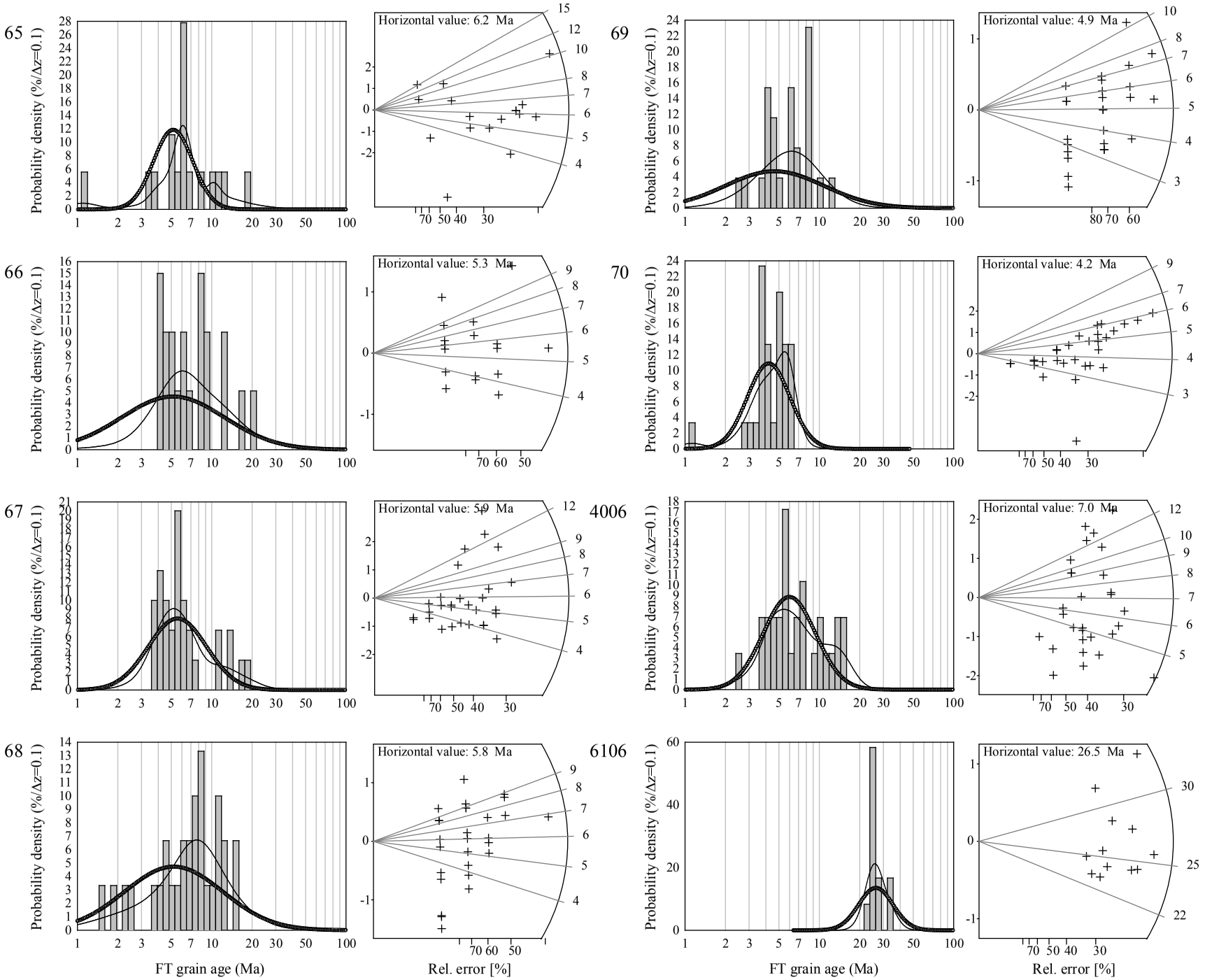

Figure A2 (cont.) . Probability density and radial plots of in-situ fission-track samples (see Table A2).

APPENDIX 8

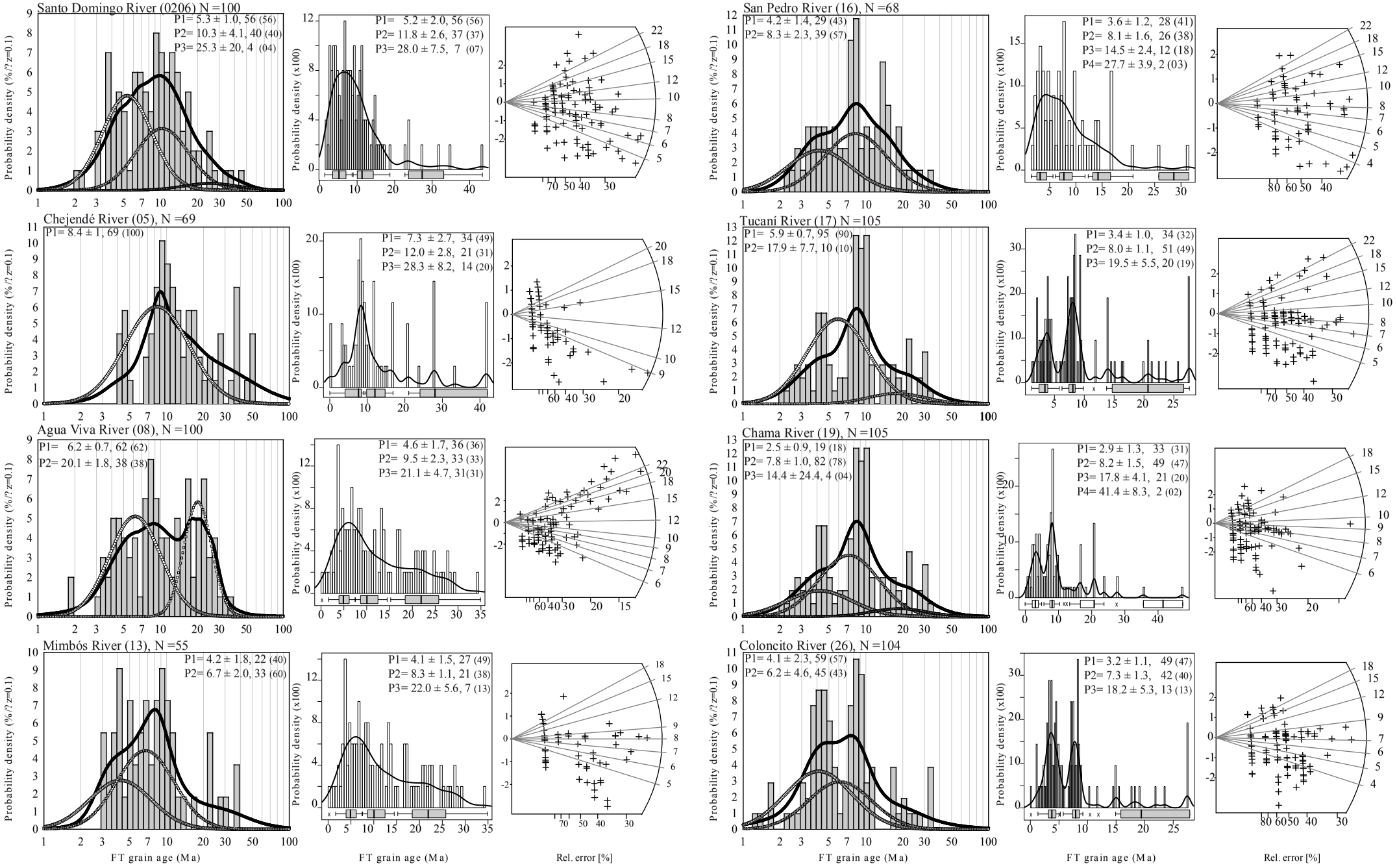

Figure A3. Decomposition into significant ages populations using Binomfit and p-partition,. Radial plots of modern river fission-track samples (see Table A2).

APPENDIX 9

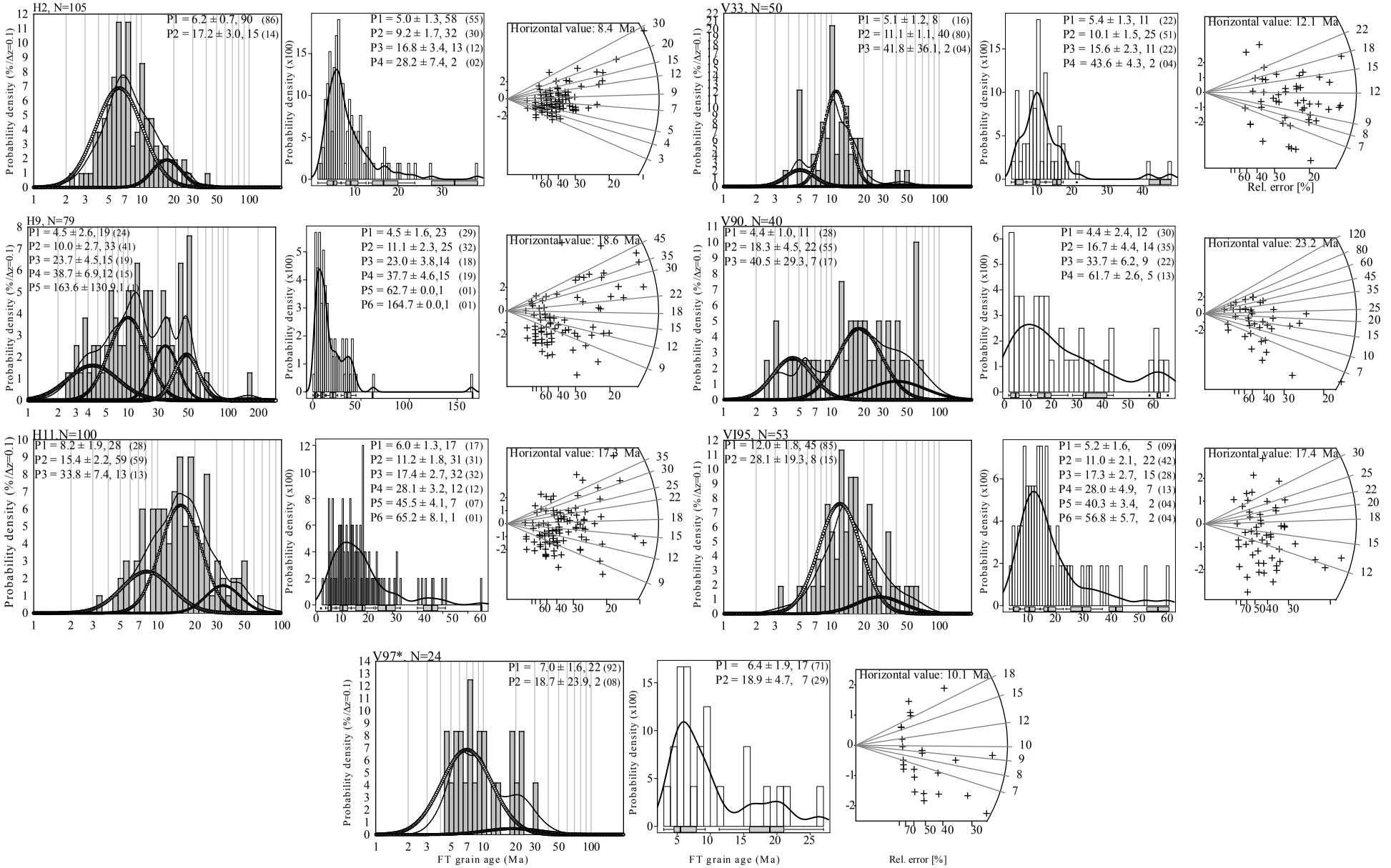

Figure A4. Decomposition into significant ages populations using Binomfit and p-partition. Radial plots of synorogenic fission-track samples (see Table A2).

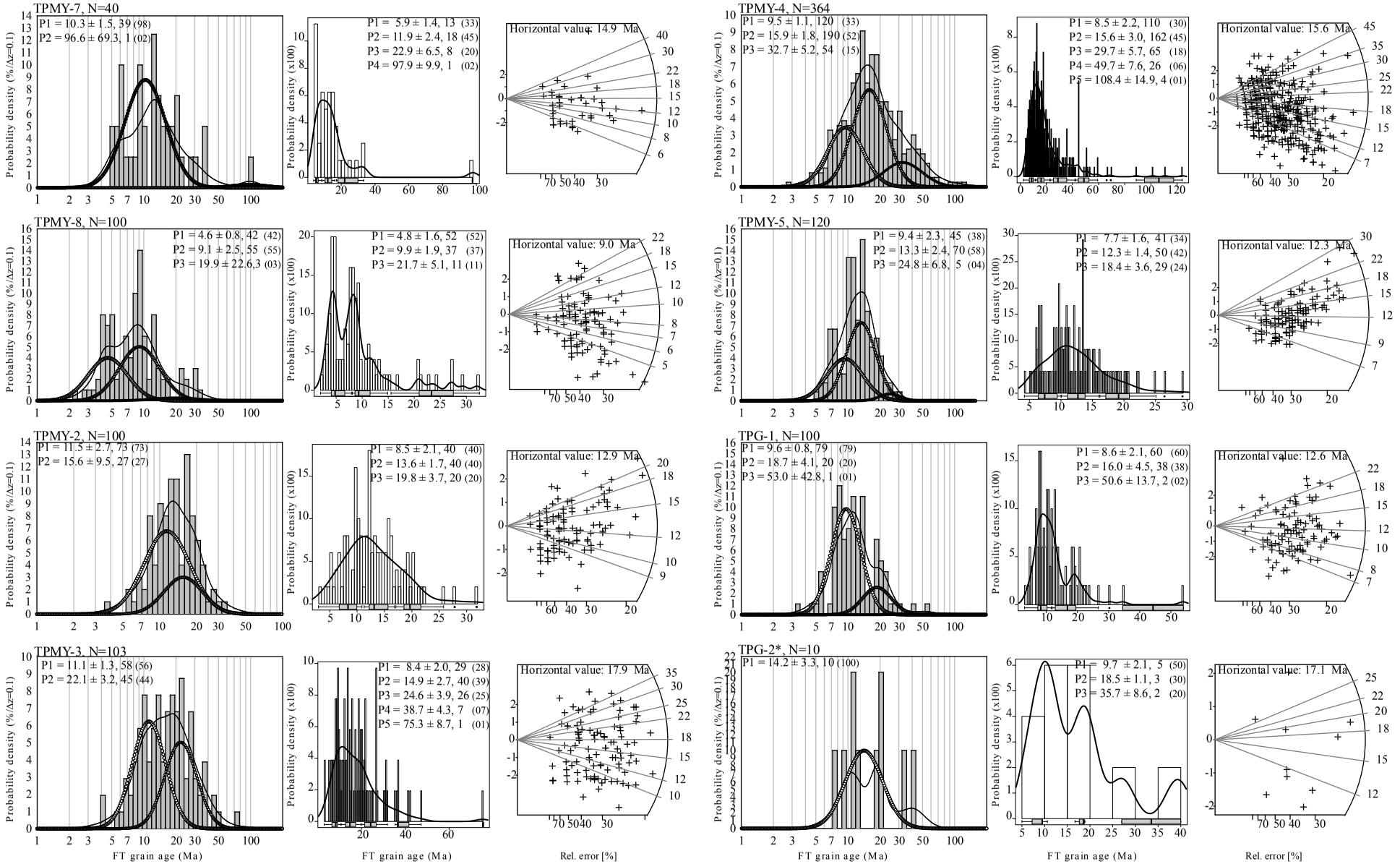

* The discrimination in populations for this sample is not statistically significant.

Figure A4 (cont.). Decomposition into significant ages populations using Binomfit and p-partition. Radial plots of synorogenic fission-track samples (see Table A2).

APPENDIX 10

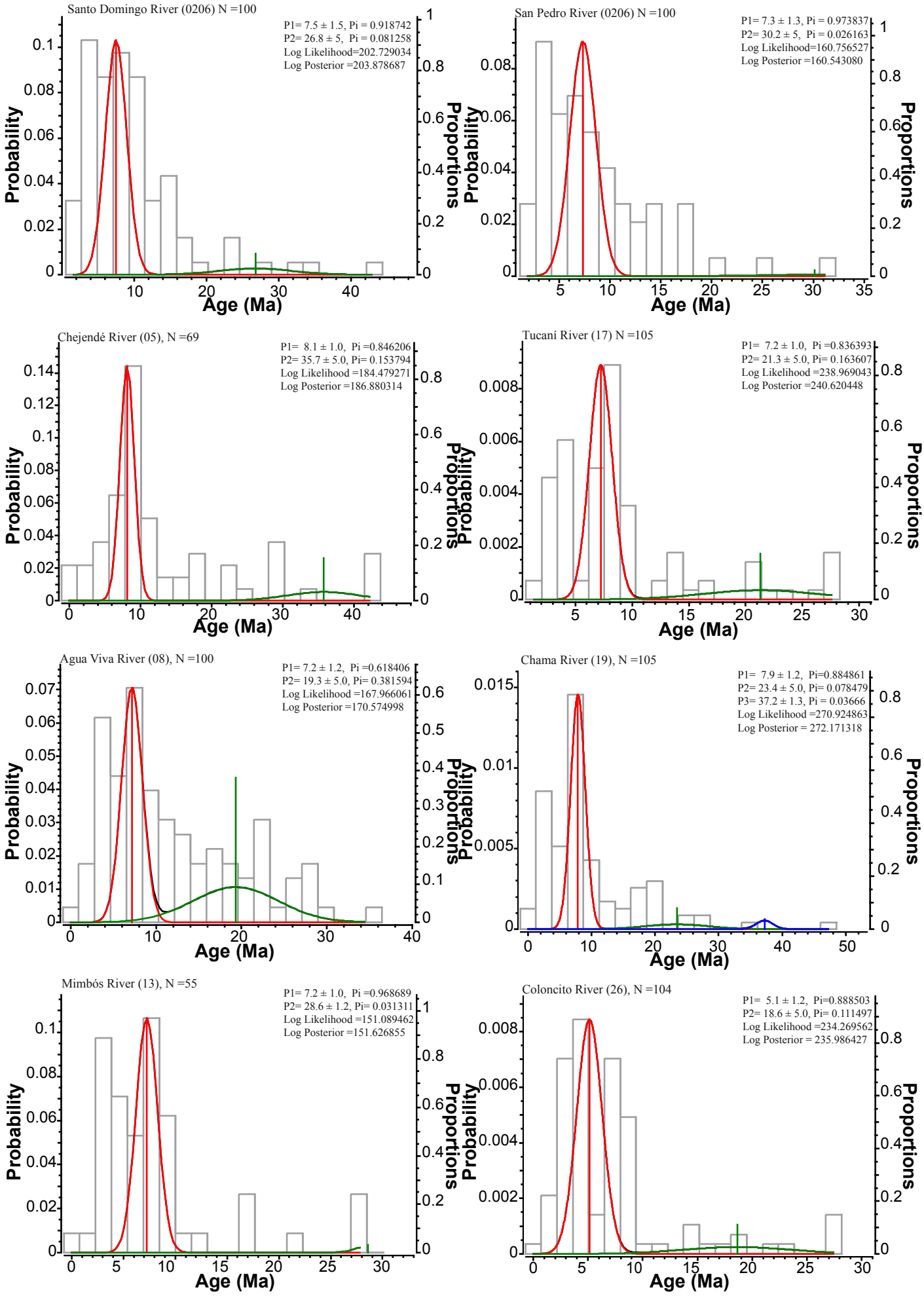

Figure A5. Decomposition into significant ages populations using BayesQt of moder rivern sediments (see Table A2).

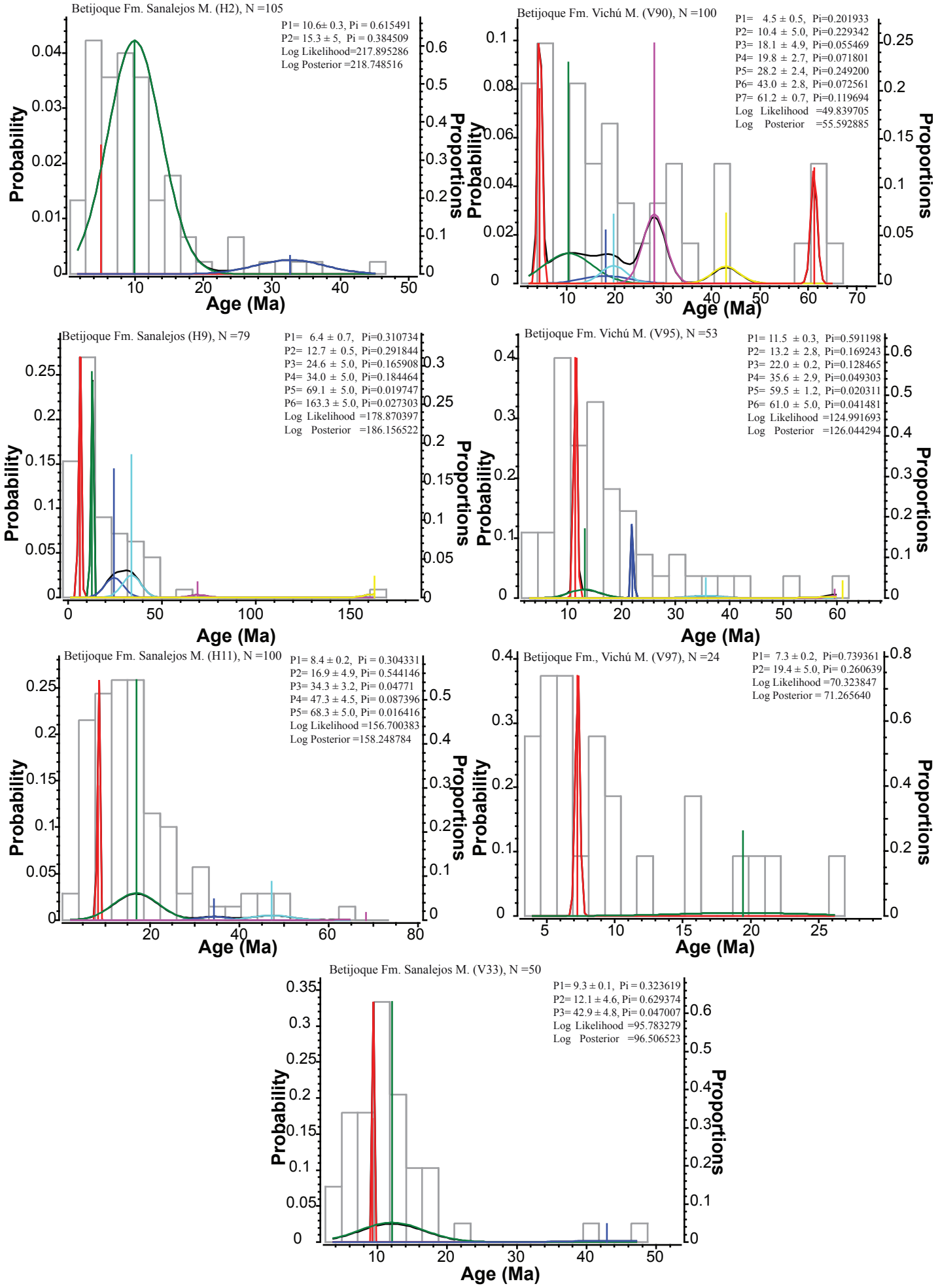

Figure A5 (cont.). Decomposition into significant ages populations using BayesQt of syonorogenic sediments (see Table A2).

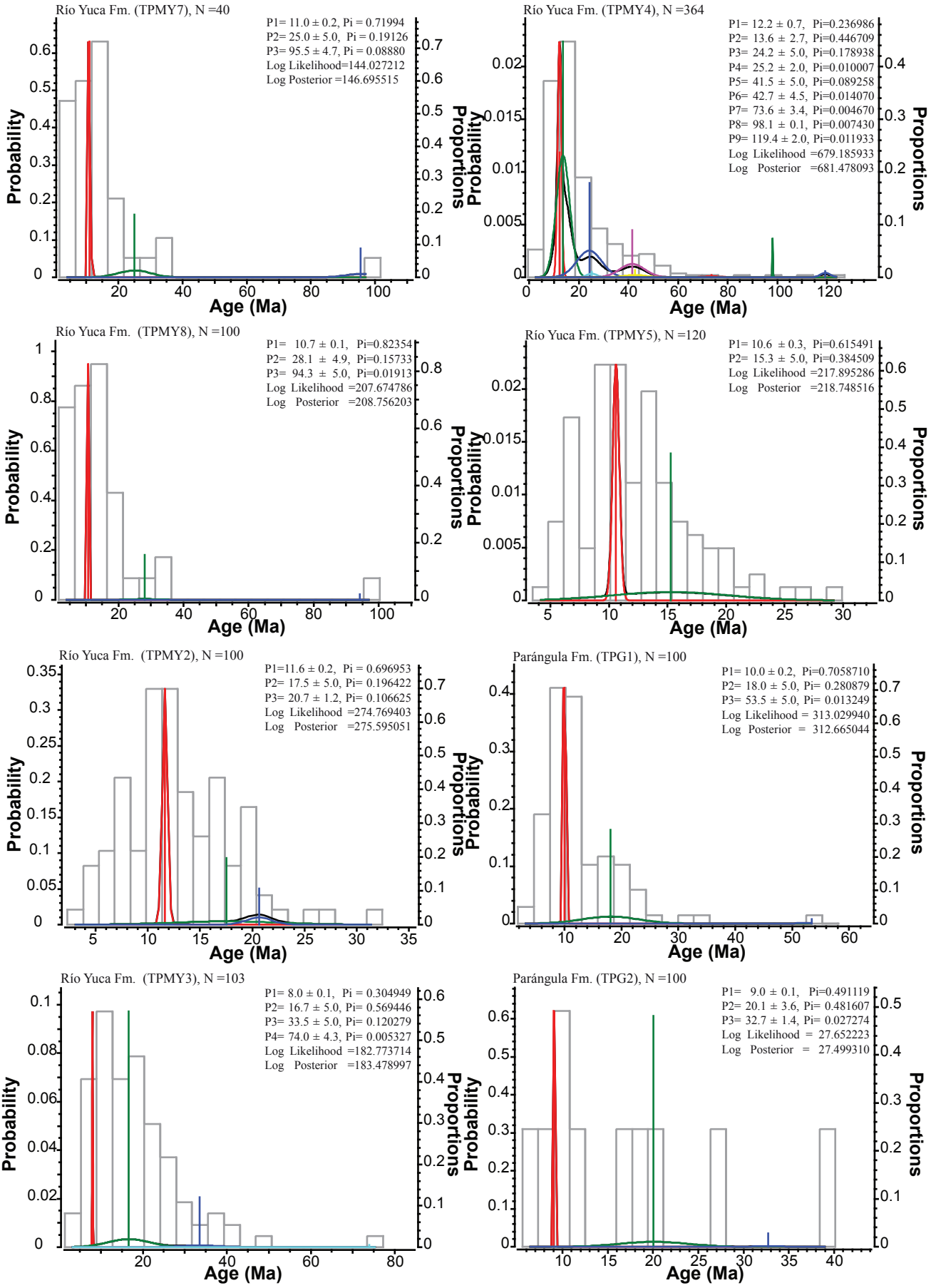

Figure A5 (cont.). Decomposition into significant ages populations using BayesQt for syonorogenic fission-track samples (see Table A2).

APPENDIX 11

TAXA REFERENCES

Cookson, I. C., 1947. Plant microfossils from the lignites of Kerguelen archipelago. Proceedings of the Linnean Society of New South Wales 72, 127-142.

Couper, R.A., 1953. Distribution of Proteaceae, Fagaceae and Podocarpaceae in some Southern Hemisphere Cretaceous and Tertiary beds. New Zealand journal of science and technology B35: 247-250.

Couper, R.A., 1960. New Zealand Mesozoic and Cainozoic plant microfossils. N. Z. Geol. Surv. Paleontol. Bull., 32: 1-87.

Dueñas, H., 1979. Estudio palinológico del pozo Q-E-22 oligoceno superior a mioceno inferior, Planeta Rica, norte de Colombia. Boletín geológico, Bogotá, 22(3), p. 108-109,.

Dueñas, H., 1980. Palynology of Oligocene-Miocene strata of borehole Q-E-22, Planeta Rica, Northern Colombia. Rev. Palaeobot. Palynol., 30: 313-328.

Dueñas, H., 1983. Fluctuaciones del nivel del mar durante el depósito de los sedimentos basales de la Formación Cienaga de Oro. Rev. Acad. Col. Cienc. Exactas, Fis. Nat., 15 (58): 67-76.

Dueñas, H., 1986. Geología y Palinología de la Formación Cienaga de Oro, Región Caribe Colombiana. Bol. Geol. Ingeominas, Publ. Esp., Bogotá, 18, 51 pp.

Frederiksen, N. O., 1988. Sporomorph biostratigraphy, floral changes, and paleoclimatology, Eocene and earliest Oligocene of the eastern Gulf Coast. Unites States Geological Survey Professional Paper, 1448: 1-68.

Germeraad, J. H., Hopping, C.A., and Muller, J., 1968. Palynology of Tertiary sediments from tropical areas. Review of Palaeobotany and Palynology, v. 6, p. 189-348.

González Guzmán, A.E., 1967. A palynological study on the Upper Los Cuervos and Mirador Formations (Lower and Middle Eocene; Tibu area, Colombia). Brill, Leiden, 68 pp.

Hoorn, C., Guerrero, J., Sarmiento, G.A. and Lorente M.A., 1995. Andean tectonics as a cause for changing drainage patterns in Miocene northern South America. Geology 23 (3): 234-240.

Hoorn, C., 1994. Miocene palynostratigraphy and paleoenvironments of northwestern Amazonia: Evidence for marine incursions and the influence of Andean tectonics. Ph. D. thesis, University of Amsterdam, 156 pp.

Hoorn, C., 1994. Fluvial palaeoenvironments in the intracratonic Amazonas Basin (Early Miocene - early Middle Miocene, Colombia). Palaeogeography, Palaeoclimatology, Paleoecology 109: 1-54.

Hoorn, C., 1994. An environmental reconstruction of the palaeo-Amazon River sytem (Middle to Late Miocene, NW Amazonia). Palaeogeography, Palaeoclimatology, Paleoecology 112: 187-238.

Hoorn, C., 1993. Marine incursions and the influence of Andean tectonics on the Miocenedepositional history of northwestern Amazonia: Results of a palynostratigraphic study. Palaeogeography, Palaeoclimatology, Paleoecology 105: 267-309.

Hoorn, C., 1993. Geología del Nororiente de la Amazonia Peruana: la Formación Pebas. In: Amazonia Peruana-vegetación húmeda tropical en el llano subandino. Ed. R. Kalliola, M. Puhakka and W. Danjoy, Paut and Onern, Jyväskylä, Finland.

Hoorn, C., 1993. Book review: Lacustrine facies analysis by Anadon et al.. Geologie en Mijnbouw 72(1): 87-88.

Jaramillo, C., and Dilcher, D., 2001. Middle Paleogene palynology of Central Colombia, South America: A study of pollen and spores from tropical latitudes. Palaeontographica, Vol. 58, p. 87-213.

Kedves, M., and Sole de Porta, N., 1963. Comparación de las esporas del género Cicatricosisporites R. Pot., y Gell. 1933 de Hungria y Colombia. Bol. Geol. Univ. Industr. Santander, 12, p. 51-76.

Krutzsch, W., 1970: Atlas der mittel- und jungtertiaren dispersen Sporen- und Pollen-sowie der Mikroplanktonformen des nordlichen Mitteleuropas. Lieferung 7: Monoporate, monocolpate, longicolpate, dicolpate und ephedroide (polyplicate) Pollenformen. Veb Gustav Fischer Verlag Jena, Berlin. 175 pp.

Krutzsch, W., 1970: Zur Kenntnis fossiler disperser Tetradenpollen. Palaontologische Abhandlungen Abteilung B., Palaeobotanik 3: 399-430.

Krutzsch, W., 1970: Reevesiapollis, ein neues Pollengenus der Sterculiaceen aus dem mitteleuropaischen Tertiar. Feddes repertorium 81: 371-384.

Leidelmeyer, P., 1966. The Paleocene and Lower Eocene pollen flora of Guyana. Leidse Geol. Meded., 38: 49-70.

Lorente, M.A., 1986. Palynology and palynofacies of the Upper Tertiary in Venezuela. Dissertationes Botanicae, 99, 222 pp

Muller, J., 1968. Palynology of the Pedawann and Plateau sandstone formations (Cretaceous–Eocene) in Sarawak, Malasia. Micropaleontology 14, 1-37.

Muller, J., Di Giacomo, E. and Van Erve, A.W., 1987. A palynological zonation for the Cretaceous, Tertiary, and Quaternary of Northern South America. AASP Contrib. Set., 19, 7-76.

Nakoman, E., 1965. Description d'un nouveau genre de forme, Corsinipolleneites. Soc. Geol. Nord Ann., 85: 155-600.

Pflug, H., 1952. Palynologie und Stratigraphie der eozänen Braunkohlen von Helmstedt, Paläontologische Zeitschrift, Volume 26, Numbers 1-2, p. 112-136.

Pierce, R.L., 1961. Lower Upper Cretaceous plant microfossils. Minn. Geol. Surv. Bull., 42: 1-86.

Potonié, R., 1956: Synopsis der Gattungen der Sporae dispersae. I. Teil: Sporites. Beihefte zum Geologischen Jahrbuch 23, 103 p

Potonié, R., 1960: Synopsis der Gattungen der Sporae dispersae. III. Teil: Nachtrage Sporites, Fortsetzung Pollenites. Mit Generalregister zu Teil I-III. Beihefte zum Geologischen Jahrbuch 39, 189 p

Potonié, R., and Gelletich, J., 1933. Über Pteridophyten-Sporen einer eozänen Braunkohle aus Dorog in Ungarn. Sitzungsberichte der Gesellschaft Naturforschender Freunde zu Berlin, 33: 517–528.

Regali, M.S., Uesugui, N. and Santos, A., 1974. Palinologia dos sedimentos Meso-Cenozoicos do Brasil (If). Bol. Tecn. Petrobras, Rio de Janeiro, I7 (4): 263-362.

Takahashi, K.; Jux, U., 1989: Palynology of middle Tertiary lacustrine deposits from the Jos Plateau, Nigeria. Bulletin of the Faculty of Liberal Arts, Nagasaki University, natural science 29: 181-367.

Takahashi, K.; Jux, U., 1989: Palynological investigation of Late Eocene to Early Oligocene lignites from Fayum Oasis, Egypt. Bulletin of the Faculty of Liberal Arts, Nagasaki University, natural science 29: 369-463.

Thiergart, F., 1938 (37): Die Pollenflora der Niederlausitzer Braunkohle, besonders im Profil der Grube Marga bei Senftenberg. Jahrbuch der Preussische geologischen Landesanstalt und Bergakademie zu Berlin 58: 282-356. (Issued separately in 1937; published 1938.)

Thiergart, F., 1949. Der stratigraphische Wert mesozoischer Pollen und Sporen. Palaeontographica, Abteilung 89, 1-29.

Thomson, P.W. & Pflug, H. 1953. Pollen und Sporen des mitteleuropäischen Tertiärs. Palaeontographica Abteilung B, 94: 1–138.

van der Hammen, T. 1956. A palynological systematic nomenclature. Bol. Geol., Bogota v.4, 2-3, p. 63-101.

Van der Hammen, T. and Wijmstra, T.A., 1964. A palynological study on the Tertiary and the Upper Cretaceous of British Guyana. Leidse Geol. Meded., 30:183 241.

Van der Hammen, T. and Garcia de Mutis, C., 1965. The Paleocene pollen flora of Colombia. Leidse. Geol. Meded., 35: 105-16.

Van Hoeken-Klinkenberg, P.M.J., 1964. A palynological investigation of some Upper Cretaceous sediments in Nigeria. Pollen Spores, 6(1): 209-231.

Wodehouse, R.P. 1933. Tertiary pollen II. The oil shales of the Eocene Green River Formation. Torrey Botanical Club Bulletin, 60: 479–524.